Drying Inkjet Droplets - Internal Flows and Deposit Structure

TALBOT, EMMA,LOUISE

Drying Inkjet Droplets - Internal Flows and Deposit Structure

A thesis submitted in partial fulfilment of the requirements for the degree of Doctor of Philosophy in the University of Durham by,

Emma L. Talbot

Department of Chemistry

University of Durham

April 2014

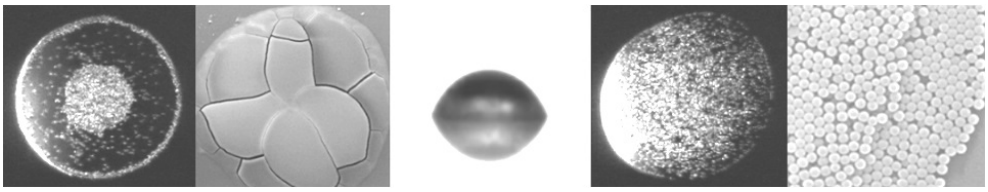

Abstract

Inkjet printing delivers droplets with picolitre volumes onto a substrate. This thesis focuses on improving the quality of inkjet prints by controlling the particle distribution in the deposit. To this end, the internal flows in evaporating droplets were compared on purpose-built imaging rigs. Formulations were developed for deposit control based on the results of this analysis.

Initial studies of pure solvents determined the influence of the substrate wettability and thermal conductivity on evaporation. It was demonstrated that an isothermal model accurately predicted the drying times of picolitre droplets, provided that evaporative cooling was insignificant.

Evaporation of simplified model inks (two solvents + latex particles) was then considered. Marangoni flows transported particles along streamlines, with a circulating region that switched from the droplet centre to the edge on reversing the flow direction. Particles also migrated across streamlines towards the centre of the droplet, independent of the Marangoni flow direction. Large particles migrated faster than smaller particles, forming a tighter central group. Migration mechanisms were considered: Thermophoresis was ruled out due to particle migration in droplets with negligible thermal effects. Chemophoresis was not consistent with all observations of particle migration, though chemophoretic velocities are large enough to contribute. Shear-induced migration to regions of low shear rate is a promising potential migration mechanism.

The deposit macro/microstructures were investigated for pure and binary mixtures. In pure solvents, evaporation-driven radial flow built up a ring stain at the contact line. This stain was inhibited for some binary solvent mixtures. However, in most cases, a ring stain developed after the Marangoni flow period ended. Hence, alternative routes of deposit control were investigated.

Two strategies were developed to control the deposit structure: i) a sol−gel transition in a suspension of a nano-particulate clay (laponite), or ii) depletion flocculation induced by a free polymer (PSS). The latter strategy was the most successful for ethanol/water mixtures, producing a printed dot smaller than the droplet contact area. In water droplets, the sol−gel transition proved a successful method for obtaining a uniform particle distribution in the deposit.

Acknowledgements

Many thanks to my supervisor, Prof. Colin Bain, for the fruitful discussions and opportunities opened to me during my PhD. Thank you also to EPSRC for finacially supporting the project (under grant number EP/H018913/1), and to all the members of the I4T consortium for their help and advice. In particular, Arganthaël Berson, Lisong Yang, Phil Brown and Grace Yow, as without their expertise I would not have managed half so much.

Thank you to my family and friends for their support over a lifetime. I can always count on you to keep me on track. Especially, Jacob, who short of Colin read the most of this thesis.

Last, I would like to extend my appreciation to a fantastic group, whose open friendliness has kept me going all these years at Durham.

Publications List

The following publications were made during the course of this thesis:

Journals

1. E.L. Talbot, A. Berson, P.S. Brown and C.D. Bain, Evaporation of picoliter droplets on surfaces with a range of wettabilities and thermal conductivities, *Phys. Rev. E*, (2012), 85, 061064, 6.

2. E.L. Talbot, L. Yang, A. Berson and C.D. Bain, Control of Particle Distribution in Inkjet Printing through an Evaporation-Driven Sol−Gel Transition, *Appl. Mater. Interf.*, (2014), 6, 12, 9572–9583.

Conferences

1. E.L. Talbot, A. Berson and C.D. Bain, Drying and Deposition of Picolitre Droplets of Colloidal Suspensions in Binary Solvent Mixtures, *NIP28: 28th International Conference on Digital Printing Technologies, and Digital Fabrication 2012, September 2012, The Society for Imaging Science and Technology*, (2012), 420−423, ISSN: 978-0-89208-301-5.

2. E.L. Talbot, A. Berson and C.D. Bain, Internal Flows and Particle Transport Inside Picoliter Droplets of Binary Solvent Mixtures, *NIP29: 29th International Conference on Digital Printing Technologies, and Digital Fabrication 2013, September/October 2013, The Society for Imaging Science and Technology*, (2013), 307−312, ISSN: 978-0-89208-307-7.

Declaration

MATLAB post-processing routines were composed as a joint effort with myself, Arganthaël Berson and Lisong Yang at the University of Durham and further developed by myself for this thesis. The rheology measurements in Chapters 5 and 6 were collected with the aid of Lisong Yang. The interpretation of the data is my own.

The idea and formulation design behind Chapter 6, Section 6.4 of this thesis was devised in collaboration with Simon Biggs and Grace Yow at the University of Leeds. However, all measurements and interpretations are my own.

Polystyrene spheres used in this project were synthesised by Grace Yow at the University of Leeds, who provided the zeta-potentials. Coated substrates were fabricated by Phil Brown at the University of Durham (in conjunction with Prof. J.P.S. Badyal), who provided the XPS and AFM characterisation.

Copyright notice

Contents

Symbols list

In order of appearance:

Re	Reynolds number
ρ_f	fluid density, $\mathrm{kg\,m^{-3}}$
v_d	droplet impact velocity, $\mathrm{m\,s^{-1}}$
D_0	droplet diameter in flight, m
η	fluid viscosity, mPas
We	Weber number
σ	surface tension of fluid
Oh	Ohnesorge number
R	contact radius of droplet, m
t	time, s
N	constant in Tanner's law
Bo	Bond number
g	gravitational acceleration, $\mathrm{m\,s^{-2}}$
Ca	Capillary number
σ_sv	solid-vapour interfacial tension, $\mathrm{N\,m^{-1}}$
σ_sl	solid-liquid interfacial tension, $\mathrm{N\,m^{-1}}$
σ_lv	liquid-vapour interfacial tension, $\mathrm{N\,m^{-1}}$

r_{c}	radius of curvature, m
P	Laplace pressure, Pa
h	apex height of droplet, m
θ	three phase apparent contact angle
V	volume of droplet, m^3
θ_{A}	advancing contact angle
θ_{R}	receding contact angle
θ_{W}	Wenzel contact angle on a rough surface
r_{s}	roughness factor
θ_{eq}	equilibrium contact angle on a smooth surface
B	proportion of heterogenous surface with wettability type B
C	proportion of heterogenous surface with wettability type C
θ_{B}	contact angle on a heterogeneous surface B
θ_{C}	contact angle on a heterogeneous surface C
θ_{CB}	Cassie-Baxter contact angle on a rough surface
x_{A}	mole fraction of component A
x_{B}	mole fraction of component B
p_{s}	total vapour pressure of solvent s, Pa
p_{A}	partial vapour pressure of solvent A, Pa
p_{B}	partial vapour pressure of solvent B, Pa
p_{A}^*	vapour pressure of solvent A, Pa
p_{B}^*	vapour pressure of solvent B, Pa
γ_{A}	activity coefficient of component A
μ_{A}	chemical potential of component A, Jmol^{-1}

$\mu_{\mathrm{A}}^{\ominus}$	chemical potential of A in the standard state, $\mathrm{J\,mol^{-1}}$
R_{u}	universal molar gas constant, $\mathrm{J\,mol^{-1}\,K^{-1}}$
T	temperature, K
a_{A}	activity of component A
c	concentration, $\mathrm{mol\,dm^{-3}}$
D	vapour diffusion coefficient in the ambient atmosphere, $\mathrm{m^2\,s^{-1}}$
t_{diff}	diffusion timescale, s
t_{dry}	drying time, s
n_{s}	saturation vapour density, $\mathrm{kg\,m^{-3}}$
n_{∞}	ambient vapour density, $\mathrm{kg\,m^{-3}}$
J	evaporative flux, $\mathrm{kg\,m^{-2}\,s^{-1}}$
r	radial distance from the centre of the droplet, m
θ_i	initial contact angle
R_i	initial contact radius of droplet, m
m	constant exponent relating to motion of contact line
x	tangential co-ordinate
n	normal co-ordinate
v_{s}	settling velocity, $\mathrm{m\,s^{-1}}$
ρ_{p}	density of the particle, $\mathrm{kg\,m^{-3}}$
a	radius of the particle, m
σ_{c}	yield stress, Pa
G'	elastic storage modulus, Pa
G''	loss modulus, Pa
γ_{c}	critical strain

λ	wavelength, nm
n_{a}	refractive index of air
n_{w}	refractive index of water
θ_{in}	angle of incidence
θ_{r}	angle of refraction
n_{i}	refractive index
$\bar{x}_{\mathrm{B}}$	mean Brownian displacement, m
D_p	diffusion coefficient of a particle in a fluid, $\mathrm{m^2\,s^{-1}}$
t_{c}	characteristic timescale, s
k_{B}	the Boltzmann constant, $\mathrm{kg\,m^2\,s^{-2}\,K^{-1}}$
$v_{\mathrm{n,dry}}$	normalised particle velocity using the drying time
$v_{\mathrm{n,Rg}}$	normalised particle velocity using the time to reach a minimum radius of the collected particle group
R_{n}	radius of intersection from droplet centre to contact line
t_{Rg}	time for collecting particle group to reach minimum radius
$\bar{v}_{\mathrm{r}}$	mean radial particle velocity, $\mu\mathrm{m\,s^{-1}}$
$\bar{w}$	mean ring width, μm
ϕ_{n}	fractional area of coverage of the deposit, pix^2
ϕ_{t}	total area of coverage of the deposit, pix^2
$\phi_{\mathrm{n,norm}}$	normalised fractional area of coverage of the deposit
Pe	Péclet number
u	velocity of fluid, $\mathrm{m\,s^{-1}}$
α	thermal diffusivity, $\mathrm{m^2\,s^{-1}}$
M	mass of droplet, kg

t_p	drying time in constant contact radius mode, s
$t_{\mathrm{p},\theta}$	drying time in constant contact radius mode in the small angle approximation, s
t_M	drying time in constant contact angle mode, s
t_hem	drying time of hemisphere with freely moving contact line, s
κ	thermal conductivity of substrate, $\mathrm{W\,m^{-1}\,K^{-1}}$
t_exp	experimentally observed drying time, s
p	vapour pressure, kPa
t_Rg	time to reach the minimum radius of the particle group, s
σ'	surface tension variation with composition, $\mathrm{N\,m^{-1}}$
x_v	volume fraction
u_max	maximum flow velocity at liquid-vapour interface, $\mu\mathrm{m\,s^{-1}}$
u_0	fastest flow velocity close to substrate, $\mu\mathrm{m\,s^{-1}}$
h_0	height above substrate that fastest flow velocity occurs, μm
h_1	height below liquid-vapour interface of zero velocity, μm
h_2	height above substrate of zero flow velocity, μm
H	height of the liquid-vapour interface above substrate, μm
u_r	radial velocity of fluid, $\mu\mathrm{m\,s^{-1}}$
η_i	initial viscosity, mPa s
D_s	vapour diffusion coefficent of solvent s in air, $\mathrm{m^2\,s^{-1}}$
D_w	vapour diffusion coefficent of water in air, $\mathrm{m^2\,s^{-1}}$
RH_s	relative humidity solvent s
RH_w	relative humidity
p_w	partial vapour pressure of water, Pa
p^*_w	vapour pressure of water, Pa

x_{w}	mole fraction of water
a_{PM}	radius of a methoxypropanol molecule, m
M_{PM}	molecular weigh of methoxypropanol, $\mathrm{g\,mol^{-1}}$
N_{A}	Avogadro's constant, $\mathrm{mol^{-1}}$
d_{PM}	collision cross-section for methoxypropanol, $\mathrm{m^2}$
a_{N}	radius of nitrogen, m
λ_{PM}	mean free path for methoxypropanol in air, m
p_{atm}	atmospheric pressure, Pa
$\bar{c}$	mean speed, $\mathrm{m\,s^{-1}}$
D_{PM}	vapour diffusion coefficent of methoxypropanol in air, $\mathrm{m^2\,s^{-1}}$
ϵ_{r}	dielectric constant
R_{g}	radius of the collecting particle group, μm
R_{h}	radius of hole at the centre of collecting particle group, μm
$R_{\mathrm{g,min}}$	minimum radius of the collecting particle group, μm
D_{ew}	mutual diffusion coefficent of ethanol/water mixture, $\mathrm{m^2\,s^{-1}}$
v_{g}	velocity of the collecting particle group, $\mu\mathrm{m\,s^{-1}}$
$R_{\mathrm{g,L}}$	radius of collecting particle group for large particles, μm
$R_{\mathrm{g,S}}$	radius of collecting particle group for small particles, μm
$R_{\mathrm{t,L}}$	group centric radius for large particles in toroid, μm
$R_{\mathrm{t,S}}$	group centric radius for small particles in toroid, μm
R_{t}	group centric radius for particles in the toroid, μm
Re_{p}	particle Reynolds number
δ	solubility parameter, $\mathrm{J^{1/2}\,cm^{-3/2}}$
F_{σ}	force attributed to a gradient in the surface tension, N

E	surface energy, J
F_{d}	drag force, N
ρ_{e}	density of ethanol, $\mathrm{kg\,m^{-3}}$
r_0	pre-impact radius, μm
Q	heat loss, J
ΔH_ν	latent heat, $\mathrm{J\,kg^{-1}}$
d_{g}	diffusion length in glass, m
d_{s}	diffusion length in sapphire, m
$D_{\mathrm{th,g}}$	thermal diffusivity of glass, $\mathrm{m^2\,s{-}1}$
$D_{\mathrm{th,s}}$	thermal diffusivity of sapphire, $\mathrm{m^2\,s{-}1}$
V_{g}	diffusion volume in glass, $\mathrm{m^3}$
V_{s}	diffusion volume in sapphire, $\mathrm{m^3}$
ρ_{g}	density of glass, $\mathrm{kg\,m^{-3}}$
ρ_{s}	density of sapphire, $\mathrm{kg\,m^{-3}}$
c_{p}	specific heat capacity, $\mathrm{J\,kg^{-1}\,K^{-1}}$
$\dot{\gamma}$	shear rate, $\mathrm{s^{-1}}$
ϵ	ratio of the elastic modulus to the capillary pressure
u_{e}	velocity of droplet ejection from the nozzle, $\mathrm{m\,s^{-1}}$
R_{nz}	radius of the nozzle orifice, m
z	deposit height, nm
r_{D}	Debye length, m
ϵ_0	relative permittivity of free space
e	elementary charge
I	ionic strength, $\mathrm{mol\,dm^{-3}}$
D_{av}	average diffusion coefficent for a disk, $\mathrm{m^2\,s^{-1}}$

$D_{\parallel}$	diffusion coeffient parallel to the face of a disk, $\mathrm{m^2\,s^{-1}}$
$D_{\perp}$	diffusion coeffient perpendicular to the face of a disk, $\mathrm{m^2\,s^{-1}}$
D_{sp}	diffusion coeffient for a sphere, $\mathrm{m^2\,s^{-1}}$

Abbreviations

CIJ	continuous inkjet
DOD	drop-on-demand
PZ	piezoelectric device
RH	relative humidity
LED	Light Emitting Diode
NA	Numerical Apperture
PM	methoxypropanol
IPA	isopropanol
PnP	propoxypropanol
PEGMA	poly(ethylene glycol) monomethyl ether methacrylate
PNVP	poly(N-vinylpyrrolidone)
HEC	hydroxyethylcellulose
PSS	polystyrene sulfonate
SEM	scnning electron microscope
WLI	white light interferometer
RMS	root mean squared
VS	vapour shroud
EG	ethylene glycol

1 Introduction

1.1. Motivation and chapter summary

Inkjet printing is used for a diverse range of applications across many sectors. The diversity of inkjet printing conveys the value placed on improving inkjet systems and gaining a deeper understanding of the behaviour and processes involved during deposition. Relatively little research explores the internal flows and evaporation of the picolitre-scale droplets used for inkjet printing. Instead, the bulk of the literature covers microlitre droplets. However, the assumption that the results of microlitre studies are applicable to picolitre droplets is not necessarily true.

Furthermore, few literature studies deal with the entirety of the drying period, often only investigating the end deposit. For a clear picture of the transport processes during drying, it is necessary to follow the internal flows throughout the lifetime of the droplet to discover how the end deposit is built-up. This thesis aims to reach a better understanding of the fundamental flows and transport processes that occur inside inkjet-size drying droplets and to use these concepts to develop methods for controlling the end deposit. Relatively simple model inks (solvent plus spherical particles) are used in place of the largely complex industrial inks. Complexity is added gradually by first looking at pure solvents, prior to investigating binary mixtures with particles included to investigate the effect of multiple solvents on the deposit. Knowledge of the particle transport is then implemented to develop new fixing strategies for the end deposit using structured complex fluids. This work is important for the development of industrial inkjet printing as well as furthering academic research in the area of evaporating droplets. While there are many areas to improve on, this thesis focuses on the drying behaviour after the droplet impact and

spread on the substrate.

There are three separate issues dealt with in this thesis: First, the effect of the substrate conductivity on the evaporation of single solvent droplets is investigated. Second, the internal flows and particle transport inside binary solvent mixtures are explored. Last, fixing strategies are developed for controlling the particle distribution in the deposit. This last angle of investigation is subdivided into methods for obtaining a uniform deposit and for producing a small circular dot for high resolution printing.

In this chapter, the motivation behind the work comprising the thesis and the potential benefits for the field of inkjet printing are discussed. The main theoretical concepts relevant to the work undertaken are introduced here, including impact, spreading and wetting, evaporation (and evaporative cooling), the "coffee ring effect", and Marangoni flows. There is also a review of the main literature contributions for droplet evaporation, internal flows, and control of the deposit. The evaporation of single solvent droplets and binary solvent mixtures are discussed, including both experimental and theoretical results. Pattern formation in drying colloidal droplets is reviewed with reference to suppressing the "coffee ring effect".

Chapter 2 describes the main methods and set-ups used for the experimental work carried out. Also, post-processing routines for image analysis and particle tracking are described herein.

Chapter 3 investigates the relationship between the substrate conductivity and the evaporation rate for picolitre droplets, to determine the validity of isothermal models for drying time estimates. Both pinned and moving contact line drying modes are considered for contact angles above and below 90°.

Chapter 4 compares the internal flows of evaporating single solvent droplets with binary solvent mixtures that exhibit Marangoni flows. Particle transport mechanisms are reviewed in detail here, including phoresis and shear-induced migration. The circulating flows that develop in the binary mixtures are tracked throughout the drying lifetime. Particle migration is followed during the Marangoni flow period and mechanisms for the migration are discussed. The deposit morphology of the dried droplets is related to both transport mecha-

nisms.

Chapter 5 concentrates on a fixing method for a uniform particle distribution using laponite clay. An evaporation-driven sol-gel transition, resulting from the concentration of the laponite particles during drying, controls the extent of radial motion of particles towards the contact line. Particle positions are fixed as they reach the gelling front, which propagates inwards. The result is a uniform particle distribution in the end deposit, rather than the typical ring stain.

Chapter 6 combines the particle migration observed in binary solvent mixtures with a mechanism for fixing the particle distribution. This fixing strategy retains the particles in a concentrated central group, allowing the printing of a deposit with a smaller diameter than the initial droplet diameter. In this manner, the resolution of printed features can be enhanced even for droplets drying with a pinned contact line. Potential fixing strategies are reviewed in detail here, before selecting two promising mechanisms for investigation. The two fixing methods chosen were: first, the sol-gel method from Chapter 5, and second, a method based on depletion flocculation of the concentrated particle group due to the addition of a free polymer.

Concluding remarks are given in Chapter 7, with reference to future development.

1.2. Inkjet printing

Inkjet is a highly versatile printing method capable of delivering precise volumes of colloidal suspension to a substrate through non-contact deposition [1]. There are two main modes of inkjet printing: continuous inkjet (CIJ), wherein droplets are formed in a continuous manner, and drop-on-demand (DOD), wherein droplets are formed only when they are required.

CIJ was developed following early observations of the break-up of a liquid jet into droplets [2]. Fluid is forced through a small orifice (nozzle) forming a jet, which is broken-up into droplets due to an applied perturbation (Fig. 1.1a). The perturbation induces a Plateau-Rayleigh instability, causing bulges to form in the cylindrical jet. These bulges have lower curvature (and lower pressure)

than the neck regions (negative curvature). The pressure gradient drives a fluid flow towards the lower pressure, enhancing the bulge and depleting the neck. Eventually, pinch-off occurs when the neck radius reaches zero, forming a spherical droplet to minimise its surface energy. The applied perturbation ensures this break-up produces droplets with a controlled size and frequency.

The continuous formation of droplets requires a mechanism to allow printing onto a substrate to be switched on or off to form patterns. Commonly, droplets are charged by an electrode at the break-up length, then deflected by a set of charged plates further downstream. To print onto the substrate, no deflection is applied. To leave a gap in the print, charged droplets are deflected into a collection area (which is often re-circulated to the nozzle to reduce waste).

DOD has a more refined ejection technique than simply forcing fluid through a nozzle. Typically, ejection is actuated via a piezoelectric device (PZ) [3, 4] or via a thermal mechanism (referred to as the "bubble method") [5, 6]. The piezoelectric method has a PZ situated either near or around the nozzle (Fig. 1.1b), which expands or contracts in response to an applied electric field. If the PZ is close to the nozzle, an expansion of the PZ reduces the volume inside the nozzle, increasing the pressure and thus expelling the fluid. If the PZ is surrounding the nozzle, when the PZ contracts fluid is forced out the orifice. Thermal DOD processes utilise a small heater in close proximity to the nozzle. The temperature of the ink immediately next to the heater is increased rapidly, causing the ink to boil. Upon boiling, a vapour bubble forms, expanding to displace ink from the nozzle. The

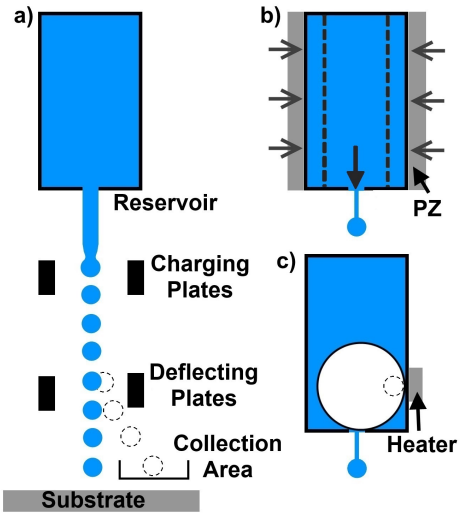

Figure 1.1. a) Jet ejection and droplet break-up from a CIJ nozzle. Droplet ejection for a DOD printhead actuated by b) contraction of a piezoelectric (PZ) device surrounding the nozzle, and c) thermal bubble formation and expansion.

bubble remains only while the heater is on, and thus by switching the heater on and off, repeated droplet formation can be achieved.

Once the droplet has been actuated, the behaviour on exiting the nozzle is similar for each DOD technique: Fluid ejected from the nozzle forms a droplet with a connected ligament [7, 8]. Under the appropriate conditions, the ligament pinches-off, retracting back into the nozzle and leaving a spherical droplet (Fig. 1.2a). "Suck-back", can invert the meniscus post-drop-ejection (e.g. Fig. 1.2aiii and Fig. 1.3b). Alternatively, pinch off at the nozzle may result in the ligament joining the droplet, forming a droplet of larger volume. If pinch-off does not occur, the droplet remains attached and can be pulled back into the nozzle (Fig. 1.2b). The re-entry of the droplet into the nozzle can cause a misfire of the subsequent droplet in addition to the retracted one, due to disturbance of the meniscus. The ligament may also pinch-off at both ends or break-up into multiple fragments, forming satellites (smaller secondary droplets) along with the primary droplet (Fig. 1.2c). These satellites can degrade the print quality.

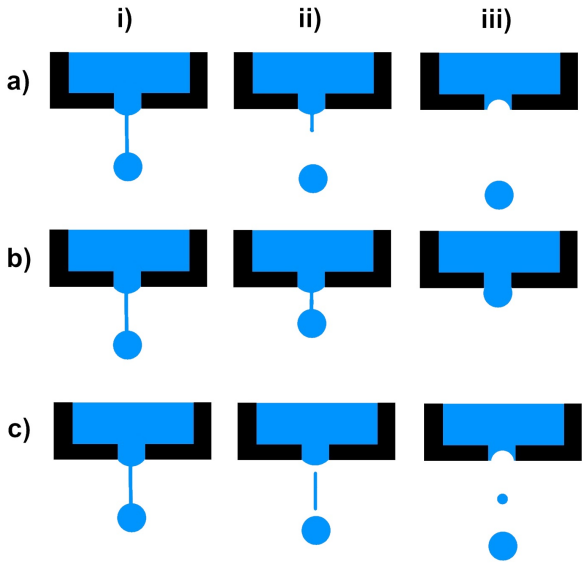

Figure 1.2. Cartoon representation of ligament formation, pinch-off and droplet formation in a DOD printhead. a) Ideal droplet formation; the ligament stretches, pinch-off occurs near the droplet and the ligament retracts into the nozzle. b) Bungee-behaviour; the ligament stretches but does not pinch-off, the droplet and ligament retract back into the nozzle. c) Satellite formation; the ligament stretches and pinch-off occurs at both ends of the ligament, forming a satellite that follows the main droplet. The sequence i) to iii) indicates the progression of time.

Common problems during inkjet printing include print failure (where no

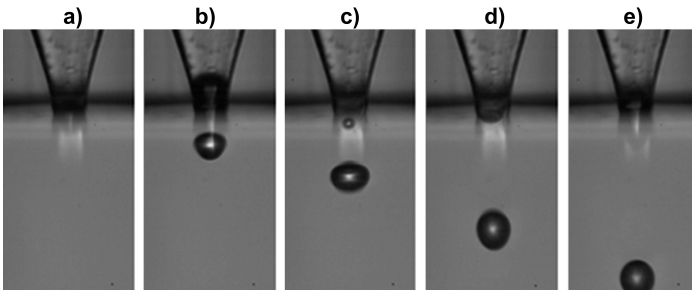

Figure 1.3. Drop-on-demand ejection of a droplet from a Microfab printhead, demonstrating suck-back of the meniscus after ligament break-up and drop formation.

droplet is ejected), and mis-directed droplets (where the droplet is not deposited at the desired location). Potential causes for print failure include misfiring [9,10] (retracted droplets [8], air bubbles [11,12], or an incorrect perturbation waveform [13]), obstruction of the nozzle resulting from material deposits (e.g. drying in the nozzle or blocking by large aggregates) [14,15], and flooding of the nozzle plate [16]. An example of nozzle obstruction is the formation of a particulate film across the nozzle (referred to as clogging). Clogging occurs if the fluid at the meniscus remains there for sufficient time to allow particulates to build-up across the orifice. CIJ print-heads clog less frequently than DOD print-heads (despite the use of volatile solvents), as the fluid at the meniscus is constantly replenished, reducing the likelihood of drying in the nozzle. Hence, more volatile solvents do not present the same problems as for DOD, and indeed are often required for the high speed (fast drying) printing applications of CIJ. Both CIJ and DOD are susceptible to nozzle blockage due to large particles in the ink (comparable to the orifice dimensions) or aggregates in the nozzle. Mis-direction of droplets can result from satellites, or tail-hooking [17], whereby the ligament is not formed centrally, but to one side of the nozzle opening. Such defects can be disastrous for the high precision deposition required for many DOD applications (e.g. micro-circuity), but are less problematic for low-quality, high-throughput applications (e.g. bar-coding) which often make use of the faster print speeds of CIJ.

Inkjet offers many benefits over conventional printing methods. Layers of functional material can be built up through an additive process by multiple passes of the print-head, wasting less material. Relative to lithographic me-

thods the speed at which components can be produced is faster and does not require a mask. The printed output can also easily be changed on-the-fly, with no need for repeating patterns. Precise control over the droplet volume lends itself well to dosing tablets or preparing biodegradable polymeric particles or drug capsules with accurately predicted sizes and shell widths for timed drug delivery [18].

The wide range of printable fluids makes inkjet printing accessible for numerous applications far exceeding the standard graphical inkjet printer (see Fig. 1.4). Examples include the printing of metallic nanoparticles for wires on micro-circuit boards [19–22], conducting/semi-conducting or doped polymers for organic electronic devices [23–26], biological samples for high throughput micro-assays, tissue engineering applications or cellular scaffolds [27–30], pharmaceutical compounds for accurate dosing of tablets [31], dyes for bar-codes for tracking and security [32], and ceramics for rapid prototyping, 3D printing and prostheses [33–37]. The range of substrates is equally large, encompassing rigid, flat, flexible, porous, rough and 3D structures.

Figure 1.4. Examples of inkjet applications, including a flexible display (from [38]), a microassay of DNA (from [39]), printed labels on pharmaceutical tablets (adapted from [40] and [41]), a 3D mock-up of a turbine (from [42]), 3D-printed shoes (from [43]), and packaging labels.

Although inkjet is capable of printing a broad range of fluids, formulation of an ink can be a complex process. The life of the ink must be considered from the shelf to the end deposit. The ink must therefore be stable for long periods on the shelf, and while in the print-head. The ink must also comply

with the surface tension, viscosity, and elasticity limitations required to allow jetting from the print-head, which in turn limits the pigment loading of the ink. Typical inks can comprise multiple-component fluids which are often laden with surfactants and/or polymers as dispersants for a particulate pigment. The flows inside even simple colloidal dispersions can quickly become very complicated, with Marangoni flows and particle interactions [44, 45]. These flows are often poorly understood and attributed only to "Marangoni effects".

Desirable features in a printed deposit usually include a uniform particle distribution and high optical density. For example, in graphics printing a uniform deposit requires the minimum amount of ink for a given colour density. However, printing a lower pigment concentration results in a lower optical density within the deposit. Additionally, a contact line that is pinned at a constant radius is desirable to produce a well-defined edge to the deposit: contact lines that retract during drying often lead to irregular deposits and poorly controlled properties. Thus, the wetting behaviour of the ink on the substrate must be controlled to obtain an optimum deposit.

1.3. Delivery onto substrate: Impact, spreading and wetting

Once a droplet has been actuated it is deposited onto a substrate via impact, spreading and drying. The pressure change on drop impact results in a deformation of the droplet shape dependent on the magnitude of inertial forces, kinetic energy and the angle of impact. The impact and spreading regimes can be characterised by dimensionless numbers. For micrometer droplets, four main impact/spreading regimes were characterised by the Reynolds and Weber numbers (and hence the Ohnesorge number) [46].

The Reynolds number, Re, represents the ratio of inertial forces to viscous forces, and is given by

$$Re = \frac{\rho_{\mathrm{f}} v_{\mathrm{d}} D_0}{\eta}, \tag{1.1}$$

where D_0 is the droplet diameter in flight, ρ_{f} is the fluid density, v_{d} is the impact velocity and η is the fluid viscosity. The Weber number, We, describes

the ratio of the inertial forces to the surface tension, σ, and is given by

$$We = \frac{\rho_{\mathrm{f}} v_{\mathrm{d}}^2 D_0}{\sigma}. \tag{1.2}$$

Drop-on-demand inkjet devices deliver droplets to the substrate with impact speeds of $\backsim 1{-}5\ \mathrm{m\,s^{-1}}$. For an ethanol droplet ($\rho_{\mathrm{f}} \backsim 780\ \mathrm{kg\,m^{-3}}$, $\eta \backsim 1.2\ \mathrm{mPa\,s}$, $\sigma \backsim 22\ \mathrm{mN\,m^{-1}}$), with an impact velocity of $1.5\ \mathrm{m\,s^{-1}}$ and pre-impact diameter of $50\ \mu\mathrm{m}$, the corresponding Reynolds and Weber numbers are $\backsim 49$ and $\backsim 4$ respectively.

The Ohnesorge number describes the ratio of viscous forces to surface tension effects, and corresponds to

$$Oh = \sqrt{We}/Re = \eta/\sqrt{\rho_{\mathrm{f}} \sigma D_0}. \tag{1.3}$$

For the ethanol droplet described above, the Ohnesorge number is $\backsim 0.04$.

The breadth of printable inkjet fluids is limited by the surface tension and viscosity of the fluid. In order to eject a droplet for adequate printing (i.e. without satellites or splashing) using DOD methods, the Ohnesorge number must fall in the range $0.1{-}1.0$ [47]. The Weber number must also reach a threshold value ($We \gtrsim 4$) for droplet ejection from the nozzle. In this regime, the droplet has enough kinetic energy to overcome surface tension during ejection [47]. For $Re > 1$, the droplet has sufficient kinetic energy to overcome viscous dissipation. For a kinetic energy of impact lower than the surface energy of the droplet ($We < 12$), the droplet undergoes only small shape deformations on impact. As We increases, the droplet is deformed more and spreads to a diameter greater than the equilibrium diameter before recoiling.

On impact the droplet may wet the substrate and the contact line will spread/recede in accordance with the advancing and receding contact angles. Tanner's law [48] predicts the spreading of the contact radius, R, with time, t, to be

$$R(t) \propto t^N, \tag{1.4}$$

where N is a constant that depends on the rate of energy dissipation near to the contact line ($N = 0.1$ for the viscous spreading of small drops).

Both gravity and surface tension may determine the shape of a sessile droplet. Surface tension strives to maintain a spherical cap shape, while gravity acts to flatten the profile. The ratio of these effects is parametrised by the Bond number

$$Bo = \rho_f g R^2/\sigma, \tag{1.5}$$

where g is the gravitational acceleration. For the picolitre droplets discussed in this thesis, the Bond numbers, Bo, are typically of the order 10^{-2}. Viscosity may also deform the droplet shape from a spherical cap.

The Capillary number, Ca, represents the relative influence of the surface tension and viscous effects

$$Ca = \eta v_d/\sigma, \tag{1.6}$$

and is typically of the order of 10^0 (for ethanol or water droplets).

As $Bo \ll 1$, gravitational deformation of the droplet is negligible, and as $Ca \ll 1$, the droplet profile is determined by the surface tension, forming a spherical cap. For a sessile droplet at equilibrium on an ideal substrate, (i.e. smooth and chemically homogeneous), the surface tension balance is described by the Young-Laplace equation,

$$\sigma_{sv} = \sigma_{sl} + \sigma_{lv}\, cos(\,\theta\,), \tag{1.7}$$

which dictates the equilibrium contact angle (Fig. 1.5a). Here, σ_{sv} is the solid-vapour interfacial tension, σ_{sl} is the solid-liquid interfacial tension and σ_{lv} is the liquid-vapour interfacial tension. The capillary pressure inside a water droplet in this thesis with radius of curvature, r_c, can be estimated by the Laplace pressure ($P \backsim 2\sigma/r_c$), which is typically $\backsim 10^2$ Pa. The droplet profile is a spherical cap with an apex height, h, given by

$$h = R\, tan\,(\theta\,/\,2)\,, \tag{1.8}$$

where R is the contact radius (footprint) and θ is the three-phase contact angle (Fig. 1.5b). The volume of a droplet conforming to a spherical cap, V, can be

calculated using

$$V = \frac{\pi h}{6}\left(3R^2 + h^2\right) = \pi R^3 \, \frac{\cos^3\theta - 3\cos\theta + 2}{3\sin^3\theta}. \tag{1.9}$$

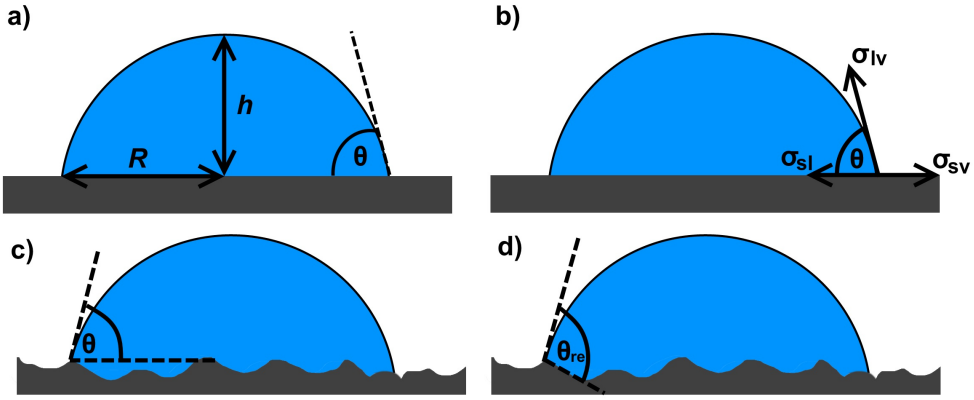

Figure 1.5. Schematic of a partially wetting sessile droplet indicating a) the equilibrium surface tension balance at the three-phase contact line, b) the apex height, h, contact radius, R, and contact angle, θ, c) the apparent (measured) contact angle on a rough substrate, θ , and d) the real contact angle on a rough substrate, θ_{re}.

In practice, the substrate is non-ideal with surface roughness and chemical heterogeneity. The contact angle may take any value between the advancing contact angle, θ_A and receding contact angle, θ_R. The difference between θ_A and θ_R describes the contact angle hysteresis [49,50].

The roughness of a surface can determine the spreading of a droplet depending on the scale of roughness [51]. The effect of surface roughness on the contact angle, compared to a smooth surface, is described by the Wenzel equation [52],

$$cos\,\theta_{\mathrm{w}} = r_s \, cos\,\theta_{\mathrm{eq}}, \tag{1.10}$$

where θ_{w}, is the apparent contact angle on a rough surface (Wenzel contact angle), θ_{eq} is the apparent contact angle on a smooth surface, and r_s is the roughness factor (the ratio of the surface area accounting for roughness features, compared to that of a smooth surface). The contact angle is defined as an equilibrium contact angle if the Gibbs free energy is at a minimum. The apparent contact angle (see Fig. 1.5c) is defined by the contact angle between

a tangent to the liquid-vapour interface at the contact line and the apparent substrate (ignoring surface roughness). The actual real contact angle follows the roughness features of the substrate (Fig. 1.5d).

When the surface is not homogeneous, the Wenzel equation no longer gives a sufficient description of the wetting behaviour and instead the Cassie-Baxter model is required [53]. For a heterogeneous surface with areas of different wettability in proportions B and C, with apparent contact angles of θ_{B} and θ_{C} respectively, the apparent contact angle on the heterogeneous surface (Cassie-Baxter angle), θ_{CB}, is given by

$$cos\,\theta_{\mathrm{CB}} = B\,cos\,\theta_{\mathrm{B}} + C\,cos\,\theta_{\mathrm{C}}. \tag{1.11}$$

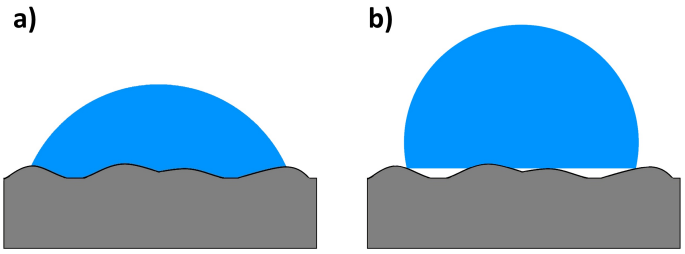

Figure 1.6. Cartoon of a droplet in a) a Wenzel wetting regime, penetrating the surface roughness features, and b) in a Cassie-Baxter wetting regime, sitting ontop of the roughness features.

When a droplet fully penetrates the roughness features of a homogeneous surface, a Wenzel wetting regime occurs (Fig. 1.6). If the surface is chemically heterogeneous then a Cassie-Baxter wetting state occurs. The surface can be considered heterogeneous if the droplet does not penetrate the roughness features but sits on top of air pockets, forming a composite air-solid surface. In the Cassie-Baxter regime, the contact area with the surface is minimised, resulting in a smaller contact angle hysteresis than for the Wenzel regime. A transition between the two wetting regimes can be observed on the collapse of the Cassie-Baxter state to wet the substrate [54].

Many inkjet substrates are porous (e.g. paper). Depending on the surface porosity, a droplet can both spread across the surface and penetrate the surface. Fast draining of fluid into large pores can reduce the "coffee ring effect" [55],

but particles may also be pulled into the pores, leaving little on the surface. For most inkjet printed droplets, the pigment is required to remain on the surface, while the solvent penetrates for quick drying.

In summary, a printed droplet impacts the surface, spreads and wets (depending on the surface energy of the substrate). Post-impact, the shape of the droplet on the substrate is influenced by the fluid properties (such as surface tension and viscosity), but also by the topography and hydrophobicity/hydrophilicity of the substrate. Each of these properties must be engineered carefully to match an ink and substrate to their application.

1.4. Thermodynamics of fluids

At the liquid-vapour interface of a solvent droplet, the vapour exists in equilibrium with the liquid. The pressure exerted by the vapour on the liquid phase is known as the vapour pressure, p_{s}, for a solvent s. In a solvent mixture, the vapour pressure of the mixture depends on the partial vapour pressures of the component fluids. In an ideal mixture, the vapour pressure is described by Raoult's law, whereby the total vapour pressure, p_{s}, depends on the molar ratios of the component fluids (x_{A} and x_{B}), as

$$p_{\mathrm{s}} = p_{\mathrm{A}} + p_{\mathrm{B}} = p^*_{\mathrm{A}} x_{\mathrm{A}} + p^*_{\mathrm{B}} x_{\mathrm{B}}, \tag{1.12}$$

where p_{A} and p_{B} are the partial vapour pressures of component A and B, and p^*_{A} and p^*_{B} are the vapour pressures of component A and B respectively. Hence, the saturated vapour pressure of the mixture is lower than the value for either pure component.

Raoult's law assumes the fluid is ideal (i.e. that each component fluid interacts with itself and the other component identically). In practice, interactions between like and unlike components in a solvent mixture are not the same, and deviations from Raoult's law arise (following Henry's law in dilute cases). Azeotropes are mixtures that deviate from Raoult's law sufficiently to give a maximum or minimum in the vapour pressure with composition (ethanol/water is one example). If the deviation from Raoult's law is negative, the

boiling point of the mixture exceeds that of either component fluid. If the deviation is positive, then the mixture boiling point is lower than that of the component fluids. Ethanol/water mixtures exhibit a positive azeotrope. The deviation from Raoult's law arises from the associative behaviour of the fluid. Interactions between like-components and unlike-components are not the same. The deviation from ideality can be represented by the activity coefficient of the component in the mixture (γ_{A} for component A). For an ideal mixture the activity coefficient is equal to one.

Molecules move to lower their chemical potential. The chemical potential of component A, μ_{A}, is given by

$$\mu_{\mathrm{A}} = \mu_{\mathrm{A}}^{\ominus} + R_{\mathrm{u}} T \ln(a_{\mathrm{A}}), \tag{1.13}$$

where $\mu_{\mathrm{A}}^{\ominus}$ is the chemical potential of component A in the standard state, R_{u} is the universal molar gas constant, T is the temperature in Kelvin and a_{A} is the activity of component A in the mixture. The activity coefficient, γ_{A}, is defined as

$$a_{\mathrm{A}} = \gamma_{\mathrm{A}} x_{\mathrm{A}}. \tag{1.14}$$

In summary, the behaviour of associative fluids can differ greatly from the ideal case. Simple relationships like Raoult's law are not obeyed, so cannot be used for model predictions.

1.5. Evaporation

Droplets deposited onto a substrate dry by evaporation unless a curing process is used. Understanding the principles behind droplet evaporation is of importance for applications such as spray cooling, inkjet printing, crop-spraying, heat transfer and fuel combustion. By gaining a complete understanding of the underlying principles governing droplet evaporation, improvements to the aforementioned applications can be made. To this end, a large number of studies into droplet evaporation have been carried out in the last two decades including experimental investigations and modelling [56–60].

A droplet evaporates by the transfer of mass from the liquid to the vapour phase. Evaporation is endothermic, requiring energy for the phase change from liquid to vapour. Molecules must overcome the energy barrier to evaporation before they can change phase and cross the liquid-vapour interface. If the kinetic energy of the molecule is insufficient, the molecule remains in the liquid phase. The molecules with the highest probability of escape are those with the larger kinetic energy and therefore higher thermal energies. On losing the molecules with the higher thermal energies, the droplet becomes colder, a process known as evaporative cooling. Heat transfer to the liquid-vapour interface is then required before molecules in the vicinity of the interface have enough energy to transfer into the vapour phase. The evaporation rate may be limited by the kinetic transfer of molecules across the interface or by the transfer of heat to the liquid-vapour interface [57,59].

The second rate-limiting mechanism that influences the evaporation rate is the transport of molecules away from the liquid-vapour interface; which can be due to diffusive transport alone [61, 62], or in combination with free convective transport [63,64]. Under normal atmospheric conditions, the kinetic transfer of molecules across the liquid-vapour interface is fast (10^{-10} s for non-associated liquids [57]), saturating the air close to the interface of the droplet. For molecules to diffuse away from the liquid-vapour interface, there must be a gradient in the vapour concentration close to and far away from the droplet. If the droplet is in an atmosphere saturated with its own vapour, then there is no vapour concentration gradient and so no net evaporative flux.

As the droplet evaporates, the position of the liquid-vapour interface changes. The vapour concentration in the vicinity of the liquid-vapour interface then has a time dependence governed by the unsteady diffusion equation,

$$\frac{dc}{dt} = D\nabla^2 c, \tag{1.15}$$

where c is the vapour concentration, D is the diffusion coefficient of vapour in the ambient atmosphere and t is the time. When the velocity of the liquid-vapour interface is negligible compared to the time required for a concentration profile to build-up due to diffusion, then the time dependent terms in (1.15)

can be ignored and the vapour concentration profile is considered to be quasi-steady, following the Laplace equation,

$$\nabla^2 c = 0. \tag{1.16}$$

For the picolitre droplets considered in this thesis, the time scale for the build-up of a concentration profile around the droplet by diffusion (t_{diff}=R^2/D with a length scale R) is much smaller than the drying time t_{dry} (i.e. $t_{\text{diff}}/\ t_{\text{dry}} \ll 1$). Therefore only quasi-steady, diffusion-limited evaporation is considered. In this case the vapour close to the droplet is saturated, reaching the saturation vapour density, n_s. Far from the droplet, the vapour density is equal to the ambient vapour density, $n_\infty = RH \times n_s$.

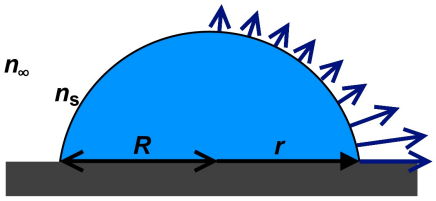

Figure 1.7. Schematic of a sessile droplet drying by diffusion-limited evaporation. The evaporative flux is highest at the contact line (blue arrows).

For a partially wetting sessile droplet with a contact angle $< 90°$, the evaporative flux is not uniformly distributed along the liquid-vapour interface (Fig. 1.7). Evaporation is enhanced at the contact line compared to the apex of the droplet [65]. The vapour concentration is analogous to the electrostatic potential around a charged conductor, and the evaporative mass flux is analogous to the electric field [66]. At sharp edges (i.e. the contact line), the evaporative flux diverges, enhancing the evaporation in this region.

Solving the analogous electrostatic problem analytically to find the evaporative flux is a complex process [62,65]. Under the small-angle approximation and in the diffusion-controlled limit, the evaporative flux, J , is given by

$$J(r) = \frac{2}{\pi} \frac{D(n_s - n_\infty)}{\sqrt{R^2 - r^2}}, \tag{1.17}$$

where D is the diffusivity in the vapour phase, and r is the distance from the

centre of the droplet [67].

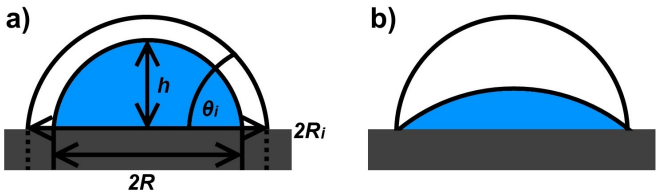

Figure 1.8. Schematic of an evaporating sessile droplet in a) constant contact angle mode and b) constant contact area mode. The initial contact angle is θ_{i} and the initial contact radius is R_{i}.

There are two main limiting modes during the evaporation of a drying droplet [66]; the constant contact angle mode and the constant contact area mode (Fig. 1.8). For the constant contact angle mode, the droplet dries with a receding contact line and constant contact angle. For the constant contact area mode, the droplet dries with a pinned contact line at a fixed contact radius and a decreasing contact angle.

A number of studies relate to the evaporation of microlitre, single solvent droplets [56–59, 67, 68]. The evaporation mode can have a large effect on the evaporation rate. For millimetre-sized droplets, the evaporation rate can be measured by weighing the droplets and inferring the volume change from the mass loss over time [69]. This technique is not appropriate for micrometer-sized drops, so instead imaging techniques facilitating video capture of the droplet profile are used. In the case of a droplet evaporating with a constant contact area, and a contact angle below 90°, the evaporation rate is linear with time [66]. For a droplet with a moving contact line, the evaporation rate decreases with time. If the contact line is free to move, then often $R(t) \propto (t_{\mathrm{dry}} - t)^m$ where m is typically $\backsim 0.5$ [70, 71], increasing when vapour transport is not purely diffusive. For example, water droplets have shown an exponent of 0.6, where convection occurs as water vapour is less dense than air [63]. Lower contact angles and larger contact areas result in faster evaporation rates as heat transfer is quicker when the droplet is thinner and has a larger contact area [72]. Far fewer examples relate to the evaporation of picolitre droplets [73–75]. One of the initial objectives of this thesis is to investigate the evaporation of single solvent picolitre droplets and fill this gap in understanding.

Most models refer only to limiting mode evaporation (usually with a pinned contact line). Only a few models/simulations incorporate intermediate modes [76], which are present in single solvent droplets (for example stick-slip recession of the contact line [58]). On rough substrates, stick-slip motion of the contact line can occur when the contact angle falls below the receding contact angle and the contact line de-pins (slipping). On de-pinning, the contact angle may increase as the contact line retracts, and the periphery can then re-pin (sticking). When the contact angle falls below the receding contact angle the contact line moves again. Alternatively, solvent mixtures with a freely moving contact line can exhibit an increase in the contact angle during drying when the composition at the contact line varies [77].

Sefiane *et al.* [77] investigated the evaporation of binary solvent mixtures of alcohol and water. They noted that the initial evaporation rate was close to that of ethanol and at the late stages of drying the evaporation rate was close to that of water. This non-linear evaporative behaviour strongly contrasted with the linear behaviour observed for single solvent droplets, and indicated the motion of the more volatile component to the liquid-vapour interface before subsequent evaporation of the less volatile component. As the ethanol was depleted and the contact line became water-rich, the contact angle increased. Hence, in binary solvent mixtures, the evolution of the evaporation rate and contact angle (in a droplet with a freely moving contact line) is determined by the components and their proportions. In addition to these findings, residuals [78, 79] of the more volatile component - left after the evaporation of the less volatile component - were observed in an unsaturated atmosphere during the evaporation process. This gave rise to a discrepancy between the contact angles measured in a saturated and an unsaturated system.

In summary, the evaporation of the picolitre droplets in this thesis is limited by diffusion. Mass lost due to evaporation causes a decrease in the contact angle or contact radius of the droplet throughout drying. The limiting mode of drying influences the evaporation rate. Additionally, for binary mixtures the evaporation rate is dominated by the more volatile component at early times, and the least volatile component at late times.

1.6. Particle transport in drying droplets

When particles are introduced into the droplets discussed above, particle transport by internal flows determines the deposit morphology. Inside evaporating droplets, the internal flows depend on the contact line motion, the evaporative flux across the droplet, and the motion of the liquid-vapour interface. In this section, the two main causes of particle transport in droplets are described, which follow the fluid flow: evaporation-driven flow and Marangoni flow.

1.6.1. The "coffee ring effect"

In a sessile droplet with $\theta < 90°$, the evaporative flux is highest at the periphery. In order to maintain the spherical cap profile imposed by the surface tension, there is a capillary flow to the contact line to replenish lost liquid (see Fig. 1.9). This flow transports particles inside the droplet radially outwards, where a ring stain forms. Under certain conditions all material can be transferred to the ring. This phenomena was first explained by Deegan *et al.* [61] and is commonly known as the "coffee ring effect".

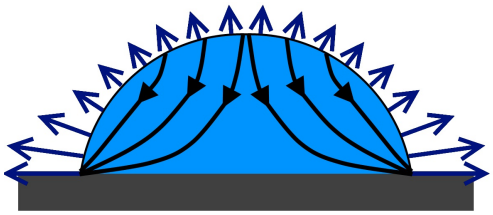

Figure 1.9. Schematic of the "coffee ring effect" in an evaporating sessile droplet with a pinned contact line. The evaporative flux is indicated by the blue arrows, and the internal convective flow by the black arrows.

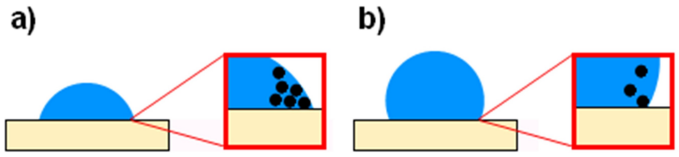

Figure 1.10. Particles trapped at the contact line can cause self-pinning. For a lower contact angle particles wedge at the contact line a), whereas a larger contact angle is less likely to trap particles.

The "coffee ring effect" only takes place when there is evaporation from the contact line of a droplet and the contact line is pinned. For a freely moving contact line, there is an additional inward component to the internal flow [80]. Pinning is common on rough [81, 82] or chemically inhomogeneous substrates [83, 84], and for fluids containing high solid loadings [85–87]. In the latter case, droplets self-pin where particles wedge at the contact line (Fig. 1.10). The formation of coffee rings - sustained by the pinning effect - has a minimum characteristic length corresponding to a critical droplet diameter, below which no coffee ring forms [88]. This characteristic length is related to the time scales for evaporation and the diffusive transport of particles in the droplet. If the diameter of the droplet is sub-critical, particles collecting at the contact line will be able to diffuse back to the centre, provided that the convective flow induced by the evaporation can be overcome.

Figure 1.11. Spilled coffee leaves a ring deposit, with a high particle concentration in the ring and low particle concentration at the centre of the spill. Supersaturation of the dissolved coffee causes precipitation near the contact line.

A ring stain is not always an unfavourable outcome. For crop spraying applications, the "coffee ring effect" can lead to the optimal combination of adjuvant oil and the active particulate ingredient [89]. Similarly, nanotechnology applications (e.g. size sorting of particles [90], self-assembly of minute structures, the alignment of carbon nanotubes [91], and stretching of DNA [92]) all rely on the "coffee ring effect". In biomedical applications, close analysis of the patterns formed from dessicated blood samples has proven effective for the diagnosis of certain diseases and health problems [93]. In printed electronics, deposition of a highly conductive print has also been managed by the dense packing of particulates in ring stains and further by overlapping rings [94, 95], though this is not suitable for all applications. However, in many cases the "coffee ring effect" (Fig. 1.11) can be a hindrance, causing reduced particle density at the centre of a deposit. For this reason, a large amount of research has been undertaken into alternative particle transport mechanisms, pattern formation and suppressing the ring stain to get the best arrangement of depo-

sited material for the application in question. Particle transport mechanisms are described further in Chapter 4, and methods for suppressing the ring stain are discussed more thoroughly in Chapter 5.

In summary, the "coffee ring effect" causes particles in a droplet to build up a ring stain at the contact line. A ring stain is detrimental to optimising print uniformity, but can be a useful tool for self-assembly of nanoparticles.

1.6.2. Marangoni flows

Marangoni flows were first observed in 1855 [96] and offer an alternative particle transport mechanism to the "coffee ring effect". Marangoni flows arise when a surface tension gradient exists along the liquid-vapour interface due to a temperature or compositional gradient. In order to balance tangential stresses, the fluid moves from low to high surface tension in accordance with

$$\frac{d\sigma}{dx} = -\eta \frac{du}{dn}, \tag{1.18}$$

where x is the tangential co-ordinate, n is the normal co-ordinate, σ is the surface tension, η is the fluid viscosity, and u is the tangential component of the fluid velocity at the liquid-vapour interface. The Marangoni flow at the interface causes fluid inside the droplet to re-circulate in cells with a central stagnation point (Fig. 1.12). Modification of the internal flow profile from the radial flow regime seen in Fig. 1.9 can reduce particulate transport to the contact line, reducing ring staining.

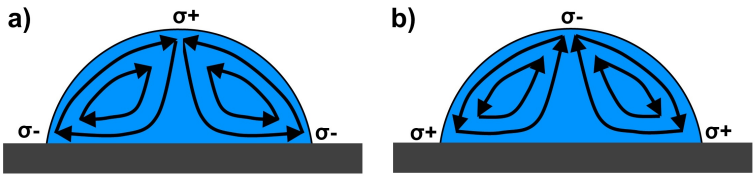

Figure 1.12. Cartoon of Marangoni re-circulation cells with a flow direction along the liquid-vapour interface from a) apex to contact line, b) contact line to apex.

In single solvent droplets, thermal gradients can arise due to evaporative cooling. Enhanced evaporation at the contact line relative to the apex can cause the contact line to become comparatively cooler, introducing a temperature gradient along the liquid-vapour interface. If the heat transfer within

the droplet is fast enough, evaporative cooling may be negated. The ratio of the thermal conductivity of the liquid and substrate plays a large role in the direction of the thermal Marangoni flow, as does the contact angle of the droplet [97]. If the substrate conductivity is above a critical value, then energy transfer to the droplet makes the droplet warmest at the contact line (where the conduction pathway is smallest) and colder at the droplet apex (where the conduction pathway is longest). If the substrate is a poor conductor, then little energy is available to maintain the droplet temperature. Thus, the contact line region becomes colder than the rest of the droplet, as the evaporative flux is largest here. Hu and Larson [68] modelled the thermal Marangoni flow inside a water droplet using a finite element method and a lubrication approximation. Temperature fields were found by applying a finite element analysis to the heat equation, from which the surface temperature profile was obtained. Analytical expressions for the temperature profile along the liquid-vapour interface were used based on fits to the finite element analysis. They noted the change in direction of the Marangoni flow at a critical contact angle (below $\backsim 14°$ for a water droplet on glass), in agreement with Ristenpart et al. [97].

Heating or cooling of the substrate can also induce thermal gradients [98, 99]. If the contact line of the droplet is coolest, then the Marangoni flow is directed from the contact line to the apex along the liquid-vapour interface (Fig. 1.12a). Infra-red thermography has previously revealed the thermal waves and temperature gradients associated with evaporating droplets (on heated substrates) [99–101]. The droplets exhibited a cool centre relative to the contact line region, with thermal waves processing around the droplet.

Solutal Marangoni flows can be introduced to single solvent droplets through the addition of a surfactant or polymer [102–104]. For an additive that lowers the surface tension, capillary flow can gather the surface active agent at the contact line. Accumulation of the additive at the periphery of the droplet causes a Marangoni flow directed from contact line to apex along the liquid-vapour interface (Fig. 1.12a). Alternatively, solvent mixtures with differential evaporation of components of different surface tension can introduce solutal Marangoni flows into evaporating droplets [45, 105–108]. For binary solvent

mixtures, the Marangoni flow direction is dependent on whether the more volatile component possesses a lower/higher surface tension compared to the less volatile component. If the more volatile component has the higher surface tension, then the Marangoni flow direction is described by Fig. 1.12a. In the opposite case, the Marangoni flow direction is described by Fig. 1.12b.

Christy *et al.* [45, 107] used particle imaging velocimetry to visualise the flows inside macroscopic ethanol/water droplets. At early times, they observed chaotic vortex flows driven by concentration variations, decaying to radial flow during the late stages of evaporation. Hence, particles may be transported to the contact line towards the end of drying.

In summary, Marangoni flows driven by surface tension gradients can be introduced using temperature or compositional gradients at the liquid-vapour interface of a droplet. Recirculating cells can redistribute particles inside the droplet, counter-acting the "coffee ring effect".

1.7. Pattern formation and control of the deposit morphology

Control over the morphology and micro-structure of the deposit is necessary to tailor the printed material to the intended application. The optimal morphology may not always be the same, but may vary from a ring stain (for stretching DNA) or a uniform deposit (for graphical applications) to something entirely different (Fig. 1.13). Likewise, the microstructure may be required to be close-packed or loose, crystalline or amorphous, or to be orientated in a particular direction. A cracked deposit can be informative for disease diagnostics, but is usually undesirable for other applications as the print quality is diminished.

Many studies have been undertaken investigating pattern formation to further fields such as evaporative self-assembly and the manipulation of colloids for functional deposits. Pattern formation can largely be divided as patterning due to modified droplet wetting, modified internal flows, or particle effects. The wetting behaviour of a droplet can be altered by changing the substrate hydrophobicity or surface roughness, or by changing the deposited fluid. By permitting a moving contact line, a number of patterning possibilities arise;

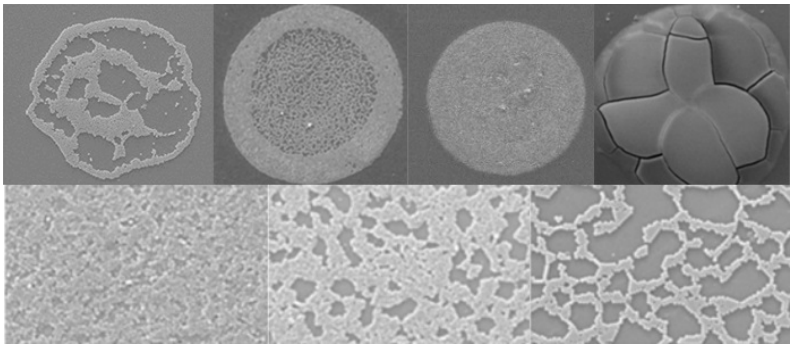

Figure 1.13. Inkjet deposits of varied shape (top) and interior morphology (bottom). Deposits exhibit a range of desirable and undesirable features (depending on the application). From left to right; non-circular contact line, ring stain, uniform particle distribution, cracking.

particles can be dragged by the receding contact line and form a small central dot [109], spoke-like bands [110], or saw-tooth patterns [85]. Stick-slip behaviour of the contact line can result in a series of rings [58, 85] formed at each pinned location. A pinned contact line usually results in a ring stain [61].

Substrate patterning has also been implemented as a method for modifying the wetting over separate regions on the same substrate. By alternating hydrophobic and hydrophilic stripes on a scale smaller than the droplet diameter, Leopoldes *et al.* [83] were able to form droplet contact lines with lozenge or butterfly shapes. The geometry of the surface is as important as the surface patterning. The spreading of droplets across a surface can be hindered by the size and shape of various geometric protuberances [111]. Polygonal posts have also been implemented to attain non-circular contact lines [112]. Deposits resulting from these deformed droplets would also be non-circular.

By modifying the internal flow in a pinned droplet, the "coffee ring effect" can be suppressed. Particles can be transported away from the contact line by Marangoni flows, reducing ring formation [105, 108, 113, 114] and allowing the growth of ordered crystalline structures [106]. Capillary forces induced by particles at the liquid-vapour interface can cause inward motion of particles [115, 116] . The inward motion depends on the particle size and contact angle of the droplet on the substrate. Alternatively, the evaporative flux across the droplet may be altered to eliminate non-uniformity. Deegan *et al.* [65] modified the evaporative flux across a water droplet by using a pinhole to enhance

evaporation at the apex, or a surrounding water bath to reduce the evaporation near the contact line. The inhibition of evaporation at the contact line resulted in suppression of the ring stain. Evans *et al.* [117], used a wall to reduce evaporation on one side of a droplet relative to the other, forming arched deposits when the "coffee ring effect" was enhanced on one side of the droplet.

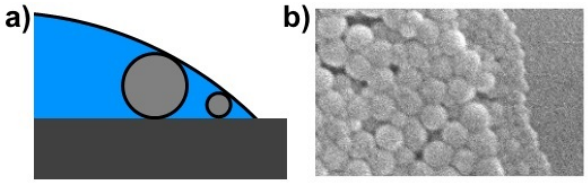

Figure 1.14. a) Cartoon of particle size segregation at the contact line. Larger particles cannot travel as close to the contact line as smaller particles. b) Example SEM showing the size segregation.

The particle size, shape and interactions (particle-particle or particle-substrate) may all influence the morphology of the deposit. Particle size sorting has been observed in dried deposits, with smaller particles collecting in the thin lamellar film close to the periphery. Larger particles remained excluded further inward due to the height restriction near the contact line [90] (see Fig. 1.14). A thin precursor film containing no particles is left immediately at the contact line. Due to the finite-size of the nanoparticles, a film of solvent was left at the outer rim, thinner than the nanoparticles themselves. Larger particles may also settle, rather than following internal flows.

The shape of the particles can have an effect on the width and height of the ring stain, depending of the stacking ability of the particles. Hodges *et al.* [118] noted the higher ring stain resulting from plate-shaped laponite particles compared to spherical ludox silica particles of comparable size. This higher ring is a consequence of the higher affinity for stacking of the plates. Anisotropic particles such as ellipsoids have been shown to form a more uniform deposit than spherical particles [119]. Once carried to the droplet interface by radial flow, strong capillary forces between the ellipsoidal particles keep particles in a raft and prevent motion towards the contact line. Similarly, Bigioni *et al.* [120] utilised attractive particle interactions between surface active spherical particles to grow a film at the liquid-vapour interface. The film then dried vertically

downwards to form a more uniform deposit than the ring stain observed when particle interactions were not present.

As well as particle-particle interactions, particle-substrate interactions can also play a key role in the deposit morphology (e.g. van der Waals interactions and electrostatic interactions) [116]. By charging the particles and the substrate with opposite sign, the mobility of the particles can be hindered, reducing the "coffee ring effect" to form a disordered structure at the contact line [121]. When particles had the same charge as the substrate there was no attraction and an ordered lattice formed at the contact line by capillary flow.

By varying the concentration of microspheres in a droplet, a range of deposit patterns was obtained by Deegan *et al.* [85]. Variations in both the deposit shape and the fine structure were observed. Deposit patterns included multiple rings of different thickness, and fine structure of radial lines or saw-tooth patterns. Park and Moon [105] also found the microsphere concentration to have structural implications for the deposit when using a mixed-solvent ink: An increased microsphere concentration allowed the build-up of a monolayer in some cases, where lower concentrations led to a ring deposit.

The deposit structure at the contact line can differ greatly from the structure at the droplet centre. Often the deposit at the contact line is more ordered and "crystalline" in structure compared to the centre of the droplet, as particle speeds at the start of drying are lower [122]. This allows more time at the beginning of drying for particles to align at the contact line, whereas at the end of drying, the comparative rush of particles leaves greater disorder closer to the centre of the deposit.

In summary, the deposit resulting from a dried droplet can be influenced by the droplet wetting behaviour (movement and shape of the contact line), particle transport by internal flows, particle interactions with each other or the substrate, particle shape, and by the particle concentration.

1.8. Rheology of structured complex fluids

Most commercial inks are structured complex fluids comprising colloidal particles, polymers, surfactants, and/or interacting networks. Hence, an understanding of the underlying rheology is necessary to predict the jetting and deposition behaviour of the ink. Many inks utilize shear-thinning behaviour to bypass the viscosity limit on inkjet devices (<20 mPa s for the DOD printheads used in this thesis). Additionally, shear-thinning inks can have the added benefit of reducing the formation of satellites [123]. The high shear rate inside the nozzle lowers the viscosity of the fluid, allowing jetting, before the fluid recovers at low shear rates at the substrate.

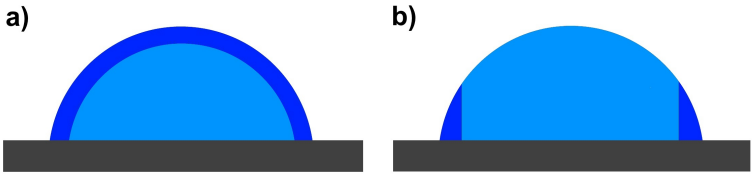

Figure 1.15. Cartoon of solute segregation inside a drying droplet due to evaporation and evaporation driven flows. a) Crust/skin formation at the liquid-gas interface. b) segregation to the contact line due to capillary flow.

The viscosity may also change during drying due to concentration of solids on evaporating the solvent (see Fig. 1.15), segregation of solids near the contact line [61] or liquid-gas interface [124,125], or due to thixotropy in Non-Newtonian fluids [126]. Thixotropic effects depend on the recovery time of the ink, which may be rapid or slow on the timescale of drying. The rheology of the ink affects particle transport during drying. An increased viscosity can distort the shape of the droplet from a spherical cap, or reduce Marangoni effects and inhibit the settling of particles. The settling velocity, v_s, is given by

$$v_s = \frac{2(\rho_p - \rho_f)ga^2}{9\eta}, \tag{1.19}$$

where ρ_p and ρ_f are the density of the particle and fluid respectively, g is the acceleration due to gravity, a is the particle radius and η is the viscosity of the fluid. Hence, an increase in the viscosity lowers the settling velocity and decreases sedimentation.

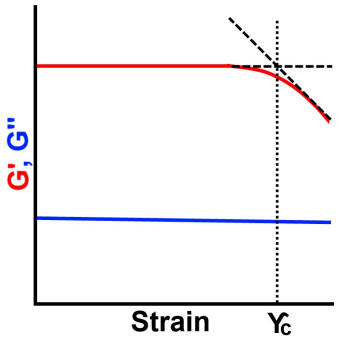

Figure 1.16. Schematic of an oscillatory strain sweep for a viscoelastic fluid. The critical strain, (γ_c, shown by the dotted line), indicates the end of the linear viscoelastic region where the elastic storage modulus, G', is constant with strain. The resulting structural breakdown beyond this point allows the fluid to flow. An illustrative example of the loss modulus, G'', is also plotted.

Due to the complex structure of some inks, flow does not occur until the applied stress exceeds the yield stress (σ_c) of the ink. Below the yield stress, the ink behaves as an elastic solid, while above the yield stress, the fluid structure breaks down and the ink flows. The limit to linear viscoelasticity is shown by the elastic storage modulus (G') under increased strain (see Fig. 1.16). The yield stress and critical strain mark the point at which the linear elastic region ends and the structure breaks down. The yield stress can be estimated by the product of the elastic storage modulus in the linear elastic region and the critical strain, γ_c, as $\sigma_c \approx G' \gamma_c$.

Viscoelasticity is also an important consideration for the jettability of an ink [8, 123]. If the viscoelasticity of the ink is not sufficient, ligament breakup results in multiple satellites, which are detrimental to print quality. However, if the ink is too viscoelastic, the ligament can remain attached to the droplet, reducing print speeds, or forming a thin thread until the droplet reaches the substrate.

In summary, the rheology of an ink provides a useful tool for predicting whether the ink will be printable from an inkjet nozzle, what the ligand breakup will be like, and how the ink might behave on the substrate (e.g. whether it will flow).

2 | Experimental Method

2.1. Development of Experimental Set-up

This section describes the experimental set-ups used for high speed imaging of drying droplets and their development throughout this project. Early work on evaporative cooling used Rig A (Fig. 2.1) to collect shadowgraph images of the droplet profile with a high-speed camera (Photron APX RS) and collimated side illumination. Images were collected at a shutter speed between 50 μs and 111 μs and a frame rate between 66 and 10,000 fps (depending on the fluid and droplet characteristics). A 20× magnification objective (Nikon MPlan, NA 0.4, WD 10 mm) was used to magnify the images. The resolution was limited by the pixel size, which was on average $\sim 0.97 \times 0.97$ μm^2. This was sufficient to resolve the end stages of drying.

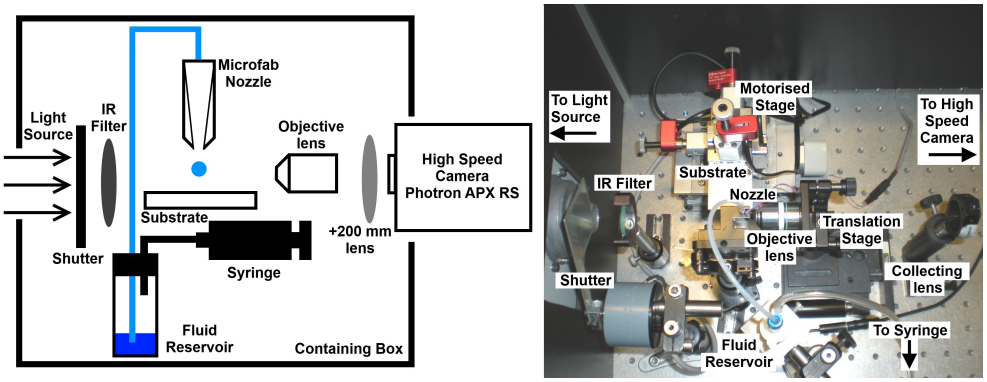

Figure 2.1. Schematic of Rig A for imaging the droplet profile during evaporation (left) and labeled photograph of the rig (right).

Evaporation rates and internal flows are sensitive to temperature. To prevent temperature gradients across the droplet, a cold LED light source (Beaglehole instruments, $\lambda = 455$ nm) was used. An alternative high intensity light source (Thorlabs, HPLS-30-02) can replace the LED for imaging impact

and spreading where higher shutter speeds limited light intake, and acquisition times were fast enough that temperature gradients were less problematic. An infra-red filter and a shutter (for blocking the light source between image acquisitions) were also implemented to reduce heating of the droplet. The relative humidity and temperature in the region of the nozzle were measured with a thermohygrometer (Extech), with maximal systematic errors associated with the calibration of the relative humidity, RH $\pm 4\%$ and temperature, T ± 1 K respectively. The temperature was typically maintained between $293-296$ K. The entire set-up was contained within a box to reduce air currents and limit convective cooling.

Picolitre droplets were ejected from a Microfab piezoelectric printhead (MJ-ABP-01, Horizon instruments) with a 30 μm, 50 μm, or 80 μm orifice. The device was connected to a fluid reservoir pressurised by a syringe. The syringe was used to bring the meniscus to the nozzle orifice, but not to push fluid through. For fluids with a low surface tension, a small negative pressure was sometimes required to prevent dripping from the nozzle. In cases where fluid in the tubing moved back into the reservoir after positive-pressure from the syringe ceased, extra PTFE tape was used to ensure complete pressure sealing of the reservoir. It was necessary to ensure there were no air bubbles in the tubing, particularly close to the printhead, as these often prevented jetting. Drop-on-demand printing was controlled using a Microfab driver unit (Microfab JetDrive III Controller CT-M3-02). Single droplet emission was initiated by the electronic pulse sent to the piezoelectric device contained within the nozzle. The waveform of this pulse was symmetric, and typically of the form shown in Fig. 2.2. The voltage of the waveform was adjusted depending of the fluid viscosity and surface tension, in order to allow emission of single droplets with impact velocities of approximately $1-2\,\mathrm{ms}^{-1}$. The typical voltage range to emit a single water droplet from a new nozzle was $20-30$ V (and $70-80$ V for an old nozzle). The nozzle-substrate separation was $\backsim$ 2 mm. Satellites were controlled through altering the time period for each part of the waveform, and through reduction of the applied voltage. By imaging the droplet before impact, a check was made to ensure that single droplets were emitted with no trailing satellite droplets. A motorised stage (Newport) was used to move a

clean section of substrate under the nozzle before the next droplet was deposited. Stage control also allowed lines or droplet arrays to be printed for deposit analysis. A small number of droplets were ejected from the nozzle before image acquisition to ensure replenishment of the fluid at the nozzle. Such practice was particularly important for volatile fluids or fast diffusing particulates to avoid depletion of the volatile solvent or concentration of particulates in the nozzle. The latter can lead to the formation of a dried particulate film across the nozzle orifice which stops jetting.

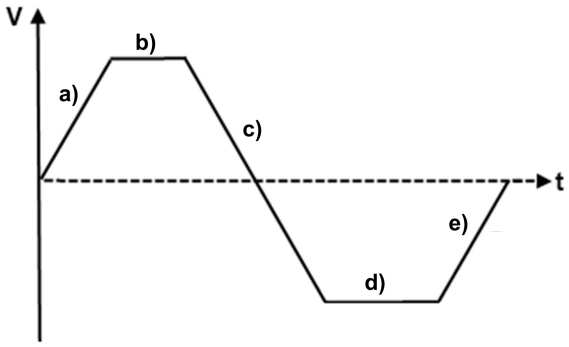

Figure 2.2. Example profile of a typical symmetric waveform used for droplet emission. Typical time periods used for water droplets were a) a rise time of 13 μs, b) a dwell time of 8 μs, c) a fall time of 13 μs, d) an echo time of 10 μs, and e) a final rise time of 13 μs.

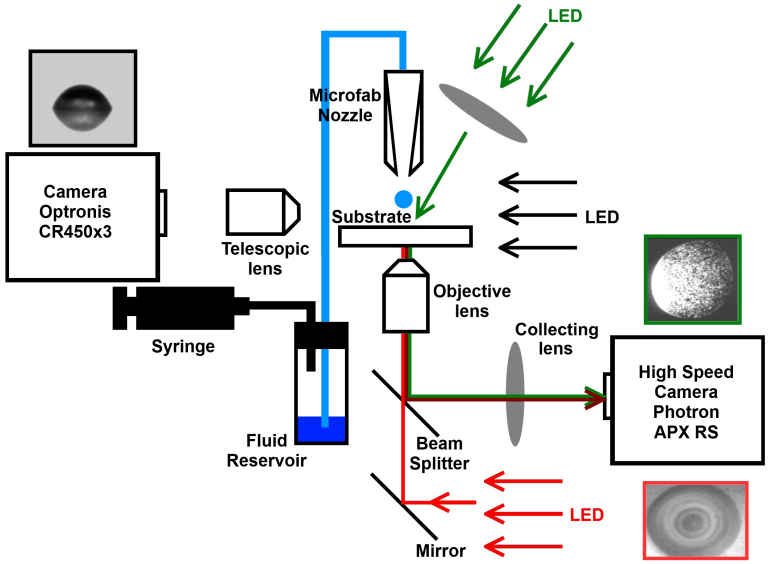

Figure 2.3. Schematic of Rig B for simultaneously imaging the droplet profile during evaporation and the internal flows (using tracer particles contained in the fluid). Two illumination options are shown, dark field (green LED) and bright field (red LED). Colours are for illustration only and do not relate to the LED wavelength.

Later, Rig B (Fig. 2.3) was built, which combined a side-profiling rig similar to Rig A, and an inverted microscope, allowing both the profile of the droplet and internal flows to be imaged simultaneously. A mid-speed camera (Optronis CR450×3), coupled with collimated illumination from an LED (Beaglehole Instruments, $\lambda = 455$ nm), was used to image the droplet profile. A telecentric lens (LaVision, serial: VZ11-0068) magnified the droplet. For the inverted microscope, a high speed camera (Photron APS RX) and 50× magnification objective lens (Olympus LMPLFLN, NA 0.5, WD 10.6 mm) were used for image capture. To image the internal flows, tracer particles were included within the fluid and imaged using dark field microscopy (green LED on Fig. 2.3). The light source for the inverted microscope was a cold LED ($\lambda = 530$ nm, Thorlabs), focused onto the substrate from above, at an angle to avoid the nozzle. This angle was chosen such that image contrast was maximised. Polystyrene tracer particles were visualized as bright spots (from back-scattered light) on a dark field. A shutter speed between 50 μs and 100 μs was used to allow enough light to image the particles, while still enabling the distinct particle positions to be resolved. Frame rates between 100−3000 fps were used depending on the solvent and particle velocities inside the fluid. For volatile solvents or fast Marangoni flows, the higher frame rate (3000 fps) and faster shutter speed (50 μs) were required. Particles inside the droplet were imaged from below (through the substrate), requiring both the fluid and substrate to be adequately transparent. The smallest resolvable particle size was $\backsim$ 410 nm, limited by the pixel size of approximately 0.41×0.41 μm^2.

Limitations on the dark field imaging technique include a bright region to one side of the droplet where no particles can be imaged (see inverted microscope image in Fig. 2.3). The origin of this bright region is due to refraction of the incident light at the liquid-vapour interface of the droplet, and depends on the angle of the LED, the contact angle of the droplet, the refractive index of the fluid, and the numerical aperture (NA) of the objective lens. Light entering the liquid-vapour interface on the side of the droplet closest to the LED is refracted to give a larger angle from the optical axis (see Fig.

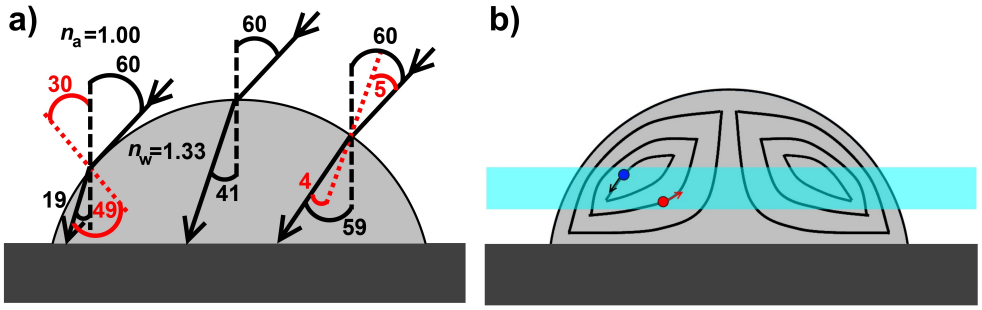

Figure 2.4. Cartoon of a) refraction at the liquid-vapour interface from a light source incident at 60° to the optical axis (dashed black lines). Red dotted lines indicate the normal to the liquid-vapour interface. The refractive indicies of the air and of water are given as n_a and n_w. Angles are not to scale. b) the zone of focus (cyan) within a sessile droplet. Particles with both inward (red) and outward (blue) motion can be imaged at the same time.

2.4a). Refraction angles are calculated from Snell's law

$$n_a sin\theta_{in} = n_w sin\theta_r, \tag{2.1}$$

where n_a and n_w are the refractive indices of air and water respectively, θ_{in} is the angle of incidence and θ_r is the angle of refraction.

For the objective lens used in Rig B, the numerical aperture is 0.5, corresponding to a half-cone angle of 30° in air. Any light deviating from the optical axis by less than 30° will be collected by the objective lens, giving a bright region. For light deviating from the optical axis by more than 30°, only light scattered from the particles is collected. In the bright region, if the scattered light intensity is less than the intensity from the incident LED light, then particles cannot be imaged in this region. Another limitation is the finite depth to the zone of focus (see Fig. 2.4b), such that particles at different heights in the droplet can be imaged at the same time. This can result in simultaneous imaging of particles traveling both inward and outward within the same time frame. Note that for a droplet with higher curvature, a particle with the same mean speed travels for a longer distance along the liquid-vapour interface in the same time period (i.e. velocities parallel to the streamlines at the interface are larger than the mean speed). This gives some bias to the imaging of particles traveling parallel to the substrate, as particles traveling vertically pass out of focus too quickly for particle tracking.

The depth of focus, d_{F}, can be estimated from

$$d_{\mathrm{F}} = \frac{\lambda n_{\mathrm{a}}}{\mathrm{NA}^2} \backsim \pm 2\,\mu m, \tag{2.2}$$

where NA is the numerical aperture, λ is the wavelength of the light source in air, and n_{a} is the refractive index of air. The algorithm can detect particles that are not sharply in focus, so the depth over which particles are imaged will exceed this $4\,\mu$m estimate.

It was also possible to use bright field microscopy (red LED on Fig. 2.3) by illuminating the droplet from below (through the objective lens), using a beam-splitter to return reflected light to the camera. The bright field method was not favoured for particle tracking, due to the interference fringes present when the droplet became thin. Interference fringes prevent easy visualisation of the particles, where dark fringes obscure dark particles. However, for pure solvents where the refractive index, n_{i} is known, the interference fringes can be used to calculate the droplet apex height, h, (assuming a spherical cap) using

$$\theta = tan^{-1}\left(\frac{N_{\mathrm{f}}\lambda}{2n_{\mathrm{i}}f}\right) \tag{2.3}$$

and

$$h = R\,tan\left(\theta\,/\,2\right), \tag{2.4}$$

where θ is the contact angle, N_{f} is the number of interference fringes, λ is the wavelength of the illuminating light source, f is the fringe width, and R is the contact radius of the droplet.

A humidity control cell was used to regulate the relative humidity in the vicinity of the droplet between a RH of $\backsim$ 0.25−0.70. The regulation of the relative humidity was not only useful for investigating the influence of the RH on evaporation, but also for preventing clogging at the nozzle orifice. To raise the RH inside the cell, compressed air was pumped in through a miniature bubbler (containing water). To lower the RH, compressed air was instead pumped through tubing filled with silica gel. The compressed air was

then turned off once the desired relative humidity was reached, ensuring that no air currents affected the droplet during image acquisition. The relative humidity and temperature inside the humidity control cell were measured using a thermohygrometer (Extech) with a probe inside the cell.

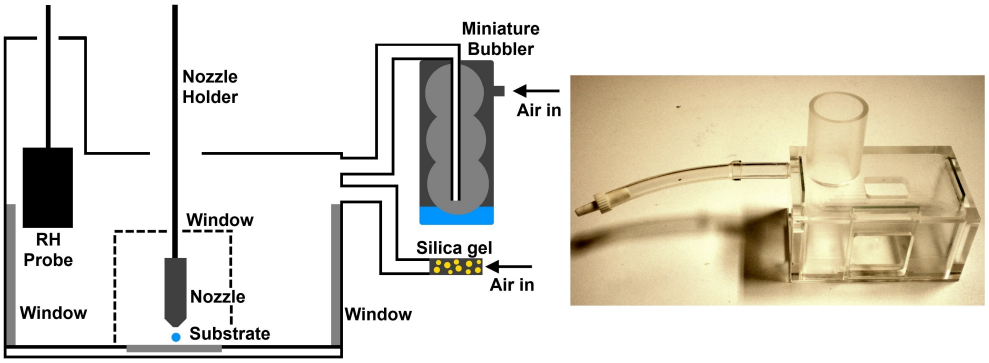

Figure 2.5. Humidity control cell schematic diagram (left) and photograph of cell (right).

As still images are not sufficient to fully describe the internal flows within the droplets in this thesis, supplementary videos are provided (on a USB stick) as a visual aid.

2.2. Fluid Preparation

Solvents were filtered through a 0.45 μm pore filter before use in the fluid reservoir, with no other pre-treatment. Table 2.1 summarizes the physical properties of the selected fluids. The water was high purity water (MilliQ, 18.2 MΩ cm) and the remaining solvents were purchased from Sigma Aldrich, with the exception of the 1-methoxy-2-propanol (>99% 1-methoxy-2-propanol isomer, DOW company) and 1-propoxy-2-propanol (>95% 1-propoxy-2-propanol isomer, DOW company). The solvents were used alone to explore evaporative cooling, or as a mixture to explore Marangoni flows.

To track internal flows, polystyrene spheres were added to a single solvent or a solvent mixture to act as tracer particles. Polystyrene spheres with a 1 μm hydrodynamic diameter were added at a concentration of 0.01%v for particle tracking. To investigate the end deposit resulting from a dried droplet, a higher particle concentration was necessary. For deposit investigation, 200 nm

Table 2.1. Surface tensions, σ, vapour pressures, p, viscosities, η, densities, ρ, and dielectric constants, ϵ_r, at 20°C.

Fluid	σ / mN m^{-1}	p/kPa	η / mPa s	ρ / kg m^{-3}	ϵ_r
Water	72.9 [127]	2.34 [127]	1.0 [127]	998 [128]	77 [129]
Ethylene glycol	48.0 [130]	0.008 [130]	17.9 [131]	1110 [131]	38 [130]
1-Methoxy-2-propanol (PM)	27.7 [132]	1.16 [132]	1.7 [132]	921 [132]	12 [133]
Methanol	23.0 [134]	12.9 [127]	0.5 [135]	787 [135]	32 [129]
Ethanol	22.4 [127]	5.95 [127]	1.1 [135]	790 [128]	24 [129]
Isopropanol (IPA)	21.3 [127]	4.41 [127]	2.0 [136]	781 [136]	18 [129]
Isooctane	18.6 [137]	6.35 [138]	0.5 [137]	686 [137]	2 [139]
1-Propoxy-2-propanol (PnP)	25.4 [140]	0.38 [140]	2.4 [140]	885 [140]	9 [141]

polystyrene spheres were added to the solvent at a concentration of 1%v or 5%v. Polystyrene suspensions were ultra-sonicated for 15 min prior to use to break up any aggregates.

For the majority of experiments the polystyrene spheres were sterically stabilised by a grafted layer and well dialysed to ensure that no surfactants were available to desorb. For solvents containing water, the stabilisation was by poly(ethylene glycol) monomethyl ether methacrylate (PEGMA, 2000 g mol^{-1}) polymer chains. For mixtures containing ethanol but no water, poly(N-vinyl pyrrolidone) (PNVP, $\backsim$ 40,000 g mol^{-1}) stabilised spheres were used, as the PEGMA-stabilised spheres became unstable in suspension when the water concentration dropped below $\backsim$ 2%v. A small number of experiments were made with charge stabilised polystyrene spheres to verify that observations were not due to the manner of stabilisation. Note that a small interaction from the electrical double layer could still occur for particles with a steric stabilising layer in water-rich solvent. Sterically stabilised polystyrene spheres were prepared at Leeds University, UK (Grace Yow, Simon Biggs) and charge stabilised polystyrene spheres were purchased from Bangs Laboratories. Electrolyte was not added to avoid concentration gradients due to added salt.

Hydroxyethylcellulose (HEC) solutions, laponite suspensions and polystyrene sulfonate (PSS) solutions were required for the development of deposit fixing strategies. Details for the preparation of each are given in the appro-

priate chapters (5 and 6).

2.3. Substrate Preparation

The substrate base material was selected depending on the experimental goal. For experiments investigating evaporative cooling, substrates were chosen for their thermal conductivity (silicon, glass, PTFE), ranging between $0.25-149$ $\mathrm{W\,m^{-1}\,K^{-1}}$. For the imaging of internal flows, transparent glass substrates were used.

Coatings were used to achieve higher contact angles, allowing the investigation of drying modes for both $\theta \geq 90^\circ$ and $\theta < 90^\circ$, as well as providing easier side-on visualisation for measuring contact angles and evaporation rates. In the case of particle tracking, transmitted light levels through the coating needed to be high enough to visualize the droplet and particles within. For lower contact angles, glass cover-slips were used as purchased or first cleaned either by rinsing in IPA or 2%w decon 90 (alkaline cleaning solution containing anionic and non-ionic surfactants), followed by a rinse in high-purity water. The rinsed substrates were then dried in nitrogen and left in an oven overnight to ensure complete drying. Before use, the substrates were cooled to room temperature. By coating the substrates, not only could the contact angle be increased, but also the surface roughness. Thus, pinning of the contact line could be achieved. Cover slips (used as received from the manufacturer) have varying levels of chemical contamination that increase the receding contact angle of a droplet resting on the substrate and provide pinning sites. By cleaning the substrates before use, the receding contact angle of a water droplet was lowered (although a zero receding contact angle was not reached), making de-pinning easier, and the number of pinning sites was reduced. Further details for coating and cleaning procedures are given in the experimental section of each chapter. Contact angles from microlitre water droplets ($\sim$1.0 μL) were measured on each substrate using a video capture system (AST Products, VCA250XE) and related software (VCA 2500, Version 1.12a, AST Products). Droplets were gently placed on the substrate for measurement by drop shape analysis, which fitted a spherical cap to the droplet profile.

2.4. Analysis of fluid properties

Rheological data were collected at 293 K using an AR 2000 Rheometer (TA Instruments) with a cone (2° angle) and plate geometry for laponite suspensions and HEC solutions in water (without the inclusion of polystyrene spheres). The steady-state viscosity of each fluid was recorded over shear rates from 0.1−1500 s^{-1}, where the upper limit was set by the rheometer. The reported steady-state viscosities are an average of three consecutive readings within 2% of each other, and a maximum measurement time of 5 min per reading. Recovery times were investigated by applying a stepped shear rate with fast sampling. The shear rate was held at 0.1 s^{-1} for 10 minutes, then 1000 s^{-1} for 4 minutes, before returning to the lower value. The yield stress of each laponite suspension was found using oscillatory measurements with small deformations, performed by running a strain sweep (for strain values between the rheometer's lower limit of 2.88×10^{-3} and 0.35) at a frequency of 1 Hz. The yield stress was estimated from the product of the critical strain and the elastic modulus in the linear elastic region. The critical strain was defined as the strain at which linear fits to the elastic region and viscoelastic region intersected (see Chapter 1, Fig. 1.16).

Surface tension measurements for binary solvent mixtures were made using a pendant drop tensiometer (First Ten Angstroms, FTA200). For solvents with low evaporation rates, surface tensions were recorded for a hanging droplet in the ambient atmosphere. For very volatile solvents, a J-shaped needle was immersed in the binary mixture and surface tension measurements were made for a bubble expanded into the solution (thus avoiding composition changes resulting from evaporation).

2.5. Post-Deposition Analysis Methods

Dried deposits of polystyrene spheres were imaged using a scanning electron microscope (SEM, Philips XL30 Environmental SEM) to determine the morphology of the deposit, the packing arrangement of the spheres and the radial distribution of material throughout the deposit. The deposits were sputter

coated with gold (three to five coats at 1.2 kV, 35 mA for 30 s, Edwards Scancoat Six) to ensure conduction through the sample and improve the image quality. The sample was subjected to three pump-vent cycles down to 8 mbar in an argon atmosphere before sputter coating. The deposits were then imaged using the SEM with a beam voltage of 30 kV.

A white light interferometer (WLI, Zygo NiewView 5000) provided vertical profiles of the dried deposits. The vertical noise for the interferometer was approximately ± 20 nm. In this case, deposits were sputter coated with gold (five coats) to ensure that the light would reflect off the top surface of the sample. The vertical profiles of the deposits were azimuthally averaged in MATLAB.

2.6. MATLAB Image Processing

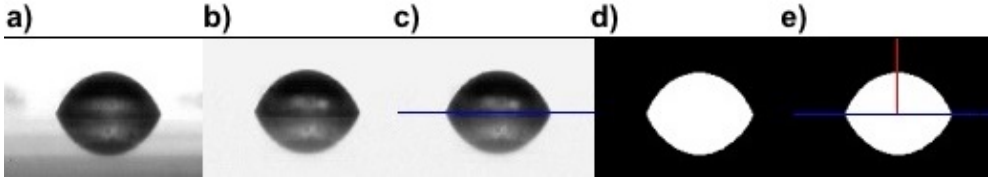

Figure 2.6. Post-processing images from a drying water droplet showing a) the original image, and the image after b) background subtraction, c) binary conversion and filling in of reflections, d) finding the substrate baseline, and e) finding the height and contact diameter.

Shadowgraph images of the droplet profile were post-processed in MATLAB using an automated routine. First, the background was subtracted from the original image (Fig. 2.6b). Second, a threshold grey level was applied for a binary conversion and any remaining reflections inside the droplet were filled in to give a solid, white image of the droplet on a black background (Fig. 2.6c). The filling in of reflections was possible as the reflections were always enclosed on all sides. Next, the substrate baseline was found (Fig. 2.6d), either automatically (in the case of contact angles below 90°), or manually (in the case of contact angles above 90°). The automatic method finds the row containing the most white pixels and sets this as the horizontal baseline. When the contact angle is above 90°, the droplet contact diameter may be smaller than the maximum droplet diameter, in which case the automated method is no longer suitable. Instead, two points on the baseline were selected manually,

and the line intersecting both these points was taken as the baseline. This manual method can also be used for inclined substrates where the baseline is not horizontal. The droplet height was then measured by summing the largest number of pixels in the vertical direction, and the diameter was measured by summing the number of pixels along the substrate baseline (Fig. 2.6e). A calibration was made using a glass sphere of known diameter in order to convert dimensions from pixels to μm.

As picolitre droplets have Bond numbers $\ll 1$, gravitational effects are negligible and a sessile droplet can be considered as a spherical cap with a volume, V, and contact angle, θ, given by:

$$V = \frac{\pi h}{6}\left(3R^2 + h^2\right) \tag{2.5}$$

and

$$\theta = 2\tan^{-1}\left(\frac{h}{R}\right), \tag{2.6}$$

where R is the contact radius and h is the apex height.

Images of the particle motion resulting from internal flows were also post-processed using MATLAB and particle tracking velocimetry (PTV) was carried out to determine the particle velocities. The PTV code was adapted from routines developed at Georgetown University [142]. First a spatial bandpass filter was applied to the original image (Fig. 2.7a), with a lower limit of one pixel and an upper limit similar to the particle diameter in pixels (Fig. 2.7b). Second, the centre of each particle was located by calculating the centroid (Fig. 2.7c), and was tracked through subsequent frames (Fig. 2.7d).

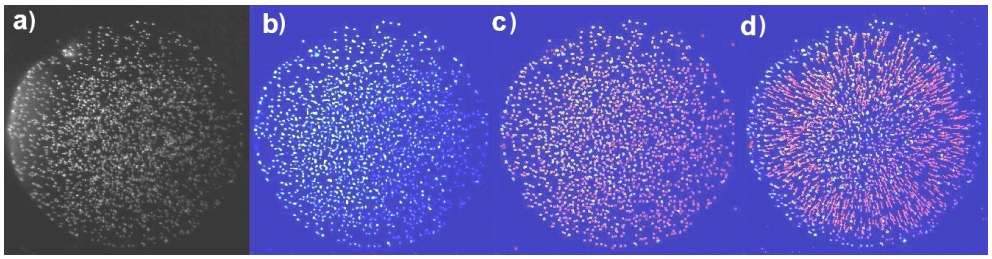

Figure 2.7. Post-processing images from a drying water droplet showing a) the original image, and the image after b) applying a spacial bandpass filter, c) locating the centre of each particle, and d) tracking each particle over subsequent frames (in this case 20).

Particle locations differing by two pixels or less were considered to be stationary over the time period of a frame. Image sequences taken at the same frame rate could be directly compared in this manner. Brownian motion could also be ignored to some degree by dismissing particle tracks with an overall displacement less than the mean Brownian displacement of a particle, given by

$$\bar{x}_B = \sqrt{2D_p t_c} = \sqrt{2k_B T t_c / 6\pi\eta a}, \tag{2.7}$$

where D_p is the diffusion coefficient of the particle in the fluid, t_c is the characteristic timescale, k_B is the Boltzmann constant, T is the temperature in Kelvin, η is the fluid viscosity, and a is the particle radius.

In some cases, particles drifted in and out of focus as their vertical position within the droplet changed. To ensure the reliable tracking of each particle, every particle was issued an identification number. If a particle drifted out of focus (disappearing) for more than a few frames, a particle reappearing in the same location was then issued a new identification number. A threshold was also placed for the maximum expected motion of a particle between subsequent frames, to ensure that the same particle was followed between frames.

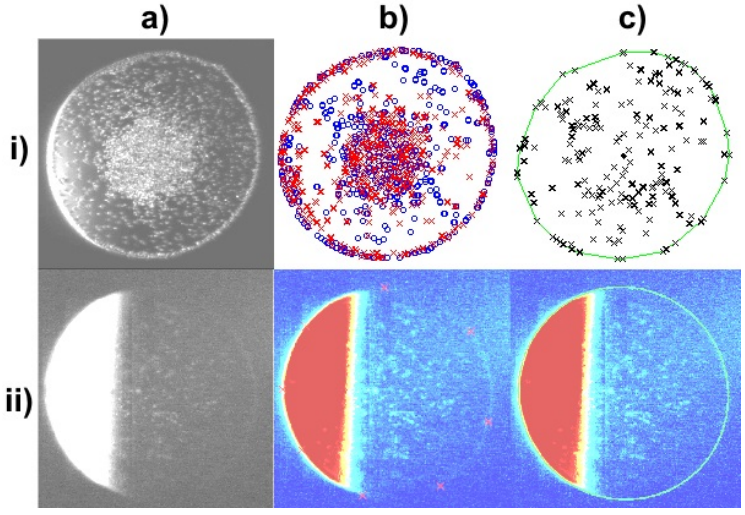

Figure 2.8. Post-processing images showing the i) automatic fitting method for a non-scattering substrate where the contact line is well defined by particles. Stationary particle locations from early and late frames are plotted (bi), and a convex hull is fitted to the overlapping points (ci). The manual fitting method ii) is shown for a non-scattering substrate and contact line un-defined by particles. Points on the contact line are manually selected (bii) and an elliptical fit is made to these points (cii). Dark field images for each method are shown in ai) and aii).

To normalise particle positions and velocities by the droplet contact radius, R, the contact line of the droplet was fitted by an ellipse. For droplets in which particles clearly defined the contact line due to the build up of a ring, the contact line fitting was automatic. Stationary particles were found for two consecutive early frames pre-ring formation (Fig. 2.8bi, blue circles), and two consecutive late frames post-ring formation (Fig. 2.8bi, red crosses) by finding any particles whose position had moved by less than two pixels between consecutive frames. Stationary particles sharing the same position for the early and late frames were considered to be the substrate. Any remaining stationary particles were within the droplet and a convex hull was fitted to these to determine the contact line (Fig. 2.8ci). An elliptical fit was then made to the convex hull. If there were no available data points at the contact line due to dilute particle concentrations and a non-scattering substrate, then a manual fit was made instead by selecting eight points around the contact line (Fig. 2.8bii) and fitting an ellipse to those points (Fig. 2.8cii). The colour-map in MATLAB was adjusted before selecting these points to ensure maximum sensitivity to the intensity change at the contact line. For a scattering substrate, bright patches of substrate were also detected by the particle location algorithm. Either the automatic fit can be used, masking any bright points from the substrate that were not previously removed by the algorithm manually, or the manual contact line fit can be used as the scattering substrates clearly define the contact line.

Normalised particle velocities were defined as

$$v_{\mathrm{n,dry}} = \frac{v\, t_{\mathrm{dry}}}{R_{\mathrm{n}}} \tag{2.8}$$

or

$$v_{\mathrm{n,Rg}} = \frac{v\, t_{\mathrm{Rg}}}{R_{\mathrm{n}}}, \tag{2.9}$$

depending on whether the drying time, t_{dry}, or the time to reach a minimum radius of the collected particle group, t_{Rg} (relevant only to Chapter 4 onwards) was used for the normalisation. R_{n} is the radius of intersection from

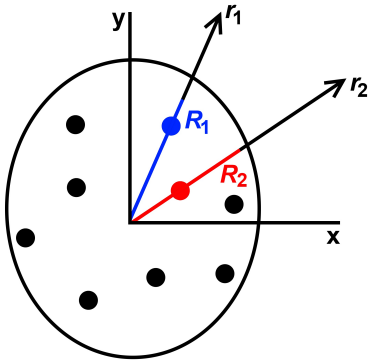

Figure 2.9. A schematic diagram of a droplet containing particles (ellipticity accentuated). The lines of intersection of the droplet centre with particle 1 (blue) and particle 2 (red) are indicated by r_1 and r_2 respectively. The contact radii used for the normalisation of the position and velocity of particle 1 and particle 2 were R_1 and R_2 respectively.

the centre of the droplet to the ellipse, passing through the location of particle n (see Fig. 2.9). Particles moving outwards (towards the contact line) were processed separately from those moving inwards (towards the centre of the droplet) to ensure that negative and positive velocities were considered separately and did not average each other out. Particle velocities were binned spatially in increments of $0.1R$ and temporally by $0.1\,t_{\mathrm{dry}}$ (or $0.1\,t_{\mathrm{Rg}}$), where R is the contact radius of the droplet. The mean radial velocity, $\bar{v}_{\mathrm{r}}$, was then found for each bin, with normalisation methods as described in equations 2.8 and 2.9.

The SEM images of deposits were post-processed in MATLAB to calculate the ring width and fractional area of coverage radially across the deposit. For the ring width, an elliptical fit was applied to the outside and inside of the ring in a similar manner to the manual contact line fit described above (see Fig. 2.10). The centre of the droplet corresponding to the centre of the outer ellipse was found. The intersection of the outer and inner rings with a vertical and horizontal line through the ellipse centre were determined. The ring width in each quadrant was calculated from the co-ordinates of the intersections. A mean ring width, $\bar{w}$, was calculated from the four quadrants.

To calculate the fractional area of coverage radially across the deposit, the deposit image was first converted into binary form (using a threshold grey-level just above the background value). The coverage was not sensitive to small

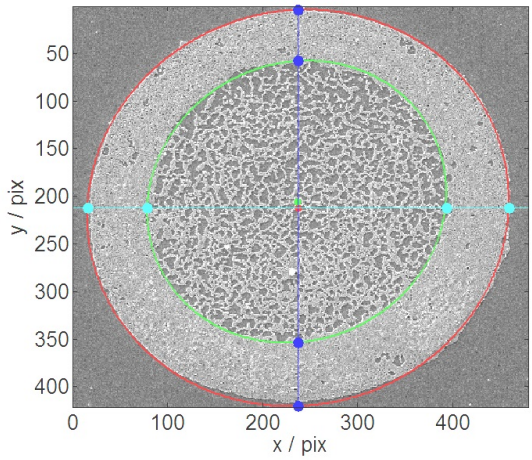

Figure 2.10. Post-processing of an SEM image for the deposit of a dried 90%v ethylene glycol/water droplet containing 1%v 200 nm polystyrene spheres. The ring stain was fitted with an inner and outer ellipse, and the intersections of each ellipse with a vertical and horizontal line through the centre of the deposit were found. The mean ring width was calculated from the intersection separation in each quadrant.

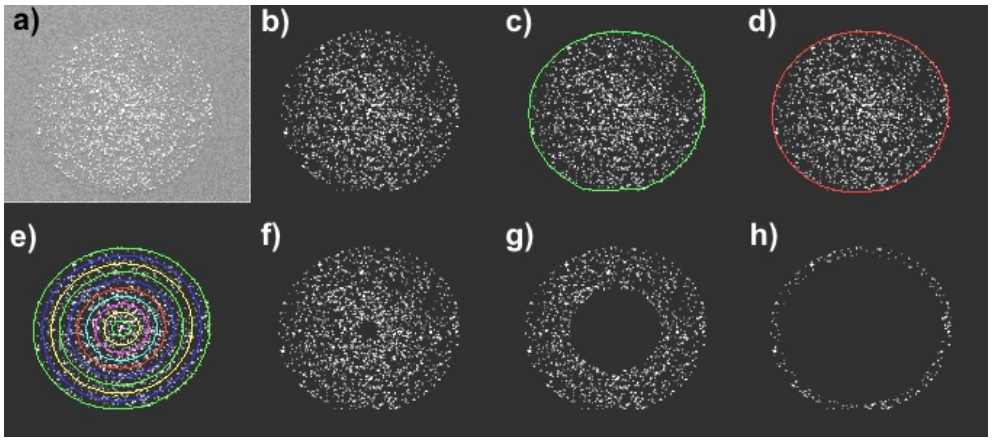

Figure 2.11. Post-processing of an SEM image for the deposit of a dried 2%w laponite/water droplet containing 0.05%v 1 μm polystyrene spheres. The deposit was b) converted to binary, c) fitted with a convex hull, d) fitted with an ellipse, and e) separated into ten concentric rings based on the elliptical fit. Each concentric ellipse was patched to calculate the area of the deposit within the ellipse. Examples are given for f) the first, g) the fifth, and h) the ninth ellipse from the deposit centre.

variations in the threshold value. The ellipse enclosed by the contact line was sectioned into ten concentric ellipses of equal separation (see Fig. 2.11 c–e). The fractional area of coverage, ϕ_{n}, where n indicates the ring number (one for the innermost ring), was determined from the number of white pixels within the annulus, divided by the total number of pixels in the annulus. The total area of coverage, ϕ_{t}, is defined by the total number of white pixels divided by the total number of pixels within the ellipse fit to the deposit periphery. The normalised fractional area of coverage within ring n is then $\phi_{\mathrm{n,norm}} = \phi_{\mathrm{n}} \ / \ \phi_{\mathrm{t}}$.

3 Evaporation of picolitre droplets on surfaces with a range of wettabilities and thermal conductivities

3.1. Introduction

The evaporation of sessile droplets depends on the properties of the fluid and on the ambient atmosphere (e.g. temperature and relative humidity), but is also influenced by the characteristics of the substrate. This chapter focuses on the effect of the wetting properties of the substrate on the evaporation of sessile droplets. The influence of contact line retraction during drying is addressed for two limiting drying modes [66]: the constant contact angle mode, in which the droplet radius decreases with time and the contact angle remains fixed, and the constant contact area mode, wherein the contact line is pinned throughout drying. The former mode occurs on substrates with low contact angle hysteresis and is often observed on hydrophobic substrates [143]. Contact line pinning is enhanced by surface roughness, chemical heterogeneities or particles inside the droplet.

A number of studies have investigated the evaporation of microlitre droplets [56–59]. Under normal laboratory conditions (an air atmosphere at approximately 1 atm and 300 K), the evaporation rate is limited by the diffusion of vapour from the liquid-vapour interface into the ambient atmosphere. When evaporation takes place in the droplet's own vapour, or for very small droplets ($\sim$100 nm in diameter), evaporation may be governed by the kinetics of the transfer of molecules across the interface [57]. Only diffusion-controlled evapo-

ration is considered here.

For a partially wetting sessile droplet, the evaporative flux is not uniformly distributed along the liquid-vapour interface. The flux is larger near the contact line, and smaller at the apex of the droplet. This can be modelled by the equivalent problem of the capacitance of a lens, which was solved theoretically by Picknett and Bexon [66] for the full range of contact angles. Numerical models for contact angles below 90° were later established for pinned droplets by Deegan *et al.* [65] and Hu and Larson [68]. Popov [62] also proposed an analytical model for the full range of contact angles, which is similar to the model proposed by Picknett and Bexon, but can be solved without the use of an infinite series.

Theoretical drying curves [66] predict an increase of the drying time with increasing contact angle. A notable difference in drying times is also expected between pinned and de-pinning droplets at contact angles, θ, below 90°. As θ increases above 90°, the difference in drying times becomes less marked, until at $\theta \backsimeq 140°$ the drying times are similar. The diffusion-controlled model by Popov has been verified for pinned droplets [81,144] over a large range of contact angles. Comparisons between pinned and de-pinning droplets were performed only for contact angles below 60° [58,81].

All the aforementioned studies were performed for microlitre droplets (typically $0.5 - 15\ \mu L$), whereas inkjet droplets typically have picolitre volumes ($4 - 65\ pL$), i.e. five or six orders of magnitude smaller. At present, there have been no measurements comparing the drying of picolitre droplets to a diffusion-limited model for the full range of contact angles and both limiting evaporative modes.

First, the assumptions made in modelling the evaporation of microlitre droplets are revisited, with a view to questioning whether they remain valid for picolitre droplets. The diameter of inkjet droplets ranges between 10 μm and 100 μm. Evaporation should still be limited by diffusion at this scale.

Convective motion occurs within evaporating sessile droplets [80] where, to maintain the spherical cap geometry for the droplet, evaporating liquid is replenished by a convective flow. This convective flow is responsible for

the "coffee-ring" deposits formed from droplets drying with a pinned contact line [85]. In addition, thermal or concentration gradients at the free surface of the droplet can drive Marangoni flows.

Convection of vapour can affect the evaporation rate by influencing the heat transfer inside the droplet. Kelly-Zion *et al.* [64] demonstrated that free convection has to be taken into account for very large droplets (6 mm in diameter) otherwise the evaporation rate is underestimated. For picolitre droplets however, convective heat transfer due to internal flows is negligible compared to conduction. The relative effect of convection and conduction is seen in the Péclet number, $Pe = uR/\alpha$, where α is the thermal diffusivity of the fluid, u is the velocity and R the contact radius of the droplet. For a droplet of water ($\alpha = 1.4 \times 10^{-7}$ m^2 s^{-1}) with a radius $R = 25$ μm and internal velocities of the order of $u = 100$ μm s^{-1}, $Pe = 0.018 \ll 1$, which means that conduction predominates.

Evaporative models for sessile droplets (e.g. [62]) usually assume that the process is isothermal. Several studies [97, 145–148] have recently shown that this assumption breaks down when the substrate has a poor thermal conductivity. When the substrate acts as an insulator, heat transfer from the surroundings is insufficient to balance the latent heat of vaporization and the liquid in the droplet cools down. As a consequence, the saturation vapour pressure at the liquid-vapour interface decreases and evaporation slows down.

Evaporative cooling was neglected in recent studies on microlitre droplets [58, 81, 144], because the substrates (silicon wafers or aluminum plates) had large thermal conductivities. Inkjet printing often involves substrates with poor thermal conductivities such as paper, for which evaporative cooling might not be negligible. Here, it is investigated whether evaporative cooling is important in the case of picolitre droplets or whether the process can still be assumed to be isothermal.

In this chapter, the isothermal, diffusion-controlled model by Popov is verified on a scale relevant to inkjet printing for both pinned droplets and those with a moving contact line. This work addresses the evaporation of picolitre water droplets on a number of substrates with apparent contact angles in the range of 10° to 135° and thermal conductivities in the range $0.25 - 149$

$Wm^{-1}K^{-1}$.

3.2. Experimental

3.2.1. Evaporative Model

Picolitre droplets have Bond numbers $\ll 1$, therefore gravitational effects are negligible. Sessile droplets can be considered as a spherical cap with a mass given by

$$M = \pi \rho_{\mathrm{f}} R^3 \, \frac{\cos^3\theta - 3\cos\theta + 2}{3\sin^3\theta}, \tag{3.1}$$

where R is the droplet radius, ρ_{f} is the liquid density, M is the droplet mass, and θ is the apparent three-phase contact angle. Figure 3.1 indicates the relevant droplet parameters.

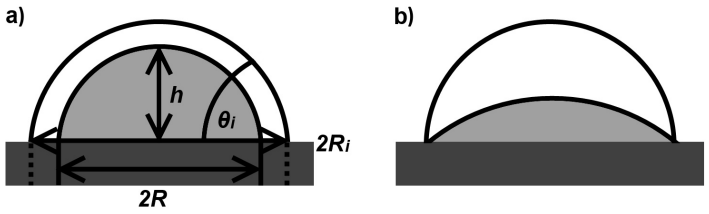

Figure 3.1. Schematics for drying with a) a moving contact line with constant contact angle, and b) a pinned line. R_i is the initial radius, h is the height, R is the current radius and θ_i is the initial contact angle (i.e. the apparent contact angle at time t=0).

Evaporation is limited by diffusion, and diffusion is considered quasi-steady. The time scale for the build-up of a concentration profile around the droplet by diffusion is $t_{\mathrm{diff}} = R^2/D$ (with a length scale R), where D is the diffusion coefficient of vapour in the ambient atmosphere. Indeed, t_{diff} is much smaller than the drying time t_{dry} (i.e. $t_{\mathrm{diff}}/\, t_{\mathrm{dry}} \ll 1$). The dynamics of the droplet surface are neglected, and it is assumed that at any instant the droplet has its equilibrium shape [62]. The Kelvin correction to the vapour pressure is negligible for the droplet sizes considered. Thermal effects due to evaporative cooling are also neglected, as are Marangoni effects.

The rate of mass loss over time, t, is given as [62]

$$\frac{dM}{dt} = -4\pi R(t) D(n_s - n_\infty)\left[\frac{\sin\theta(t)}{4(1+\cos\theta(t))} + \int_0^\infty \frac{1+\cosh(2\theta(t)\tau)}{\sinh(2\pi\tau)}\tanh[(\pi-\theta(t))\tau]\,\mathrm{d}\tau\right], \tag{3.2}$$

where n_s is the saturation vapour density and n_∞ is the ambient vapour density, given as $n_\infty = RH \times n_s$ for a relative humidity, RH. The term outside of the square bracket gives the evaporation rate for a spherical droplet. The terms inside the square bracket account for the non-uniformity of the evaporation rate along the interface of a sessile droplet.

The time dependence of the contact angle for a pinned droplet, $R(t) = R_i$, can be obtained from combining equations 3.1 and 3.2, then solving for a constant droplet radius [62], yielding

$$\frac{d\theta(t)}{dt} = -\frac{D(n_s - n_\infty)}{\rho R_i^2}(1+\cos\theta(t))^2\left[\frac{\sin\theta(t)}{1+\cos\theta(t)} + 4\int_0^\infty \frac{1+\cosh(2\theta(t)\tau)}{\sinh(2\pi\tau)}\tanh[(\pi-\theta(t))\tau]\,\mathrm{d}\tau\right]. \tag{3.3}$$

Equation 3.3 was solved using the *ode45* function in MATLAB. The numerical integration was computed by a trapezoidal method, the *trapz* function in MATLAB. The drying time t_P of a pinned droplet is defined by the time when the contact angle reaches zero. In the limit of small contact angles, the drying time, $t_{P,\theta}$, reduces to

$$t_{P,\theta} = \frac{\pi\rho R_i^2 \theta_i}{16 D(n_s - n_\infty)}, \tag{3.4}$$

with θ_i being the initial contact angle [62].

Alternatively, Equation 3.2 can be solved for a constant contact angle to find the time dependence of the radius for a droplet with a moving contact

line, as in [80, 149], giving

$$R(t)^2 = R_i^2 - 2\frac{D(n_s - n_\infty)}{\rho}\frac{\sin^3\theta}{\cos^3\theta - 3\cos\theta + 2}\,t\Bigg[\frac{\sin\theta}{1+\cos\theta} + 4\int_0^\infty \frac{1+\cosh(2\theta\tau)}{\sinh(2\pi\tau)}\tanh((\pi-\theta)\tau)d\tau\Bigg]. \tag{3.5}$$

The drying time t_M for a droplet evaporating with a constant contact angle, is defined as the time when the radius reaches zero. Note that the square of the radius decreases linearly with time [57].

Finally, the drying time t_{hem} is defined for a hemisphere with a freely moving contact line. For the hemisphere, evaporation is uniform along the interface and the drying time for a hemisphere of equivalent volume to the droplet will be used in the following for normalisation.

3.2.2. Experimental Set-up and Procedure

Picolitre droplets of high purity water (MilliQ) or ethanol, were deposited onto the substrate as described in the experimental section (Chapter 2, Section 2.1). A number of substrates were prepared to provide a range of wettabilities. Glass microscope slides were given different treatments. First, substrate G was simply wiped with lint-free tissue. Second, substrate RG was rinsed with high purity water (MilliQ). Third, substrate DG was left overnight in 2%w decon 90 alkaline cleaning solution, before rinsing with high purity water. Rinsed substrates were dried in nitrogen and left in an oven to ensure full drying. PTFE and sapphire (SP) substrates were prepared in the same manner as substrate G.

Substrate VBC (fabricated by P.S. Brown, University of Durham) was a glass slide placed in an evacuated plasma chamber and exposed to vinylbenzylchloride monomer [150] (Sigma Aldrich +97% purity) at a flow rate of 1.6 x 10^{-7} kgs^{-1} with a pressure of 0.2 mbar. Purging for 5 minutes was followed by ignition of the electrical discharge. The pulse duty cycle consisted of 100 μs

on and 4 ms off. The radio frequency used was 13.56 MHz. Plasma deposition was for a duration of 1 minute, followed by 5 minutes of quenching.

Substrates S1, S2, S3 and S4 (fabricated by P.S. Brown, University of Durham) were silicon wafers spin-coated with polybutadiene solution in toluene before undergoing plasmachemical fluorination [151] with CF_4 gas (Air products, 99.7% purity). S1 and S2 were treated at a power of 30 W and 10 W respectively for 10 minutes. S3 and S4 were treated at 10 W for 5 minutes at different locations in the reactor, resulting in different roughnesses. S1 showed a root mean squared (rms) roughness of ∼130 nm by Atomic Force Microscopy (AFM, Digital Instruments Nanoscope III scanning probe microscope), whereas S2 had an RMS roughness of ∼90 nm. S3 and S4 had rms roughnesses of ∼95 nm and ∼75 nm respectively. All four substrates had the same surface chemistry (measured by X-ray Photoelectron Spectroscopy, XPS) but different surface roughness.

The substrate base materials were chosen to give a range of thermal conductivities in order to examine the effects of evaporative cooling on the evaporation rate. Substrates with a silicon wafer base had a high thermal conductivity, while PTFE gave a low thermal conductivity (Table 3.1).

Table 3.1. Thermal conductivities, κ, of the substrates.

Base Material	Substrates	κ / $Wm^{-1}K^{-1}$
PTFE	PTFE	0.25
Glass	DG, RG, G, VBC	0.96
Silicon	S1, S2, S3, S4	149
Sapphire	SP	35

3.3. Results and Discussion

Typical initial contact angles from microlitre droplets and picolitre droplets on each substrate are compared in Table 3.2. Example image sequences for drying droplets are shown in Fig. 3.2 with corresponding videos for substrates G (pinned contact line, Video G) and S4 (moving contact line, Video S4).

Table 3.2. A comparison of apparent contact angles post-spreading for microlitre and picolitre water droplets on the same substrate.

Substrate	θ μL drop	θ pL drop	Drying Mode
S1	174°± 2°	133°± 8°	Pinned
S2	173°± 2°	130°± 3°	Pinned
S3	130°± 1°	118°± 1°	Pinned
S4	118°± 1°	109°± 1°	Moving
VBC	80° ± 2°	65° ± 6°	Pinned
G	33° ± 7°	40° ± 10°	Pinned
RG	24° ± 7°	15° ± 3°	Moving
DG	17° ± 6°	14° ± 2°	Moving
PTFE	108°± 1°	100°± 3°	Moving
SP	95° ± 7°	88° ± 14°	Moving

Water droplets drying on substrates VBC, S1, S2, S3, and G dried with a pinned contact line (see Fig. 3.3). On substrates DG, RG, PTFE, SP, and S4, water droplets dried with a moving contact line (see Fig. 3.3). The actual drying behaviour was intermediate between the two limiting modes (see S4 in Fig. 3.2). Slow contact angle reduction or contact line recession marked the pinned or moving contact line modes, rather than the ideal case of a perfectly fixed contact angle or contact line (see Fig. 3.3 and Fig. 3.4). The drying mode was categorised as closest to the pinned mode if the droplet diameter varied by $\leq$25% in 85% of the drying time. Ethanol droplets were deposited only on substrates S3, S4, SP, and PTFE. In each case, ethanol droplets dried with a moving contact line.

On all substrates with the exception of G, the apparent contact angles for the picolitre droplets were smaller than for microlitre droplets. This difference may result from the influence of the droplet scale relative to microscopic features on the substrate [152–154], or it may be due to impact [155]. The micolitre droplets have millimeter scale contact diameters, and so are sensitive only to macroscopic surface roughness. Picolitre droplets have micrometer scale contact diameters, and so are sensitive to microscopic surface roughness features and chemical inhomogeneities. The sensitivity of picolitre droplets to chemical contamination of a much smaller scale could explain the higher

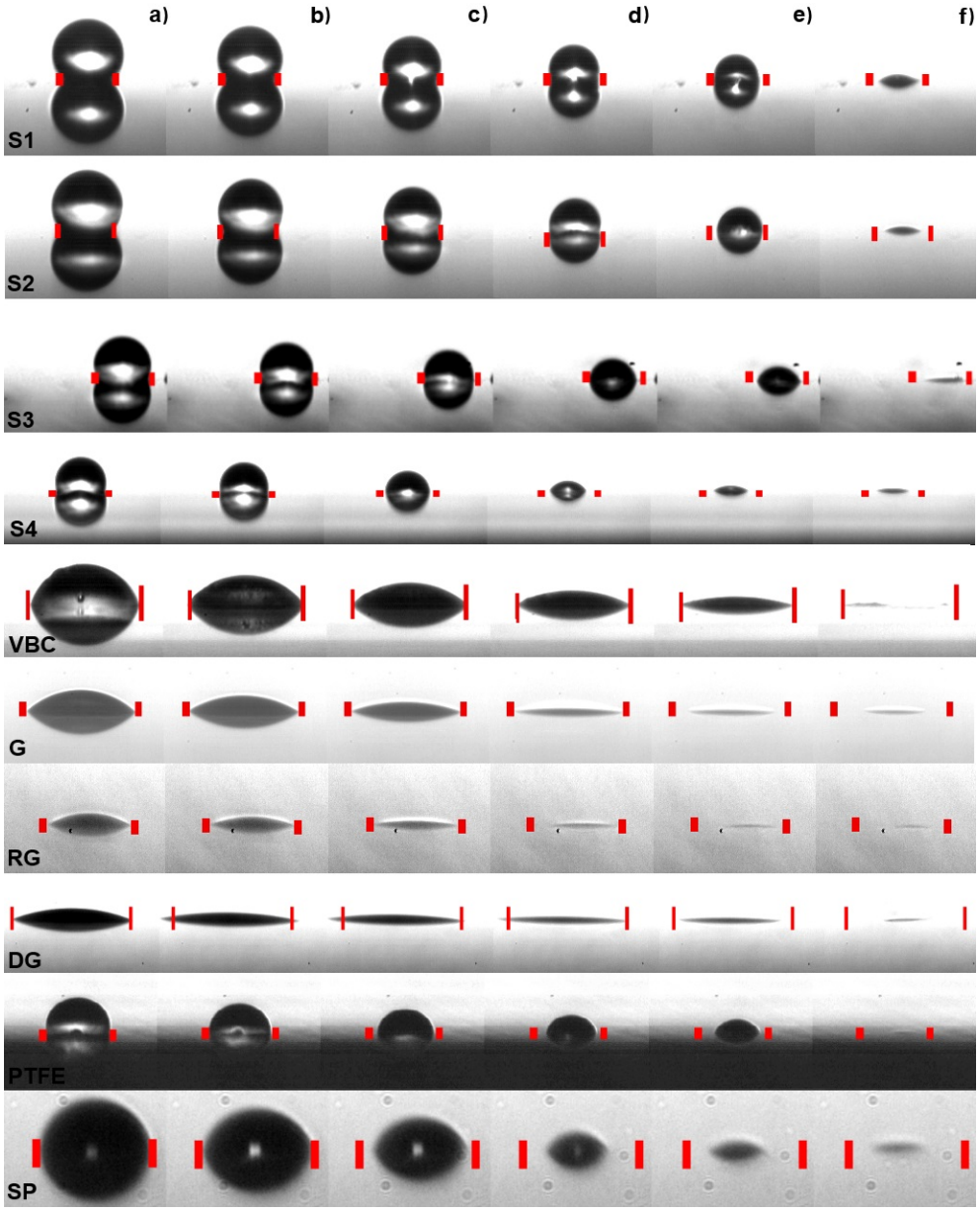

Figure 3.2. Example images for water droplets drying on substrates S1, S2, S3, S4, VBC, G, RG, DG, PTFE and SP after a) $0.0 t_{\mathrm{dry}}$, b) $0.2\ t_{\mathrm{dry}}$, c) $0.5\ t_{\mathrm{dry}}$, d) $0.8\ t_{\mathrm{dry}}$, e) $0.9\ t_{\mathrm{dry}}$ and f) $0.95\ t_{\mathrm{dry}}$. Vertical red lines indicate the initial position of the contact line pre-spreading.

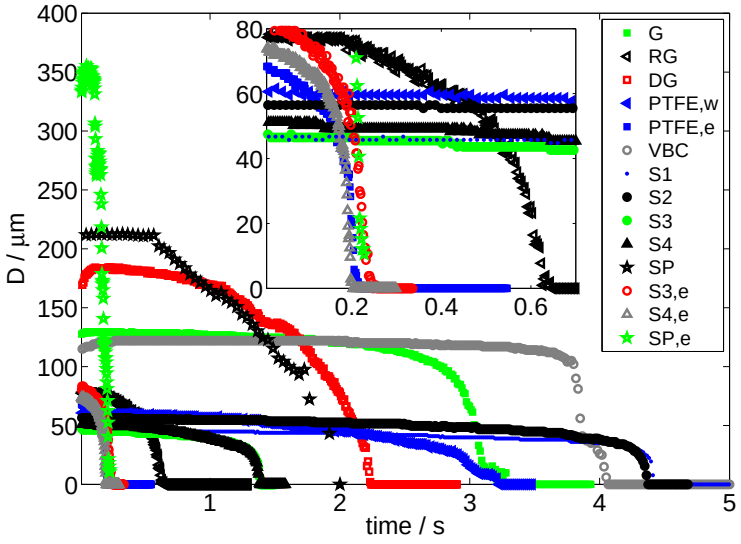

Figure 3.3. Typical evolution of droplet diameters during the drying lifetime for each substrate, with the insert showing a zoom for the faster drying droplets.

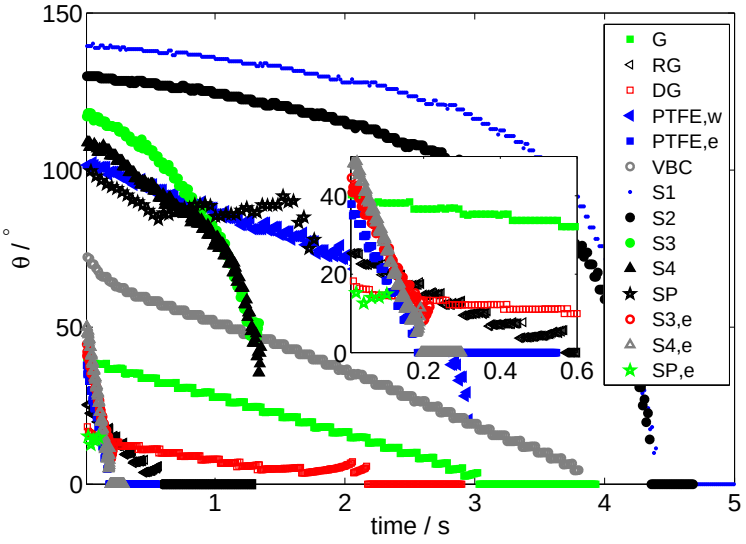

Figure 3.4. Typical evolution of droplet apparent contact angles during the drying lifetime for each substrate, with the insert showing a zoom for the faster drying droplets.

apparent contact angle of the picolitre droplet on substrate G compared to a microlitre droplet. The higher impact speeds of the picolitre droplets compared to the gentle deposition of the microlitre droplets could also serve to drive the picolitre droplet into the surface features, reducing the apparent contact angle.

In the evaporative model, the evaporative flux depends on the shape of the droplet. Therefore, the necessary input for the initial contact angle in the model is the apparent contact angle at the picolitre scale. An input contact angle measured from microlitre droplets will not provide an accurate estimate of the drying time on the picolitre-scale. Note that the actual thermodynamic contact angle involved in the Young-Laplace equation never appears in the model.

The results for picolitre droplets in each contact angle regime (above and below 90°) and for each drying mode (pinned and moving contact line) are shown in Figs. 3.5, 3.6, and 3.7 for water droplets on the substrates VBC, S2, and S4, and for ethanol droplets on S4. For clarity, only one example for each drying mode is plotted. Note that droplet volumes and the relative humidity differ between droplets and so drying times cannot be directly compared. Data from five or more droplets were collected on each substrate. For easier readability, the trends shown in Figs. 3.5, 3.6, and 3.7 are for one representative droplet on each substrate only.

The evolution of the droplet diameter and contact angle with time are presented in Figs. 3.5 and 3.6. The diameters of water droplets drying on substrates VBC and S2 remain pinned for most of the droplet lifetime. On substrate S4, water and ethanol droplets dried with a moving contact line, although the apparent contact angle was not constant. Some droplets show an initial increase in their diameter, which corresponds to the end of spreading. The part of the signals corresponding to the end of spreading is discarded by removing the first 0.2 s of the datasets for water droplets and the first 0.02 s for ethanol (before finding R_i or θ_i for model inputs).

The results from the theoretical model for substrates with base materials of glass or silicon are in good agreement with the experimental data, both quan-

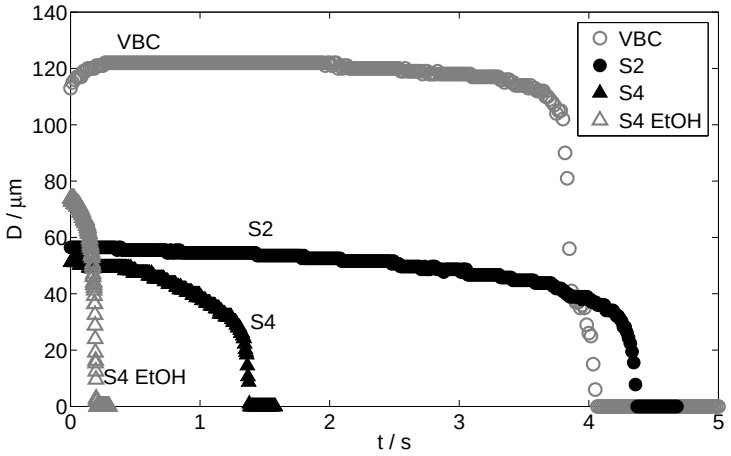

Figure 3.5. Typical evolution of droplet diameters during the drying lifetime for each drying regime. Data points marked ○ represent pinned drying, and △ represents a moving contact line. Closed symbols represent contact angles $\geq 90°$ and open symbols represent $< 90°$.

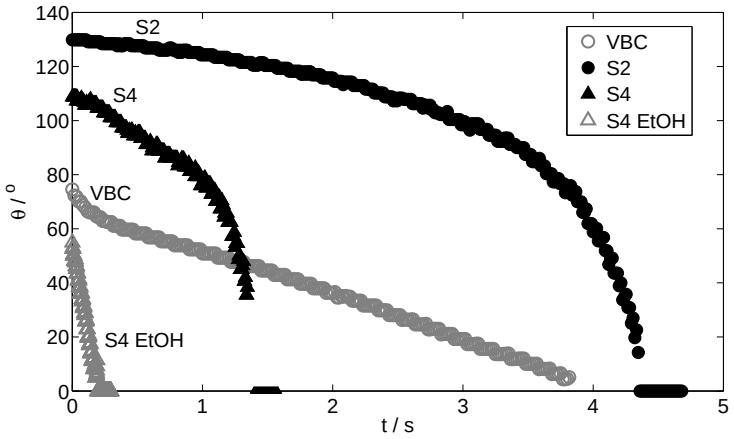

Figure 3.6. The evolution of droplet contact angles during drying. Data points marked ○ represent pinned drying, and △ represents a moving contact line. Closed symbols represent contact angles $\geq 90°$ and open symbols represent $< 90°$.

titatively (Table 3.3) and in the shape of the mass loss rate (Fig. 3.7), despite any intermediate behaviour between limiting regimes. The drying mode was always intermediate to some extent as the droplets did not stay fully pinned or maintain a perfectly constant apparent contact angle during their whole lifetime. However, the drying times remained close to the limiting mode predictions. The results confirm the validity of the diffusion-controlled isothermal evaporation model in the picolitre regime on substrates with thermal conductivities of $\geq 1\,\mathrm{W\,m^{-1}\,K^{-1}}$. The model has no fitting parameter, which makes it particularly suitable for predicting the drying time of inkjet droplets.

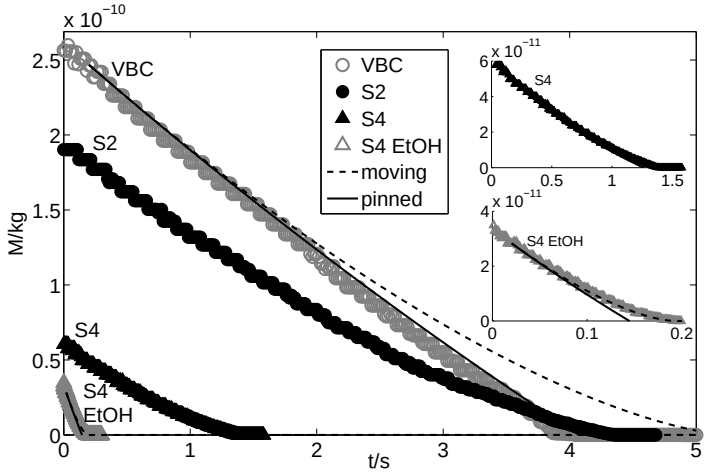

Figure 3.7. The mass loss rate during the drying lifetime. Data points marked ○ represent pinned drying, and △ represents a moving contact line. Closed symbols represent contact angles $\geq 90°$ and open symbols represent $< 90°$. Inserts show evaporation on substrate S4 with water above and ethanol below.

Table 3.3. Predicted drying times for the moving contact line regime t_{M} (from Eqn. 3.5 when $R = 0$), the pinned contact line regime t_{P} (from Eqn. 3.3 when $\theta = 0$), and the pinned regime in the limit of small contact angles $t_{\mathrm{P},\theta}$ (Eqn. 3.4), compared to the experimental drying time, t_{exp}, for each substrate. Drying times for droplets on each substrate are for a single representative droplet. The drying time predictions are dependent on the volume of each specific droplet, so drying times cannot be compared between different rows in the table. Fluid type is indicated by w for water and e for ethanol. Temperatures ranged between 293.5 K and 295.0 K.

Surface, fluid	t_{exp} / s	$t_{\mathrm{P},\theta}$ / s (Eqn. 3.4)	t_{P} / s (Eqn. 3.3)	t_{M} / s (Eqn. 3.5)	RH
G, w	3.03	2.92	2.95	4.06	0.59
RG, w	0.57	0.47	0.47	0.60	0.47
DG, w	2.18	1.85	1.83	2.61	0.50
PTFE, w	3.21	1.61	2.39	2.72	0.49
PTFE, e	0.18	0.10	0.10	0.13	0.00
VBC, w	3.93	3.67	4.07	5.27	0.48
S1, w	4.09	1.65	4.18	4.34	0.50
S2, w	4.36	1.76	4.22	4.41	0.50
S3, w	1.46	0.85	1.40	1.53	0.26
S4, w	1.40	0.87	1.27	1.42	0.26
SP, w	2.01	1.28	1.70	2.06	0.34
S3, e	0.24	0.16	0.17	0.23	0.00
S4, e	0.19	0.14	0.14	0.19	0.00
SP, e	0.23	0.15	0.15	0.22	0.00

In contrast, on the low conductivity PTFE substrate the drying times are under-predicted by the model due to evaporative cooling slowing the evaporation. Estimates of the degree of evaporative cooling were made by adjusting the temperature input to the model in order to best fit the experimental data. Temperature differences from ambient conditions for droplets on the PTFE substrates were estimated at $\sim 2.7 \pm 1$ K for water droplets on PTFE and $\sim 5.8 \pm 1$ K for ethanol droplets on PTFE. The magnitudes of these estimates agree well with experimental values reported in [147] for microlitre droplets. Hence, the model cannot be used for predictions of the drying time on substrates with thermal conductivities lower than that of glass, as the isothermal assumption does not hold.

For droplets with initial contact angles below 90°, pinned droplets show a linear mass loss rate, represented in Figure 3.7 by drying on VBC (data points marked $\circ$). In contrast, droplets with a moving contact line, demonstrated on S4 with ethanol (data points marked $\triangle$), exhibit a decrease in the mass loss rate towards the end of drying. The drying times for droplets of equal volume on hydrophilic substrates can vary significantly depending on whether the contact line is pinned or moving. It is interesting to note that both evaporative modes behave similarly during the initial stage of evaporation and diverge only towards the end of drying. The dependence of the drying time on the late stages of drying could prove especially important for transitory modes or stick-slip motion [58], where the droplet de-pins part way through drying. As there is little dependence of the drying time on the drying mode for the initial stages of drying, early de-pinning will give drying times corresponding to droplets drying with a moving contact line. In contrast, late transitions in the drying mode or stick-slip motion may give behaviour in between the pinned and moving contact line predictions.

At large contact angles ($\theta \gtrsim 90°$), the mass loss rate becomes non-linear for both drying modes. The difference in the drying time between constant contact angle and constant contact area modes decreases, until at a contact angle of $\backsim 140°$ the drying times are very similar (Fig. 3.8). Therefore, for hydrophobic surfaces, the dependence of the drying time on the drying mode is much less than on hydrophilic substrates.

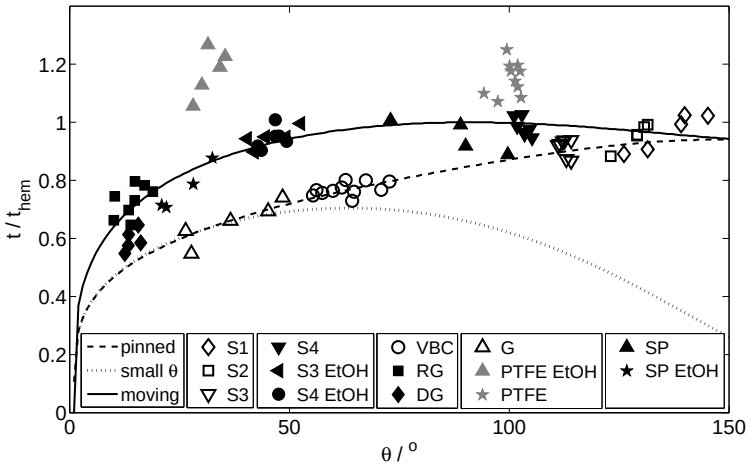

Figure 3.8. The drying times are plotted for each drying mode, normalised by the time for a free hemisphere of the same volume to dry. Open symbols indicate pinned drying, filled symbols indicate a moving contact line. The contact angle used is at 0.2 s for water and 0.02 s for ethanol to ensure spreading has ended. Theoretical models for isothermal diffusion-limited evaporation are shown for drying with a pinned contact line (from Eqn. 3.3 when $\theta = 0$), a moving contact line (from Eqn. 3.5 when $R = 0$), and in the limit of small contact angles (Eqn. 3.4).

Figure 3.8 shows the drying times predicted by the theoretical model. Drying times are normalised by t_{hem}, the drying time of a hemisphere of equal volume with a freely moving contact line. The agreement between the predicted drying times and the experimental ones is very good for both fluids on glass and silicon substrates, further validating the model for picolitre droplets on substrates with thermal conductivities of 1 $Wm^{-1}K^{-1}$ or above. For droplets deposited on PTFE substrates, with lower thermal conductivity, the experimental drying times deviate from the model predictions as a result of evaporative cooling. Small angle predictions (Equation 3.4) are in agreement with the experiment for contact angles below 45°, but fail above 45° as expected. The drying time for the pinned contact line mode increases with apparent contact angle until predictions coincide with the model curve for the moving contact-line mode.

3.4. Summary

Diffusion-limited evaporative models have previously been validated for microlitre droplets, but not for picolitre droplets considering a full range of contact

angles and limiting evaporative modes. Picolitre droplets of water and ethanol on substrates with thermal conductivities $\geq 1\ Wm^{-1}K^{-1}$ follow a diffusion-limited isothermal evaporative model [62]. The model has been verified on these substrates for contact angles ranging between 10° and 135°. In addition, the model successfully captures the two limiting modes of evaporation. The drying time is dependent on both the substrate hydrophobicity and the drying mode. Pinned droplets dry faster than those with a moving contact line, and evaporation on hydrophilic substrates is faster than on hydrophobic substrates. The difference between drying times for each drying mode is more pronounced for contact angles below 90°.

The model and experimental measurements are in good agreement for substrates of silicon or glass, allowing drying times to be predicted accurately for both evaporation modes on substrates with thermal conductivities ≥ 1 $Wm^{-1}K^{-1}$. Such estimates of the drying times could be particularly useful in applications such as spray cooling, where the rate of evaporation must be critically controlled. The only input parameters are the thermophysical properties of the fluid and surrounding atmosphere, the ambient conditions (temperature and RH) and the apparent radius and contact angle of the droplet. Hence, no fitting parameter is required.

Glass represents the threshold for thermal conductivity below which evaporative cooling is no longer negligible. On lower conductivity substrates ($\kappa \leq$ $1\ Wm^{-1}K^{-1}$) such as PTFE, the evaporation rate is slowed significantly due to evaporative cooling. As a consequence, the isothermal model breaks down, under-predicting the drying time. A more complex model including energy balances is needed to account for evaporative cooling. This conclusion has implications for inkjet printing, where low conductivity paper substrates are common.

4 | Internal flows inside picolitre droplets of binary solvent mixtures

4.1. Introduction

The prediction and control of the particle distribution and micro-structure in a deposit is important for optimising both print quality and functionality. The transport processes inside a drying droplet need to be understood to obtain the best deposit for a given application. However, many existing studies only consider the final deposit structure [105,106,113,156,157] or still images at time frames throughout drying [109]. Without following particle motion throughout the whole drying period, it is difficult to infer particle transport mechanisms and the manner in which the deposit is built up. Without knowledge of the particle transport, it is harder to devise effective control strategies for the deposit. There are a handful of studies considering the internal flows throughout the whole drying period [45,103,158] but these deal with microlitre droplets (often only at the contact line), not the picolitre droplets used in inkjet printing.

A range of techniques have been used to image flows inside evaporating droplets, including conventional microscopy [90, 103], fluorescence microscopy [102, 109], particle tracking velocimetry [158, 159] and particle imaging velocimetry [45, 160, 161]. The imaging of flows inside picolitre droplets is much more involved than for microlitre droplets. Due to the high curvature of the liquid-vapour interface of picolitre droplets, tracer particles in the fluid need to be viewed through the substrate, which limits substrates to transparent materials. The smaller particles necessary for tracking flows inside picolitre droplets scatter less light, making collection more difficult. Additionally, flow velocities are often faster in the smaller picolitre droplets, therefore higher frame rates

and faster shutter speeds are required.

Internal flows inside sessile droplets of binary mixtures can exhibit very different flow patterns from droplets of each pure component [44, 45]. In pure solvents, particles are transported radially outwards towards the contact line, forming a ring stain [61]. In a binary mixture, differential evaporation of each component [79, 162] leads to a surface tension gradient along the liquid-vapour interface, causing Marangoni stresses. A recirculating flow is set up inside the droplet to balance the tangential stress at the interface [68, 113]. Consequently, Marangoni flows have been employed to minimise the formation of ring stains [103, 105, 106, 113].

Transport mechanisms other than Marangoni flow or evaporation-driven radial flow can affect the deposit. Particles may not follow the motion of the carrier fluid if there is sufficient force to move particles off the streamlines. Particle migration across streamlines has been observed due to chemophoresis (diffusiophoresis) along a chemical potential gradient [163–166], thermophoresis (the Soret effect) along a temperature gradient [167–171], electrophoresis along a gradient in an applied electric field [172–176], and magnetophoresis along a gradient in an applied magnetic field [175, 177, 178]. As particles of a particular size or surface chemistry may behave differently depending on the applied field, phoretic mechanisms can be an effective way of sorting particles by size or character [177,179], or for particle manipulation and self-assembly [180,181]. Particle motion due to capillary forces has also been noted [115,182], and shear-induced migration is capable of accumulating particles to build up structures in numerous geometries [183, 184].

When a concentration gradient in the solvent exists across a particle, the surface of that particle experiences non-uniform interactions with the surrounding fluid/solute. Particle migration along the concentration gradient is known as chemophoresis. The particle moves towards a region where its chemical potential is lowered. This could be a region containing a preferred solvent, or a region rich in an adsorbing solute that lowers the surface energy of the particle. A concentration gradient may arise across the whole sample (e.g. due to

a gradient in the solvent composition or from added polymer or surfactant). Alternatively, concentration gradients can be produced by a reaction of the migrating species itself [181, 185–187]. In the latter case, the concentration gradients are much more localised. However, an asymmetrical particle must be used, to prevent the nullification of concentration gradients at the particle solid-liquid interface resulting from reaction products and depleted reactant.

Thermodiffusion (in liquid mixtures) and thermophoresis (in colloidal suspensions) can arise due to temperature gradients, and depends on the solvent composition and fluid structure [188–190]. For example, in ethanol/water mixtures (amongst other aqueous systems), the migration direction of the water molecules due to thermodiffusion switched at an ethanol mole fraction of 0.14 ($\backsim$ 35%v ethanol) [188, 189]. For high water concentrations (low ethanol concentrations) the water molecules moved towards cooler regions. For low water content, the migration direction was reversed. In associative fluids, inter-component and intra-component interactions may be of different strengths. If inter-component interactions are larger than intra-component interactions, the dilute component is more strongly bound (i.e. it experiences relatively more inter-component interactions). The more strongly bound component migrates towards cooler regions [188]. Hence, the migration direction is reversed when the composition of the mixture changes such that the dilute component is switched.

For colloidal suspensions, a temperature gradient across the surface of a particle results in an inbalance of the interfacial stress in the region close to the solid-liquid interface, driving thermophoretic motion. As migration depends on forces localised around the particle surface, particle-solvent interactions (electrostatics, dispersion interactions etc.) and particle-particle interactions can greatly effect thermophoretic mobility. When the colloid-solvent interaction is of entropic origin, the solute-solvent interactions are temperature dependent. The temperature gradient across the particle then results in local variations in particle-solute interactions, driving migration [169]. Often, the direction of migration switches if the average temperature of the sample falls below a threshold temperature [170]: Typically, particles migrate to warm regions when the average temperature is low (below the threshold temperature) and

to cold regions when the average temperature exceeds the threshold temperature. Thermal diffusion coefficients for polymeric samples are typically of the order 10^{-12} $m^2 s^{-1} K^{-1}$ [170,191].

Shear induced migration has been noted in colloidal suspensions when there is a gradient in the shear rate. Particles migrate from regions of high shear to regions of low shear, causing segregation [183, 184, 192]. The segregation can depend on the flow geometry [184], and the shape [193] and size [183] of the particles. The shear-induced migration may result either from lift on the particles [194, 195] or from asymmetry in particle collisions [183, 196]. For the latter, a small imperfection or roughness on the particle surface, influences the proximity of approach of a second particle. As the second sphere moves past the first sphere, particles may move off their current streamline due to the hard sphere repulsive force. The probability of finding a particle behind the sphere is then reduced (hence fore-aft asymmetry). In shear flow the probability of approach is larger on the high velocity side of a particle.

In this chapter, the internal flows inside sessile droplets are considered for picolitre volumes relevant to inkjet printing. High-speed imaging of tracer particles inside drying droplets of ethanol/water and 1-methoxy-2-propanol (PM)/water gave details about the internal flows. Simultaneously, side-on shadowgraph imaging was used to view the droplet profile during drying and extract information on the evaporation rate and contact angle. The particle transport within droplets was monitored and later compared to the end deposit (imaged on a scanning electron microscope). In this manner, the complete drying process was recorded to discover the influence of the flows on the deposit morphology and microstructure.

Complex internal flows were observed inside binary solvent mixtures during drying. Differential evaporation of solvents resulted in circulating Marangoni flows that transported particles along fluid streamlines. As drying progressed, particles migrated across fluid streamlines to gather at the centre of the droplet, independent of the Marangoni flow direction. Marangoni flows driven by concentration gradients determined the shear-rate throughout the droplet.

The strong coupling between the compositional gradients and shear flow made it very difficult to separate individual mechanisms for the migration. First, the flow regimes present depending on the Marangoni flow direction are explored. In a separate section (4.3.2), potential mechanisms for particle migration are discussed, that could be responsible for particle collection at the centre of the droplets (including thermophoresis, chemophoresis and shear-induced migration). Last, the influence of the strength, duration, and direction of the Marangoni flow, and the extent of the central collection on the end deposit are investigated. The Marangoni strength is determined by the magnitude of the surface tension gradient and is controlled by the chemical composition of the mixture and the relative evaporation rates of the solvents. The duration is the period of time the Marangoni flow lasts for, relative to the drying time, and is dependent on the component ratio.

4.2. Evaporation of binary solvent mixtures

In this section, the internal flows within picolitre droplets of binary solvent mixtures are compared with droplets of each pure component. Droplets were printed and imaged as described in Chapter 2, Section 2.1 (using a nozzle with a 50 μm diameter). Plasma fluorinated substrates were prepared as described in Chapter 3, Section 3.2.2. The binary mixtures primarily investigated were ethanol/water, and PM/water. Table 4.1 shows the properties of the solvents, and Figure 4.1 gives the trends in surface tension, density, and viscosity with the composition of the mixture. Ethanol and PM were chosen as both solvents have a surface tension much less than water, but ethanol has a higher vapour pressure than water and PM has a lower vapour pressure than water.

Table 4.1. Surface tensions, σ, and vapor pressures, p, of different solvents at 20°C.

Fluid	σ/ mNm^{-1}	p/ kPa
Ethanol	22.4 [127]	5.95 [127]
1-Methoxy-2-propanol (PM)	27.7 [132]	1.16 [132]
Water	72.9 [127]	2.34 [127]

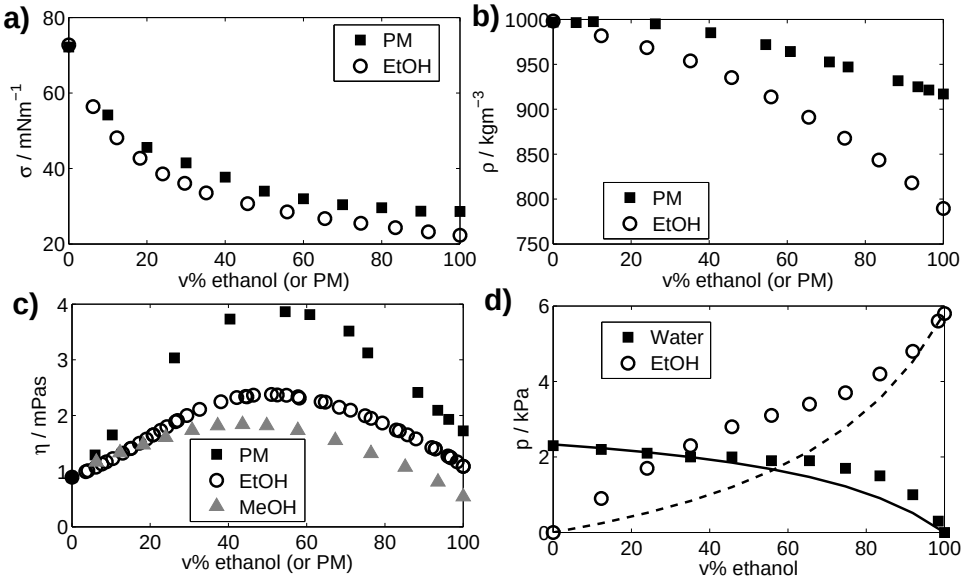

Figure 4.1. The variation in the a) surface tension, σ, ([134] for ethanol) b) density, ρ [128, 197], and c) viscosity, η [197–200], for ethanol/water, PM/water, and methanol/water mixtures of varied composition at 20 °C. The partial vapour pressures of water and ethanol above ethanol/water mixtures of varied composition are given in d) [201] with dashed and solid lines indicating Raoult's law for ethanol and water respectively.

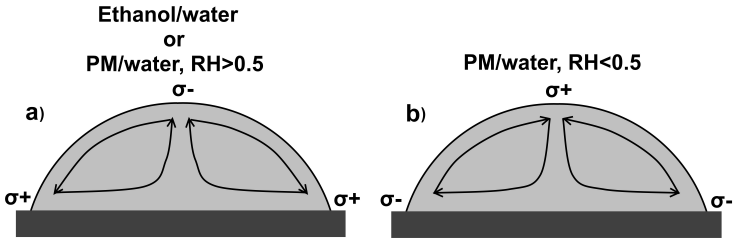

Figure 4.2. Marangoni flow directions along the liquid-vapor interface in binary mixtures. a) Apex to contact line. b) Contact line to apex.

The volatility of a component is determined by the evaporation rate relative to volume fraction of that component in the fluid. By varying the relative humidity, the volatility of the water can be changed so it is greater or less than that of PM. When water is the least volatile component, the ethanol (or PM) is depleted at the liquid-vapour interface. Evaporation is enhanced at the contact line compared to the apex [67]. These two factors combine to give a larger depletion of ethanol (or PM) at the contact line compared to the apex, leaving the contact line relatively water-rich. As water has a higher surface tension than ethanol (or PM), the surface tension at the contact line is therefore higher than at the apex. This gradient in surface tension drives

a Marangoni flow directed from the apex towards the contact line along the liquid-vapour interface (Fig. 4.2a). When water is the more volatile component (PM/water at $RH \leq 0.5$), the contact line becomes rich in PM, and the Marangoni flow direction is reversed (Fig. 4.2b). The following subsections (4.2.2 and 4.2.3) explore the Marangoni flows inside binary solvent mixtures resulting from differential solvent evaporation.

4.2.1. Internal flows inside single solvent droplets

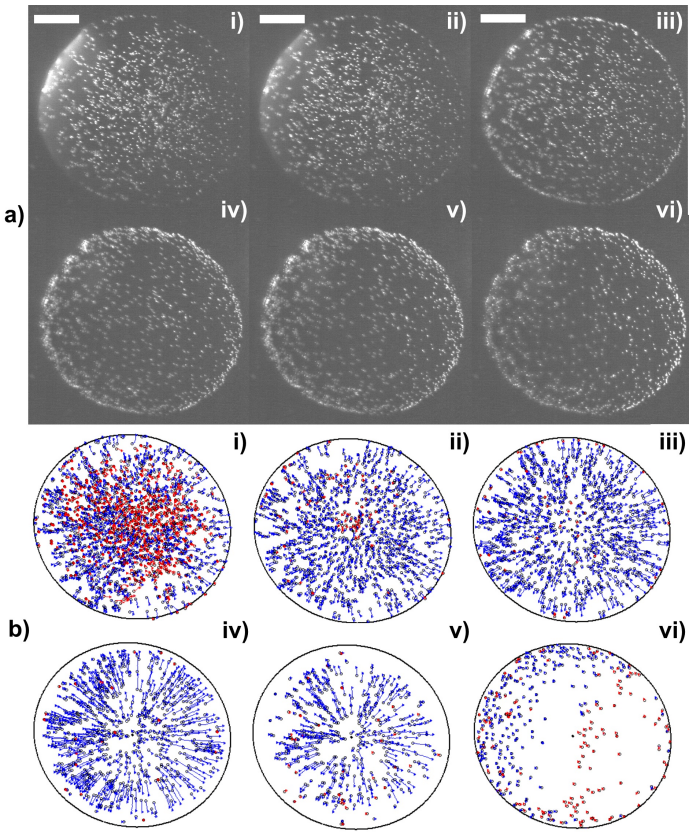

Figure 4.3. Radial flow in a water droplet containing 0.05%v 1 μm polystyrene spheres (sterically stabilised by PEGMA) on a glass substrate (as received). A ring stain builds up during drying (see Video W). Dark field images are shown in a) for i) $0.1\,t_{\mathrm{dry}}$, ii) $0.2\,t_{\mathrm{dry}}$, iii) $0.5\,t_{\mathrm{dry}}$, iv) $0.8\,t_{\mathrm{dry}}$, v) $0.9\,t_{\mathrm{dry}}$, and vi) $1.0\,t_{\mathrm{dry}}$, where the drying time, t_{dry} is 3.80 s. The scale bars are 20 μm. The particle tracks are given in b), between i) 0–$0.1\,t_{\mathrm{dry}}$, ii) 0.1–$0.2\,t_{\mathrm{dry}}$, iii) 0.4–$0.5\,t_{\mathrm{dry}}$, iv) 0.7–$0.8\,t_{\mathrm{dry}}$, v) 0.8–$0.9\,t_{\mathrm{dry}}$, and vi) 0.9–$1.0\,t_{\mathrm{dry}}$. Tracks radially inward are in red and outward tracks in blue. The initial position of the contact line is indicated by the black line.

The overall focus of this chapter is on binary solvent mixtures. However, to make a clear comparison, pure solvents are considered first. The particle distribution and corresponding particle tracks within pure water and pure ethanol droplets are shown in Fig. 4.3 and Fig. 4.4 respectively. The polystyrene tracer

particles were not sterically stable in 100% PM and formed large aggregates, so internal flows in pure PM were not imaged.

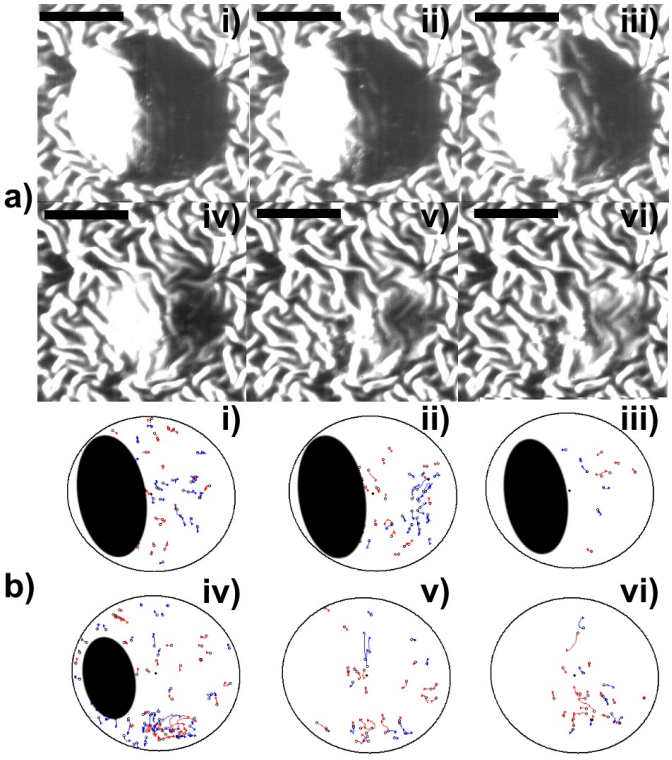

Figure 4.4. Radial flow in an ethanol droplet containing 0.05%v 1 μm polystyrene spheres (sterically stabilised by PNVP) on glass (fluorinated by plasma treatment). a) Dark field images demonstrate the de-pinning contact line after i) $0.1\,t_{\mathrm{dry}}$, ii) $0.2\,t_{\mathrm{dry}}$, iii) $0.5\,t_{\mathrm{dry}}$, iv) $0.8\,t_{\mathrm{dry}}$, v) $0.9\,t_{\mathrm{dry}}$, and vi) $1.0\,t_{\mathrm{dry}}$, where the drying time, t_{dry} is 0.40 s. Scale bars are 50 μm. Particles cannot be distinguished easily by eye, however MATLAB can follow the particle tracks which are given in b), between i) 0–$0.1\,t_{\mathrm{dry}}$, ii) 0.1–$0.2\,t_{\mathrm{dry}}$, iii) 0.4–$0.5\,t_{\mathrm{dry}}$, iv) 0.7–$0.8\,t_{\mathrm{dry}}$, v) 0.8–$0.9\,t_{\mathrm{dry}}$, and vi) 0.9–$1.0\,t_{\mathrm{dry}}$. Tracks radially inward are in red and outward tracks in blue. The initial position of the contact line is indicated with a black line. The bright region in which no particles can be imaged is shown by the black ellipse.

The water droplet (on as-received glass) remained pinned throughout the drying lifetime (Fig. 4.3a). During the initial stage of drying, there was a small amount of inward motion of the particles due to the end of the spreading and impact stages (Fig. 4.3bi). Subsequently, radial flow transported particles outwards to the contact line, where a thin ring stain was formed (Fig. 4.3avi). Due to the finite zone of focus, particles with both inward and outward motion may be imaged in the same time frame (see Chapter 2, Fig. 2.4). The particle tracks show that there was no re-circulation due to thermal Marangoni effects, demonstrating that water droplets on glass based-substrates had no significant evaporative cooling (as expected from Chapter 3). The overall flow behaviour

was consistent with the "coffee ring effect" [61], with an increase in the mean particle speed with time as the droplet became thinner, and as particles moved closer to the contact line (Fig. 4.5a).

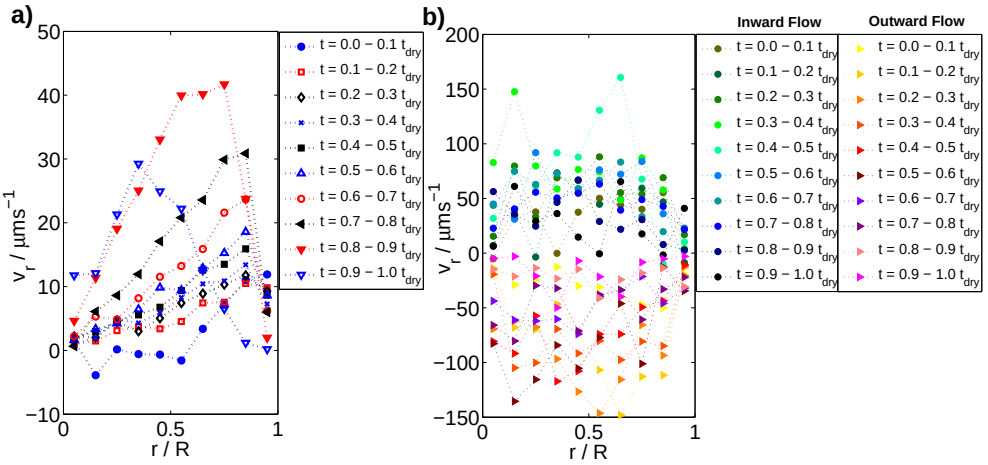

Figure 4.5. The evolution with time of the radial particle velocity inside a) a single representative water droplet at RH 0.5 and b) an average over ten ethanol droplets, for spatial bins of size $0.1R$. The tracer particles are 700 nm polystyrene spheres at a concentration of 0.01%v. The zone of focus was close to the substrate.

For a droplet of ethanol on a plasma-fluorinated substrate, the contact line de-pinned during drying (Fig. 4.4aiii–avi), resulting in an inward component of the flow velocity [80]. Consequently the velocity profile of particles inside the droplet did not increase throughout drying, and particles moved both towards and away from the contact line throughout the lifetime of the droplet (Fig. 4.5b and Fig. 4.4b). Note that particles inside the bright region could not be imaged (see Chapter 2, Fig. 2.4), and worm-like features are due to the polymer coating on the substrate. The maximal mean speeds obtained for particles inside the ethanol droplet were larger than those inside the water droplet by a factor of three, due to the faster evaporation rate of the ethanol droplet.

4.2.2. Marangoni flows in ethanol/water mixtures

The flows inside evaporating droplets of binary solvents were more complex than inside the individual components. The particle transport inside ethanol/water mixtures can be split into two main categories. First, circulating flows driven by surface tension gradients, which carried particles along the

fluid streamlines. Second, particle migration towards the centre of the droplet, crossing the fluid streamlines. The migratory flux in the following experiments was found to be approximately two orders of magnitude slower than the circulatory flow. The combined effect of the two particle transport mechanisms was to form a region of circulatory flow, and a quiescent region, with particles gathered at the droplet centre. This resulted in a highly concentrated region of particles at the centre of the droplet until the Marangoni flows ceased, at which point particles moved radially outwards towards the contact line. Figure 4.6 exemplifies the overall result of the transport processes during drying; the circulating Marangoni flow and particle migration across fluid streamlines (Fig. 4.6a−c), followed by the evaporation-driven radial flow to the contact line (Fig. 4.6d−g). As only limited detail can be gained from still images supplementary videos are provided as an aid. The corresponding video for Fig. 4.6 is Video E1.

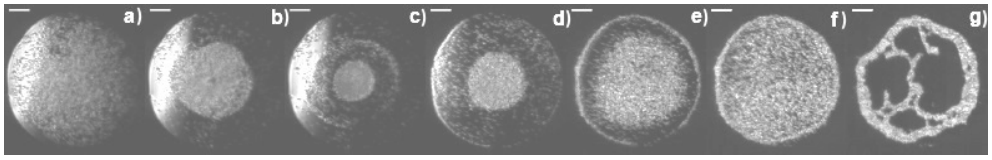

Figure 4.6. A droplet of 10%v ethanol/water containing 0.1%v 1 μm polystyrene spheres at a RH of 0.50 on glass (as-received). Particles collect in a central group which undergoes circulating Marangoni flow. Snapshot times relative to the drying time ($t_{\mathrm{dry}} = 3.27$ s), are a) $0.001\,t_{\mathrm{dry}}$, b) $0.05\,t_{\mathrm{dry}}$, c) $0.10\,t_{\mathrm{dry}}$, d) $0.51\,t_{\mathrm{dry}}$, e) $0.82\,t_{\mathrm{dry}}$, f) $0.92\,t_{\mathrm{dry}}$, g) $1.00\,t_{\mathrm{dry}}$. The scale bars are 50 μm.

Particles collected at the centre of the droplets independent of the stabilisation method used for the polystyrene spheres. Both charge-stabilised spheres and sterically stabilised spheres (with PEGMA chains) with a 600 nm diameter exhibited the same collection behaviour in the ethanol/water droplets. The chemical composition of the stabiliser (PEGMA or PNVP) also had no noticeable effect on the collection.

From here onward, the circulating Marangoni flow and the particle migration are considered separately. In this section (4.2), the focus is on the circulating Marangoni flows. Then, in Section 4.3, the particle migration and consequent collection at the centre of the droplet is discussed.

Figure 4.7 illustrates the variation in the circulating Marangoni flow with

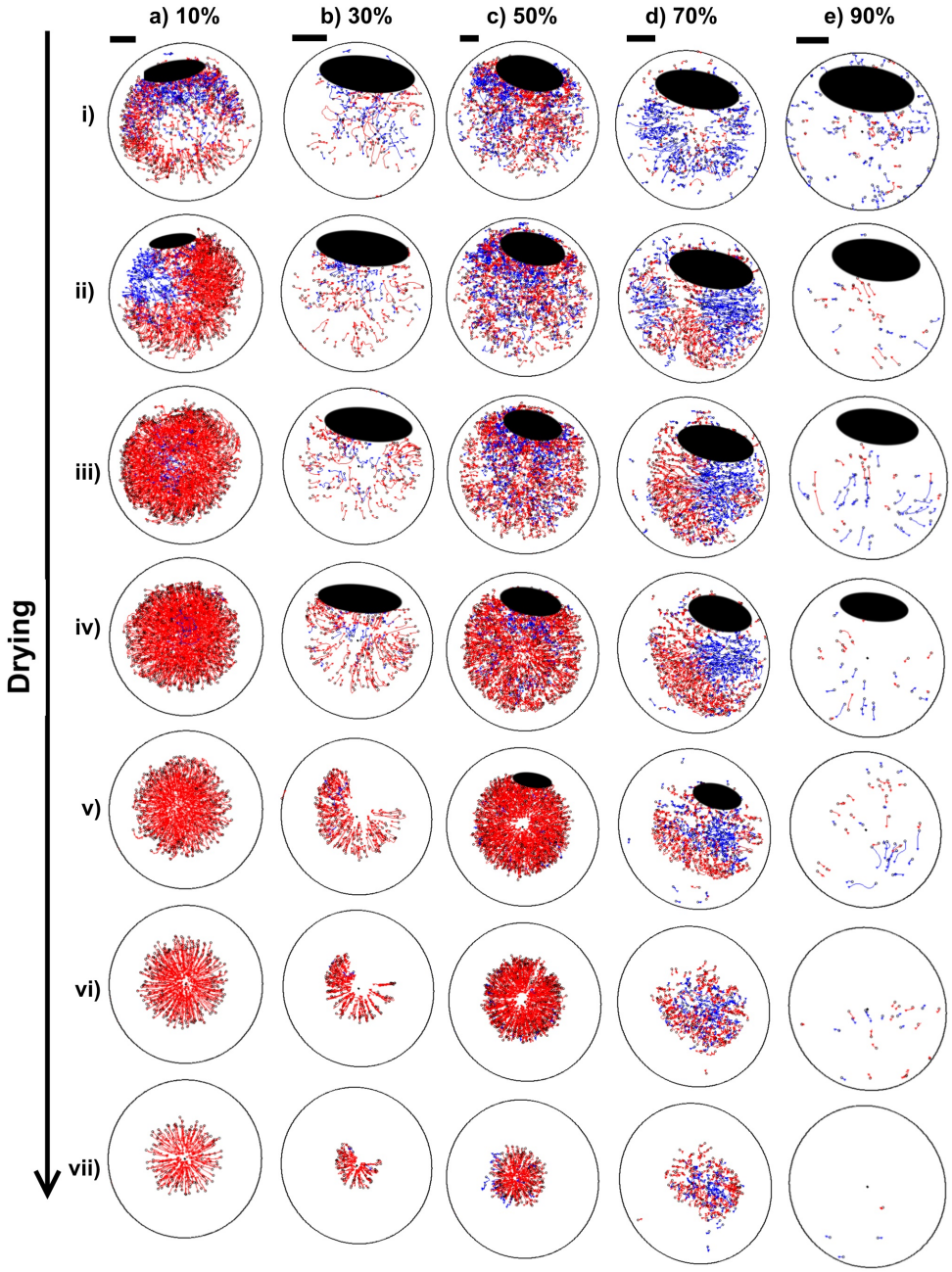

Figure 4.7. Particle tracks for ethanol/water droplets at RH 0.26 with an ethanol content of a) 10%v, b) 30%v, c) 50%v, d) 70%v and e) 90%v. The tracks are shown for time bins between i) $0-0.05\,t_{\mathrm{Rg}}$, ii) $0.2-0.25\,t_{\mathrm{Rg}}$, iii) $0.4-0.45\,t_{\mathrm{Rg}}$, iv) $0.55-0.6\,t_{\mathrm{Rg}}$, v) $0.75-0.8\,t_{\mathrm{Rg}}$, vi) $0.85-0.9\,t_{\mathrm{Rg}}$, and vii) $0.95-1.0\,t_{\mathrm{Rg}}$, where t_{Rg} is the time for the collected group to reach a minimum radius. As the 90%v ethanol droplet does not show collection of particles, t_{Rg} is taken as t_{dry}. Note the contact line de-pins for the 90%v ethanol/water droplet. Values for t_{Rg} are a) 0.96 s, b) 0.83 s, c) 0.75 s, d) 0.55 s and e) 0.49 s. Polystyrene tracer particles with 1 μm diameter were included at 0.01%v. Inward tracks are in red and outward tracks in blue. The initial contact line is indicated by a black line. The zone of focus was just above the substrate to avoid the no-slip region. No particles can be imaged within the black ellipse. Scale bars are 20 μm.

ethanol concentration. Flows are observed in a zone of focus near to the solid-liquid interface. Note that flows can only be observed where there are particles (i.e. not within the depleted region). At the start of drying, the particles were uniformly dispersed throughout the droplet and exhibited chaotic motion. As drying progressed, differential evaporation of the solvents established a surface tension gradient along the liquid-vapour interface, driving a Marangoni flow in droplets with ethanol concentrations 10−70%v. Once Marangoni flow was initiated, particle motion was more ordered and symmetric. A circulating group formed with a central hole, even at dilute particle concentrations (for example Fig. 4.7aiii). Just above the substrate, particles moved inwards. The direction of the Marangoni flow is consistent with that expected for an ethanol/water mixture (Fig. 4.2a). Thermal Marangoni flow near the substrate would be directed outwards towards the contact line, returning to the colder apex along the liquid-vapour interface. Hence, solutal effects dominate in these ethanol/water mixtures.

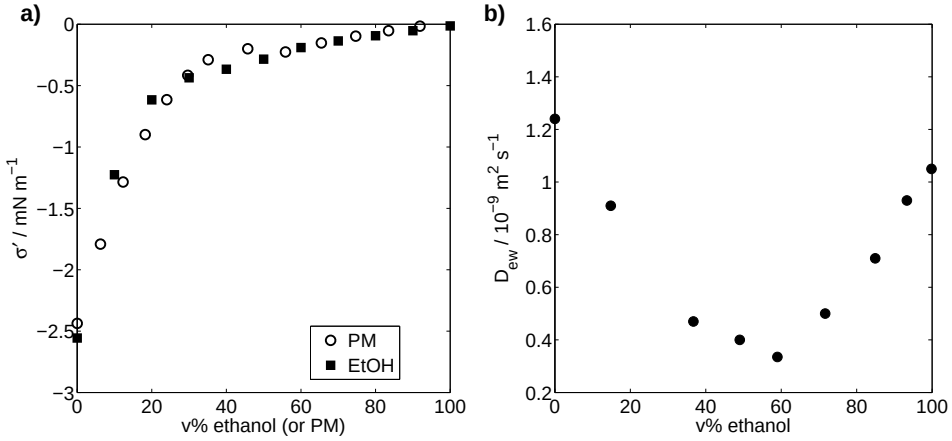

Figure 4.8. a) Variation in surface tension with composition (σ') at each ethanol/water or PM/water concentration. b) Mutual diffusion coefficients of ethanol-water, D_{ew}, at various ethanol concentrations [202]. Diffusion is slowest at 60%v ethanol.

For the 90%v ethanol/water droplet, the contact line de-pinned early in the drying, and the particle tracks were very similar to the 100%v ethanol droplet. Note that circulatory flows and particle collection at the centre of a droplet still occurred for 10−70%v ethanol/water droplets that de-pinned. The variation in surface tension with small differences in the volume fraction ($x_{\mathrm{v,e}}$ for ethanol) is defined as $\sigma' = \mathrm{d}\sigma/\mathrm{d}x_{\mathrm{v,e}}$ (at constant temperature). At

90%v ethanol, σ' is much smaller than for low ethanol concentrations ($\leq$ 50%v ethanol, see Fig. 4.8a), which could explain why Marangoni flows were not evident. The lower contact angle due to high ethanol content also leads to a strong evaporation-driven radial flow which would compete with any solutal Marangoni effects.

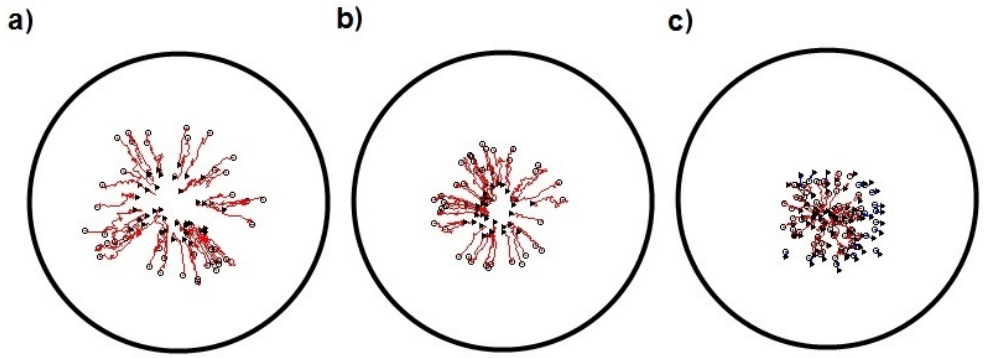

Figure 4.9. Particle tracks obtained using PTV for a 50%v ethanol/water droplet containing 0.01%v 1 μm polystyrene spheres on a coated glass substrate at a RH of 0.26. The zone of focus was just above the substrate. Particles move inwards from the contact line to the droplet centre close to the substrate, consistent with solutal Marangoni flow. A $\circ$ marks the beginning of a track, and a $\blacktriangle$ the end. a) 0.44–0.46 t_{dry}, b) 0.50–0.52 t_{dry}, c) 0.53–0.55 t_{dry}. The drying time, t_{dry}, is 1.65 s, the initial contact diameter is $\backsim$ 200 μm (black ellipse) and the initial contact angle is $\backsim$ 50°.

The particle tracks in Figure 4.9 reveal the flow behavior close to the transition from circulatory to radial flow. A 50%v ethanol droplet is used as the example, with smaller temporal bins than in Figure 4.7 to highlight details near the transition. Before the transition to radial flow, the circulating collection of particles formed an annulus in the x-y plane, indicated by the central hole seen in Figure 4.9a and Figure 4.9b. The hole was maintained even at dilute particle concentrations and so was not associated with hydrodynamic interactions between particles. The exclusion of particles from the central hole is in distinct contrast to the work by Hu and Larson [113], where particles interacted with the substrate to "stick" centrally at the stationary point. In the droplets observed in this thesis, the particles do not reach the stationary point, as demonstrated by the central hole, and particle-substrate interactions are not strong enough to cause fixation to the substrate.

On approaching the transition to radial flow, the circulatory motion died out from the contact line inwards. The blue tracks in (Fig. 4.9c) show the particles closest to the contact line moving outwards while those near the centre

still circulate inwards (red tracks). The transition from circulatory flow to radial flow was sharp, suggesting a sudden switch-off of the interfacial flows.

It is plausible that the sudden switch-off of Marangoni flows from the contact line inwards is linked to the depletion of ethanol from the periphery to the centre. If the volatility of components becomes such that the ethanol composition remains unchanged despite evaporation, this would result in the lack of a surface tension gradient, and hence shut off Marangoni flow. Consideration of the transport of ethanol to the surface is also necessary to determine the depletion. The diffusion coefficient of ethanol depends on the ethanol concentration (in water), with an ethanol concentration of $\backsim$ 60%v resulting in the slowest replenishment of ethanol to the liquid-vapour interface (see Fig. 4.8b).

The mean radial speeds for inward and outward moving particles within ethanol/water droplets are compared in Figure 4.10. Note that speeds are mean values binned spatially and temporally within a slice above the substrate (corresponding to the zone of focus). As such, there is some bias over the speeds observed as particles at the liquid-vapour interface (with fast speeds) are not imaged until late times when the droplet height is small. Hence, the plots in Fig. 4.10 are meant to provide an order of magnitude for the mean particle speed, and a qualitative description of the spatial and temporal variation in the Marangoni flow speed. For ethanol concentrations exhibiting Marangoni flow (10$-$70%v), particles reached higher mean speeds than in pure ethanol ($\backsim$ 150 μm s^{-1}, Section 4.2.1). Marangoni flow speeds within droplets of 10$-$30%v ethanol were of the order 10^3 μm s^{-1}. As the radius of these droplets was approximately 70 μm, the particles circulated at approximately 10^2 Hz. The mean particle speeds in the 90%v ethanol droplet, which did not exhibit Marangoni flow, were very similar to the particle speeds in the pure ethanol droplet.

For particles with a diameter of 1 μm, the particle diffusion coefficient, D_p in a 50%v ethanol/water droplet is

$$D_\mathrm{p} = \frac{k_\mathrm{B}T}{6\pi a \eta_\mathrm{f}} \backsim 2 \times 10^{-13}\,\mathrm{m^2\,s^{-1}}, \tag{4.1}$$

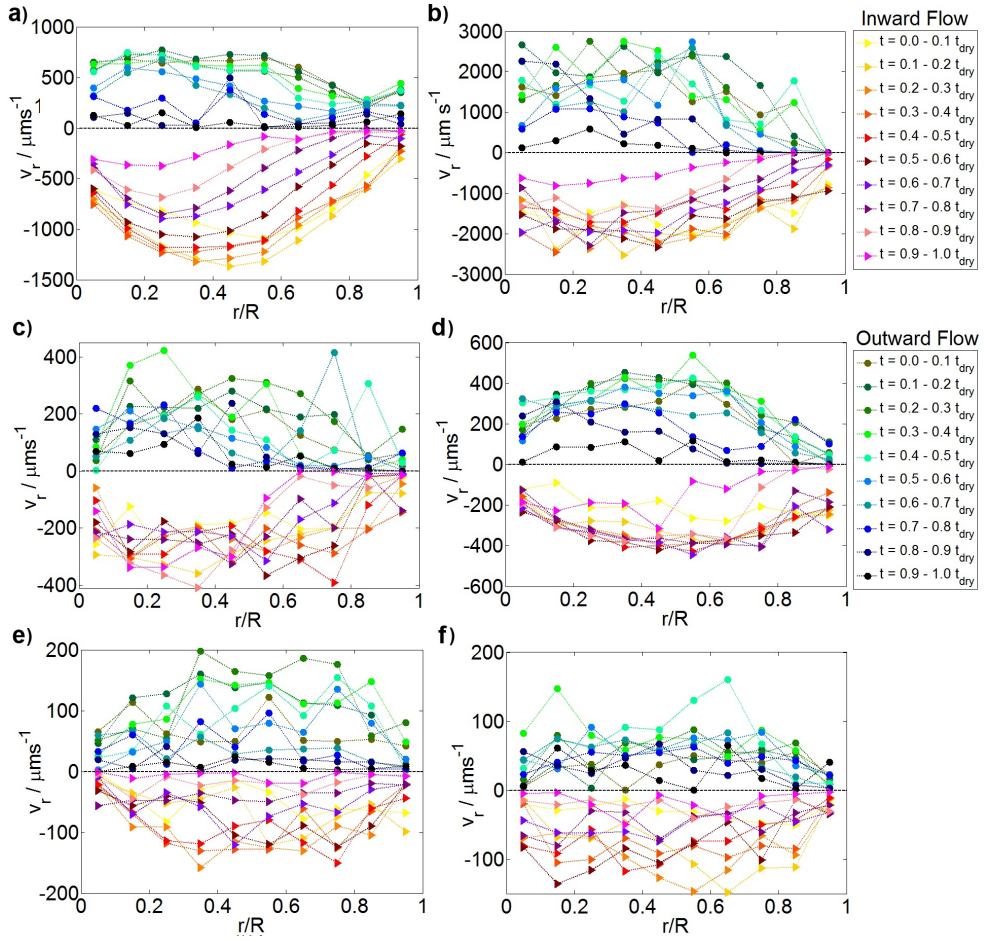

Figure 4.10. The evolution of the mean particle speed, v_{r}, radially inwards and outwards for at least five ethanol/water droplets in each temporal bin across the radius of the droplet (R) for ethanol concentrations of a) 10%v, b) 30%v, c) 50%v, d) 70%v, e) 90%v, and f) 100%v. The RH was 0.26. The tracer particles were 1 μm polystyrene spheres at a concentration of 0.01%v. Particles in focus were just above the substrate. Negative velocities are directed towards the centre of the droplet (judged by best-fit ellipse to the contact line) and positive velocities are directed towards the contact line. For 90%v and 100%v ethanol with no particle group, t_{Rg} is taken to be t_{dry}.

where k_{B} is the Boltzmann constant, T is the temperature, a is the particle radius and η_{f} is the fluid viscosity. The displacement of a particle due to Brownian motion ($\bar{x}_{\mathrm{B}}$) for a time bin of $0.1\,t_{\mathrm{dry}}$ (0.165 s for the 50%v ethanol/water droplet in Fig. 4.7c) is then

$$\bar{x}_{\mathrm{B}} = \sqrt{2D_{\mathrm{p}}t} \backsim 0.3\,\mu\mathrm{m}. \tag{4.2}$$

Hence, Brownian motion was not significant enough to strongly influence the mean particle speeds. The tracks in Figure 4.9 show displacements greater than $1\,\mu$m perpendicular to the direction of travel of the particle, which could

be attributed to imperfections in the particle location algorithm.

As a droplet of ethanol/water evaporates, the total droplet composition becomes more water-rich. The change in composition influences the Marangoni flows in the following ways. For a droplet with an initial volume of ethanol $\leq$50%, the viscosity of the mixture decreases throughout drying (Fig. 4.1c). The decreasing viscosity will increase the speed of the Marangoni flow (with all other parameters constant). Variations in the volume fraction of ethanol result in a variation in the surface tension (Figs. 4.1a and 4.8a). At lower ethanol concentrations, σ' is larger. Thus, for the same composition gradient but lower initial ethanol content, the surface tension gradient will be larger, and Marangoni flow will be faster. However, as the ethanol concentration decreases, gradients in the bulk composition decrease, slowing diffusion to the liquid-vapour interface. The mutual diffusion coefficients in ethanol/water mixtures increase at lower ethanol concentrations (for $\leq$60%v ethanol, see Fig. 4.8b), speeding up diffusion. Furthermore, as the droplet becomes thinner, evaporation-driven radial flow is enhanced. These competing effects influence the evolution of the flow velocity in a complex way throughout drying. This makes it difficult to interpret the flow velocities quantitatively without full fluid dynamical modelling.

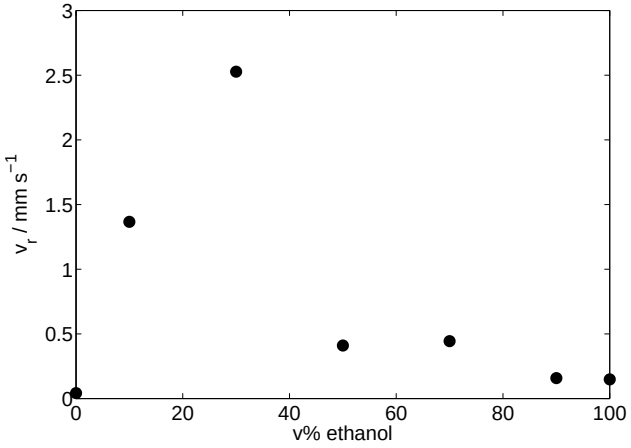

Figure 4.11. The maximum Marangoni flow speed near the substrate is plotted for each ethanol concentration. The highest flow speed was observed in the 30%v ethanol/water mixture.

The speed of the observed Marangoni flows throughout drying is plotted in

Figure 4.11 for each ethanol concentration. The Marangoni flow speeds at low ethanol concentrations (10−30%v ethanol) were faster than the flow in water, with the highest Marangoni flow speed observed in the 30%v ethanol/water droplet. The Marangoni flow speed at higher ethanol concentrations decreased, with similar speeds seen in the 50%v and 70%v ethanol/water droplets. The 90%v ethanol/water droplet had an even lower flow speed, of similar magnitude to the 100%v ethanol. Despite the lower viscosity and higher σ' in the 10%v ethanol/water droplet the Marangoni flow was slower than for the 30%v ethanol droplet. Hence, using these values alone as a guide to Marangoni flow is not always sufficient. The similarity in the flow speeds of the 50%v ethanol/water droplet and the 70%v ethanol/water droplet could result from the higher viscosity of the 50%v ethanol/water mixture reducing the velocity of the Marangoni flow in droplets of this initial composition.

At higher ethanol concentrations the non-ideality of the vapour pressures reduces the preferential evaporation of the ethanol (see Fig. 4.1d). For example, in 80%v ethanol/water, the partial vapour pressure of the ethanol is about 2.5× higher than that of water. Vapour diffusion coefficients for ethanol and water in air at 20°C are $1.3\times10^{-5}\,\mathrm{m^2\,s^{-1}}$ and $2.6\times10^{-5}\,\mathrm{m^2\,s^{-1}}$ respectively [203]. Hence, the evaporation rate of the ethanol is approximately 1.25× higher than that of water at a RH of zero, and 2.5× higher at a RH of 0.5. However, the ethanol mole fraction is also 1.5× larger. Hence, the net change in composition at a RH of 0.5 is small. The decreased depletion of ethanol could explain the reduced Marangoni flow at 70%v ethanol, and lack of Marangoni flow at 90%v ethanol.

It is interesting that the droplets with high ethanol content (70−90%v ethanol) did not show an increase in Marangoni flow during drying as the ethanol was depleted (due to the larger σ'). This may be in part due to the viscosity increase until the ethanol concentration is reduced below 50%v, and also due to the decreased ethanol depletion at higher ethanol volume fractions. One might expect that on reaching a lower ethanol content (e.g. 10%v ethanol), the speed of the Marangoni flow would increase to resemble that inside a droplet with an initial ethanol concentration of 10%v ethanol. However, this is not the case, and the mean particle speeds decreased with time until Marangoni flows ceased

at t_{Rg}, and radial flow began towards the contact line. The decrease in the Marangoni flow speed with time could result from a reduction in the compositional gradient along the liquid-vapour interface due to slower mass transport, as well as increasing competition between Marangoni and evaporation-driven flows at the lower contact angles.

For initial ethanol concentrations of 10−50%v, the radial position at which the fastest Marangoni flow speeds were observed shifted closer to the centre of the droplet (r/R=0) as drying progressed. This shift was the most pronounced in the 10%v ethanol/water droplet (Fig. 4.10a). The implications will be discussed further in Section 4.3 with relation to the flow profile.

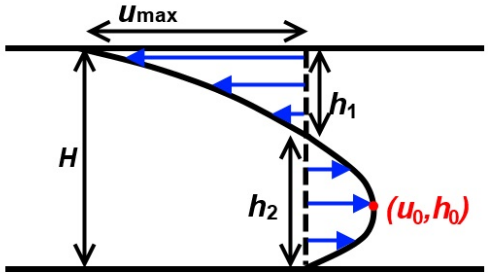

Figure 4.12. Representation of the Marangoni flow profile inside a droplet of height H under the lubrication approximation. The maximum fluid velocity, u_{max}, occurs at the liquid-vapour interface. The highest positive flow velocity, u_0, occurs at a height, h_0 from the substrate. The flow direction changes at a distance h_1 from the liquid-vapour interface.

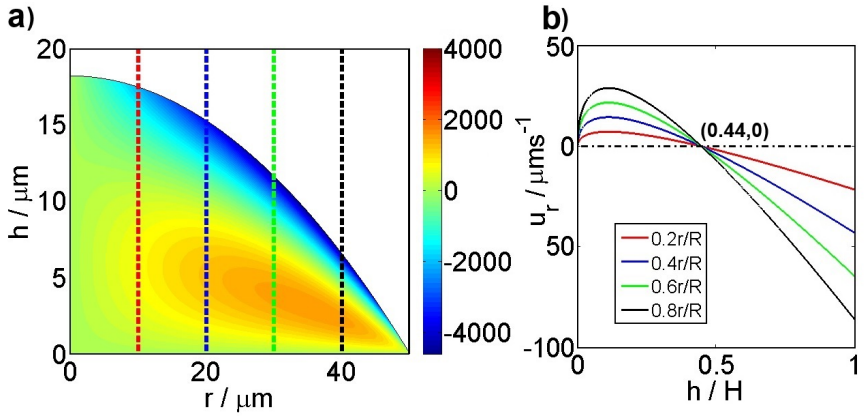

Figure 4.13. a) The radial velocity map of a droplet exhibiting a thermal Marangoni flow profile [68]. The velocity scale is in $\mu\mathrm{m\,s^{-1}}$. b) The corresponding radial velocity with height for fixed values of r. The height h is normalised by the height of the droplet (at that radial-coordinate), H. The velocity changes sign at $0.56H$ from the top of the droplet at any value of r (i.e. $h_1 = 0.56\,H$ on Fig. 4.12).

A lubrication approximation was used to make an order of magnitude estimate of the difference in surface tension across the liquid-vapour interface from the Marangoni flow speeds at each ethanol concentration (Table 4.2). Figure 4.12 describes the Marangoni flow within a droplet under the lubrication approximation. The zone of focus for the flows in this section was close to the substrate, hence the maximum Marangoni flow speeds observed correspond to u_0. Note that the observed speeds are a mean value and so will be an underestimate of u_0. The Marangoni flow speed at the liquid-vapour interface ($u_{\max}$) can be calculated under the lubrication approximation as $u_{\max} = -3u_0$ (see Appendix A). Indeed, Figure 4.13b shows that this is the case for thermal Marangoni flow. The change in velocity with height near the liquid-vapour interface is then estimated by $u_{\max}/h_1 = -3u_0/h_1$. This will be an underestimate as the flow is not linear, but should provide an order of magnitude approximation. In order to calculate h_1, the evolution of the radial velocity with height was determined based on the Hu and Larson model [68] for thermal Marangoni flow (see Chapter 1, Section 1.6.2 for details on the model). Figure 4.13b shows the normalised height at which the zero radial velocity occurs (i.e. h_1/H) for the four radial positions in the droplet indicated by the dashed lines in Figure 4.13a. At any radial position, h_1/H was calculated from the model as 0.56. Hence estimates of the difference in surface tension between the contact line and apex were made using a scaling calculation across the whole droplet,

$$\Delta\sigma = \eta R \frac{3\,\bar{u}_0}{0.56\,H}, \tag{4.3}$$

where η is the fluid viscosity, R is the droplet radius, $\bar{u}_{0\max}$ is the fastest flow speed (determined from mean particle speeds) close to the substrate, and H is the droplet height.

For all ethanol concentrations, the difference in surface tension between the apex and contact line is estimated between $\backsim 10^{-3}$–10^{-2} mN m^{-1}. The change in composition across the droplet required to make this surface tension difference was estimated from the surface tension plot against ethanol concentration given in Figure 4.1a. The composition at the apex was assumed to be equal to the initial composition of the ethanol/water droplet. Only small

Table 4.2. Estimates of the surface tension difference, $\Delta\sigma$, along the liquid-vapour interface for droplets of ethanol/water evaporating at a RH of 0.26, exhibiting Marangoni flows. Substrates were plasma fluorinated glass. Corresponding estimates in the composition variation from the initial ethanol concentration are given (Δx_{v}). The initial contact angle, θ_i, and viscosity η_i are provided.

Ethanol content / %v	$\bar{u}_0$ / μm s^{-1}	R / μm	H / μm	θ_i / degrees	η_i / mPa s	$\Delta\sigma$/ mN m^{-1}	Δx_{v} / %v
10	1000	70	85	100	1.2	5×10^{-3}	0.003
30	2800	70	57	78	2.0	4×10^{-2}	0.10
50	400	65	50	70	2.4	7×10^{-3}	0.04
70	500	80	55	68	2.1	8×10^{-3}	0.04

composition changes were required to achieve the estimated surface tension differences (a tenth of a % in the volume of ethanol or less). Such small variations in the ethanol composition across the droplet suggest that the circulation of the Marangoni flow cell and diffusion of the ethanol (and water) even out the compositional differences from differential evaporation of the component fluids.

4.2.3. Marangoni flows in methoxypropanol/water mixtures

For aqueous solvent mixtures in ambient air, the evaporation rate depends on the relative humidity. A higher relative humidity slows the evaporation rate of the water. For some water-based mixtures, the relative volatility of the components can be reversed by altering the RH. The approximate switch-over RH (defined here as RH_{w}) can be estimated from the pure solvent vapour pressures using

$$D_{\mathrm{s}}\, p_{\mathrm{s}}(1 - RH_{\mathrm{s}})/x_{\mathrm{s}} = D_{\mathrm{w}}\, p_{\mathrm{w}}(1 - RH_{\mathrm{w}})/x_{\mathrm{w}}, \tag{4.4}$$

where p_{s} and p_{w} are the partial vapour pressures of the organic solvent and water, x_{s} and x_{w} are the mole fractions of the organic solvent and water in the mixture, and D_{s} and D_{w} are the vapour diffusion coefficients of the organic solvent and of water in air. RH_{s} is the partial pressure of the organic solvent in the ambient atmosphere relative to the saturated vapour pressure (which

is zero for PM or ethanol unless a vapour shroud is used - denoted VS). In the absence of vapour pressure data, the simplest model is Raoult's law, which gives

$$p_{\mathrm{s}} = p_{\mathrm{s}}^{*}\, x_{\mathrm{s}}, \tag{4.5}$$

and

$$p_{\mathrm{w}} = p_{\mathrm{w}}^{*}\, x_{\mathrm{w}}, \tag{4.6}$$

where

$$x_{\mathrm{s}} + x_{\mathrm{w}} = 1, \tag{4.7}$$

and where p_{s}^{*} and p_{w}^{*} are the vapour pressures of the second solvent and of water respectively. The switch over relative humidity is then

$$RH_{\mathrm{w}} = 1 - \frac{D_{\mathrm{s}}\, p_{\mathrm{s}}^{*}}{D_{\mathrm{w}}\, p_{\mathrm{w}}^{*}}. \tag{4.8}$$

For a droplet of PM/water, the switch in the relative volatility of components is estimated from Equation 4.8 at $RH \backsim 1{-}0.5 D_{\mathrm{s}}/D_{\mathrm{w}}$. The vapour diffusion coefficient for PM in air can be estimated from the solvent density, ρ_{f}, assuming a spherical molecule. The radius of a PM molecule, a_{PM}, is estimated as

$$a_{\mathrm{PM}} = \left(\frac{3M_{\mathrm{PM}}}{4\pi N_A \rho_{\mathrm{f}}}\right)^{1/3} \backsim 3.4 \times 10^{-10}\,\mathrm{m}, \tag{4.9}$$

where M_{PM} is the molecular weight of PM, and N_{A} is Avogadro's number. The collision cross-section, d_{PM}, can be estimated from the Lennard-Jones parameter of N_2 gas ($a_{\mathrm{N}} = 1.96{\times}10^{-10}\,\mathrm{m}$ [204]) and the radius of a PM molecule as

$$d_{\mathrm{PM}} = \pi(a_{\mathrm{N}} + a_{\mathrm{PM}})^2 \backsim 9.0 \times 10^{-19}\,\mathrm{m}^2. \tag{4.10}$$

The mean free path, λ_{PM}, at atmospheric pressure ($p_{\mathrm{atm}}{=}1.01{\times}10^5\,\mathrm{Pa}$) is then

$$\lambda_{\mathrm{PM}} = \frac{k_{\mathrm{B}} T}{2^{1/2} d_{\mathrm{PM}} p_{\mathrm{atm}}} \backsim 3.2 \times 10^{-8}\,\mathrm{m}, \tag{4.11}$$

where k_{B} is the Boltzmann constant and T is the temperature (293 K). The mean speed, $\bar{c}$, is

$$\bar{c} = \sqrt{\frac{8 N_{\mathrm{A}} k_{\mathrm{B}} T}{\pi M_{\mathrm{PM}}}} \backsim 262\,\mathrm{m\,s^{-1}}. \tag{4.12}$$

The vapour diffusion coefficient for PM in air, D_{PM}, is then

$$D_{\mathrm{PM}} = \frac{\lambda_{\mathrm{PM}}\bar{c}}{3} \backsim 2.8 \times 10^{-6}\,\mathrm{m^2\,s^{-1}}. \tag{4.13}$$

For this estimate of the vapour diffusion coefficient of PM in air, the switch over RH is $\backsim$0.95 if Raoult's law holds. However, reversal of the Marangoni flow direction was observed experimentally at a RH of 0.5. Fig. 4.1d demonstrates how poor a fit Raoult's law can be for non-ideal mixtures. It is therefore just a coincidence that the difference in the diffusion coefficients is cancelled out by deviations from Raoult's law.

The reversal in the Marangoni flow direction in PM/water mixtures at a RH of 0.5 allows a comparison to be made between Marangoni flow directions in mixtures with similar initial compositions. The Marangoni flow directions for each solvent mixture are indicated in Figure 4.2. No switch in the Marangoni flow direction was observed for ethanol/water mixtures, because in the RH range studied, the relative evaporation rate of the ethanol was always sufficiently high that the droplet was never enriched in ethanol.

To compare PM/water droplets with opposite Marangoni flow directions observations were made at a RH of 0.35 and 0.70. Figures 4.14 and 4.15 show the particle tracks for droplets containing 10−90%v PM in water at a RH of 0.70 and a RH of 0.35. For PM/water mixtures evaporating at a RH of 0.70, the Marangoni flow direction is the same as for the ethanol/water droplets (see Fig. 4.2a). The internal flow regimes showed some similarities (particularly at higher PM content, see Fig. 4.14d), with a circulating central group. Depletion of particles near the contact line increased at higher PM concentrations with the exception of the 90%v PM droplet. If the vapour pressure data for PM/water resembles ethanol/water, the relative evaporation rates of PM and water may be reversed at high PM content. A few individual tracks are shown in Figure 4.16a, showing the inward motion of the circulating particles just above the substrate. Some particles at the edge of the group "escape" and move towards the contact line.

For a RH of 0.35, the Marangoni flow direction was reversed (see Fig. 4.2b),

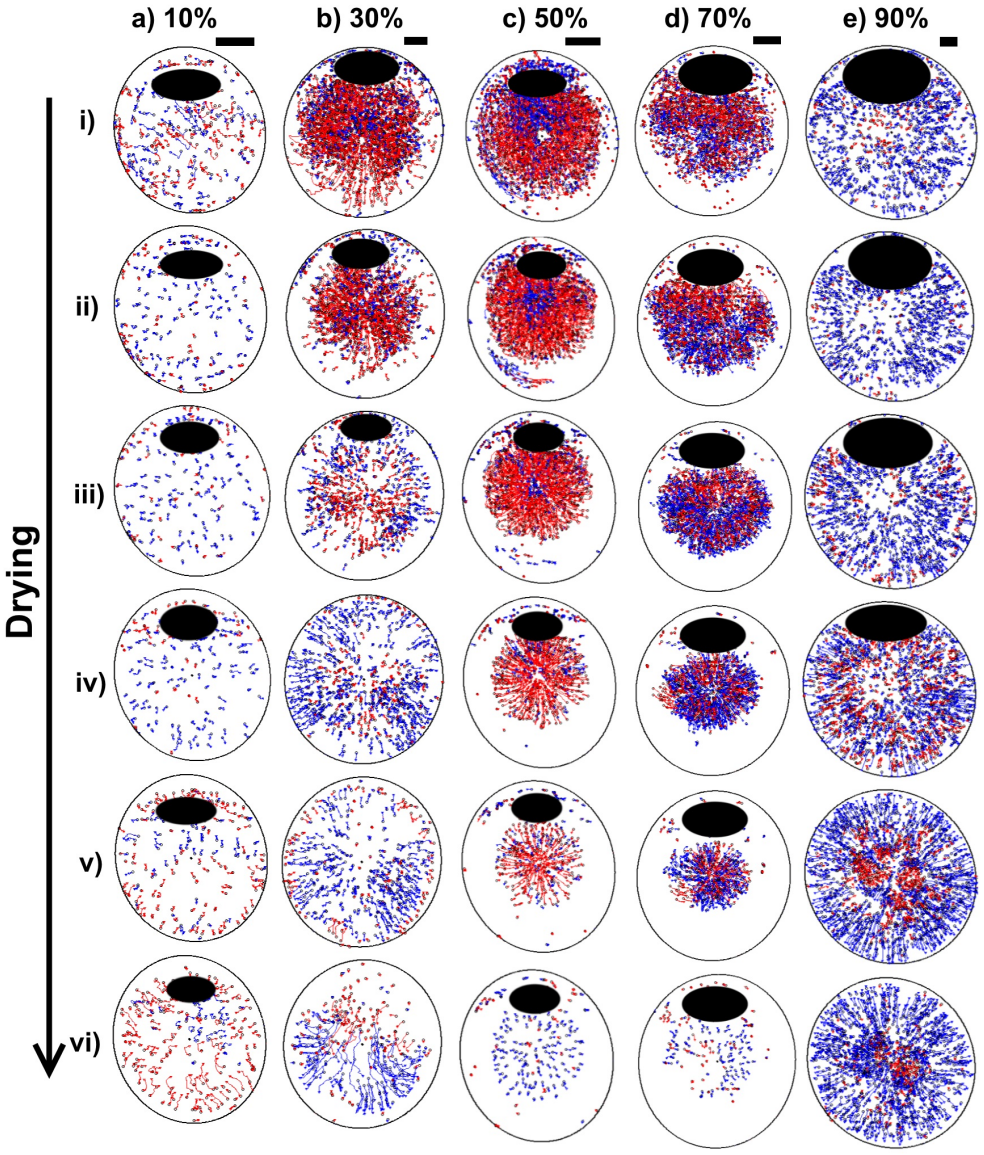

Figure 4.14. Particle tracks for droplets of PM/water mixtures on glass substrates with a PM concentration of a) 10%v, b) 30%v, c) 50%v, d) 70%v and e) 90%v at an RH of 0.70. The tracks are shown for time bins between i) $0-0.1\,t_{\mathrm{dry}}$, ii) $0.1-0.2\,t_{\mathrm{dry}}$, iii) $0.2-0.3\,t_{\mathrm{dry}}$, iv) $0.4-0.5\,t_{\mathrm{dry}}$, v) $0.6-0.7\,t_{\mathrm{dry}}$, and vi) $0.7-0.8\,t_{\mathrm{dry}}$, where t_{dry} is the drying time (except for 50%v PM and 70%v PM where time bins are normalised by t_{Rg}). Values for t_{dry} at each PM concentration are a) 10.51 s, b) 7.71 s, and e) 21.76 s. Values for t_{Rg} are 2.45 s for 50%v PM and 1.40 s for 70%v PM. The tracer particles were 1 μm polystyrene spheres at a concentration of 0.01%v. Inward tracks are in red and outward tracks in blue. The contact line was found by a best fit ellipse. Black ellipses indicate bright regions where particles cannot be imaged. The zone of focus is just above the substrate to avoid the no-slip region. Scale bars are 20 μm.

and the flow regimes were very different. The flows regimes within a droplet are more easily seen at higher particle concentrations (Videos PM1 and PM2). However, singling out some individual particle tracks highlights the behaviour at lower particle concentrations too (Fig. 4.16b). Particles within the zone of

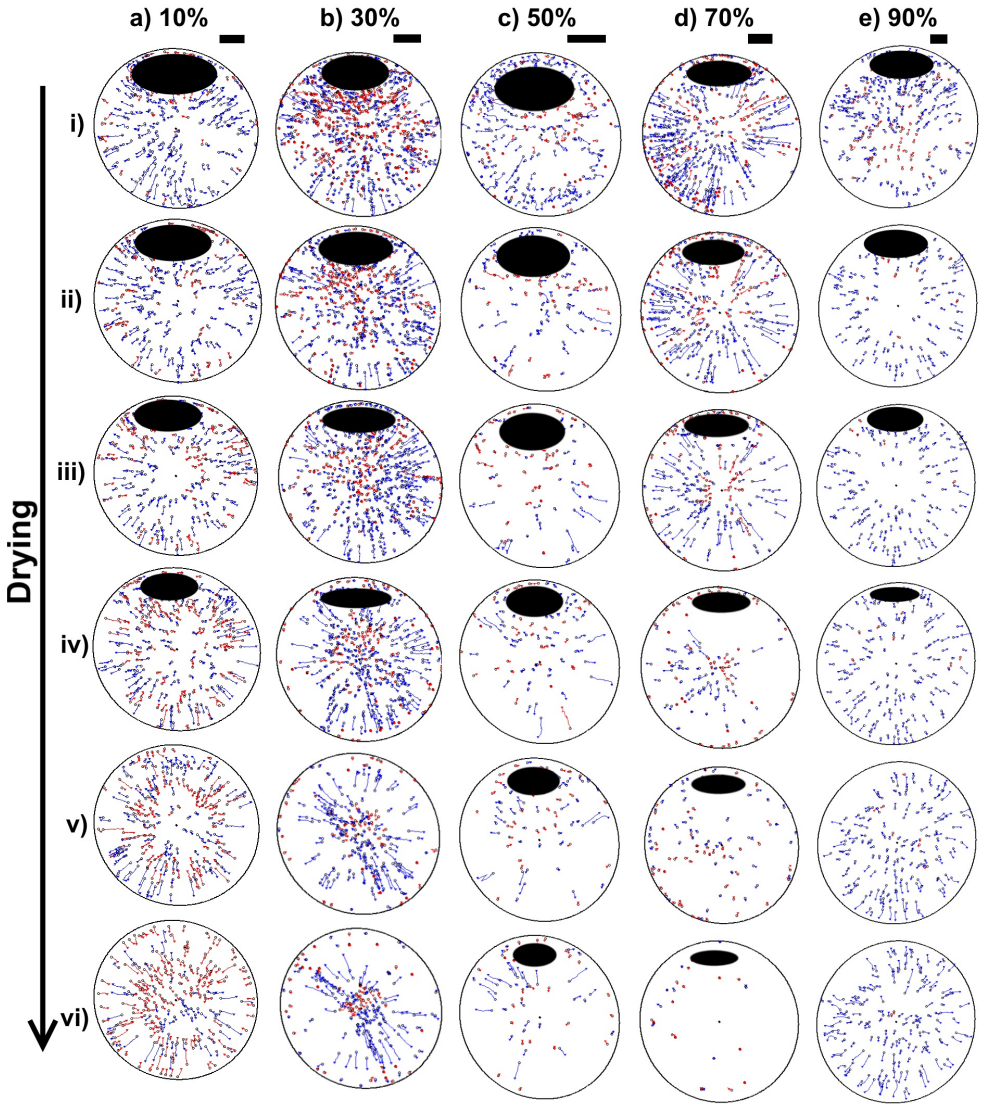

Figure 4.15. Particle tracks for droplets of PM/water mixtures on glass substrates with a PM concentration of a) 10%v, b) 30%v, c) 50%v, d) 70%v and e) 90%v at an RH of 0.35. The tracks are shown for time bins between i) $0-0.1\,t_{\mathrm{dry}}$, ii) $0.1-0.2\,t_{\mathrm{dry}}$, iii) $0.2-0.3\,t_{\mathrm{dry}}$, iv) $0.4-0.5\,t_{\mathrm{dry}}$, v) $0.6-0.7\,t_{\mathrm{dry}}$, and vi) $0.7-0.8\,t_{\mathrm{dry}}$, where t_{dry} is the drying time. Values for t_{dry} at PM concentrations a–e are a) 5.64 s, b) 3.14 s, c) 1.78 s, d) 1.91 s and e) 4.90 s. The tracer particles were 1 μm polystyrene spheres at a concentration of 0.01%v. Inward tracks are in red and outward tracks in blue. The contact line was found by a best fit ellipse. Black ellipses indicate bright regions where particles cannot be imaged. The zone of focus is just above the substrate to avoid the no-slip region. Scale bars are 20 μm.

focus moved both towards and away from the contact line throughout the same time bin, but did not form a circulating central group. As the PM concentration was increased (with the exception of the 90%v PM/water droplet), the inward motion was enhanced (particles traveled further in a time bin), and eventually circulating eddies developed near the contact line. Figure 4.16bi

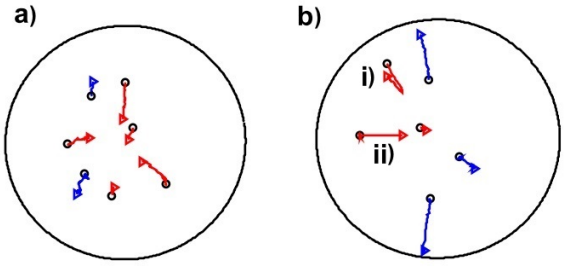

Figure 4.16. Some tracks from individual particles for a) a 50%v PM/water droplet at RH 0.70 between $0.5{-}0.60\,t_{\mathrm{Rg}}$, and b) a 50%v PM/water droplet at RH 0.20 between $0.2{-}0.3\,t_{\mathrm{dry}}$. Inward tracks are in red and outward tracks in blue. The zone of focus is just above the substrate. i) Particle in eddy, ii) particle outside eddy.

shows one example of a particle moving inwards and then suddenly turning back towards the contact line. This is one example of a particle trapped in an eddy. These eddies were more evident at higher particle concentrations (Video PM2) and for 50%−70%v PM. Some of the circulating particles were able to escape the eddy (via Brownian motion) and were carried to the centre of the droplet along the liquid-vapour interface (e.g. Fig. 4.16bii). However, most particles remained trapped near the contact line, some joining the ring and reducing the number of tracked/moving particles.

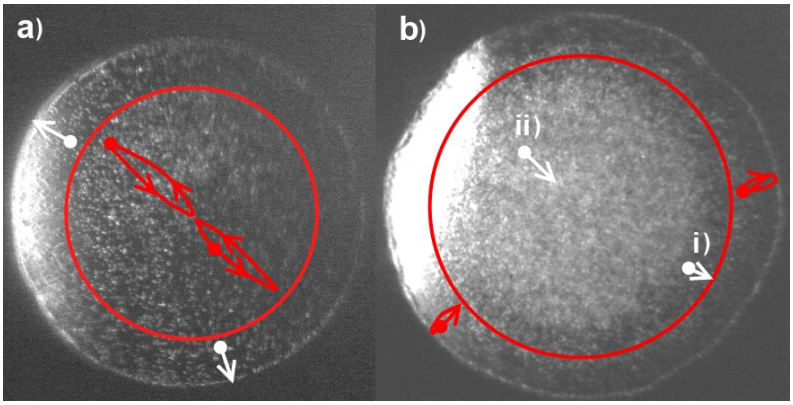

Figure 4.17. Dark field images of a 50%v PM/water droplet on glass containing a) 0.1%v 600 nm polystyrene spheres evaporating at a RH of 0.65 and ii) containing 0.5%v 600 nm spheres evaporating at RH 0.50, at $0.2\,t_{\mathrm{dry}}$. The divide between quiescent and circulating regions is indicated along with cartoon representations of the particle motion. Red arrows indicate particles in the circulating regime and white arrows those undergoing radial flow. Corresponding videos are in the supplementary information PM1 and PM2.

Figure 4.17 highlights the main features of the flow regimes within 50%v PM/water droplets with each Marangoni flow direction. In each droplet there is a region of circulating flow, and a quiescent region (divided by the red line

in Fig. 4.17). For a RH of 0.65 (Fig. 4.17a), particles circulate in a central group, but between the group and the contact line particles move outward by radial flow forming a ring stain. Note that in an ethanol/water droplet (which has the same Marangoni flow direction), depletion at the contact line remains strong even for higher particle concentrations and smaller spheres. Hence, there is no way of determining the flow behaviour in the depleted region. For a RH of 0.50 (Fig. 4.17b), particles near the contact line circulate in an eddy. Particles outside the circulating annulus move in two layers. The first layer (near the substrate) moves radially outwards (Fig. 4.17bi). The second layer (near the liquid-vapour interface) moves inwards to the centre of the droplet (Fig. 4.17bii). Similar eddies at the contact line have been observed inside surfactant-laden droplets of millimeter size [103], which should exhibit the same Marangoni flow direction as the PM/water at RH <0.5. Note that the eddy width remains fixed throughout drying. Figure 4.18 gives a cartoon representation of what the flow regimes inside the droplets may look like for a vertical slice through the side of a droplet. Note that not all particles follow the streamlines (as will be discussed in Section 4.3), hence, Fig. 4.18b does not portray inward motion of particles at the centre of the droplet.

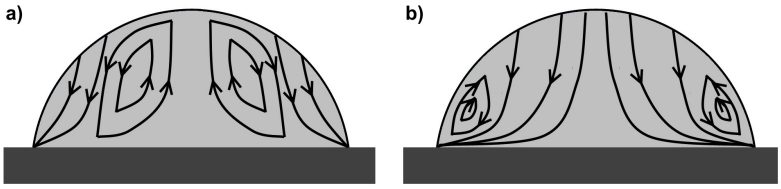

Figure 4.18. Cartoon representation of potential flow regimes inside PM/water droplets with Marangoni flow direction from a) apex to contact line and b) contact line to apex, along the liquid-vapour interface.

The switch in flow regimes in PM/water mixtures around a RH of 0.5 is explored in further detail in Figure 4.19. At a RH between 0.20 and 0.51, the flow regime remained similar, with particle motion both inward and outward, and a few small eddies near the contact line. Then at a RH of 0.52 (and above), the flow regime changed to a circulating central group and depleted contact line. The transition in flow regimes was sudden with no gradual transition between the two regimes.

The notable difference between the ethanol/water and PM/water mixtures

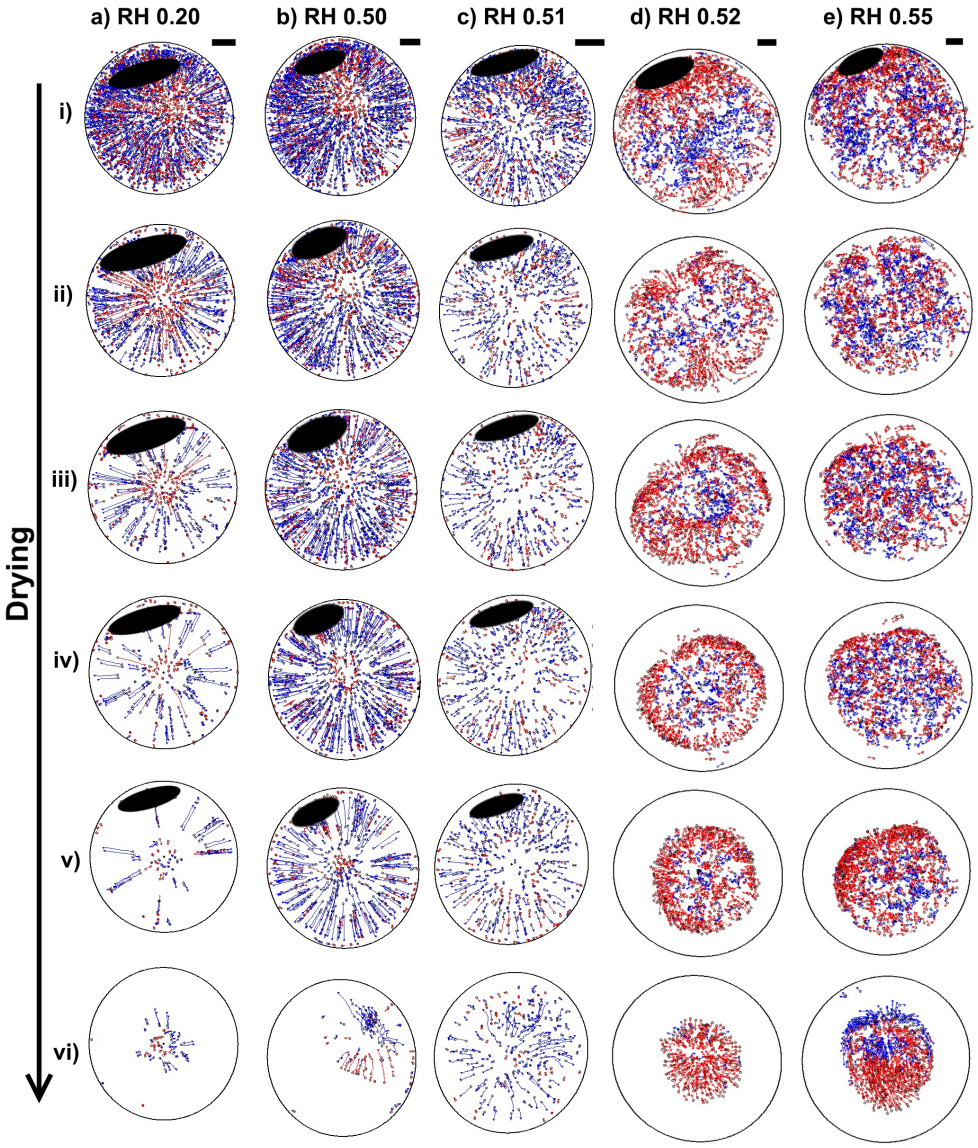

Figure 4.19. Particle tracks for droplets of 50%v PM/water on plasma fluorinated substrates containing 0.1%v 1 μm polystyrene spheres at relative humidities of a) 0.20, b) 0.50, c) 0.51, d) 0.52 and e) 0.55. For RH values of 0.51 and below times are normalised by the drying time, t_{dry}, for periods i) $0{-}0.1t_{\mathrm{dry}}$, ii) $0.1{-}0.2t_{\mathrm{dry}}$, iii) $0.2{-}0.3t_{\mathrm{dry}}$, iv) $0.3{-}0.4t_{\mathrm{dry}}$, v) $0.5{-}0.6t_{\mathrm{dry}}$ and vi) $0.8{-}0.9t_{\mathrm{dry}}$. Values of t_{dry} for corresponding PM concentrations are a) 2.07 s, b) 3.67 s, and c) 1.96 s. For RH values above 0.51, the time is normalised by the time at which the minimum group radius is reached, t_{Rg}, for the same ranges. Values of t_{Rg} for corresponding PM concentrations are d) 3.49 s, and e) 4.54 s. Droplets in avi, bvi and cvi have a de-pinning contact line. Scale bars are 20 μm.

with the same Marangoni flow direction, was that the circulating central group trapped more particles with increased PM concentration, but fewer particles with increased ethanol concentration. For the ethanol/water mixtures, at high ethanol concentrations, the width of the circulating group increased and more

particles escaped due to evaporation-driven radial flow. For the PM/water mixtures, low PM concentrations corresponded to a central circulating group with a smaller radius. Additionally, more particles escaped to travel radially outwards at low PM concentrations, despite similar surface tension/concentration profiles for the ethanol/water and PM/water mixtures (Fig. 4.1a). This may be related to the vapour pressure curves.

The flow regimes observed for PM/water droplets with opposite Marangoni flow directions were very different. As such, the Marangoni flow velocities were investigated for PM/water mixtures at an RH of 0.35 and 0.70 (Fig. 4.20). During the lifetime of a PM/water droplet, the PM concentration increases for a RH of 0.35 and decreases for a RH of 0.70. For compositions containing $\leq$55%v PM, the viscosity will initially increase during drying at RH 0.35, and decrease at RH 0.70 (see Fig. 4.1c). Additionally, σ' is larger at lower PM concentrations (see Fig. 4.8a). Therefore, small changes in the composition will result in larger surface tension gradients during drying at RH 0.70, and smaller surface tension gradients at RH 0.35. As with the ethanol/water droplets, bulk composition gradients will decrease at lower concentrations of the more volatile component.

The Marangoni flow speeds are given in Figure 4.20, with the fastest Marangoni flow at each concentration compared in Figure 4.21. For RH 0.70, the mean particle speed was slow and remained approximately constant across the radius of the droplet for low PM concentrations (10%v, Fig. 4.20aii), despite the contact line remaining pinned for most of the drying lifetime. The constant nature of the mean particle speed with distance from the contact line suggests competition between the Marangoni flow and evaporation-driven radial flow, with neither prevailing. At 30%v PM, the inward flow speed increased by a factor of five (compared to the 10%v PM droplet). The rise in speed was due to the increased Marangoni flow, overcoming evaporation-driven radial flow, and resulted in the small circulating region at the centre of the droplet (Fig. 4.14b). For 50%v PM, the mean speed of the particles increased to the order 10^2 μms^{-1} and a larger number of particles were trapped in the circulating group. The fastest Marangoni flows were observed for the 70%v PM/water dro-

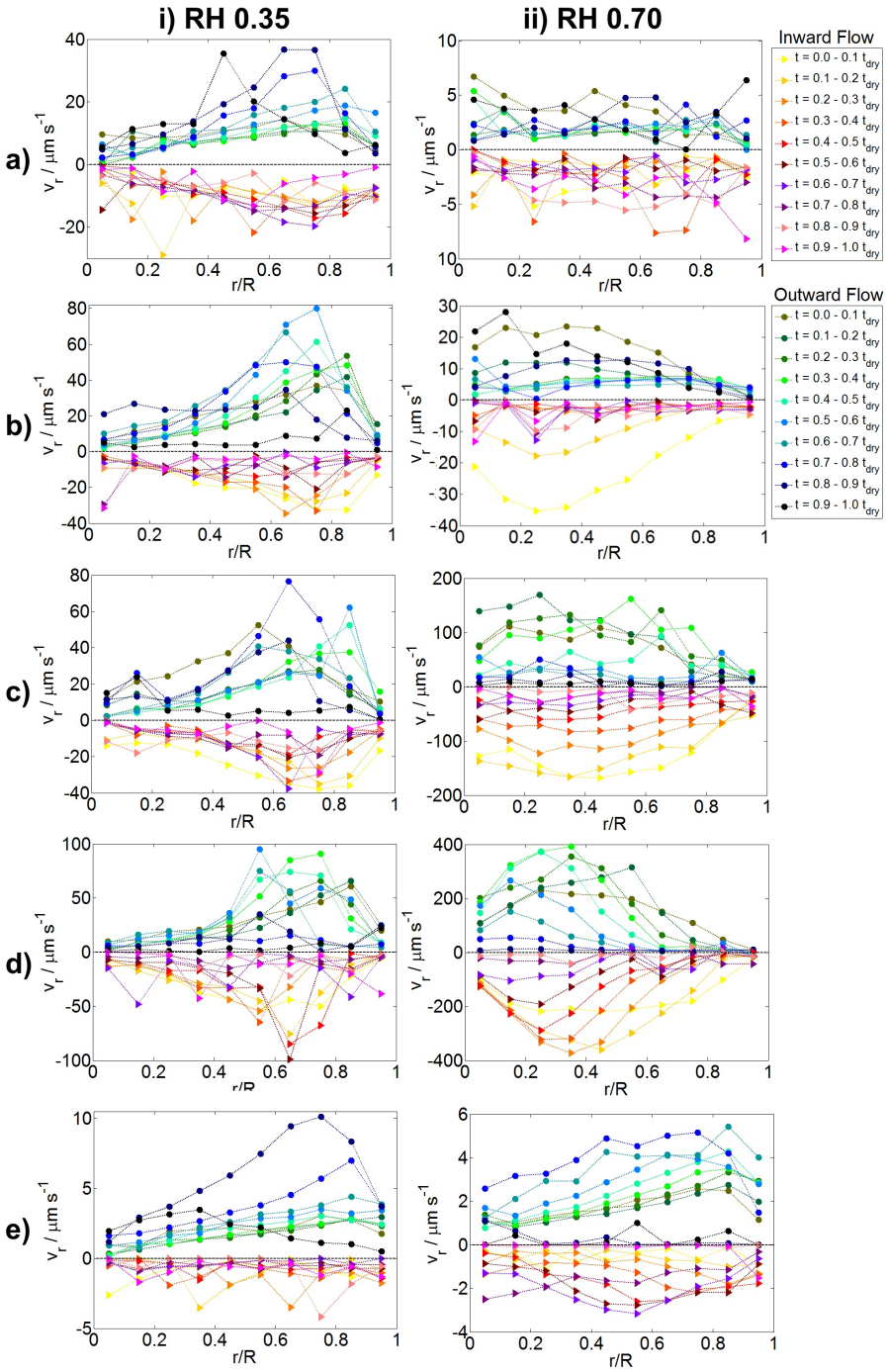

Figure 4.20. The evolution of the mean speed of particles (for five droplets) in each temporal bin across the radius of the droplet for PM/water droplets with a PM concentration of a) 10%v, b) 30%v, c) 50%v, d) 70%v, and e) 90%v, at i) *RH* 0.35 and ii) *RH* 0.70. The tracer particles were 1 μm polystyrene spheres at a concentration of 0.01%v. Particles in focus were just above the substrate. Negative velocities are towards the centre of the droplet (judged by best-fit ellipse to the contact line) and positive velocities are towards the contact line. Each temporal bin is $0.1\,t_{\mathrm{dry}}$, except for 50%v and 70%v PM at *RH* 0.7, where a temporal bin is $0.1\,t_{\mathrm{Rg}}$ due to the faster particle speeds.

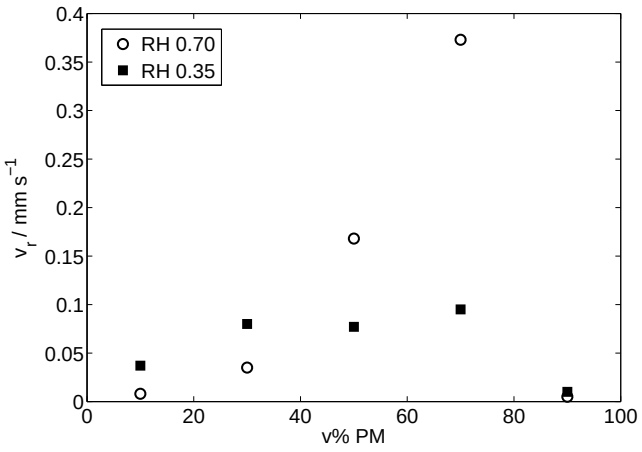

Figure 4.21. The maximum Marangoni flow speed near the substrate is plotted for each PM concentration (at RH 0.35 and 0.70). The highest flow speeds were observed in the 70%v PM/water mixture at either RH.

plet. At 90%v PM/water, the Marangoni flow speed was slower than in any of the other investigated PM/water mixtures. This could be due to the non-ideal vapour pressures changing the relative evaporation rates by a substantial margin. The increase in the Marangoni flow speed at higher PM concentrations (up to 70%v PM) is counter to the trend observed for ethanol/water droplets, despite the same trends during drying for the viscosity and surface tension variation with composition. This demonstrates that simply following the surface tension and viscosity trends cannot be relied on for an accurate description of flows inside these droplets. Diffusion and mass transport may have a large role.

For RH 0.35, the Marangoni flow speeds increased with PM concentration. The highest mean particle speeds were again observed for the 70%v PM/water droplet, but were four times smaller than at RH 0.70.

The fastest Marangoni flow speed observed in a PM/water droplet at either of the two tested relative humidity values was $\backsim$ 400 μms^{-1} (for the 70%v PM droplet at a RH of 0.70). This droplet had the same Marangoni flow direction as the ethanol/water droplets, but the fastest Marangoni flow speeds were an order of magnitude lower than those observed for the ethanol/water droplets (2800 μms^{-1}). This is in part due to the higher viscosity and slower evaporation of PM/water mixtures relative to ethanol/water mixtures, but also due to the lower aspect ratios of the PM/water (on glass) compared to the ethanol/water

(on plasma fluorinated glass).

For PM/water droplets evaporating at RH 0.70, the Marangoni flow speed decreased with time (for both inward and outward motion), except for the 90%v PM/water droplet where speeds were very low throughout drying. The decrease in Marangoni flow speed must indicate a decrease in the compositional gradient across the droplet with time. However, this is not explained by non-ideality of the mixtures which would cause increased depletion of the PM as the mixture becomes more water-rich, increasing compositional gradients. At a RH of 0.35, the Marangoni flow speeds for outward motion increased as drying progressed, likely due to an increase in the evaporation-driven radial flow as the droplet became thinner. There was a decrease in the speed of the inward flow at this RH value (although the data are noisy). The radial position of the fastest Marangoni flow speed moved closer to the centre of the droplet (r/R=0) for 30−70%v PM/water droplets drying at RH 0.70. For the PM/water droplets drying at RH 0.35, there was no noticeable change in the radial position of the maximum speed for inward moving particles. For particles moving outwards, the position of the fastest Marangoni flow was close to the contact line, until late times, when de-pinning occurred. Eddies did not die out until very late in the drying, as evidenced by inward particle motion even at late times.

Compared to ethanol/water droplets, PM/water droplets evaporating at either RH completed fewer cycles. An ethanol/water droplet in the concentration range 10−30%v circulated at approximately 10^2 Hz (with a drying time of $\backsim 0.8$ s). Comparatively, PM/water droplets with the highest mean particle speeds circulated at approximately 10^1 Hz (with a drying time of $\backsim 2$ s at a RH of 0.35 or 4 s at a RH of 0.70).

Estimates of the surface tension difference across the liquid-vapour interface based on the highest Marangoni flow speeds are displayed in Table 4.3. The surface tension differences estimated for the flow speeds are of similar magnitude to those estimated for ethanol/water droplets. Likewise, the compositional variation along the liquid-vapour interface only differs by small percentage volumes of PM. Hence, viscosity may play a larger role in determining the mean particle speeds in PM/water droplets when comparing with etha-

nol/water mixtures. For similar aspect ratios, 50%v PM/water and 50%v ethanol/water mixtures with similar estimated composition gradients have rather different Marangoni flow speeds (see Table 4.4).

Table 4.3. Estimates of the surface tension difference, $\Delta\sigma$, along the liquid-vapour interface for droplets of PM/water at RH 0.35 (calculation uses equation 4.3). Corresponding estimates in the composition variation from the initial PM concentration are given (Δx_v). Note that the aspect ratios here are lower in Table 4.2 due to the difference in the substrate, hence values are not directly comparable.

PM /%v	η_i / mPa s	$\bar{u}_0$/ μm s^{-1}	R/H	$\Delta\sigma$/ mN m^{-1}	Δx_v /%v
10	1.7	40	15	5×10^{-3}	0.009
30	3.3	70	13	2×10^{-2}	0.05
50	3.9	80	9	2×10^{-2}	0.07
70	3.5	100	12	2×10^{-2}	0.2
90	2.3	10	19	2×10^{-3}	0.06

Table 4.4. Estimates of the surface tension difference, $\Delta\sigma$, along the liquid-vapour interface for droplets of 50%v ethanol/water and 50%v PM/water, comparing droplets with similar aspect ratios. Corresponding estimates in the composition variation from the initial concentration are given (Δx_v).

Organic Solvent	RH	η_i / mPa s	$\bar{u}_0$ / μm s^{-1}	R/H	$\Delta\sigma$/ mN m^{-1}	Δx_v / %v
ethanol	0.24	2.4	577	2.7	0.02	0.1
PM	0.70	3.9	150	2.9	0.03	0.1

4.2.4. Flows inside other binary solvent mixtures

So far, this chapter has looked at ethanol/water and PM/water mixtures. Here, some alternative binary solvent mixtures will be considered whose component properties are given in Table 4.5 and particle tracks in Figure 4.22. All alternative mixtures have 50%v/50%v component ratios.

First, the particle motion inside a droplet of isopropanol/ethanol is considered. Despite the small difference in surface tension (1 mN m^{-1}) between the

Table 4.5. Surface tensions, σ, and vapor pressures, p, dielectric constants, ϵ_r, and viscosities, η, for pure liquids at 20°C.

Fluid	σ/ mNm^{-1}	p/ kPa	ϵ_r	η / mPa s
Water	72.9 [127]	2.34 [127]	77 [129]	1.0 [127]
Ethylene glycol	48.0 [130]	0.008 [130]	38 [130]	17.9 [131]
1-Methoxy-2-propanol (PM)	27.7 [132]	1.16 [132]	12 [133]	1.7 [132]
Methanol	23.0 [134]	12.9 [127]	32 [129]	0.5 [135]
Ethanol	22.4 [127]	5.95 [127]	24 [129]	1.1 [135]
Isopropanol (IPA)	21.3 [127]	4.41 [127]	18 [129]	2.0 [136]
Isooctane	18.6 [137]	6.35 [138]	2 [139]	0.5 [137]
1-Propoxy-2-propanol (PnP)	25.4 [140]	0.38 [140]	9 [141]	2.4 [140]

Table 4.6. The variation in surface tension with temperature based on linear fits to the data in [134] and [205].

Fluid	$d\sigma/dT$ / mNm^{-1}K^{-1}
Ethanol	-0.08
Isopropanol	-0.10
Isooctane	-0.10

components, the particle tracks show that there is significant Marangoni flow within the droplet (Fig. 4.22a). Cycling motion occurs throughout the isopropanol/ethanol droplet with particles near the contact line eddying as they translated along the periphery. Note that the variation in surface tension with temperature is small for both ethanol and isopropanol (Table 4.6). Also, the non-ideality for isopropanol/ethanol is expected to be small.

A PM/ethanol droplet with the opposite Marangoni flow direction (to isopropanol/ethanol) gave a collecting circulating group of particles (Fig. 4.22b). Similar to ethanol/water mixtures, the Marangoni flow died out from the contact line inwards (see Fig. 4.22biii), and radial flow transported particles towards the contact line from then on. Hence, differences in the surface tension of pure components of 5 mN m^{-1} or less were capable of generating Marangoni flows. The large surface tension gradients arising from using water as one of the components was not necessary. Similar circulating Marangoni flow was seen at the centre of methanol/water droplets (Fig. 4.22c), although there was more depletion of particles from the contact line than in the PM/ethanol case.

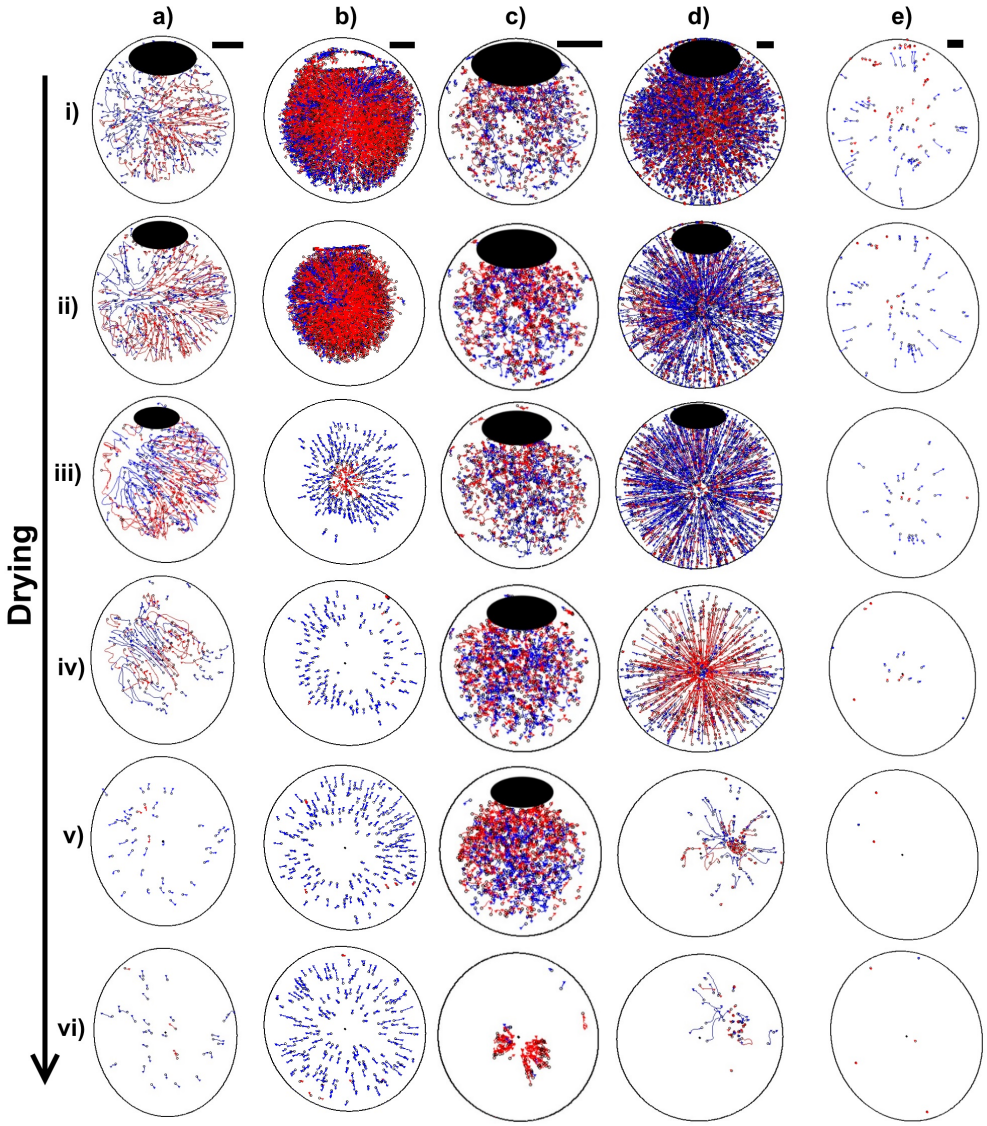

Figure 4.22. Particle tracks for droplets of a) a 50%v isopropanol/ethanol droplet, b) a 50%v PM/ethanol droplet, c) a 50%v methanol/water droplet, and d) a 50%v isooctane/ethanol droplet and e) a 50%v propoxypropanol(PnP)/water droplet. Droplets contain 0.05%v 1 μm polystyrene spheres and were evaporated at a RH of 0.5. i) 0−0.1 t_{dry}, ii) 0.1−0.2 t_{dry}, iii) 0.4−0.5 t_{dry}, iv) 0.6−0.7 t_{dry}, v) 0.7−0.8 t_{dry} and vi) 0.8−0.9 t_{dry}. For the methanol/water droplet (c) times are normalised instead by t_{Rg} (which is 0.91 s). Values for t_{dry} for each mixture are i) 0.80 s, ii) 2.08 s, iv) 2.05 s, and v) 4.96 s. The substrate was plasma fluorinated glass. Scale bars are 20 μm.

Marangoni flows were observed inside droplets of isooctane/ethanol (Fig. 4.22d) where the component fluids have very similar vapour pressures. Non-ideality of the partial vapour pressures allowed a composition gradient to build up via differential evaporation as particles moved in inward and outward directions over the full radius of the droplet. The non-ideality is expected to be high for this mixture, with the minor component (in mole fraction) having a

higher vapour pressure. Again, the surface tension variation with temperature is small for each component (Table 4.6).

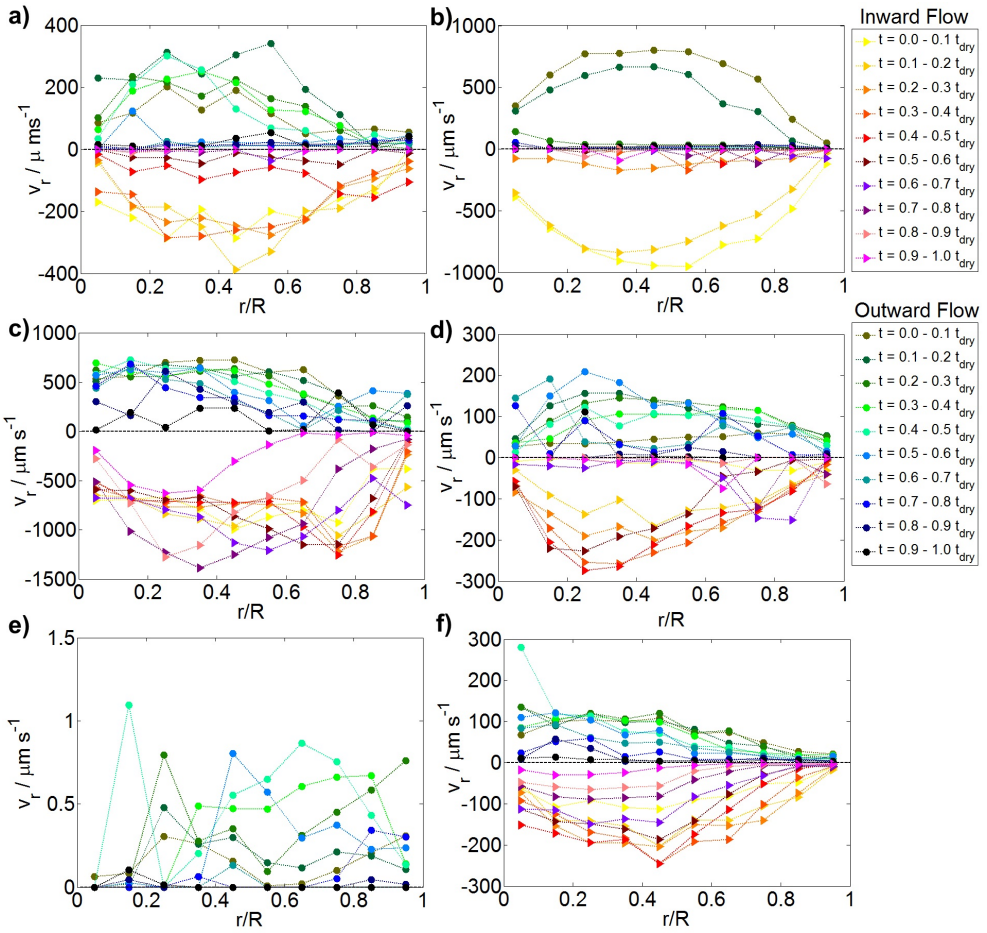

Figure 4.23. Mean radial particle velocities in droplets of a) 50%v isopropanol/ethanol, b) 50%v PM/ethanol, c) 50%v methanol/water, d) 50%v isooctane/ethanol, e) 50%v ethylene glycol/water, and f) 50%v ethylene glycol/ethanol. Droplets contain 0.05%v 1 μm polystyrene spheres and were evaporated at a RH of 0.5. The substrate was plasma fluorinated glass (except for the ethylene glycol/water mixture which was on as-received glass).

The mean particle speeds are shown for some of the mixtures in Figure 4.23. For isopropanol/ethanol (Fig. 4.23a), the Marangoni flow velocity decreased with time, whereas isooctane/ethanol (Fig. 4.23d) showed an increase in the Marangoni flow speed with time until switch off of the Marangoni flow. For the methanol/water droplet (4.23c), the Marangoni flow speeds were the fastest of the investigated mixture compositions, and the radius of the cycling group was smallest. The PM/ethanol droplet also had a central circulating group, but the Marangoni flow shut down early in the drying (Fig. 4.23b).

Ethylene glycol/water (Fig. 4.23e) and ethylene glycol/ethanol (Fig. 4.23f) provide an interesting comparison. The surface tension difference between pure components is very similar, but there is no Marangoni flow in the ethylene glycol/water droplet, whereas ethylene glycol/ethanol exhibits Marangoni flow. This could be related to the larger difference in vapour pressures of the ethylene glycol and ethanol, compared to ethylene glycol and water.

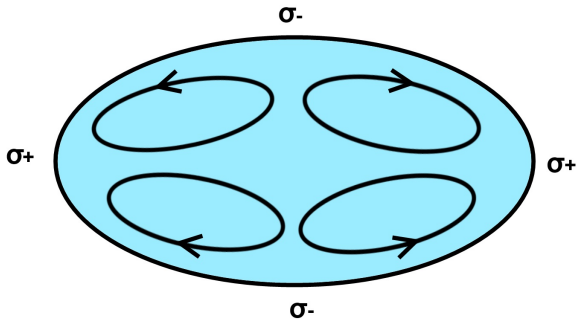

Figure 4.24. Cartoon of multiple circulating cells within a droplet of ethanol/water. At regions of higher curvature, evaporation is enhanced, resulting in more depletion of the ethanol and giving a higher surface tension.

In some cases, particularly when the droplet is very thin, multiple cells form within the circulating group (see Video CE). Localised regions rich in each solvent could result in such behaviour. Also, when droplets have an asymmetrical contact line, regions of high curvature will experience enhanced evaporation relative to regions of low curvature, resulting in surface tension gradients along the liquid-vapour interface. For an ethanol/water droplet, ethanol will be depleted most in the regions of high curvature, increasing the surface tension in these regions. Circulating cells (as illustrated schematically in Fig. 4.24) could then result.

To summarise, regions of circulating Marangoni flow develop inside binary solvent mixtures during drying. The region of circulating flow switches from the centre to the periphery of the droplet when the Marangoni flow direction is reversed. The single solvent droplets in this section do not exhibit Marangoni flow.

4.3. Migration of particles in evaporating droplets

As well as circulating within the droplets, particles migrated across streamlines to form a central collected group. To investigate the collection, a higher solid content of 0.1%v 1 μm polystyrene spheres was added to the binary solvent mixtures. The evolution of this collecting group and potential migration mechanisms will be discussed in this section.

4.3.1. Progression of the collecting group

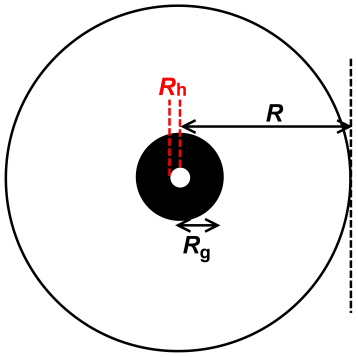

Figure 4.25. A schematic diagram indicating the contact radius of the droplet, R, the radius of the collecting group, R_{g}, and the radius of the central hole, R_{h}.

The collecting group was considered for ethanol/water droplets at higher solid content, as the shape of the collecting group was more distinct than for dilute solids content. For a Marangoni direction from apex to contact line (along the liquid-vapour interface), the circulating group had zones depleted of particles both at the droplet centre (as a small "hole"), and in a growing region next to the contact line. Circulating particles were drawn towards the centre of the droplet in a group that reduced in radius, R_{g}, over time (Fig. 4.25). The minimum radius of the collected group, $R_{\mathrm{g,min}}$, occurred at time t_{Rg}, at the end of the Marangoni flow period. Radial flow then enlarged the collected group. It was only after Marangoni flow ceased and radial flow began that a ring stain built up.

The position of the hole is considered throughout drying. The central hole is indicated in red for a droplet of 10%v ethanol/water (Fig. 4.26a) and was

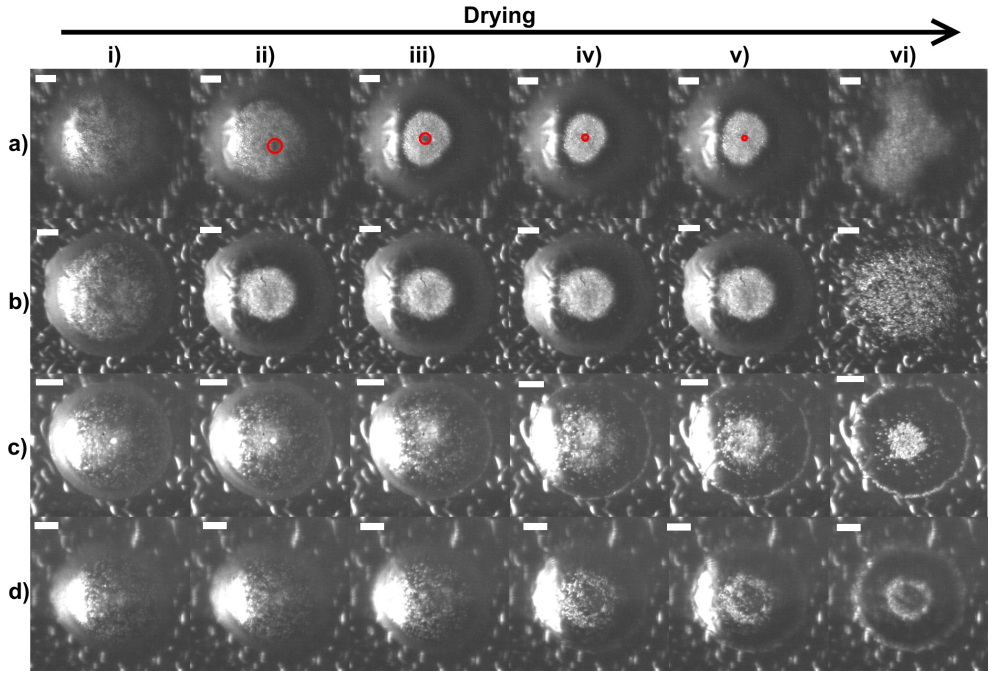

Figure 4.26. The evolution of the particle collection with time for a droplet of 10%v ethanol/water with the zone of focus a) close to the liquid-vapour interface and b) close to the substrate, and a droplet of 50%v PM/water at RH 0.35 with the focus c) close to the substrate and d) close to the liquid-vapour interface. The central hole is marked in red on a). Time bins for a) and b) are i) $0.05\,t_{\mathrm{dry}}$, ii) $0.10\,t_{\mathrm{dry}}$, iii) $0.14\,t_{\mathrm{dry}}$, iv) $0.17\,t_{\mathrm{dry}}$, v) $0.20\,t_{\mathrm{dry}}$, and vi) $0.80\,t_{\mathrm{dry}}$. Time bins for c) and d) are i) $0.05\,t_{\mathrm{dry}}$, ii) $0.10\,t_{\mathrm{dry}}$, iii) $0.30\,t_{\mathrm{dry}}$, iv) $0.50\,t_{\mathrm{dry}}$, v) $0.60\,t_{\mathrm{dry}}$, and vi) $0.80\,t_{\mathrm{dry}}$. For ethanol/water $t_{\mathrm{dry}} \backsim 3.7\,\mathrm{s}$, and for PM/water $t_{\mathrm{dry}} \backsim 2.4\,\mathrm{s}$. Scale bars are 50 μm. The substrates are glass with a plasma fluorinated polybutadiene coating.

clearly visible when the zone of focus was at the liquid-vapour interface of the droplet. Immediately after deposition, the particle distribution was uniform (Fig. 4.26ai). However, once Marangoni flow began, a hole became evident. The position of this hole was erratic, jumping about from the centre to the edge of the droplet (Fig. 4.26aii). As the chaotic flow regimes within the droplet ended, a stable Marangoni flow ensued, and the hole became centralised (Fig. 4.26aiii–av), closing when radial flow dominated (Fig. 4.26avi–avi). There was no widening of the central hole during radial flow. A video clearly showing the central hole is given for a 30%v isopropanol/water droplet that behaves similarly to the ethanol/water (Video H).

It is worth noting that, when a gradient in the RH existed across the droplet (e.g. from a nearby satellite), the collecting group shifted closest to the side at higher relative humidity. Once circulating Marangoni flow ceased, the collected group moved back to the centre of the droplet, and radial flow

progressed from the centre outwards (even if the RH still exhibited a gradient across the droplet). The motion back towards the centre may be the same reason the hole is filled in once Marangoni flows cease. The radius of the central hole decreased throughout drying in a fairly linear manner (Fig. 4.27), independent of the binary mixture (for Marangoni flow from apex to contact line along the liquid-vapour interface). When the zone of focus was switched to the substrate (Fig. 4.26b), the hole was no longer distinct.

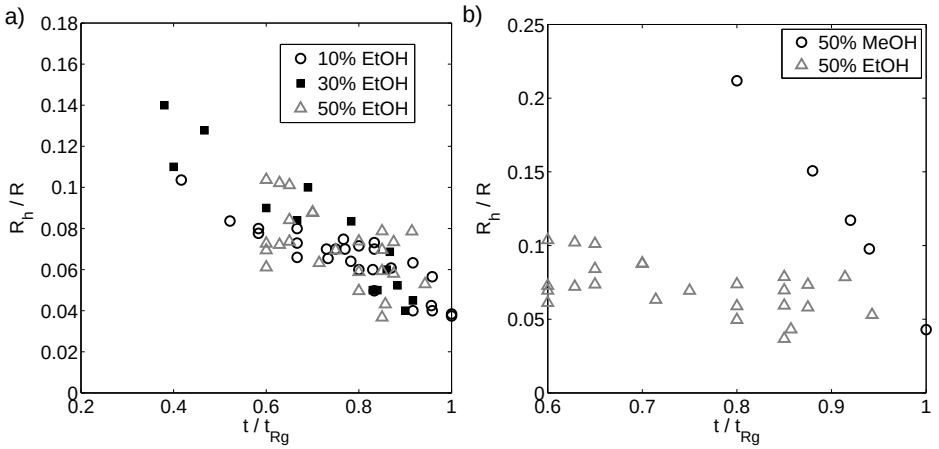

Figure 4.27. The evolution of the central hole radius, R_{h}, with time for a) ethanol/water droplets with an ethanol concentration of 10−50%v, b) 50%v methanol/water and 50%v ethanol/water droplets. Droplets were loaded with 1 μm polystyrene spheres at a concentration of 0.1%v. The substrates were plasma fluorinated glass. Ethanol/water data are for an average of 3−5 droplets at each concentration. The time is normalised by the time to reach the minimum radius of the collected particle group, t_{Rg}.

For the reverse Marangoni flow (contact line to apex along the liquid-vapour interface), a 50%v PM/water droplet (at RH 0.35) is considered as an example. Close to the liquid-vapour interface, a depleted region formed centrally and close to the contact line as drying progressed (Fig. 4.26d). Close to the substrate, only a disk-shaped centrally collecting group was evident (Fig. 4.26c). An annular-shaped collection (in 2D) was observed close to the liquid-vapour interface.

If evaporation concentrates particles at the liquid-vapour interface, the location of the zone of focus could cause selective visualisation of these particles in one horizontal slice through the droplet (which would look like an annulus, see Fig. 4.28). To ensure that the annular collection observed for PM/water droplets (Fig. 4.26d) was genuine and not a consequence of the zone of focus,

both thin droplets (where the whole depth of the droplet was in the zone of focus) and droplets with a large contact angle (where only the top of the droplet was in the zone of focus) were considered. Plasma-fluorinated substrates were used for high contact angles, and cleaned glass was used for low contact angles. For a high contact angle, when the zone of focus is near the liquid-vapour interface, particles at the interface would be viewed as an annulus whose radius and central hole would shrink as the droplet height decreased. For a thin droplet, all particles located at the liquid-vapour interface would be imaged, giving a disk-shaped collection. As an annular collection was observed for both thin droplets and those with a high contact angle, the annulus seen in Figure 4.26d is therefore a real effect and not an imaging artifact. Additionally, the hole radius of the annulus in Figure 4.26d did not shrink during drying. Furthermore, the disk-shaped collection observed near the substrate Figure 4.26c cannot be due to settled particles, or a particle layer would grow across the contact area as the collecting group moves inwards. However, the velocities near the substrate are low, and so the hole may become filled in here.

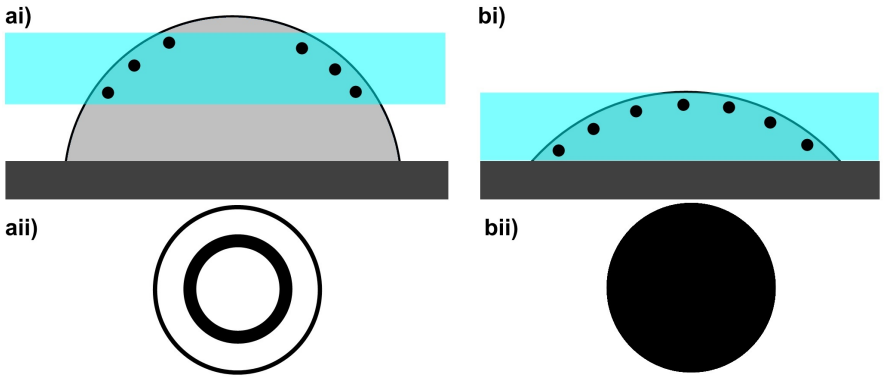

Figure 4.28. Cartoon representation of i) the zone of focus in a droplet with a) a high contact angle and b) a low contact angle, and ii) the top-down representation if only particles near the interface were imaged. All "interface-particles" are in the zone of focus of the low contact angle droplet.

For the 50%v PM/water droplet (Fig. 4.26c and Fig. 4.26d), although a central group of particles formed at low or high RH, there was also build up of a ring stain at the contact line. Particles were able to escape the central collection via Brownian motion and move by radial flow to the contact line. The same phenomena occurred at higher RH where the Marangoni direction was reversed and the central group was circulating, with some particles escaping to

the ring. Consequently there was less particle depletion near the contact line than for the ethanol/water mixtures (see Fig. 4.29 and Videos PM1 and PM2).

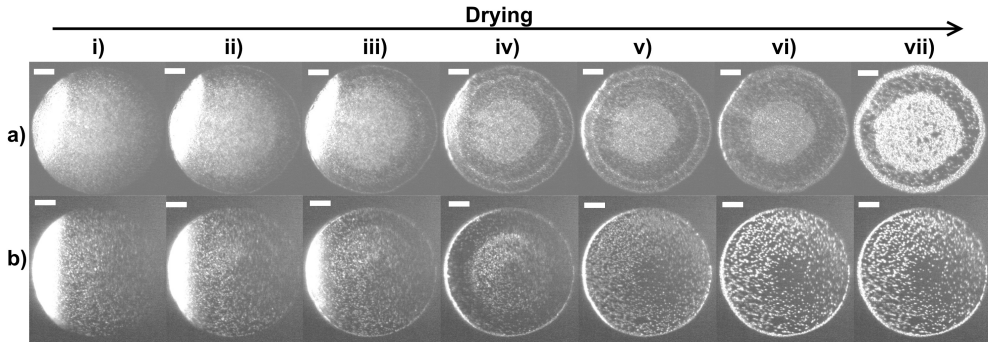

Figure 4.29. Dark field images of droplets of a) 50%v PM at a RH of 0.50 containing 0.5%v 600 nm polystyrene spheres, and b) 50%v PM at a RH of 0.65 containing 0.1%v 600 nm polystyrene spheres. i) $0\,t_{\mathrm{dry}}$, ii) $0.2\,t_{\mathrm{dry}}$, iii) $0.5\,t_{\mathrm{dry}}$, iv) $0.8\,t_{\mathrm{dry}}$, v) $0.9\,t_{\mathrm{dry}}$, vi) $0.95\,t_{\mathrm{dry}}$ and vii) $1.0\,t_{\mathrm{dry}}$. Values for t_{dry} were 1.43 s at RH 0.65 and 3.67 s at RH 0.50. Scale bars are 50 μm. Substrates were glass.

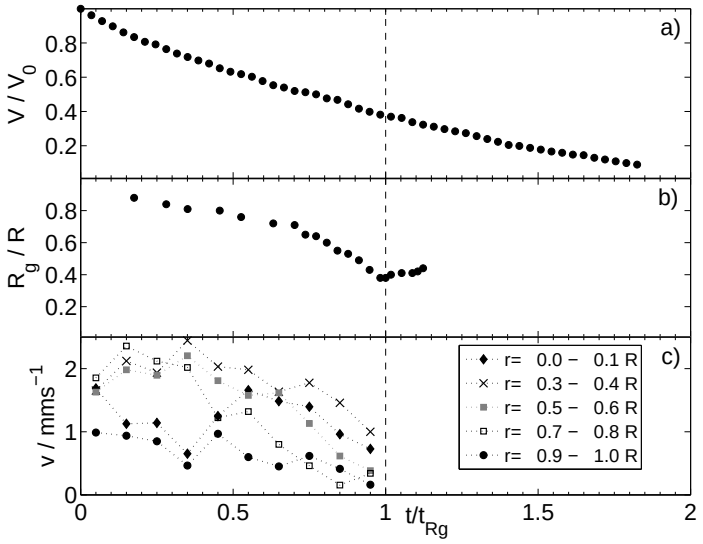

Figure 4.30. a) The evaporation rate of a 50%v ethanol/water droplet on as-received glass, containing 0.01%v 1 μm spheres at a RH of 0.26. b) The evolution of the group radius, R_{g}, with time, normalized by the initial contact radius, R. t_{Rg} is the time when the transition to radial flow occurs, indicated by the vertical dashed line. c) The mean particle speeds for spatial bins of size $0.1R$. An average is taken for 10 droplets for each spatial bin. Dashed lines are meant as a guide to the eye. The drying time is 1.65 s and the initial contact angle is $\backsim 50°$. A typical value for t_{Rg} is 0.9 s.

Figure 4.30 demonstrates how the evolution of the collecting group is related to the evaporation rate for a 50%v ethanol/water droplet on uncoated glass for a RH of 0.26. The evolution of the mean particle speeds is given for the same droplet (Fig. 4.30c). There was a gradual drop in the mean par-

ticle speed near the droplet centre from ~ 1.8 mms^{-1} at early times to ~ 1.0 mms^{-1} close to the transition time, t_{Rg}. During the Marangoni flow period ($t = 0 - t_{\mathrm{Rg}}$), the radius of the collected group decreased, restricting particles to the centre of the droplet. At the end of the Marangoni flow period, a minimum collection radius, $R_{\mathrm{g,min}}$, was reached. The mean particle velocities were lower, and particles began to move outwards with the evaporation-driven radial flow. Particles were carried towards the contact line and R_{g} increased, with faster growth as time progressed and the droplet thinned. The transition to radial flow was sharp, but Figure 4.30a indicates that the abrupt transition is not associated with a sharp change in the evaporation rate.

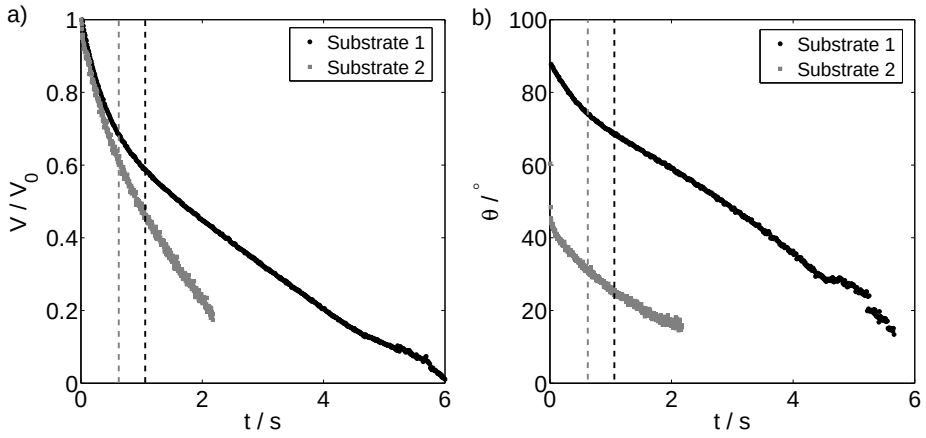

Figure 4.31. a) The droplet volume and b) the contact angle evolution of a 50%v ethanol/water droplet containing 0.1%v 1 μm polystyrene spheres on two coated substrates at a RH of 0.5. Substrate 1 has a higher initial contact angle than Substrate 2. Vertical dashed lines indicate when $R_{\mathrm{g,min}}$ occurs on each substrate (t_{Rg} in seconds). See Chapter 3, Section 3.2.2 for substrate preparation (Substrate 1 corresponds to S1 and Substrate 2 to S4).

Figure 4.31 indicates the evaporation rates and contact angles at time t_{Rg} (when the minimum radius of the collected particle group reached $R_{\mathrm{g,min}}$) for a 50%v ethanol/water droplet on two coated substrates. The chemical composition of the substrates was the same, but the surface roughness of Substrate 1 was higher, increasing the contact angle. The transition from circulatory flow to radial flow corresponded to the same normalized volume loss on each substrate (Fig. 4.31a). The droplet on Substrate 2 had the same initial composition and similar contact angle to the droplet at RH 0.26 in Figure 4.30. The minimum collection radius was reached after 40% of the droplet volume had evaporated at RH 0.50, compared to 60% at RH 0.26. This difference is due

to the slower evaporation rate of the water at RH 0.50. There was no dependence of $R_{g,min}$ on the contact angle (Fig. 4.31b). These observations suggest that it is a particular chemical composition (at fixed RH) that is important in determining when $R_{g,min}$ occurs, at least for these two initial contact angles.

The transition to radial flow occurs before all the ethanol within the droplet has been depleted. For example, in Figure 4.31, the minimum radius of the collected group, $R_{g,min}$, occurred before 50% of the droplet volume had evaporated in a 50%v ethanol droplet. Thus, compositional gradients must still exist despite cessation of the Marangoni flows. In fact, for a droplet height of 10 μm, the time for ethanol to diffuse this vertical distance (t_{diff}) is approximately

$$t_{diff} = h^2 \,/\, 2D_{ew} \backsim (10\,\mu\text{m})^2 \,/\, 10^{-9}\,\text{m}^2\,\text{s}^{-1} \backsim 0.1\,\text{s}, \tag{4.14}$$

where D_{ew} is the mutual diffusion coefficient for an ethanol/water mixture. This compares to a radial diffusion time (for R=70μm) of

$$t_{diff} = R^2 \,/\, 2D_{ew} \backsim (70\,\mu\text{m})^2 \,/\, 10^{-9}\,\text{m}^2\,\text{s}^{-1} \backsim 4.9\,\text{s}. \tag{4.15}$$

Therefore, compositional gradients within the droplet should persist after t_{Rg}, despite an insufficient compositional gradient along the liquid-vapour interface for Marangoni flow to occur. Additionally, with no Marangoni flows redistributing the solvent from the bulk to the liquid-vapour interface, compositional gradients may be enhanced.

The effect of the initial ethanol concentration was investigated for the 10−50%v ethanol/water droplets which showed significant Marangoni flows in Section 4.2.2. Figure 4.32a shows the contraction of the collected central group up until the transition to radial flow, and the expansion thereafter. The time at which $R_{g,min}$ was reached was dependent on the initial chemical composition of the droplet. The minimum size of the collected group was similar for ethanol concentrations between 10−50%v ($\backsim$0.35R), with a slightly smaller group for the 30%v ethanol droplet (see Fig. 4.32a). Particles were therefore concentrated in the x-y plane to 1/3 the initial droplet diameter when $R_{g,min}$ was reached. For the 70%v ethanol/water droplet the group radius is larger, which

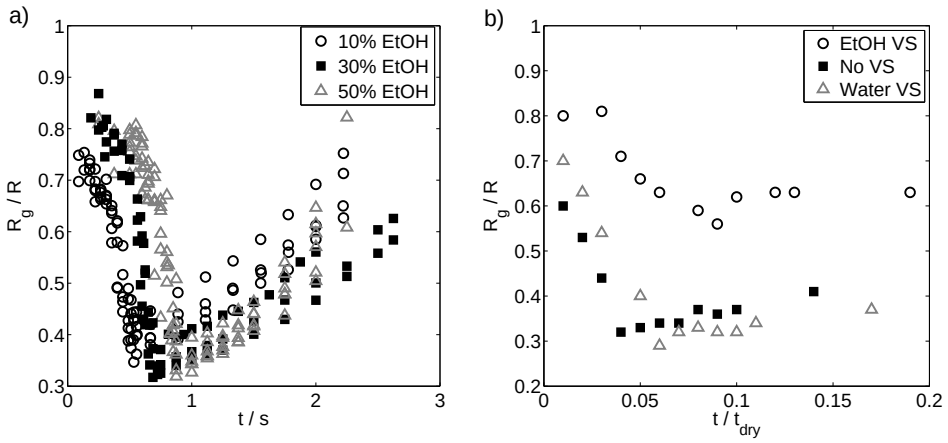

Figure 4.32. a) The progression of the group radius, R_{g}, with time for ethanol/water droplets with an ethanol concentration of 10−50%v on plasma fluorinated glass substrates. Droplets were loaded with 1 μm polystyrene spheres at a concentration of 0.1%v. Data for each ethanol concentration comprise of at least three droplets. b) The progression of the group radius with time for a 50%v ethanol/water droplet evaporating in an atmosphere high in ethanol vapour or water vapour, compared to ambient conditions ($RH = 0.5$). A vapour shroud (VS) of ethanol or water was used, or no vapour shroud for ambient conditions. Times were normalised by the drying time, t_{dry}.

could result from the decreased ethanol depletion at higher ethanol concentrations. The duration of the Marangoni flow (as a fraction of the drying time) was longer for higher ethanol concentrations in the range 10−50%v ethanol.

To determine the effect of the relative evaporation rate of the two components, a comparison was made between ethanol/water droplets evaporating in different environments (ethanol-rich vapour or water-rich vapour). By using a vapour shroud, the concentration of water vapour or ethanol vapour in the ambient air was raised. Figure 4.32b indicates the change in $R_{\mathrm{g,min}}$ for each environment. When the level of water vapour close to droplet was increased compared to normal ambient conditions ($RH = 0.5$), there was little change in $R_{\mathrm{g,min}}$. However, when the level of ethanol vapour was increased compared to normal ambient conditions (zero ethanol vapour concentration), there was a notable increase in $R_{\mathrm{g,min}}$.

Further investigation was undertaken to determine whether by increasing the difference in the evaporation rates between the two components, the minimum collection radius was reduced. To do this, observations were made for other binary mixtures (Fig. 4.33), including those without water (so RH did

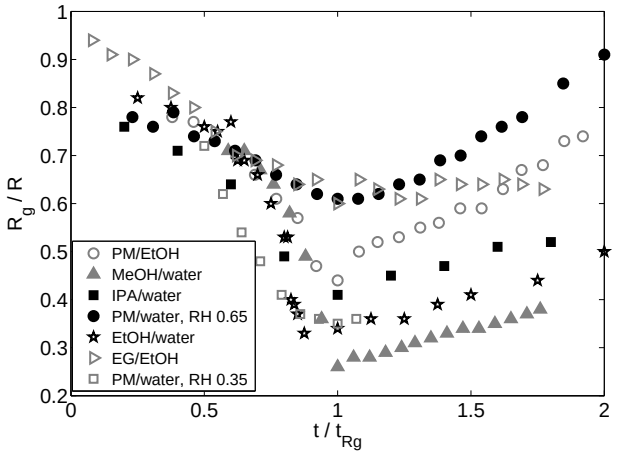

Figure 4.33. Evolution of the radius of the collecting particle group for various 50%v/50%v binary solvent mixtures at a RH of 0.5 (except PM/water which is at 0.35 or 0.65) containing 0.1%v 1 μm spheres. Times are normalised by the time to reach the minimum group radius (R_{g}), t_{Rg}. Note that data are not shown for the whole of the drying lifetime. The substrates for PM/ethanol, methanol/water, ethanol/water and PM/water (at a RH of 0.65) were plasma fluorinated glass. For the other mixtures the glass substrates were as-received.

Table 4.7. Velocities of the collecting groups, v_{g}, in various binary mixtures. Note that droplet radii and contact angles are not the same.

Fluid	RH	v_{g} / $\mu\mathrm{m\,s^{-1}}$
10%v ethanol/water	0.50	145
30%v ethanol/water	0.50	195
50%v ethanol/water	0.50	130
50%v methanol/water	0.50	189
50%v PM/water	0.20	78
50%v PM/water	0.35	21
50%v PM/water	0.50	65
50%v PM/water	0.70	10
50%v ethylene glycol/ethanol	0.50	226
50%v PM/ethanol	0.50	118

not play a role). Indeed, a droplet of 50%v methanol/water, with the largest difference in the vapour pressures of the components, resulted in the smallest group radius of the observed mixtures. Comparisons can be made between droplets on the same substrate (where aspect ratios are similar). For droplets spreading on glass (rather than plasma fluorinated glass) the droplet radius is larger and so particles have to migrate further to give the same $R_{\mathrm{g,min}}$. Hence,

migration may be lessened in larger droplets. On the plasma fluorinated glass, the group radius does indeed decrease when the vapour pressure difference between components is larger (accounting for the RH). However, on glass substrates the ethylene glycol (EG)/ethanol formed a wide group despite the large difference in component vapour pressures. Although EG/ethanol exhibited the largest Marangoni flow velocity listed in Table 4.7, the collection only lasted for a short fraction of the drying time resulting in a wide $R_{\mathrm{g,min}}$. The significance of vapor pressure difference is perhaps best shown by the 50%v PM/water mixtures at different RH, as these droplets have the same initial composition. Indeed, the PM/water at a RH of 0.35 (which has the larger difference in evaporation rates of the components) exhibits the smallest group radius (despite the larger droplet radius at RH 0.35 due to the glass substrate).

Ethanol/water and PM/water droplets containing 50%v water were chosen for comparison due to their similar initial surface tension. Ethanol and water have a large difference in evaporation rates, whereas PM and water have similar evaporation rates. The compositional gradient should be enhanced in ethanol/water by the larger vapor pressure difference. In an ethanol/water droplet with strong Marangoni flow (10−50%v ethanol), the region near the contact line became significantly more depleted of particles compared to in PM/water mixtures with the same Marangoni flow direction (compare Fig. 4.29ii and Fig. 4.29iii), where particles escaped via radial flow (see Video PM1). Particles in an ethanol/water droplet (10−50%v ethanol) with no ethanol vapour in the surrounding atmosphere collected at the droplet centre with a smaller $R_{\mathrm{g,min}}$ than for the PM/water mixtures (Fig. 4.33). The width of $R_{\mathrm{g,min}}$ for the PM/water droplet at a RH of 0.65 (with the same Marangoni flow direction as ethanol/water) was over double that of the ethanol/water droplet. The strength of the Marangoni flow was weakened in PM/water by the similarity in evaporation rates, and hence particles escaped the central collection. As the difference in vapour pressure determines the composition gradient (and hence surface tension gradient) along the liquid-vapour interface, it plays a role in determining the width of the circulating central group.

The migration velocity of the collecting group is indicated in Table 4.7 for various solvent mixtures. For the ethanol/water droplets, migration velocities

were faster inside droplets with quicker Marangoni flow speeds. However, the migration velocity was faster in methanol/water than in ethanol/water despite a lower Marangoni flow speed in the methanol/water mixture. This could relate to the lower viscosities of methanol/water mixtures compared to ethanol/water mixtures (see Fig. 4.1c). For PM/water droplets with a RH>0.5, the migration speed decreases as the difference in component evaporation rates increases. However, for the reverse Marangoni flow direction at a $RH \leq 0.5$, the migration speed increases as the difference between component evaporation rates grows.

Although particle collection only occurs during the Marangoni flow period, $R_{g,min}$ is not necessarily smaller if the Marangoni flow duration is longer. For a PM/water droplet at a RH of 0.50, the particles collected to the centre of the droplet and were then compressed. A lattice structure formed during the compression (Fig. 4.34), and the velocity of the collecting group decreased (Fig. 4.35).

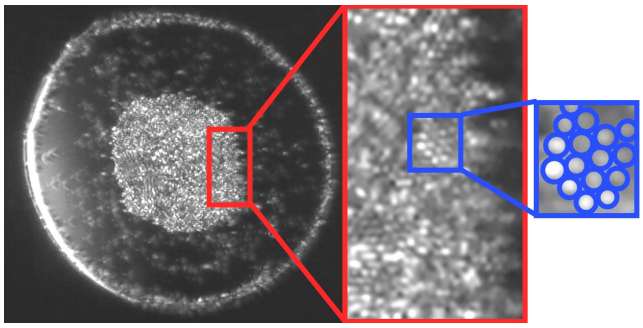

Figure 4.34. Dark field image of the collecting group with zooms highlighting regions where particles formed a lattice structure. The droplet was 50%v PM/water at a RH of 0.22, containing 0.5%v 1 μm polystyrene spheres.

For the purpose of printed lines (e.g. for micro-circuitry) it is interesting to note the behaviour of coalescing droplets. Two droplets of 50%v ethanol/water were deposited next to one another and allowed to coalesce. The particle distribution in the first droplet was initially fairly uniform (Fig. 4.36a). As drying progressed, circulating flow began and a central group formed (Fig. 4.36b). The second droplet was then deposited (which again had a uniform particle distribution). On coalescence, the collecting particles formed a continuous group connecting the two droplets (Fig. 4.36e). Depletion occurred from the

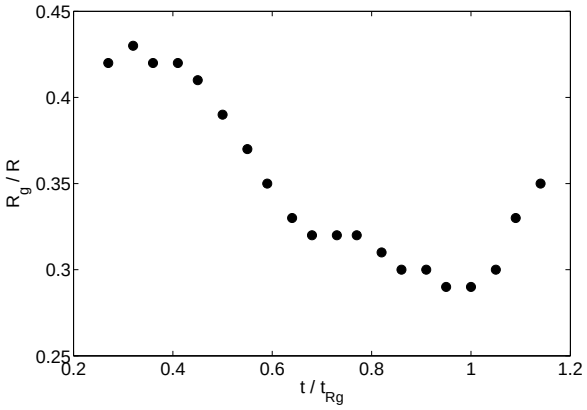

Figure 4.35. Evolution of the radius of the collecting group, R_g with time for a 50%v PM/water droplet at a RH of 0.5 containing 0.5%v 1 μm spheres. The group radius is normalised by the initial droplet radius R and the time is normalised by the time at which the minimum group radius is reached, t_{Rg}. The speed at which the particle group shrinks is faster at first, then slows as the group is compressed.

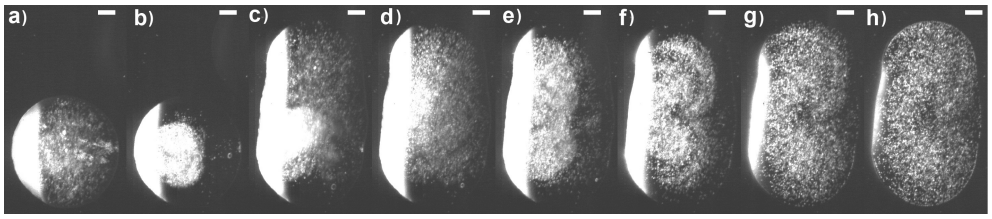

Figure 4.36. Dark field images of coalescing droplets of 50%v ethanol/water containing 0.1%v 600 nm polystyrene spheres. The RH was 0.5. Images were acquired after a) 0 s, b) 0.49 s, c) 0.50 s, d) 0.54 s, e) 0.75 s, f) 1.30 s, g) 2.50 s, and h) 3.40 s after the impact of the first droplet. Scale bars are 20 μm.

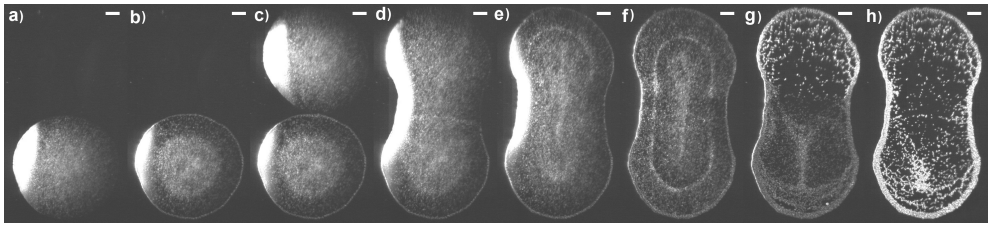

Figure 4.37. Dark field images of coalescing droplets of 50%v PM/water containing 0.5%v 600 nm polystyrene spheres. The RH was 0.5. Images were acquired after a) 0 s, b) 1.08 s, c) 1.12 s, d) 1.16 s, e) 1.80 s, f) 3.10 s, g) 4.30 s, and h) 4.60 s after the impact of the first droplet. Scale bars are 20 μm.

contact line (i.e. the collecting group followed the geometry of the droplet outline). Radial flow then took place (Fig. 4.36f–h). The corresponding video is given in the supplementary materials (Video C1).

Coalescence of the PM/water droplets followed similar trends to the ethanol/water droplets in following the geometry of the coalesced shape (Fig. 4.37). Eddies at the droplet periphery (for PM/water droplets at a RH of 0.50), and

central collection in the first droplet remained as the second droplet coalesced. The particles from the ring at the first droplet's contact line form a line in the neck when the droplets coalesce (Figure 4.37d, corresponding Video C2), which quickly disappears. The width of the eddy remained the same throughout drying, with particles concentrating at the outside of the eddy. The central collection was wider in the second droplet than the first. It is notable then that the second droplet dried out before the first, with de-pinning towards the initial droplet. Due to the time delay between droplets, the liquid-vapour interface of the first droplet will be water-rich compared to the incoming second droplet. The surface tension gradient in the coalesced droplet will cause fluid to flow towards the initial droplet, thus depleting the second.

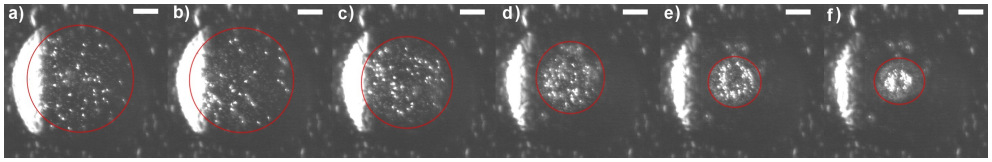

Figure 4.38. Dark field images of a 50%v ethanol/water droplet containing 0.5%v 3 μm and 0.01%v 600 nm polystyrene spheres. Scale bars are 50 μm. The red ellipses indicate the edge of the collecting group of 600 nm particles. a) $0.1\,t_{\mathrm{Rg}}$, b) $0.2\,t_{\mathrm{Rg}}$, c) $0.5\,t_{\mathrm{Rg}}$, d) $0.8\,t_{\mathrm{Rg}}$, e) $0.9\,t_{\mathrm{Rg}}$ and f) $1.0\,t_{\mathrm{Rg}}$ (where $t_{\mathrm{Rg}} = 0.95\,\mathrm{s}$). The corresponding video is Video PS1.

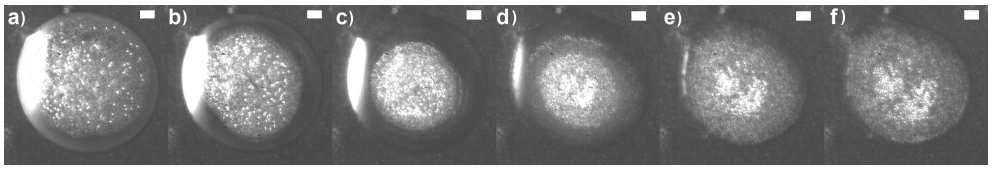

Figure 4.39. Dark field images of a 50%v ethanol/water droplet containing 0.5%v 3 μm, 0.01%v 1 μm, 0.05%v 600 nm and 0.5%v 200 nm polystyrene spheres. The scale bars are 20 μm. a) $0.1\,t_{\mathrm{dry}}$, b) $0.2\,t_{\mathrm{dry}}$, c) $0.3\,t_{\mathrm{dry}}$, d) $0.5\,t_{\mathrm{dry}}$, e) $0.8\,t_{\mathrm{dry}}$ and f) $0.9\,t_{\mathrm{dry}}$ (where $t_{\mathrm{dry}} = 4.80\,\mathrm{s}$). The corresponding video is Video PS2.

Particles of different sizes were introduced into the same droplet to investigate the effect of the particle size on the collection. Figure 4.38 shows that the brighter 3 μm particles migrate towards the centre of the droplet faster than the smaller 600 nm spheres (corresponding Video PS1). Figure 4.39 shows the same behaviour with a wider variety of sphere sizes (Video PS2). A cartoon of the collection is given for a slice through the side of a droplet in Figure 4.40. Larger spheres entered a tighter cycling radius (smaller R_{t}) faster, and

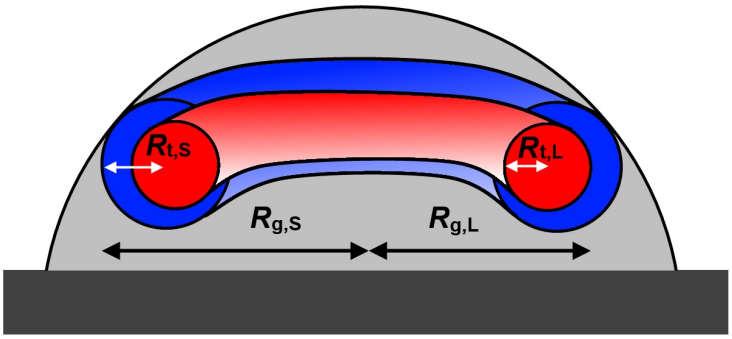

Figure 4.40. Cartoon of particle segregation into toroids within the droplet. The outer radius of the collecting group from the centre of the droplet is defined as $R_{g,L}$ for large particles and $R_{g,S}$ for small particles. The group centric radius (the minor radius of the torus) is defined as $R_{t,L}$ for large particles and $R_{t,S}$ for small particles. Smaller particles (blue) collect in a wider toroid than larger particles (red), $R_{g,L}<R_{g,S}$. Larger particles migrate inward faster and form a larger central hole . The larger particles form a toroid with a smaller cross-sectional radius, $R_{t,L}<R_{t,S}$.

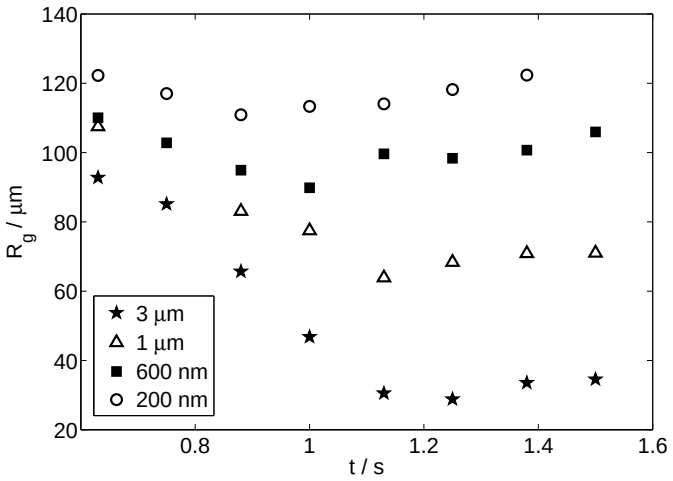

Figure 4.41. Evolution of the radius of the collecting particle group, R_g, for particles of 3 μm, 1μm, 600 nm and 200 nm within the same evaporating droplet of 50%v ethanol/water. The droplet radius was 154 μm. The time, t, is given in seconds.

the group receded further away from both the central hole and the contact line (Fig. 4.40). Therefore, smaller spheres existed either side of the group of bigger spheres. The larger spheres formed a smaller group radius, as shown in Figure 4.41. The size-dependence of the collection provides further evidence that particles migrate across the fluid streamlines.

The size dependence of the collecting group was not due to height restrictions at the contact line from the geometry of the droplet (i.e. larger spheres hitting the liquid-vapour interface before smaller spheres, see Chapter 1, Sec-

tion 1.7, Fig. 1.14). This was shown by the outward motion of particles after the Marangoni flow period. If height restriction due to the liquid-vapour interface played a role, then the larger spheres would have been incapable of moving outward.

Consideration of the internal flows

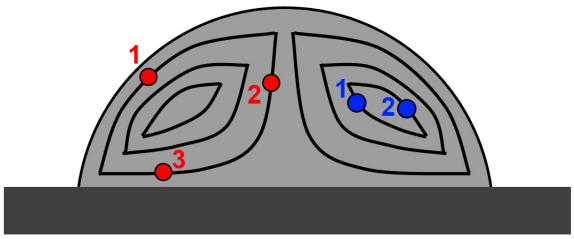

Figure 4.42. Cartoon representation of the streamlines within a droplet exhibiting Marangoni flow. A particle on the outer streamline at position 1 (red) will continue on the same streamline to position 2 and 3 unless an external force causes motion off the streamline. Inner streamlines have a smaller cell for particles to travel around.

For droplets with the thermal Marangoni streamlines of a single cell in half the droplet [68] (Fig. 4.13), a particle can only enter tighter cycles (smaller R_t, Fig. 4.40) and/or migrate to the centre of the droplet if that particle crosses the fluid streamlines. For particles on outer streamlines (red particles in Fig. 4.42), the particles circulate from position 1 to position 2 at the centre of the droplet. Due to evaporation, streamlines terminate, therefore particles (which do not evaporate) move towards the bulk of the fluid. However, particles approaching the liquid-vapour interface on outer streamlines will remain on outer streamlines (e.g. position 1), eventually returning to the centre of the droplet. Particle collection at the centre of the droplet cannot occur for particles on these outer streamlines. Particles on the inner streamline (blue particles in Fig. 4.42), do move towards to the contact line, but stay circulating on the inner streamlines. Therefore, for collection to occur, particles must migrate across the fluid streamlines. As the particle migration to the centre of droplets is size dependent (Fig 4.38) there must be a migration due to an external force. Otherwise, particles of different sizes should follow the same path along the same streamline.

The Marangoni flow model of Hu and Larson [68] (see Chapter 1, Section 1.6.2 for details), which accounts for evaporation, can be used to model solutal

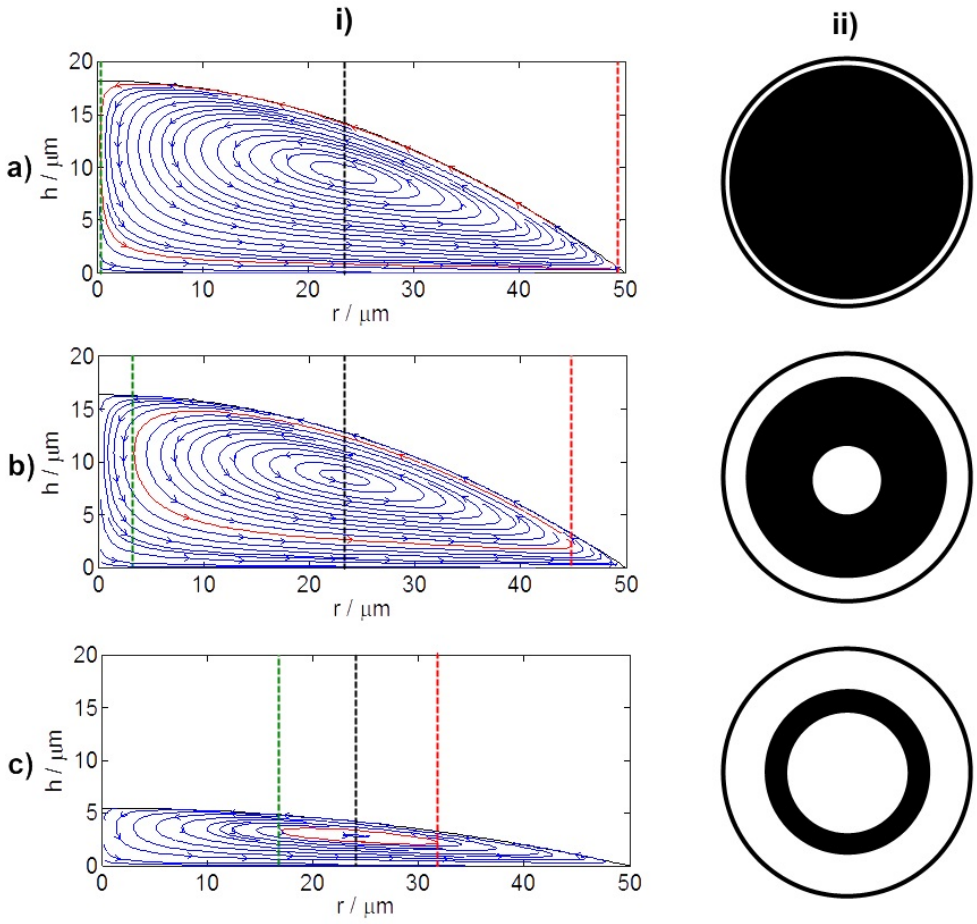

Figure 4.43. i) Streamlines for thermal Marangoni flow cells in an evaporating droplet with a 40° initial contact angle after time a) $0\,t_{\mathrm{dry}}$, b) $0.1\,t_{\mathrm{dry}}$ and c) $0.7\,t_{\mathrm{dry}}$. The red streamline suggests the possible motion of a particle moving towards inner streamlines throughout drying. The vertical dashed lines indicate the position of the stationary point at the centre of the vortex (black), the edge of where the central hole would appear (green) and the edge of the depleted zone next to the contact line (red), if the red streamline represents the outermost streamline with particles still on it. ii) A top-down representation of what the collected group might look like with the particle group in black. Note that the droplet volume is changed to simulate evaporation, but this is not a time-dependent solution. Streamlines are solved for a snapshot in time.

Marangoni flows. A surface tension profile is imposed along the liquid-vapour interface, and the radial and vertical velocities are solved under a lubrication approximation. Figure 4.43i plots the streamlines for the surface tension profile given in Figure 4.44. The images in Figure 4.43ii show how the particle density might evolve if the particles migrated towards the centre of the vortex. Neglecting evaporation, varying the magnitude of the surface tension gradient does not change the shape of the imposed surface tension profile. Evaporation gives a slight change in the profile, but the position of the centre of the vortex is largely unaffected throughout drying (vertical black dashed line on Fig.

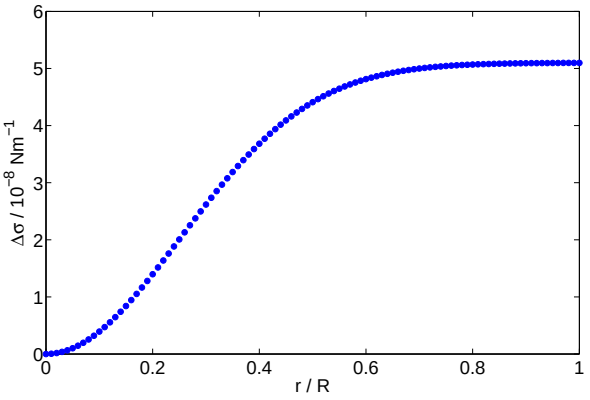

Figure 4.44. The surface tension profile across the liquid-vapour interface for a thermal Marangoni flow profile based on Hu and Larson's work [68], with Equation 4.16, where constant a=0.3, b=8 and c=-1.7×10^{-6} mN m^{-1}. The radial co-ordinate is normalised by the droplet radius R.

4.43). The surface tension profile is given in Figure 4.44 and is of the type

$$\Delta\sigma \;=\; \sigma(R) \;-\; \sigma(0) \;=\; c[a(r/R)^b + (1-a)(r/R)^2], \qquad (4.16)$$

where constant a=0.3, b=8 and c=-0.17×10^{-6} mN m^{-1}. Hu and Larson determined the form based on analytical expressions for fits to the surface temperature profile, calculated from a finite element analysis of the heat equation. The surface tension along the liquid-vapour interface was then determined from the temperature profile. Towards the late stages of drying, the centre of the vortex moves slightly towards the contact line, which hinders central collection. For a particle migrating across the fluid streamlines towards the centre of the vortex, the proposed motion is described by the red streamlines in Figure 4.43i, which indicate the outermost streamline upon which there are still particles. Particles would then be depleted from the outer streamlines, leaving a widening depleted zone close to the contact line, and a widening central hole. This behaviour is not consistent with the observations in Section 4.3.1: although particles migrating to the centre of the vortex would yield smaller values of R_t (see Fig. 4.40) and R_g, the central hole was observed to shrink during evaporation, rather than becoming enlarged. Such an observation can only occur for migration towards inner streamlines if the central coordinate of the vortex is moving towards the droplet centre throughout drying. Hence, the streamlines for the binary mixtures cannot be the same as for thermal Marangoni flow.

Indeed, the region of fastest Marangoni flow (observed in Sections 4.2.2 and 4.2.3) moved towards the droplet centre during drying.

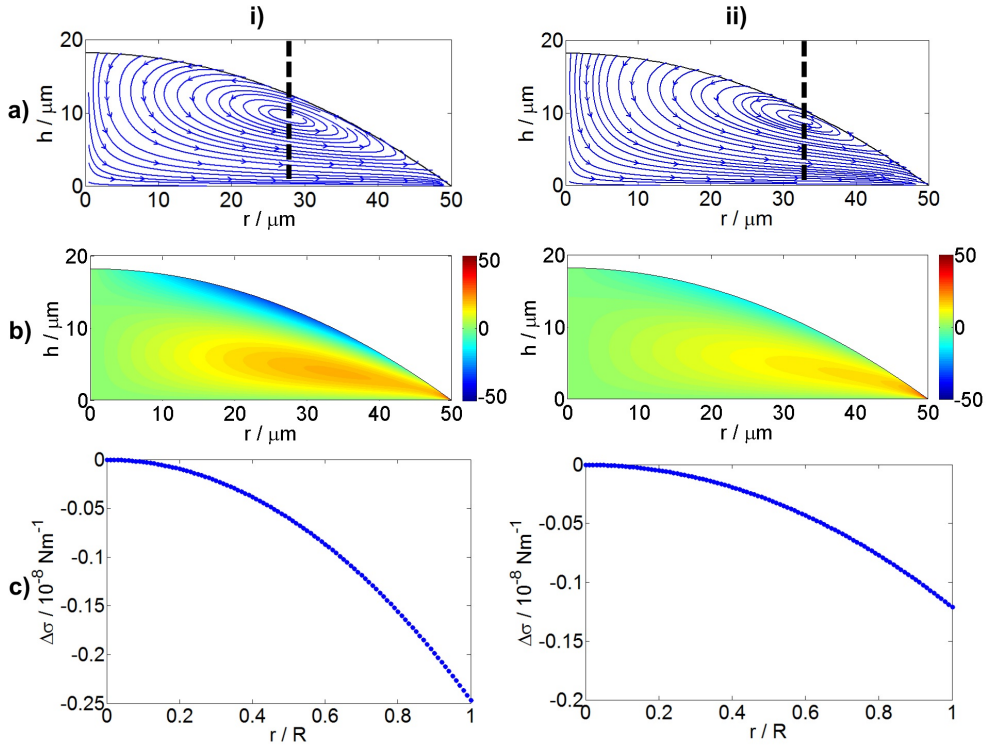

Figure 4.45. a) The flow streamlines and corresponding radial velocity map (with scale bar in μm s^{-1}) (b) based on the Gaussian surface tension profiles in (c) for a PM/water droplet at $RH \leq 0.5$. The radial co-ordinate is normalised by the droplet radius, R. The Gaussian profile is Equation 4.17, where $a = -3.4 \times 10^{-5}$ mN m^{-1}, and for ci) $b = -0.07$ and for cii) $b = -0.035$. Dashed vertical lines indicate the centre of the vortex (black). The surface tension profile is assumed to change from ci) to cii) throughout drying, changing the flows (although the droplet height is not decreased here).

Let us consider further the flow regimes discussed in Section 4.2, in particular for the PM/water droplets where no regions were completely depleted of particles (Figs. 4.29i and 4.29ii, Videos PM1 and PM2). For a Marangoni flow from apex to contact line, there was a circulating central group, and radial flow nearer to the contact line. As the radius of the collected group decreased, the circulating cells moved towards the droplet centre, and the region of radial flow extended. For the reverse Marangoni flow direction, there was a circulating eddy close to the contact line, and a quiescent region at the centre of the droplet. In this section, surface tension profiles across the liquid-vapour interface are investigated to qualitatively match the observed flows. The equations de-

veloped by Hu and Larson for thermal Marangoni flow are generalised so that any chosen surface tension profile can be input and the streamlines found for a snapshot in time (see Appendix C for the MATLAB routines). Suggestions are put forward for how the surface tension profile varies throughout drying. Note that this is not a time-dependent solution and hence the droplet volume is not changed.

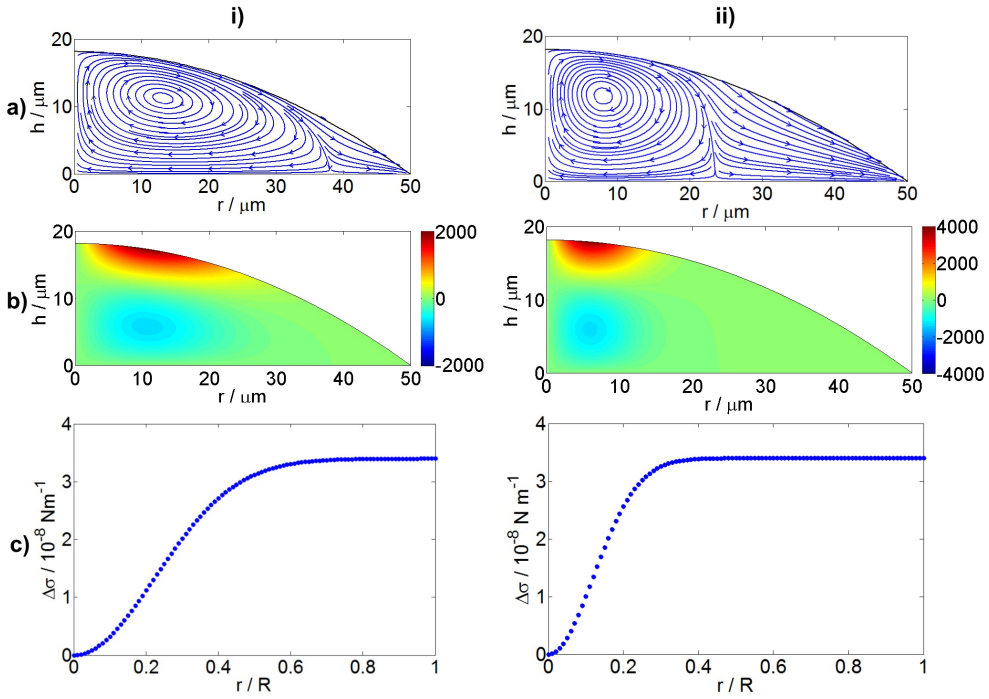

Figure 4.46. a) The flow streamlines and corresponding radial velocity map (with scale bar in $\mu m\,s^{-1}$) (b) based on the Gaussian surface tension profiles in (c) for a PM/water droplet at RH>0.5. The radial co-ordinate is normalised by the droplet radius, R. The Gaussian profile is Equation 4.17, where a=-3.4×10^{-5} mN m^{-1}, and for ci) b=10 and for cii) b=35. Dashed vertical lines indicate the centre of the vortex (black). The surface tension profile is assumed to change from ci) to cii) throughout drying, changing the flows (although the droplet height is not decreased here).

Some alternative flow profiles to the thermal Marangoni flow cell are proposed in Figures 4.45, 4.46 and 4.47. Figure 4.45, demonstrates a flow profile based on a Gaussian surface tension profile to qualitatively match the observations for PM/water at $RH\leq0.5$ (Video PM2). The Gaussian surface tension profile has the form

$$\Delta\sigma = \sigma(R) - \sigma(0) = a\left[exp(-b(r/R)^2) - 1\right], \qquad (4.17)$$

where $\Delta\sigma$ is the surface tension difference across the liquid-vapour interface, r

is the radial co-ordinate, R is the droplet radius, and the constants a and b are given in Figure 4.45. Radial flow develops at the centre of the droplet as drying progresses (from Fig. 4.45i to Fig. 4.45ii), with a circulating vortex near the contact line. The surface tension profile was chosen to qualitatively match the regions of circulating flow, but also to replicate the slower Marangoni flows observed at low RH (Section 4.2). The surface tension is highest at the centre of the droplet, where water is depleted less from the apex than the contact line. The surface tension gradient is assumed to decrease during drying, allowing convective flow to dominate at the centre of the droplet. As the droplet dries, the centre of the vortex/eddy remains towards the contact line. This reasonably describes the behaviour seen in PM/water droplets at $RH < 0.5$ (see Fig. 4.17b and Fig. 4.29i); a fast circulating eddy near the contact line, and slower motion of particles at the centre of the droplet.

Figure 4.46, shows a flow profile based on a Gaussian surface tension profile (with constants a and b given in Figure 4.46) for PM/water droplets at RH>0.5. This flow profile attempts to mimic the central circulating vortex, and radial flow near the contact line (Video PM1). The flattened surface tension profile near the contact line aims to mimic the circulating motion dying out from the contact line inward (with Fig. 4.46i representing early times and Fig. 4.46ii representing later times throughout drying). Depletion of the volatile component in this region could cause such behaviour. The centre of the vortex moves towards the centre of the droplet as drying progresses (from Fig. 4.46i to Fig. 4.46ii), which would allow the collection of particles on inner streamlines near r=0. Radial flow would then carry particles outside the circulating group (and any able to escape via Brownian motion) to the contact line.

An alternative flow profile is a dual-cell profile with a fast circulating outer vortex and slower circulating inner vortex. Figure 4.47c gives an example dual-cell profile based on a polynomial surface tension profile

$$\Delta\sigma = a(r/R)^3 + b(r/R)^2, \tag{4.18}$$

for which the constants a and b are given in Figure 4.47. The point on the

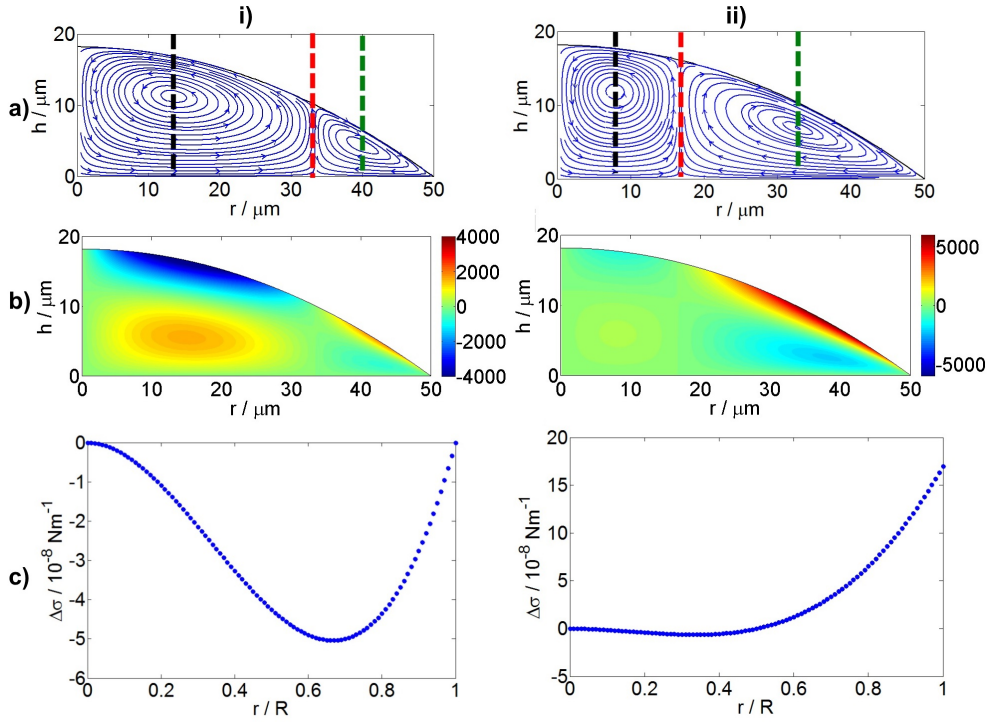

Figure 4.47. a) The flow streamlines and corresponding radial velocity map (with scale bar in $\mu m\,s^{-1}$) (b) based on the polynomial type surface tension profiles in (c). The polynomial profile equation is given in Equation 4.18 with constants a=$-0.34\times10^{-3}\,mN\,m^{-1}$ and for ci) b=$-0.34\times10^{-3}\,mN\,m^{-1}$ and for cii) b=$-0.15\times10^{-3}\,mN\,m^{-1}$. The radial co-ordinate is normalised by the droplet radius, R. Dashed vertical lines indicate the centre of the inner vortex (black) and outer vortex (green), and the stationary point between cells (red).

liquid-vapour interface where the Marangoni cells meet is the newest surface (for this Marangoni flow direction), and so the more volatile component is depleted the least in this region. For a volatile component with a low surface tension, this would give the lowest surface tension at the stationary point. Particle motion (both inward and outward) could then occur near the centre of the droplet. The centre of the inner vortex moves towards the droplet centre during drying (assuming the profile progresses from the form in Fig. 4.47i to that in Fig.4.47ii), but the outer vortex position also moves inward and the eddy enlarges (which is counter to the observations in Section 4.3.1).

4.3.2. Migration mechanisms

In this subsection, potential mechanisms for the migration of particles to the droplet centre will be discussed. The particle Reynolds number, Re_p, inside

these droplets is sufficiently small that inertial effects do not play a significant role in the collection of the particles or the shape of the circulating group. Take for example a 30%v ethanol/water droplet, which demonstrates the highest mean particle speeds;

$$Re_{\mathrm{p}} = \frac{\rho_{\mathrm{f}}\, v\, a}{\eta} \backsim \frac{966\,\mathrm{kg\,m^{-3}} \times 2800\,\mu\mathrm{m\,s^{-1}} \times 0.5\,\mu\mathrm{m}}{2 \times 10^{-3}\,\mathrm{Pa\,s}} \backsim 6 \times 10^{-4}, \qquad (4.19)$$

where ρ_{f} and η are the fluid density and viscosity, a is the particle radius and v is the particle speed. Additionally, inertial effects would cause particles to migrate away from the centre of the vortex towards the liquid-vapour interface, not inwards as is observed here. Therefore, alternative mechanisms for the migration are considered, including chemophoresis, thermophoresis (the Soret effect), and shear-induced migration.

Chemophoresis

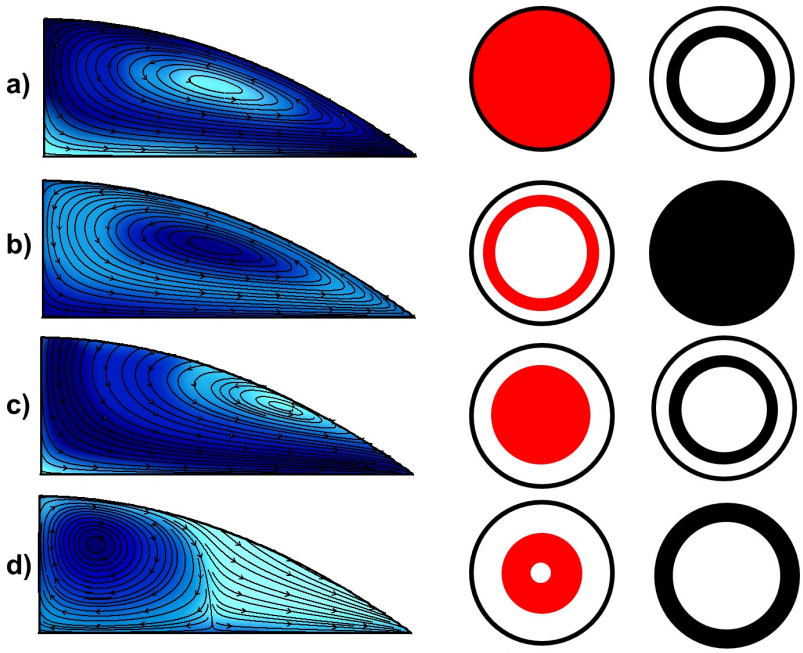

Figure 4.48. Cartoon of the compositional variation within flow profiles based on a) and b) thermal Marangoni flow and on c) and d) Gaussian surface tension profiles. The more volatile component is depleted at the liquid-vapour interface and richer at the centre of the vortices and near the substrate due to the no-slip boundary condition. Using PM as an example, dark blue indicates PM rich regions. For a) and c) the water is the more volatile component and for b) and d) the water is the least volatile component. Corresponding examples of what the collected group might look like are indicated in red for migration to PM-rich regions, and in black for migration to water-rich regions.

First, chemophoresis is discussed. For migration to be solely chemophoretic, particle motion would be towards a preferred solvent. Figure 4.48 shows a cartoon of the Marangoni flow within a droplet and the compositional variation throughout the cells. The more volatile component is depleted from the liquid-vapour interface. On the outer streamlines of a cell, the depleted solvent is carried towards the centre of the droplet, and the bulk material is carried to the liquid-vapour interface (where it is depleted). In contrast, an inner streamline remains relatively rich in the more volatile component, as does the no-slip region near the substrate. Diffusion of the component across the fluid streamlines tends to reduce the composition gradient.

In principle, a switch in the volatility of component solvents should switch the direction of the migration if chemophoresis is the driving mechanism. To test this theory, 50%v PM/water droplets were observed, one evaporating at a RH above 0.5 and the other at an RH below 0.5. The initial composition of the two droplets is identical, but the relative volatility of the components is reversed. By swapping the relative volatility of the components, the component in the majority at the contact line is different for each droplet (hence the change in the Marangoni flow direction).

Table 4.8. Solubility parameters, δ, for PEGMA, polystyrene, water, PM and ethanol.

Solvent or Polymer	δ / $(\mathrm{J\,cm^{-3}})^{\frac{1}{2}}$
PEG ($2000\,\mathrm{g\,mol^{-1}}$)	17.6 [206]
Polystyrene	9.1 [207]
Water	48.0 [208]
PM	30.7 [208]
Ethanol	26.2 [208]

The polystyrene spheres are sterically stabilised with PEGMA, and aggregate at high PM concentrations, suggesting the preferred solvent is water. However, solubility parameters (Table 4.8) suggest that the PEGMA (and also polystyrene) would prefer PM over water (due to the smaller difference in solubility parameters). Therefore, the solvent preference is unclear and both scenarios will be considered here.

Flow profiles that qualitatively match the observed flows in Section 4.2 are compared with the thermal Marangoni profile in Figure 4.48. The regions predicted to be PM rich are shown for each Marangoni flow direction. If a thermal Marangoni flow profile is considered, then by changing the relative volatility of components, the PM-rich region is swapped from the centre of the vortex to the outer streamlines (Fig. 4.48a and c). Hence, in this flow regime, chemophoresis towards a preferred solvent would result in a switch in the migration direction depending on which solvent evaporates fastest. For the flow regimes suggested in Section 4.3.1 based on Gaussian surface tension profiles, the PM rich region would be at the centre of the droplet when water evaporates fastest (Fig. 4.48b), and at the centre of the vortex when water evaporates slowest (Fig. 4.48d). In both cases, particle migration towards a water-rich region would be across streamlines towards the contact line, whereas if PM is the preferred solvent, migration would be towards the centre of the droplet. If migration is towards PM-rich regions, when water evaporates slowest (Fig. 4.48bii), migration away from the streamlines at the very centre would leave the hole seen in this regime. In Section 4.3.1, particle collection was reported at the centre of PM/water droplets for both $RH < 0.5$ and $RH > 0.5$, independent of the Marangoni flow direction. This is consistent with migration towards PM-rich regions.

It is also worth noting that compositional gradients are still present when the Marangoni flows cease. In Section 4.3.1, Marangoni flows stopped despite ethanol remaining in the droplet (<50%v lost for a 50%v ethanol/water droplet). For a chemophoretic mechanism, the migration is expected to continue until the more volatile component is fully depleted. However, the minimum radius of the collected group occurred when Marangoni flow stopped (and ethanol still remained inside the droplet). Diffusion times for ethanol in a 50%v ethanol/water droplet were estimated in Section 4.3.1 over the height of the droplet as 0.1 s, and over the radius of the droplet as 4.9 s (where h=10μm and R=70μm). Hence, radial diffusion is slower than the drying time of the droplet, and so chemophoresis is expected to persist. As only radial migration is observed by the imaging techniques used here, it is possible that chemophoresis becomes indistinguishable from convection to the contact line after t_{Rg}

(i.e. chemophoresis only slows the convective velocity). Otherwise, the growth of the collected group following the cessation of Marangoni flow could indicate that chemophoresis is not the sole driving mechanism for the migration, though it could be a major contributing factor.

The particle size dependence may reveal clues to the migration mechanism. The force attributed to a gradient in the surface tension (F_σ) across a particle of radius a is given by

$$F_\sigma = -\frac{dE}{dr} = 4\pi a^2 \frac{d\sigma_{\mathrm{sl}}}{dr}, \tag{4.20}$$

where r is the position inside the droplet, σ_{sl} is the solid-liquid surface tension, and E is the surface energy. The drag force (F_{d}) on a particle in Stokes flow is

$$F_{\mathrm{d}} = 6\pi\eta a v, \tag{4.21}$$

where η is the viscosity of the fluid, and v is the particle velocity. By equating equations 4.20 and 4.21, the migration velocity for a chemophoretic driving force, v_{g}, can be estimated as

$$v_{\mathrm{g}} = \frac{2}{3}\frac{a}{\eta}\frac{d\sigma_{\mathrm{sl}}}{dr}. \tag{4.22}$$

For a chemophoretic mechanism, the migration velocity of the collecting group should be proportional to the particle size (for particles inside the same droplet). Migration velocities for ethanol/water droplets (10−50%v ethanol) are of the order 10^2 $\mu\mathrm{ms}^{-1}$. For 1 μm particles, the surface tension difference needed across the particle diameter to reach a comparable migration velocity is $\Delta\sigma_{\mathrm{sl}} \backsim 10^{-6}$ $m\mathrm{N\,m}^{-1}$.

It is plausible that the difference in the solid-liquid surface tensions of PM and water is of the order $10^{-2}\,\mathrm{N\,m}^{-1}$, based on the difference in their liquid-vapour surface tensions. It is also plausible that the difference in the composition of the fluid near the substrate and near the liquid-vapour interface of the droplet could vary by a mole fraction of 0.1 (corresponding to a 10% variation). This would lead to a difference in σ_{sl} of $\backsim 10^{-3}\,\mathrm{N\,m}^{-1}$ between PM-rich and PM-poor regions in the droplet. Over a distance of the order

of 10μm (for the droplet height), this corresponds to $\mathrm{d}\sigma_{\mathrm{sl}}/\mathrm{d}r \backsim 10^{-4}\,\mathrm{N\,m^{-1}}$. For particles with diameters of $1\,\mu$m, in 50%v PM/water ($\eta \backsim 3.9\,\mathrm{mPa\,s}$), this relates to a migration velocity of $v_{\mathrm{g}} \backsim 8{\times}10^{3}\,\mu\mathrm{m\,s^{-1}}$. Though this estimate is larger than the observed migration velocities it demonstrates that chemophoresis could be a contending mechanism even with much lower composition gradients or solid-liquid interfacial tensions.

Thermophoresis

Thermophoresis is an alternative mechanism for migration. Evaporative cooling reduces the temperature of fluid at the liquid-vapour interface compared to fluid at the centre of the droplet. Such a temperature gradient could induce migration of solvent and particles within the droplet. Note that the migration direction for thermal diffusion in aqueous mixtures depends on the solvent composition. There is a change in the migration direction in ethanol/water mixtures at a mole fraction of 0.14 ethanol ($\backsim$ 35%v ethanol) [188]: For high water content, thermal diffusion of water and thermophoresis of the particles is towards the cooler regions [189].

The thermal conductivity of the substrate has a significant effect on evaporative cooling in ethanol and water droplets [114]. To establish whether evaporative cooling caused significant temperature gradients that could result in particle migration, droplets of 50%v ethanol/water were deposited onto glass and sapphire substrates. The glass has a lower thermal conductivity (1 $\mathrm{Wm^{-1}K^{-1}}$) than the sapphire (35 $\mathrm{Wm^{-1}K^{-1}}$). In Chapter 3, evaporation of pure solvents (ethanol and water) on sapphire did not show significant evaporative cooling. In addition, the evaporation of water droplets on glass matched an isothermal model.

Predictions of the evaporative cooling possible in ethanol droplets evaporating on each substrate can be estimated from the total heat lost during evaporation. For an ethanol droplet with a pre-impact radius of $r_0 = 25\ \mu$m, the droplet mass, M is

$$M = \frac{4}{3}\pi\rho_e r_0^3 = 5.1 \times 10^{-11}\,\mathrm{kg}, \tag{4.23}$$

where ρ_e is the density of ethanol. The heat lost (Q) on evaporating a mass, M, of ethanol is

$$Q = M\Delta H_\nu = 5.1 \times 10^{-11}\,\mathrm{kg} \times 846 \times 10^3\,\mathrm{J\,kg^{-1}} = 4.3 \times 10^{-5}\,\mathrm{J}, \qquad (4.24)$$

where ΔH_ν is the latent heat of ethanol. Thermal diffusion away from a point on the liquid-solid interface can transfer heat across a maximum distance equal to the diffusion length in any direction. Heat can therefore flow from a half-hemisphere in the solid substrate to the liquid, with a radius equivalent to the diffusion length, d (see Fig. 4.49). The diffusion lengths in glass (d_g) and sapphire (d_s) are given by

$$d_\mathrm{g} = 2\sqrt{D_{\mathrm{th,\,g}}\,t_\mathrm{dry}} = 2\sqrt{3.4 \times 10^{-7}\,\mathrm{m^2\,s^{-1}} \times 0.3\,\mathrm{s}} = 6.4 \times 10^{-4}\,\mathrm{m} \qquad (4.25)$$

and

$$d_\mathrm{s} = 2\sqrt{D_{\mathrm{th,\,s}}\,t_\mathrm{dry}} = 2\sqrt{1.04 \times 10^{-5}\,\mathrm{m^2\,s^{-1}} \times 0.3\,\mathrm{s}} = 3.5 \times 10^{-3}\,\mathrm{m} \qquad (4.26)$$

where $D_{\mathrm{th,\,g}}$ and $D_{\mathrm{th,\,s}}$ are the thermal diffusivities of glass and sapphire respectively and t_dry is the drying time of the droplet. The corresponding volumes of hemispheres with radii equal to the diffusion length represent diffusion volumes of $V_\mathrm{g} = 5.5{\times}10^{-10}\,\mathrm{m^3}$ for glass and $V_\mathrm{s} = 9.2{\times}10^{-8}\,\mathrm{m^3}$ for sapphire. The temperature reduction due to a heat loss of Q can be estimated as

$$\Delta T_\mathrm{g} = \frac{Q}{\rho_\mathrm{g}\,V_\mathrm{g}\,c_{\mathrm{p,\,g}}} = \frac{4.3 \times 10^{-5}\,\mathrm{J}}{2500\,\mathrm{kg\,m^{-3}} \times 5.5 \times 10^{-10}\,\mathrm{m^3} \times 840\,\mathrm{J\,kg^{-1}\,K^{-1}}} \backsim 0.04\,\mathrm{K} \qquad (4.27)$$

for glass, and

$$\Delta T_\mathrm{s} = \frac{Q}{\rho_\mathrm{s}\,V_\mathrm{s}\,c_{\mathrm{p,\,s}}} = \frac{4.3 \times 10^{-5}\,\mathrm{J}}{3980\,\mathrm{kg\,m^{-3}} \times 9.2 \times 10^{-8}\,\mathrm{m^3} \times 783\,\mathrm{J\,kg^{-1}\,K^{-1}}} \backsim 0.0001\,\mathrm{K} \qquad (4.28)$$

for sapphire, where $c_\mathrm{p,g}$ and $c_\mathrm{p,s}$ are the specific heat capacities of glass and sapphire, and ρ_g and ρ_s are the densities of glass and sapphire. There are two orders of magnitude difference in the thermal gradients between the two substrates. Therefore, a reduction in particle migration (or no migration at all), was expected on sapphire for a thermophoretic mechanism. However,

Figure 4.50 indicates that particle collection reached a minimum radius of a third of the droplet radius at t_{Rg}, despite de-pinning on the sapphire.

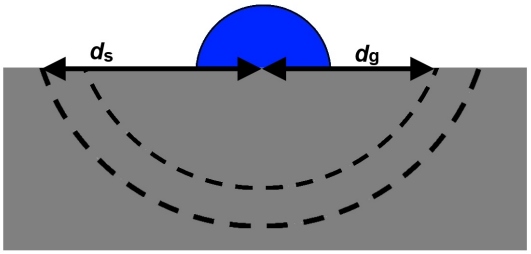

Figure 4.49. Cartoon of the diffusion of heat for a sapphire and a glass substrate. Heat can transfer to a maximum distance equal to the diffusion length, d. The diffusion length in sapphire, d_s, is longer than in glass, d_g.

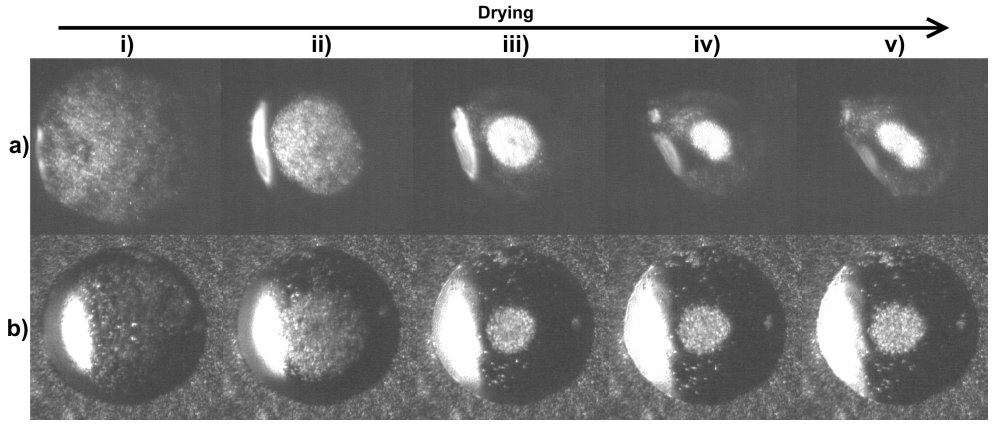

Figure 4.50. Dark field images for a 50%v ethanol/water droplet on a) a sapphire substrate and b) a fluorinated glass substrate after i) $0.1\,t_{\mathrm{dry}}$, ii) $0.2\,t_{\mathrm{dry}}$, iii) $0.3\,t_{\mathrm{dry}}$, iv) $0.4\,t_{\mathrm{dry}}$ and v) $0.5\,t_{\mathrm{dry}}$. The contact line de-pins during drying on sapphire. Scale bars are $50\,\mu$m. Values for t_{dry} are 3.19 s on sapphire and 4.85 s on glass.

Furthermore, the collection within a droplet of 50%v PM/water evaporating at a RH<0.5 was explored. The water droplets described in Section 4.2 displayed only radial flow during drying on glass substrates, demonstrating that thermal effects due to evaporative cooling were not present (Fig. 4.3). At RH values $\lesssim$0.5, water evaporates faster than PM (smaller volume of diffusion for PM in t_{dry} compared to water). Combined with a lower latent heat of vaporisation than water, no significant thermal effects are expected for a 50%v PM/water droplet evaporating on glass due to evaporative cooling. However, particle collection still occurred within these mixtures (Fig. 4.29a). Thermophoresis can therefore be ruled out as the migration mechanism.

Shear-induced migration

Last, I look at shear-induced migration, for which a gradient in the shear rate is required. Potential causes for shear-induced migration include the variation in shear rate across a particle resulting in a greater number of collisions on one side of the particle relative to the other [196], or lift on the spheres due to rotation [192] (see Fig. 4.51). Migration for both these mechanisms is from regions of high shear to regions of low shear.

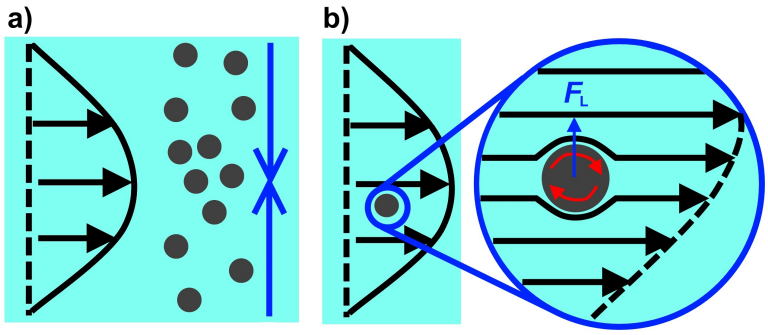

Figure 4.51. Cartoon of shear-induced migration mechanisms in parabolic flow. a) An asymmetric collision distribution driving particles to low shear rates, and ii) lift on the sphere. The velocity gradient causes rotation of the sphere with the lift force, F_L, acting towards higher velocity (and lower shear rate). There must be a gradient in the shear rate for migration.

The observations for particle migration in ethanol/water mixtures (Section 4.3.1) revealed a zone near the contact line that was depleted of particles. For the collision distribution to result in migration towards the centre of the droplet, there must be more collisions near the contact line that at the centre of the droplet. Due to the depleted zone, this cannot be the case. Additionally, even very dilute particle concentrations resulted in collection at the centre of the droplets. Hence, for a shear-induced migration to be occurring in these droplets, lift must be the driving mechanism.

The observed particle speeds along streamlines in droplets of 50%v ethanol/water (at a RH of 0.26) were approximately 2.5 mm s^{-1}. The corresponding shear rate, $\dot{\gamma}$, for a droplet height of $\sim$ 30 μm, is $\dot{\gamma} \sim u/H \sim 80$ s^{-1}. Shear induced migration in a capillary at lower Reynolds number (10^{-6}) has previously been observed by Brown *et al.* [196] at lower shear rates (below 10 s^{-1}) using nuclear magnetic resonance imaging to track the particle density.

There is also a size-dependence to the particle collection (Fig. 4.38), with

larger particles migrating to the droplet centre faster than small particles. This size-dependence is consistent with previous observations for shear-induced migration by Semwogerere and Weeks [183] for pressure-driven flows in rectangular capillaries. In their case, the driving mechanism for the migration was related to particle collisions. For shear induced migration in parabolic flow due to lift on the particles, the group velocity, v_g, should also depend on the particle size (proportional to the particle radius to the power of four [209]). Faster migration across fluid streamlines is expected for larger spheres, but the speed of spheres of any size should be the same along a particular streamline. Therefore, if the migration mechanism is shear-induced, larger spheres would be expected to enter tighter cycles faster (smaller R_t) with a smaller group radius, R_g, which is true to the observations in Section 4.3.1.

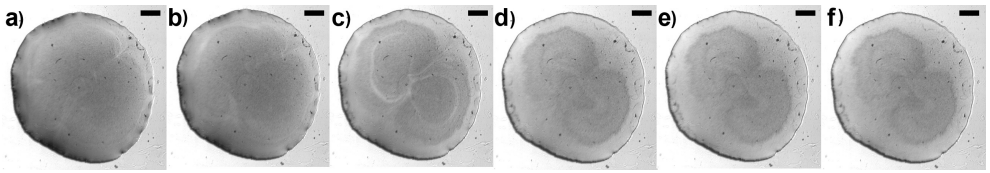

Figure 4.52. Bright field images of a millimeter-scale 50%v ethanol/water droplet containing 0.1%v 200 nm polystyrene spheres. a) $0.1\,t_{\mathrm{Rg}}$, b) $0.2\,t_{\mathrm{Rg}}$, c) $0.4\,t_{\mathrm{Rg}}$, d) $0.6\,t_{\mathrm{Rg}}$, e) $0.8\,t_{\mathrm{Rg}}$, f) $1.0\,t_{\mathrm{Rg}}$. Scale bars are $500\,\mu$m.

The size of the droplet is important for determining the extent of collection as well as the particle size. Figure 4.52 shows a microlitre-scale droplet of 50%v ethanol/water. Particle collection is less significant than in the picolitre droplet of the same initial composition, though the circulatory motion was similar. Microlitre droplets have lower shear rates which could explain the more significant migration in picolitre droplets compared to microlitre droplets. Also particles have further to migrate ($10\times$ further for a droplet of radius 1 mm compared to a radius of 100μm).

Figure 4.53 indicates the regions of low shear rate within a droplet exhibiting thermal Marangoni flow cells. Conditions for the model were chosen to give Marangoni flow speeds of the order of $10^3\,\mu\mathrm{ms}^{-1}$ (as observed for ethanol/water droplets in Section 4.2). The shear rate is lowest in the central region (r=0) and in a strip near 1/3 of the height along the droplet profile. As discussed in Section 4.3.2, the centre of the vortex does not shift significantly in r throughout drying. Hence, the region of low shear rate does not change

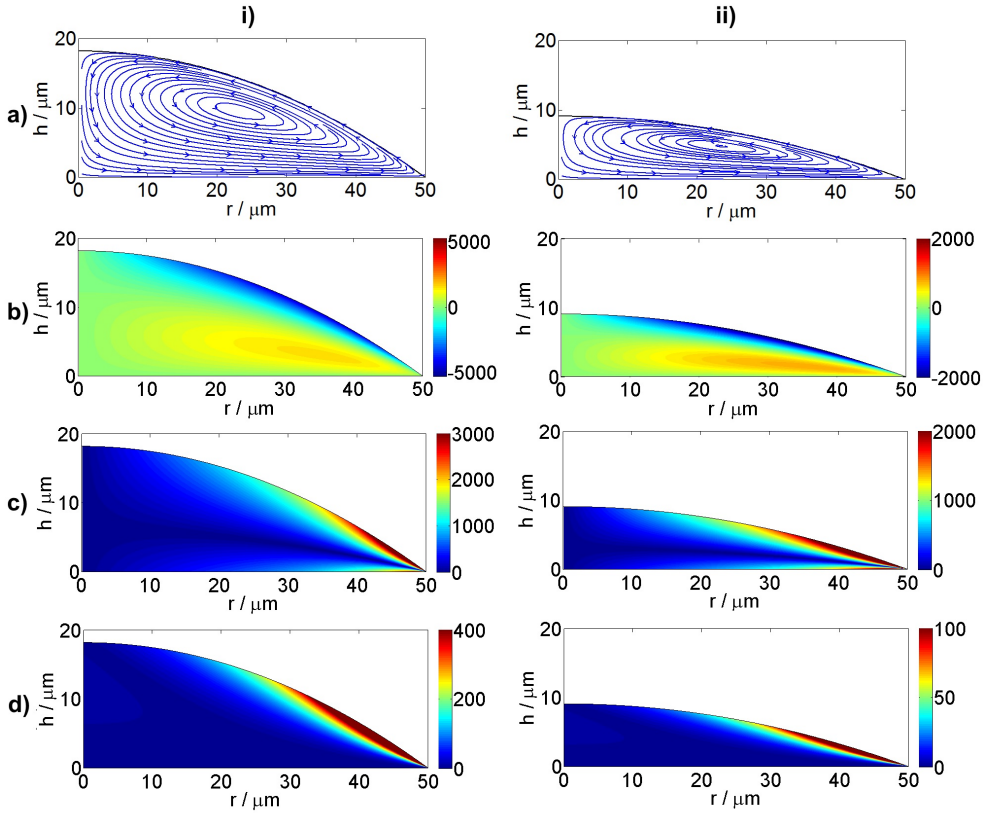

Figure 4.53. a) The streamlines, b) radial velocity map (with scale bar in μms^{-1}), c) modulus of the shear rate $\mathrm{d}u_r/\mathrm{d}z$ and d) modulus of the shear rate $\mathrm{d}u_z/\mathrm{d}r$, inside a thermal Marangoni flow cell. Scale bars for shear rates are in s^{-1}. Evaporation progresses from i) at $0\,t_{\mathrm{dry}}$ to ii) at $0.5\,t_{\mathrm{dry}}$. The initial contact angle is 40°. Conditions were chosen to match observed Marangoni flow speeds of the order 10^3 μms^{-1}.

throughout drying. Particles travelling on an outer streamline would migrate inwards when entering the high shear region near the liquid-vapour interface and substrate (Fig. 4.53c). However, particle migration towards inner streamlines in this thermal model cannot give the particle collection observed (Fig. 4.42). It is worth noting that $|\mathrm{d}u_{\mathrm{r}}/\mathrm{d}z|>|\mathrm{d}u_{\mathrm{z}}/\mathrm{d}r|$ at all times (except near r=0). Hence, the lubrication approximation is valid, especially at late times.

For the flow profiles suggested in Section 4.3.2 (Figs. 4.45 and 4.46), the corresponding shear rate maps are given in Figures 4.54 and 4.55. There is a region of low shear (in $\mathrm{d}u_r/\mathrm{d}z$) at the centre of the droplet for both flow regimes (radial flow at the centre or the periphery). For the central circulating cell (Fig. 4.55), there is also a region of low shear near the contact line. Note that there is a region of high shear at r=0 for $\mathrm{d}u_z/\mathrm{d}r$ in profiles with the central circulating cell. This could be responsible for the hole seen in the collecting

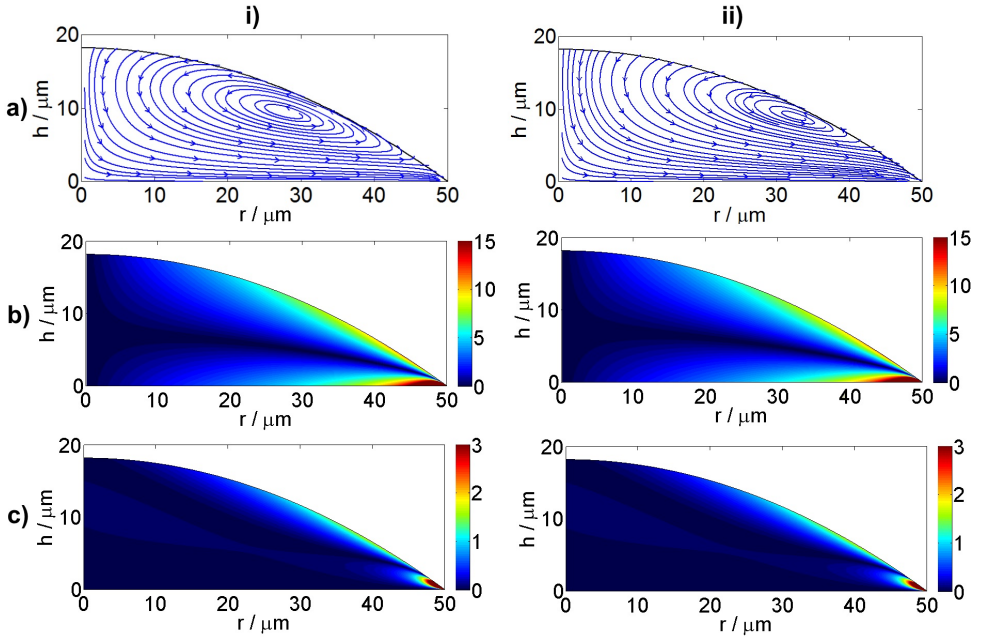

Figure 4.54. a) The streamlines, b) modulus of the shear rate $\mathrm{d}u_r/\mathrm{d}z$ and c) modulus of the shear rate $\mathrm{d}u_z/\mathrm{d}r$, inside a flow cell based on a Gaussian surface tension profile (described in Fig. 4.45). Scale bars for shear rates are in s^{-1}. The surface tension profile is adjusted such that drying is assumed to progress from i) to ii), though the height here has not been changed.

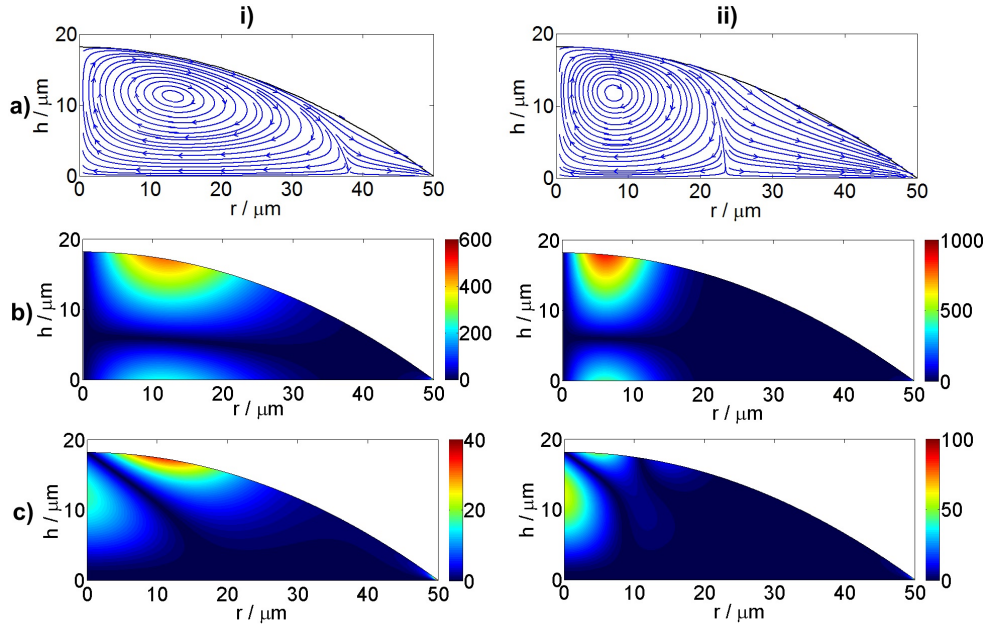

Figure 4.55. a) The streamlines, b) modulus of the shear rate $\mathrm{d}u_r/\mathrm{d}z$ and c) modulus of the shear rate $\mathrm{d}u_z/\mathrm{d}r$, inside a flow cell based on a Gaussian surface tension profile (described in Fig. 4.46). Scale bars for shear rates are in s^{-1}. The surface tension profile is adjusted such that drying is assumed to progress from i) to ii), though the height here has not been changed.

group (with Marangoni direction from apex to contact line), forming a toroidal group in 3D. Particles on outer-streamlines in the vortex would travel along the substrate and experience the shear gradient near r=0.1R, and migrate to inner streamlines. On traveling towards the liquid-vapour interface, those particles would then experience the shear gradient in $\mathrm{d}u_\mathrm{z}/\mathrm{d}r$ and be forced to inner streamlines, then by the gradient in $\mathrm{d}u_\mathrm{r}/\mathrm{d}z$ at the liquid-vapour interface.

4.4. Particle deposition from solvent mixtures

Particles have been observed to collect at the centre of droplets of binary mixtures with a collection radius determined by the solvents and their relative evaporation rates (Section 4.3). The duration of the Marangoni flow period (during which particles collect at the centre), compared to the period of radial flow (during which particles move to the contact line) will also determine the time interval in which particles move outwards from the collected group and build up a ring stain. SEM images of deposits from pure solvents are now compared with deposits from binary mixtures (with Marangoni flow). The influence of the Marangoni strength (stronger implies a higher flow velocity), duration and direction on the deposit are investigated. Ethanol/water and PM/water mixtures are contrasted with ethylene glycol (EG)/water mixtures, which do not show Marangoni flow (Fig. 4.23e) or particle collection.

Pure solvents have not showed evidence of Marangoni flows (Section 4.2.1). The SEM images corresponding to deposits from water (Fig. 4.56a) and ethanol droplets (Fig. 4.56g) demonstrate a ring stain at the contact line consistent with the "coffee ring effect".

The motion of particles in binary solvent mixtures differed from the pure solvent case (Section 4.2.2 and 4.3). From the particle collection in Section 4.3.1, ethanol/water droplets with 10−50%v ethanol showed strong depletion of particles near the contact line, and a similar minimum radius of the centrally collecting group. As a fraction of the drying time, the duration of the Marangoni flow period was longest for the 50%v ethanol/water droplet. Hence, the particles remained collected at the droplet centre for longer in the 50%v ethanol/water droplet. For the 70%v ethanol/water droplet, the particles re-

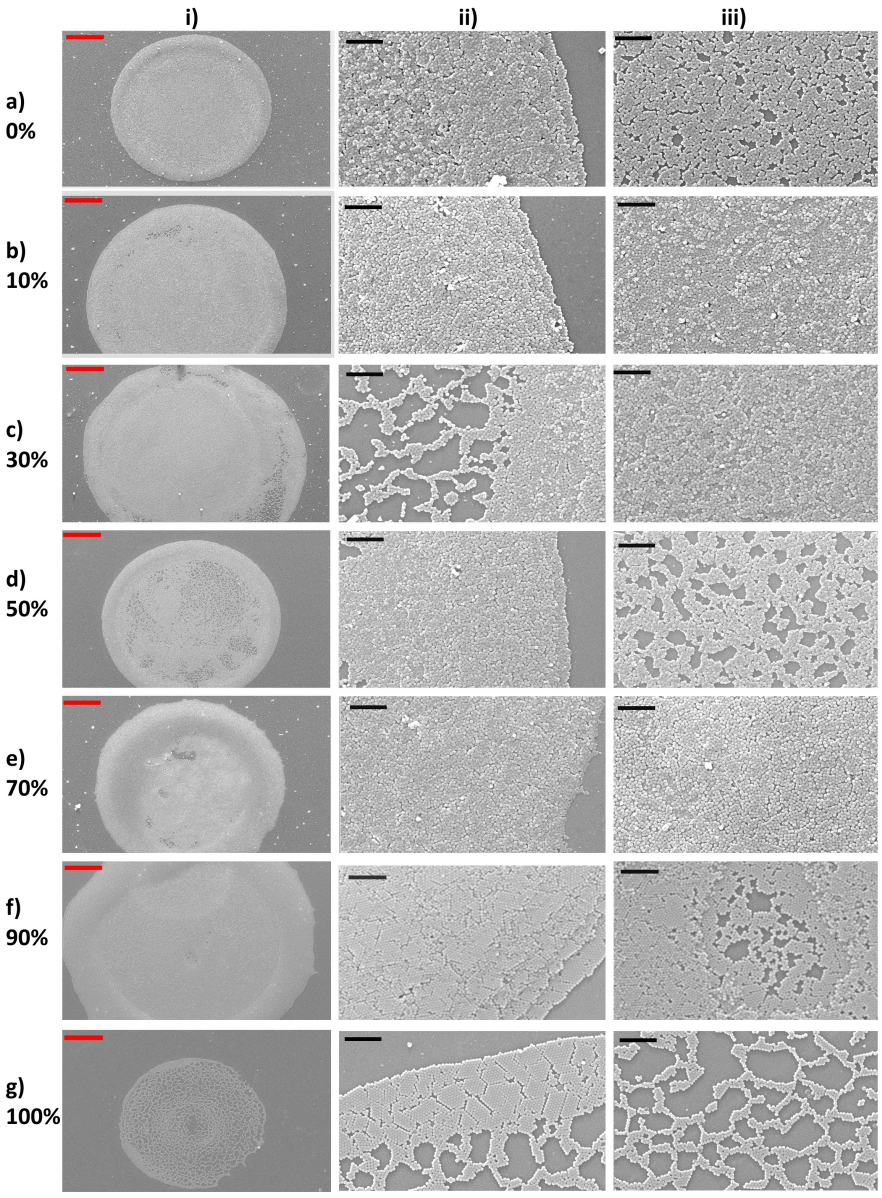

Figure 4.56. SEM images of i) the whole deposit, ii) zoom to the contact line, and iii) zoom to the interior, for deposits from droplets of ethanol/water with an initial ethanol concentration of a) 0%v, b) 10%v, c) 30%v, d) 50%v, e) 70%v, f) 90%v and 100%v. The 200 nm polystyrene spheres were loaded at a concentration of 1%v. Deposition was onto as-received glass substrates. Scale bars are 50 μm for the whole deposit (red) and 10 μm for the zooms (black). Note that droplet volumes differ e.g. the 100%v ethanol droplet was smallest in volume.

mained collected for a longer fraction of the drying time, but the group radius was wider. When Marangoni flow ceased, radial flow carried particles towards the contact line, building up material at the periphery of the droplet.

SEM images for deposits from ethanol/water mixtures are shown in Figure 4.56. The ring widths for an average of twenty deposits at each ethanol concentration are given in Figure 4.57. Ring widths were determined as described in

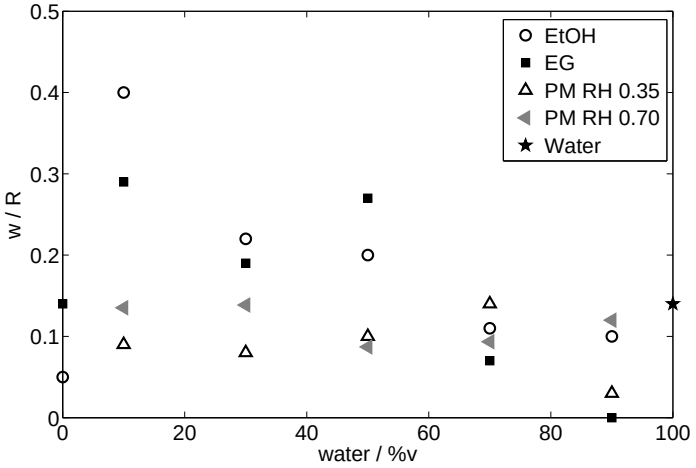

Figure 4.57. Ring widths, w, normalised by the deposit radius, R for various compositions of each binary mixture. Each data point corresponds to an average for at least 20 deposits.

Chapter 2, Section 2.6. Compared to the ring widths for pure water, the rings of the deposits from 10%v and 30%v ethanol/water droplets were narrower, indicating that Marangoni flows and migration of the particles successfully decreased the ring stain. Indeed, the interior of the deposits from 10%v and 30%v ethanol/water droplets contained at least a single layer coverage of particles. Due to the strong depletion of particles near the contact line (during drying) in 10−50%v ethanol/water droplets, the ring can only be built up following radial flow of the collected group. Hence, the region inward of the ring in the 30%v ethanol/water drop deposit likely results from de-pinning of the contact line at the end of drying.

The ring widths of the 50−90%v ethanol drop deposits increase with higher ethanol content, and are all wider than the water droplet deposit. This can perhaps be explained by the reduced contact angle in these droplets reducing stacking at the contact line, expanding the ring inwards but not as far upwards (see Fig. 4.58). Radial flow is also enhanced at lower contact angles. Hence, duration is not the most important factor over geometry, otherwise the 10%v ethanol/water droplet would have the widest ring. Due to the de-pinning contact line, the 100%v ethanol droplet has a thinner ring than any other ethanol concentration and a loose "lacy" structure at the interior. The "lacy" structure was formed right at the end of drying due to capillary forces between the particles.

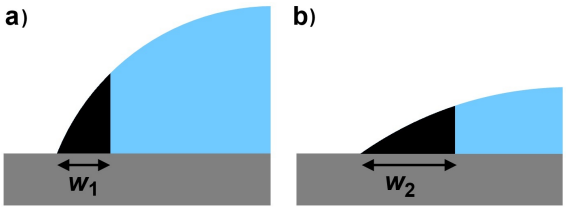

Figure 4.58. Cartoon of particle stacking in the ring stain. For low contact angles the ring stain is wider but less high i.e. $w_1 < w_2$ where w_1 and w_2 are the ring width for the higher and lower contact angle droplets respectively.

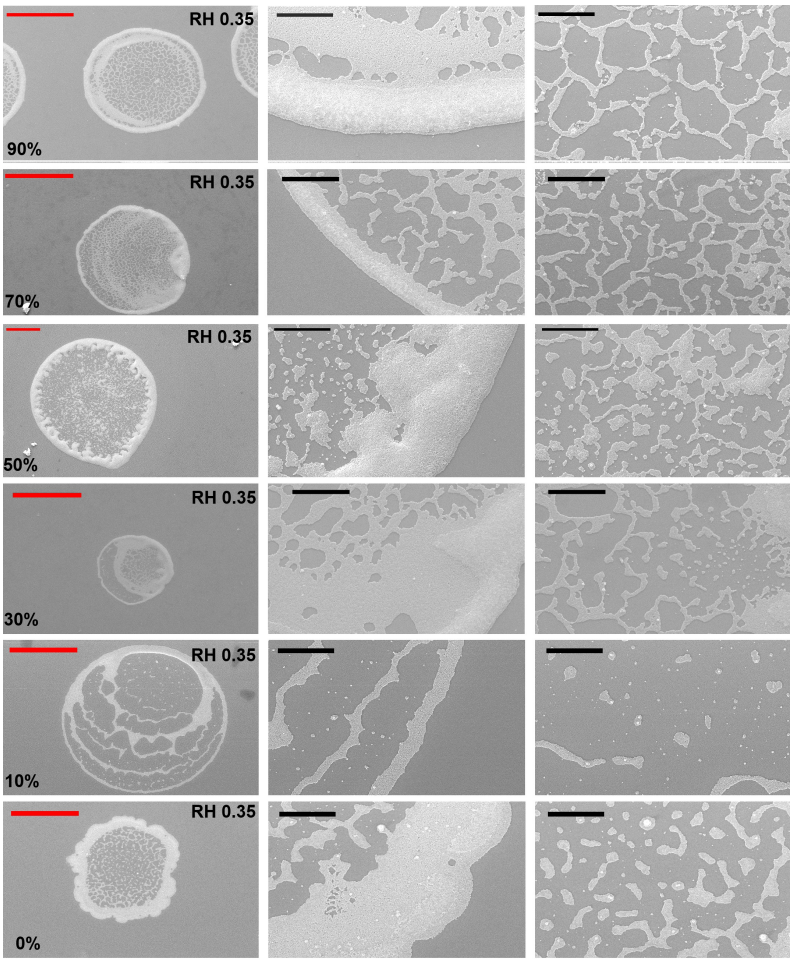

Figure 4.59. SEM images of (left to right) the whole deposit, a zoom to the contact line and a zoom to the interior for deposits from droplets of PM/water at a RH of 0.35, with an initial PM concentration of 0%v–90%v. The 200 nm polystyrene spheres were loaded at a concentration of 1 %v. Deposition was onto glass (as-received). Scale bars are 50 μm for the whole deposit (red) and 10 μm for the zooms (black).

For PM/water droplets the interesting question is whether the different directions of the Marangoni flow (at $RH > 0.5$ and $RH \leq 0.5$) affects the nature of the deposit. For PM/water at a RH of 0.35 (Fig. 4.59), multiple ring stains were left for the 10%v and 30%v PM due to stick-slip behaviour of the receding

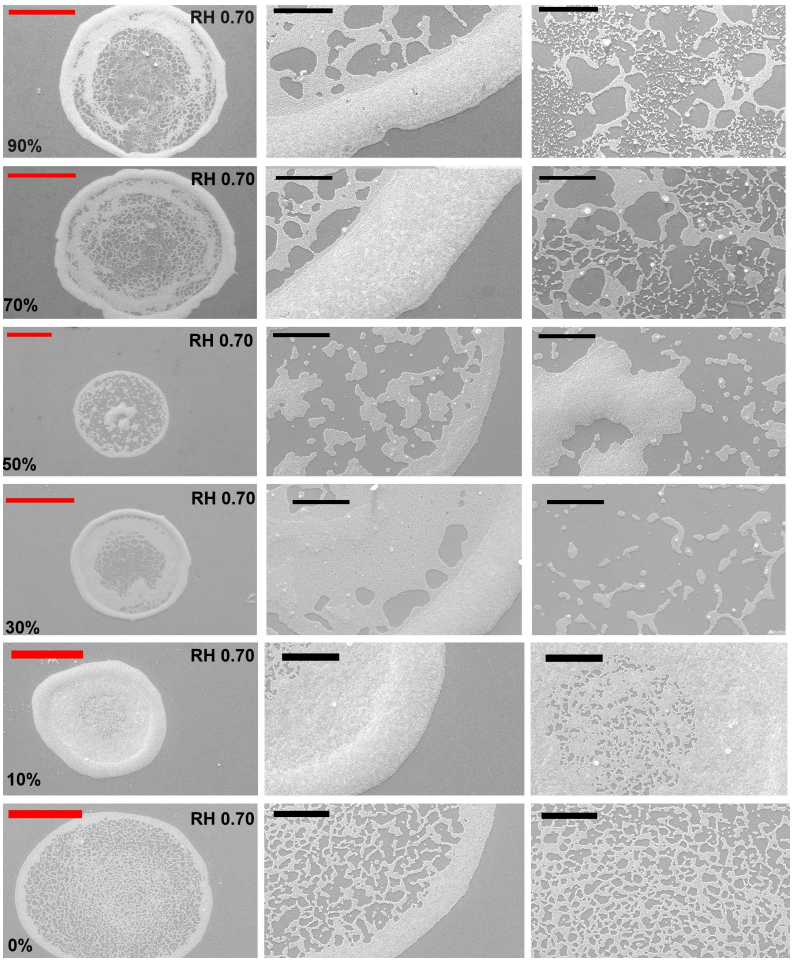

Figure 4.60. SEM images of (left to right) the whole deposit, a zoom to the contact line, and a zoom to the interior, for deposits from droplets of PM/water at a *RH* of 0.70 with an initial PM concentration of 0%v–90%v. The 200 nm polystyrene spheres were loaded at a concentration of 1 %v. Deposition was onto glass (as-received). Scale bars are 50 μm for the whole deposit (red) and 10 μm for the zooms (black).

contact line. Consequently, more particles were deposited at the interior of the droplet than a pinned droplet would have exhibited. All deposits formed a ring stain with a "lacy" structure inside. The morphology of the 30%v, 70%v, and 90%v PM deposits show evidence of a secondary ring within the main ring stain. This secondary ring is most evident in the 90%v droplet, forming a monolayer ring concentric with the outer stacked ring. The formation of the second ring in a droplet with no evident de-pinning likely results from the radial flow of the collected group post-Marangoni flow. The main ring forms during the Marangoni flow period (Fig. 4.29i/ii) due to particles "escaping" to the radial flow. Note, the pure water droplet shows only a single ring stain. Figure 4.60 shows the deposits for PM/water droplets at a *RH* of 0.70,

which differ very little from those at a RH of 0.35. Figure 4.57 confirms that there is very little change in the ring widths for PM concentrations between 30−90%v at either RH. Surprisingly, the Marangoni flow direction does not have a major influence on the final deposit, despite significant differences in the internal flows.

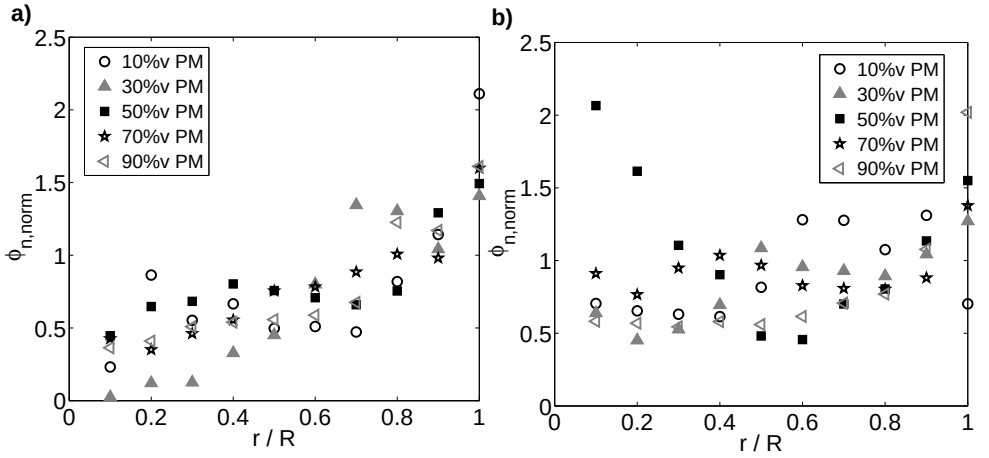

Figure 4.61. The radial distribution of the deposit consisting of 200 nm polystyrene spheres at 1%v solids content from 50%v PM/water droplets dried at a) RH 0.35, and b) RH 0.70. The normalised fractional area of coverage, $\phi_{\mathrm{n,norm}}$, is plotted at the outer radial position, r, for each ring i.e. at 0.1 for ring n=1, encompassing r/R = 0−0.1. R is the deposit radius. Values are the average of at least twenty deposits.

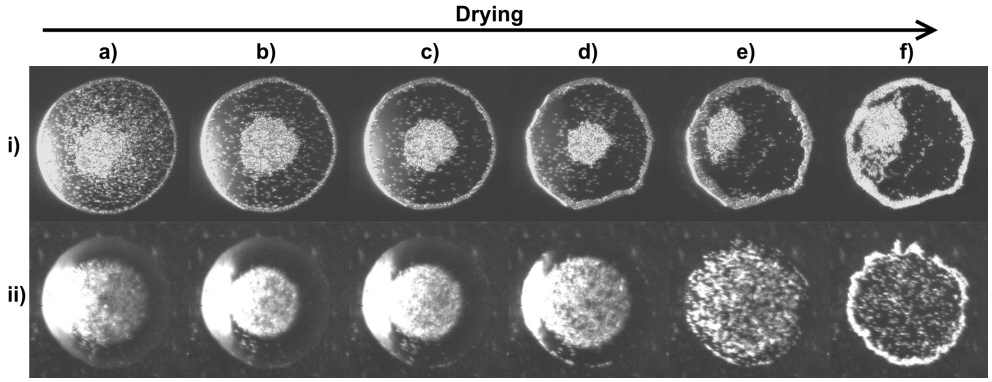

Figure 4.62. Dark field images of 50%v PM/water droplets during drying at a RH of i) 0.22 and ii) 0.70. The droplets contained 0.1%v 1μm polystyrene spheres. Images were taken after a) $0.1\,t_{\mathrm{dry}}$, b) $0.2\,t_{\mathrm{dry}}$, c) $0.3\,t_{\mathrm{dry}}$, d) $0.5\,t_{\mathrm{dry}}$, e) $0.8\,t_{\mathrm{dry}}$ and f) $1.0\,t_{\mathrm{dry}}$. See corresponding Videos PM3 and PM4. Note that deposits at RH 0.35 behave similarly to at RH 0.22.

The fractional area of coverage of particles deposited from PM/water droplets at a RH of 0.35 compared to a RH of 0.70 is shown in Figure 4.61 (calculated as described in Chapter 2, Section 2.6). The fractional coverage is similar at a RH of 0.35 and a RH of 0.70, except for the deposit from the 50%v

PM/water droplet. For this PM concentration, there is a residual deposit at the centre of the droplet, and a depleted region between the central deposit and the ring stain.

In contrast to the 200 nm particles, RH had a major influence on deposits of 0.1%v 1 μm particles from PM/water droplets (Figs. 4.62fi and 4.62fii). Migration is more significant for the larger particles, and the difference in the deposits from droplets with opposite Marangoni flow directions was more pronounced. Additionally, diffusion is slower for larger particles (i.e. diffusion to the contact line takes longer than the droplet lifetime). While there is particle migration and collection in both droplets, a ring stain forms during the Marangoni flow period at a RH of 0.22 (and similarly at a RH of 0.35) but not at a RH of 0.70. For a RH of 0.70, the group moves outwards during the radial flow period and forms a ring stain. At a RH of 0.22, the group does not separate during radial flow and settles inside the ring stain. This observation is important, as for an ink drying at different humidities, a switch in Marangoni flow direction results in a different deposit structure. This could have implications for the end product if the quality of the print is lowered. Note that the stability of suspensions to aggregation reduces during drying for PM/water at a RH of 0.22 (or 0.35), and increases for a RH of 0.70 as the polystyrene beads are more stable in water-rich solution. Hence, the reduced separation of the particles in the collected group at a RH of 0.22 could result in some aggregation of the particles.

Ethylene glycol (EG)/water mixtures have no notable Marangoni flow (Section 4.2) or migration of particles across streamlines, yet the morphology of the end deposits differs greatly depending on the EG concentration (Fig. 4.63). Pure EG and water gave ring stains resulting from radial flow to the contact line, as did EG/water mixtures with high EG content (50−90%v EG). In contrast, EG/water mixtures with lower EG content (10−30%v EG) gave a more uniform particle distribution in the deposit (see Fig. 4.57). Note that deposits from 10−30%v EG/water droplets are nearly a monolayer, unlike the stacked ring of deposits from ethanol/water droplets. A larger volume loss (due to higher water content) increases the solid content when only EG re-

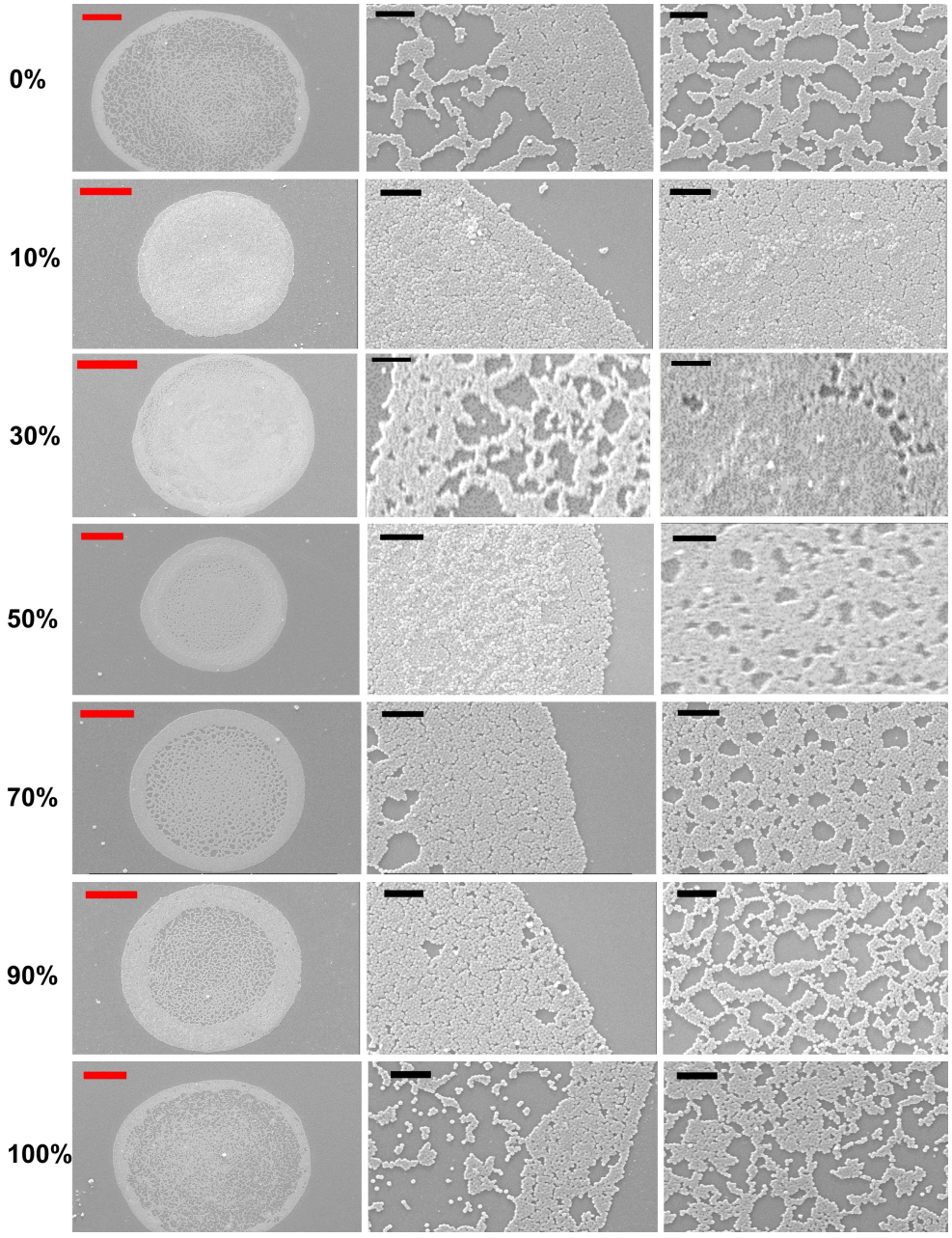

Figure 4.63. SEM images of (left to right) the whole deposit, a zoom to the contact line and a zoom to the interior, for deposits from droplets of ethylene glycol/water at a RH of 0.70 with an initial PM concentration of 0%v–100%v. The 200 nm polystyrene spheres were loaded at a concentration of 1%v. Deposition was onto as-received glass substrates. Scale bars are 20 μm for the whole deposit (red) and 2 μm for the zooms (black).

mains. There is also the particle stability in EG to consider: suspensions are stable until the EG concentration exceeds $\backsim$ 70%v. During drying, the EG concentration increases as water is the more volatile component. Once the EG content exceeds 70%v then aggregation may be enhanced. If the solid volume fraction is low then only small aggregates may form, which are carried towards

the contact line by radial flow. However, if the volume fraction of solids increases, then larger aggregates may form and settle, reducing particle motion towards the contact line. A high water content (low EG content) gives the largest solid volume fraction when the EG concentration reaches 70%v. Thus, the ring stain may be prohibited at low EG concentrations. The volume of liquid lost via evaporation before only a single solvent remains could therefore affect the deposit morphology. However, to confirm this supporting data from another solvent mixture (that does not exhibit Marangoni flow) is needed.

A second plausible explanation for the uniformity of these deposits is that the EG (which is rich at the contact line) slows the evaporation in this region, reducing convective flow. The water-rich apex experiences more evaporation, and the deposit is essentially collapsed down onto the substrate (giving a more uniform structure). This effect would be enhanced for the low EG content droplets due to the higher water content. Droplets with a high EG content would experience slow convective flow throughout drying, building up a ring stain. However, if this is the case, it is surprising that the composition gradient does not result in Marangoni flow or particle migration.

Marangoni flows resulted in the migration of particles to the centre of drying droplets, but did not prevent the formation of a ring stain for any of the mixtures studied in this section. Only some of the EG/water mixtures gave a uniform deposit, and these mixtures did not exhibit Marangoni flows. Hence, to achieve a uniform particle distribution alternative methods must be considered.

4.5. Summary

Internal flows inside single solvent droplets with a pinned contact line exhibited radial flow which built up a ring stain. Marangoni flows in binary solvent mixtures showed regions of circulating flow along fluid streamlines and a quiescent region. For a Marangoni flow directed from apex to contact line along the liquid-vapour interface, the circulating region was at the centre of the droplet, with a quiescent region near the contact line. For the reverse Marangoni flow

direction, a circulating eddy formed near the contact line, with a central quiescent region. The Marangoni flow direction in PM/water mixtures depended on the relative humidity. Hence, the internal flow regimes inside these droplets differ when jetted on a dry or wet day. This is an important factor to consider for ink formulations.

Size-dependent particle migration across fluid streamlines carried particles inward during the Marangoni flow period to form a central group. Larger particles migrated to inner streamlines faster. After the Marangoni flow period ended, particles moved radially outwards due to evaporation-driven flow, building up a ring stain. A larger difference in the evaporation rate between component solvents formed a central group with a smaller radius.

Three mechanisms for the particle migration across fluid streamlines were considered. Thermophoresis was ruled out as the migration mechanism due to the presence of particle migration in droplets with negligible thermal effects (such as evaporative cooling). Chemophoresis is inconsistent with some of the observations for particle migration (e.g. migration stops despite bulk gradients existing in the droplet), though estimated chemophoretic velocities are large enough to contribute to the migration. Shear-induced migration to regions of low shear rate is a promising potential mechanism for the migration.

Due to the size dependence of the particle migration, deposits from larger spheres differed from those formed by smaller spheres. The Marangoni flow direction only had a significant influence of the deposit structure for the larger spheres (1 μm). Despite Marangoni flow within the droplets, the most observed morphology was a ring stain. Park and Moon [105] were able to obtain a uniform deposit from solvent mixtures, by using a high boiling point solvent with a low surface tension as the minority component. However, their components (25%w formaldehyde/water or 25%w diethylene glycol/water) are similar in vapour pressure to the EG/water system seen here, and so deposit uniformity may not be due to Marangoni flow at all. Alternative routes are needed to circumvent the domination of the “coffee ring effect" on the deposit morphology.

5 | Control of the particle distribution through an evaporation-driven sol−gel transition

5.1. Introduction

Inkjet printing is a widely used non-contact method for delivering colloidal suspensions onto substrates [1]. A uniform particle distribution in the deposit is usually desired to reduce the volume of ink required to reach a given optical density. Additionally, a pinned contact line throughout the lifetime of the droplet will provide a controlled circular edge to the deposit. Receding contact lines or stick-slip behaviour can lead to irregular deposits with poorly defined outlines. Pinning is enhanced by rough substrates [81, 82], chemical inhomogeneity [83, 84], and through self-pinning by particulates, particularly at high volume fractions of solids [85–87].

While a uniform particle distribution is the ideal, often a ring stain is the reality [65,88,89,210,211]. For a sessile droplet with a contact angle less than 90°, evaporation is greatest at the contact line. If the contact line is pinned, fluid flows towards the periphery, replenishing liquid lost due to evaporation [61]. Particles inside the droplet are transported to the contact line and build up a ring stain (the "coffee ring effect") [65]. Particle migration within drying droplets can also produce a non-uniform deposit [108, 114]. A non-uniform particle distribution reduces the quality of graphical printing, since the optical density varies across the deposit. Similarly, printed electronics are limited by variation of the conductivity or porosity across a printed feature [156,212,213]. Biological assays based on inkjet technology also need a uniform concentration

of material across the deposit to be most effective [28].

A number of methods have been proposed to suppress ring stains. Mechanical methods such as selective laser sintering [214] or multiple passes of the print-head adjust the profile of the end deposit through physical addition or removal of material. Schirmer *et al.* filled in the ring stains using multiple droplets, each forming a smaller concentric ring stain [215].

Other methods exploit the underlying solvent properties or include additives to alter the flow pattern. Reducing the radial flow, or changing the flow pattern from radial to circulating, inhibits the formation of a ring stain by limiting the supply of colloidal material to the contact line. Radial flow has been reduced or prevented by adjustment of the solvent composition in the ink [104, 105, 211, 216, 217], by control of the substrate temperature [26, 218], or by a combination of flow manipulation and contact line de-pinning using electro-wetting [172, 219, 220].

Surface-tension gradients change the internal flows within drying droplets. These "Marangoni effects" produce a recirculating closed cell [45, 68, 113]. The cell transports particles away from the contact line and counteracts the build-up of a ring stain. Thermal Marangoni flows may arise on heated/cooled substrates [26, 218], or through evaporative cooling [68, 97]. Alternatively, solutal Marangoni flows can occur in solvent mixtures [105, 106, 114, 221], or in the presence of surfactants [102–104]. However, when the droplet becomes thin, the evaporation-driven capillary flow may overcome the Marangoni flow, producing a ring stain [114].

Increasing the viscosity of the droplet during drying is an appealing way of suppressing the ring stain. However, unless the increase in viscosity overcomes the capillary flow a ring stain will still result. The capillary number, Ca, describes the ratio of viscous effects to surface tension effects,

$$Ca = \frac{\mu u}{\sigma}, \tag{5.1}$$

where σ is the surface tension, μ is the viscosity and u is the fluid velocity. The order of magnitude of the velocity is $R/t_{\mathrm{dry}} \backsim 10^{-5}\ \mathrm{m\,s^{-1}}$, where R is the droplet radius ($\backsim 10^{-5}$ m in inkjet printing) and t_{dry} is the drying time (a

few seconds for water). The capillary number must approach one in order for viscous effects to become significant. If $Ca \geq 1$, then the droplet can deform from a spherical cap. For water, $Ca = \left(10^{-3}\ \mathrm{Pa\,s} \times 10^{-5}\ \mathrm{m\,s^{-1}}\right)/10^{-1}\ \mathrm{N\,m^{-1}} \backsim 10^{-7}$; a 10^7-fold increase in viscosity during drying is required to suppress radial flow. The upper viscosity limit for inkjet printing is of the order 10^1 mPa s at shear rates between 10^4–10^6 $\mathrm{s^{-1}}$ (depending on whether drop-on-demand or continuous inkjet systems are used), so even this extreme case requires a million-fold increase in viscosity.

An alternative strategy for suppressing the ring stain is to exploit the elastic (rather than the viscous) properties of complex fluids. In order to overcome the capillary flow and prevent particle motion, the elastic modulus of a viscoelastic fluid must exceed the capillary pressure (estimated by the Laplace pressure). The dimensionless number

$$\epsilon = \frac{G' r_\mathrm{c}}{2\sigma}, \tag{5.2}$$

is defined as the ratio of the elastic modulus, G', to the Laplace pressure ($P = 2\sigma/r_c$) inside the droplet, where r_c is the radius of curvature of the droplet. In order to resist deformation, ϵ must be at least of the order 1. For a water-based droplet (with contact angle 20° and radius 80 μm) achieving ϵ=1 corresponds to an elastic modulus of $G' \backsim 10^2$ Pa. This is more likely to be achievable than a viscosity increase of the order of 10^6. A phase transition is employed to achieve a sufficiently large elastic modulus when printing molten waxes or UV-cured inks [222]. Note that the elastic modulus is used rather than the yield stress as the critical strain is lower than 1 (100%), making the elastic modulus the larger value to overcome and allow deformation.

Alternatively, elasticity can be introduced into a viscous fluid by a "sol–gel" transition. A sol is a stable suspension of colloidal particles in a fluid. A gel is a complex fluid/soft solid that has elastic properties at rest but flows under shear. In a sol–gel transition, colloidal particles aggregate to form an elastic network that percolates through the fluid. A thermally activated sol–gel transition has previously been used to suppress radial convection. Printing onto a heated substrate (when the fluid gels upon heating [223, 224]), or printing heated droplets onto a cool substrate (when the fluid gels upon cooling [225]) have both been demonstrated.

Radial convection is the cause of undesirable ring stains. However, if the particles do not move at all, the final deposit will be thickest at the centre and thinnest at the edge (a dome). This profile results from the initially uniform particle distribution collapsing down as a 2D projection during drying. To produce a uniform particle distribution in the final deposit, a controlled amount of radial motion is required: too much radial flow and a ring stain forms, too little and a dome results. The necessary radial motion must therefore be switched-off after an appropriate time.

Dilute suspensions of laponite (a nano-particulate clay) were used to induce a sol−gel transition during evaporation at a constant temperature. As the laponite suspension becomes more concentrated inside a drying droplet, the elastic modulus of the suspension increases [226], forming a gel capable of resisting the capillary stresses that otherwise result in particle motion. The elasticity of the gel results from the "house of cards" structure formed by the assembly of the plate-like laponite particles with their negatively charged faces and positively charged edges into a network. Variation in the initial laponite concentration allows gelling to be induced after a controlled amount of evaporation. Thus, the extent of radial motion of the particles can be varied to control the final distribution of the deposit. The network breaks down when a shear force is applied, reducing the viscosity and allowing laponite suspensions that are highly viscous gels at low shear rates to be jetted in an inkjet printhead. The shear-thinning properties of laponite suspensions are also desirable for reducing satellites [123].

As water evaporates from a droplet, the concentration of solute (e.g. laponite) within the droplet increases, but this increase is not uniform. In the absence of convection, the concentration is highest at the air-water interface, leading to the formation of a skin if diffusion is too slow to redistribute the solute over the thickness of the droplet. Evaporation is fastest at the contact line where the drop is thinnest [67]. Consequently, the concentration of laponite increases from the apex to the contact line, and so gelation starts at the contact line and propagates inwards.

In this chapter, I show that the sol−gel transition in laponite suspensions can be used to suppress radial flow and form a uniform deposit. A comparison

is made between the behaviour of laponite suspensions and solutions of a water-soluble polymer of similar low shear viscosity (hydroxyethylcellulose) to show that laponite is more effective at suppressing ring stains.

5.2. Experimental

The profiles of droplets emitted from an inkjet printhead were imaged by high-speed shadowgraphy simultaneously with the internal flows. The experimental rig used is described in Chapter 2, Section 2.1 (Rig B). Picolitre droplets were ejected from a Microfab (AJ-ABP-01) drop-on-demand device, with an 80-μm orifice. The corresponding approximate shear rate inside the nozzle can be estimated as $u_e/R_{nz} \backsim 1$ ms$^{-1}/40\times10^{-6}$ m $\backsim 2.5\times10^4$ s^{-1}, where u_e is the velocity of ejection and R_{nz} is the radius of the nozzle orifice. Droplets dried at an ambient temperature of 21 °C and a relative humidity of 50%.

Glass cover slips were used for the deposition due to the need for a transparent substrate. The cover slips were used as received, or pre-cleaned with isopropanol to produce a more wetting substrate. Dried deposits were imaged with a scanning electron microscope (SEM, Philips XL30 Environmental SEM) and vertical profiles were measured on a white light interferometer (Zygo NiewView 5000). Pretreatment procedures for sputter coating the deposits are described in Chapter 2, Section 2.5. The vertical noise for the interferometer was approximately ± 20 nm. The vertical profiles of the deposits were azimuthally averaged in MATLAB.

A custom-written MATLAB routine was used to extract the evaporation rate, diameter, height and contact angle of each droplet. Particle velocities were calculated using particle tracking velocimetry code adapted from routines developed at Georgetown University [142]. Particle velocities were binned radially in increments of $0.1R$ and temporally by $0.1t_{dry}$, where R is the contact radius of the droplet and t_{dry} is the drying time. The contact radius depends on the particle position if the contact area is elliptical: R is the length of the line from the centre of the droplet to the contact line, passing through the location of a given particle. The mean radial velocity (in the x-y plane), $v_r(t)$, was then found for each radial bin. The tangential velocity was negligible un-

less contact line de-pinned. Contact radii were found from fitting an ellipse to the particles at the contact line. SEM images were post-processed in Matlab to find the fractional area of coverage radially across the deposit (as described in Chapter 2, Section 2.6).

Suspensions of laponite (RD grade, Rockwood) in water (MilliQ, 0.25 μm filter, pH 7.7) with 0%w, 1%w, 2%w and 3%w laponite content and containing 0.05%w 1 μm sterically stabilised polystyrene spheres (PEGMA-stabilised, zeta-potential -25 to -39 mV for pH 6–9, University of Leeds, UK) were prepared for particle tracking studies. A 2%w laponite suspension had a pH of 10.0 (without spheres). The suspension of polystyrene spheres was made first and the laponite was subsequently added. The laponite powder was fully hydrated and solutions were sonicated for 15 minutes prior to use. No large aggregates were present in the initial formulation. Samples were made fresh on the day of jetting due to the ageing properties of laponite suspensions [227]. In order to study deposits from samples with a higher solid content, laponite suspensions were prepared with 1%w and 5%w 200 nm polystyrene spheres. In some formulations, colloidal silica (LUDOX AS-40, Sigma Aldrich, particle diameter $\backsim$ 20 nm, zeta potential $\backsim -75$ mV at pH 7) was included in the laponite suspensions at concentrations up to 1%w as an anti-aggregation agent due to the large-scale aggregates formed in deposits from laponite suspensions with polystyrene spheres. The colloidal silica was purchased as a stable suspension and was added to the suspension of polystyrene spheres before the laponite powder. The polymer hydroxyethylcellulose (HEC, MW 250 kg mol^{-1}, Sigma Aldrich) was tested as a 1%w solution, as this concentration exhibits a similar low shear viscosity to a 2%w laponite solution. Rheological data were collected for laponite suspensions and HEC solutions without polystyrene spheres, as described in Chapter 2, Section 2.4.

5.3. Results and discussion

5.3.1. Shear rheology of formulations

Figures 5.1 and 5.2 present the steady-state shear viscosity of laponite suspensions and HEC solutions over a range of shear rates. The laponite suspensions

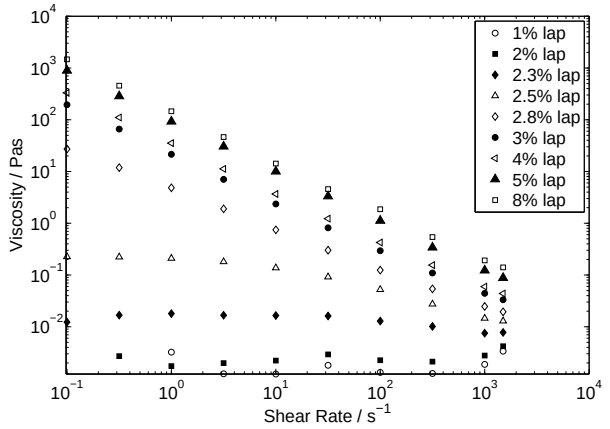

Figure 5.1. Steady-state shear viscosity of laponite suspensions in water as a function of shear rate.

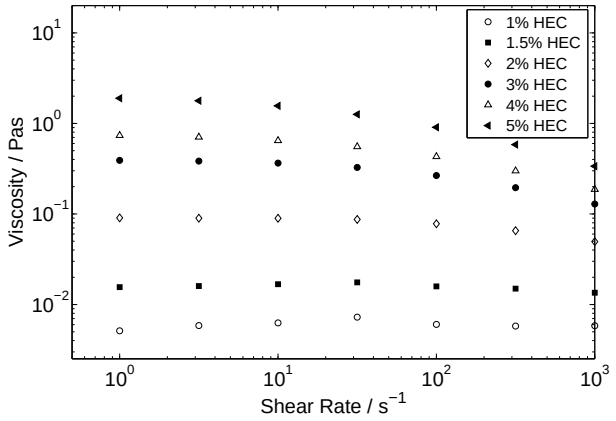

Figure 5.2. Steady-state shear viscosity of aqueous HEC solutions as a function of shear rate.

were shear-thinning when the laponite concentration exceeded about 2.5%w. Above 3%w laponite, there was no Newtonian plateau, indicating yield-stress behaviour. The HEC solutions were weakly shear-thinning for HEC concentrations of 3%w and above. Inkjet printed droplets experience high shear rates inside the nozzle (10^4–10^6 s^{-1} in commercial print-heads) [1], and low shear rates (10^0–10^1 s^{-1}) on the substrate. It is therefore necessary to determine if the laponite network can recover during the lifetime of the droplet.

Figure 5.3 shows the recovery of the shear viscosity of laponite suspensions following a period of high shear rate. Although the applied shear was an order of magnitude lower than in an inkjet print-head, the network was fully broken down, and so the recovery time should be the same as if a shear rate of

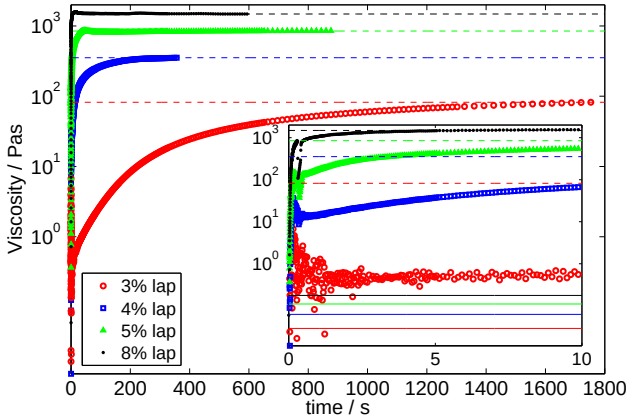

Figure 5.3. Recovery of the shear viscosity for laponite suspensions over a range of laponite concentrations, following a period of high shear. The inset shows the recovery of the shear viscosity over the first ten seconds, encompassing the typical drying time of inkjet droplets ($\backsim$ 5 s). Dashed horizontal lines indicate the viscosity after full recovery. Solid horizontal lines indicate the viscosity immediately following the switch from high shear rate (1000 s^{-1}) to low shear rate (0.1 s^{-1}).

$10^4\,s^{-1}$ was applied. For laponite concentrations $\gtrsim$2.5%w, the viscosity increased monotonically until the steady-state low-shear viscosity was attained. The recovery of the viscosity was faster for suspensions containing more laponite. For suspensions containing $\leq$5%w laponite, the network did not fully recover within the lifetime of a droplet (typically $\backsim$ 5 s). However, there was a significant viscosity increase (of order 10^2) for the 5%w laponite suspension over this time period. Once the laponite concentration reaches 8%w, the suspension fully recovers within seconds (an increase by three orders of magnitude in 5 s, see Fig. 5.3). During the droplet lifetime, the increase in laponite concentration due to evaporation will therefore facilitate total recovery of the suspension network and the associated elastic properties. While the recovery of the elasticity cannot be directly measured, recovery of the shear viscosity represents the recovery of the networked structure. If the network recovers, it can be inferred that the elasticity recovers.

Inverted bottle experiments (Fig. 5.4) show a sol−gel transition between 2.8−3%w laponite. Shear rate versus shear stress curves (Fig. 5.5) confirm the concentration range of the sol−gel transition. At 3%w laponite, the suspension had a finite yield stress (see Table 5.1), and was a shear-thinning gel. The sol-gel transition gave rise to a sharp increase in the low-shear viscosity (Fig.

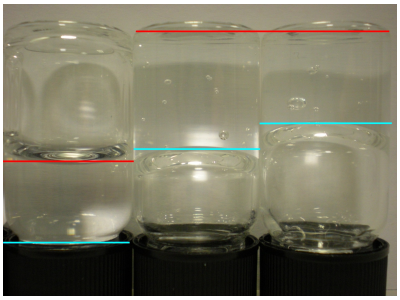

Figure 5.4. Inverted bottles indicating which laponite concentrations in water are sols and which are gels after leaving overnight. From left to right the laponite concentrations are 2.8%w, 3%w, and 4%w. The 2.8%w laponite suspension is a viscous sol. The 3%w and 4%w laponite suspensions are gels trapping bubbles. The blue horizontal lines indicate the lowest lying part of the sample in the vial and the red lines the highest part.

Table 5.1. Yield stresses determined by oscillatory measurements for laponite suspensions in water at various laponite concentrations.

Laponite concentration / %w	Yield stress / Pa
2.8	0.3
3.0	5
4.0	45
5.0	107
8.0	149

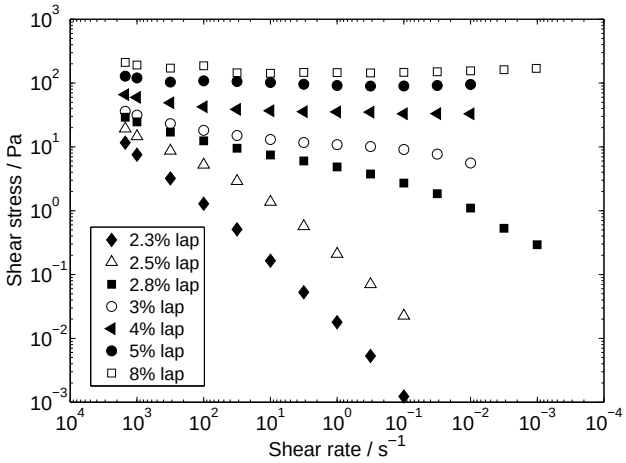

Figure 5.5. Shear stress versus shear rate data for laponite suspensions with a range of laponite concentrations.

5.1) and elastic modulus of the suspension. For our droplets, (typical contact angle $\backsim 20°$, contact radius $\backsim 80\mu$m), the capillary pressure is $p_{Ca} \backsim 2\sigma \ / \ r_c \backsim 10^2$ Pa, where σ is the surface tension of the fluid and r_c is the radius of curvature of the droplet. A yield stress of the order of 10^2 is therefore required to overcome capillary flow via network elasticity (giving $\epsilon = 1$ in equation 5.2).

Table 5.1 indicates that yield stresses of this magnitude occur for laponite concentrations of $\geq$5%w. In comparison, a viscosity increase of a million-fold required to overcome capillary flow could not be achieved without significant solvent evaporation and so would not be achievable early enough in the drying time to prevent a ring stain. Hence, recovery of the elasticity is the important factor. It can be inferred from the recovery of the shear viscosity that an 8%w laponite suspension can fully recover the networked structure and therefore the elasticity within the lifetime of the droplet.

A comparison with HEC was performed to further confirm the recovery of the laponite suspensions during drying. For HEC, the change in viscosity from high shear to low shear was less than an order of magnitude for any given concentration of the studied solutions. At low shear rates, the viscosity of HEC solutions increased by three orders of magnitude between 1%w and 5%w. At high shear rates the corresponding viscosity increase was smaller ($\backsim 10^2$) and comparable to the increase in high-shear viscosity in laponite suspensions over the same concentration range. HEC has a very low elastic modulus ($\backsim$3 Pa, see Appendix B). Thus, if the laponite network does not recover on the timescale of droplet drying, HEC and laponite may be expected to show similar drying behaviour.

If the increase in laponite concentration during the drying lifetime is sufficient for full network recovery, the suspension will show a large viscosity increase and sol−gel transition. Once the solution becomes a gel, particle motion will be prevented, and the deposits will differ greatly from those containing HEC.

Laponite was observed to cause aggregation of polystyrene latex particles. Colloidal silica was added to laponite suspensions to inhibit aggregation, but silica also affected the critical strain (Table 5.2). Increasing the ratio of silica to laponite decreased the critical strain, indicating a reduction in the ability of the network to maintain connectivity. The yield stress and speed of the recovery of the network both increased (for a fixed laponite concentration) as the total solid concentration increased (see Fig. 5.6).

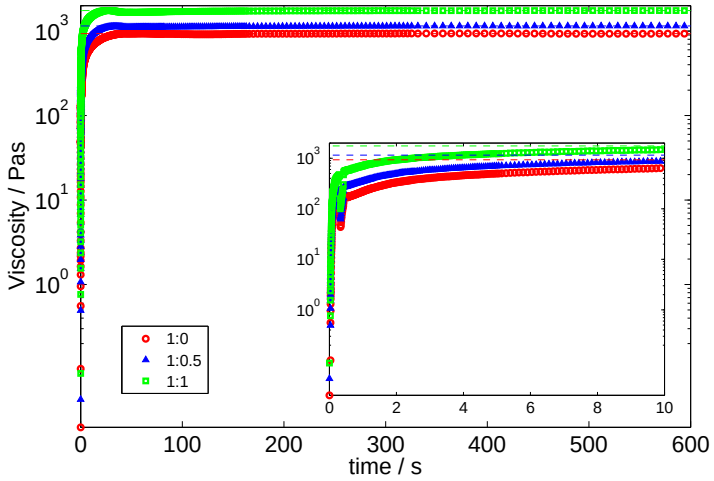

Figure 5.6. The recovery of the shear viscosity for suspensions containing 5%w laponite with ratios of laponite to colloidal silica of 1:0, 1:0.5 and 1:1.

5.3.2. Evaporation and gellation of printed droplets

Particle tracks (in blue) are shown in Figure 5.7 for an evaporating droplet of pure water, a 1%w polymer solution and two concentrations of laponite suspensions (2%w and 3%w) printed onto glass cover slips. The initial contact line is indicated by a solid black circle. For pure water (Fig. 5.7a), the tracks are purely radial until the contact line de-pins near the end of the drying time (indicated by the stationary particles in green at the right-hand side of the droplet in Fig. 5.7aiii). Figure 5.8a shows the mean radial velocity of the particles as a function of radial distance from the centre of the droplet for various time periods from the end of spreading until the contact line de-pinned (data after contact line de-pinning is shown in Appendix B). The mean

Table 5.2. Critical strains determined by oscillatory measurements for laponite/silica suspensions in water at various laponite to silica ratios. Note that yield stresses for suspensions without colloidal silica differ from those in Table 5.1 due to different ageing times.

Laponite / %w	Colloidal silica / %w	Ratio laponite : silica	Critical strain / %	Yield stress / Pa
3.0	0.0	1:0	4.1	1.7
3.0	1.5	1:0.5	2.9	4.0
3.0	3.0	1:1	2.6	5.1
5.0	0.0	1:0	4.7	60
5.0	2.5	1:0.5	4.4	72
5.0	5.0	1:1	3.7	90

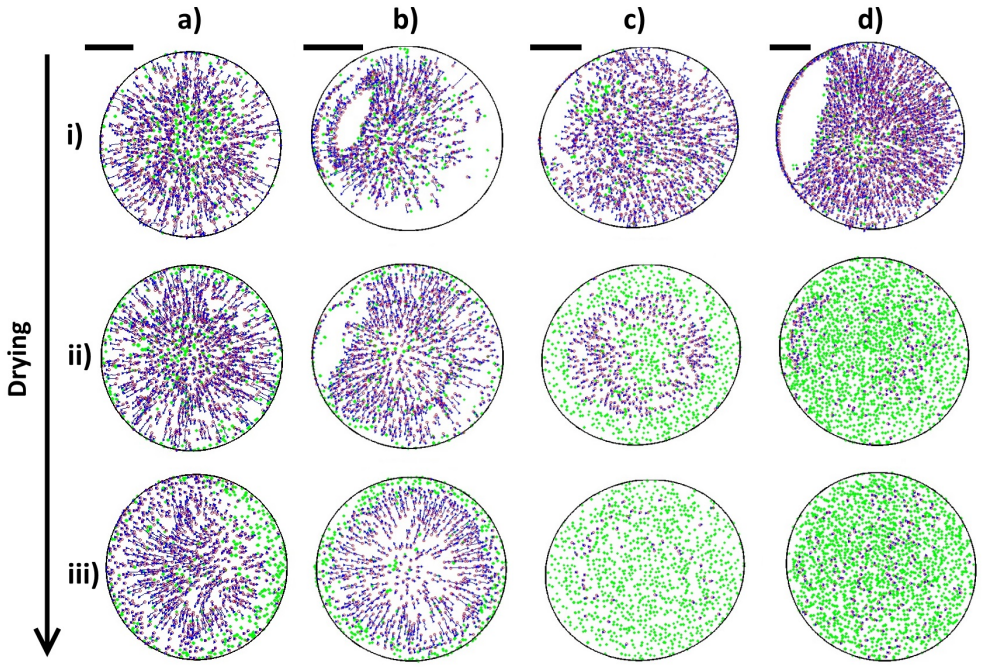

Figure 5.7. Particle tracks for droplets containing 0.05%w 1-μm polystyrene spheres and a) pure water (t_{dry} = 5.03 s), b) 1%w HEC (t_{dry} = 5.02 s), c) 2%w laponite (t_{dry} = 6.32 s) and d) 3%w laponite (t_{dry} = 8.65 s). The particle tracks are shown for i) 0.0–0.1 t_{dry}, ii) 0.4–0.5 t_{dry} and iii) 0.7–0.8 t_{dry}. Stationary particles (with movement less than two pixels in the time interval) are indicated in green. Moving particles are indicated in blue with a red circle at the start of the track and a blue triangle at the end of the track. The black line indicates the initial contact line. Refraction of light through the droplet prevents dark field imaging in some areas of some images, where no particles are shown. The glass slides were used as-received. The tracks are examples from single representative droplets. Scale bars are 50 μm.

radial velocity of the particles increased throughout drying and with increasing distance from the centre of the droplet (apart from the rim).

The 1%w HEC droplet (Fig. 5.7b) exhibited similar flows to the water droplet, with radial flow even at $0.8t_{\mathrm{dry}}$, by which point the mean HEC concentration had reached 5%w and the low shear viscosity had increased by more than two orders of magnitude. The HEC concentration was highest near the contact line leading to a small rim of stationary particles in the final stages of drying (green particles in Fig. 5.7biii). Figure 5.8b shows that the velocity profiles for 1%w HEC evolved similarly to pure water, with an increase in the mean radial velocity during drying. However, there was an initial decrease in the velocity at early times, potentially due to the small amount of motion in the contact line during the first time bin.

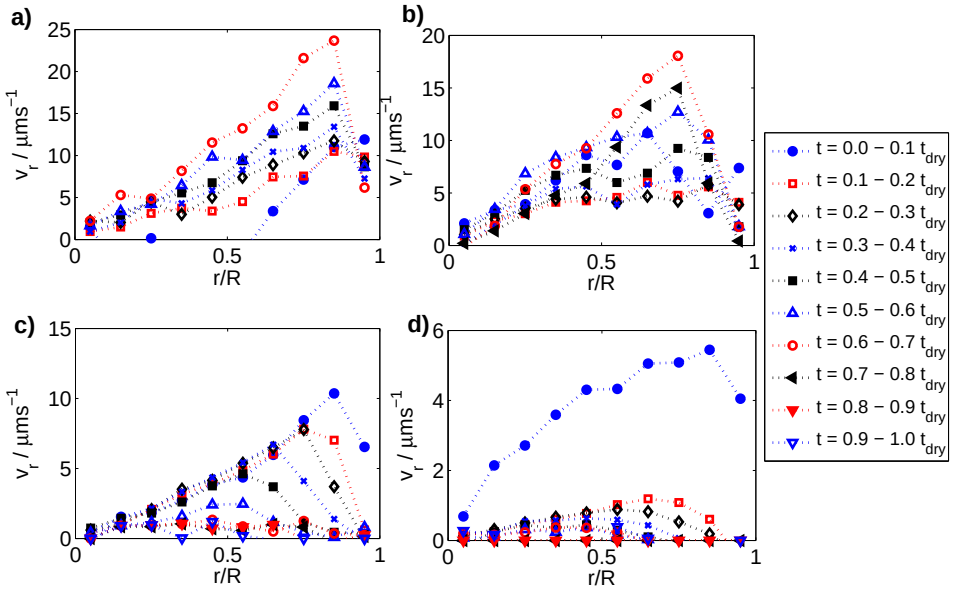

Figure 5.8. Mean radial velocities, v_r, over the normalised droplet radius are shown for incremented temporal bins for a droplet of a) pure water, b) 1%w HEC, c) 2%w laponite suspension and d) 3%w laponite suspension. Data points are plotted at the mid-point of each spatial bin. For clarity, data are shown for a single representative droplet up until the time that the contact line de-pins (complete data are in Appendix B).

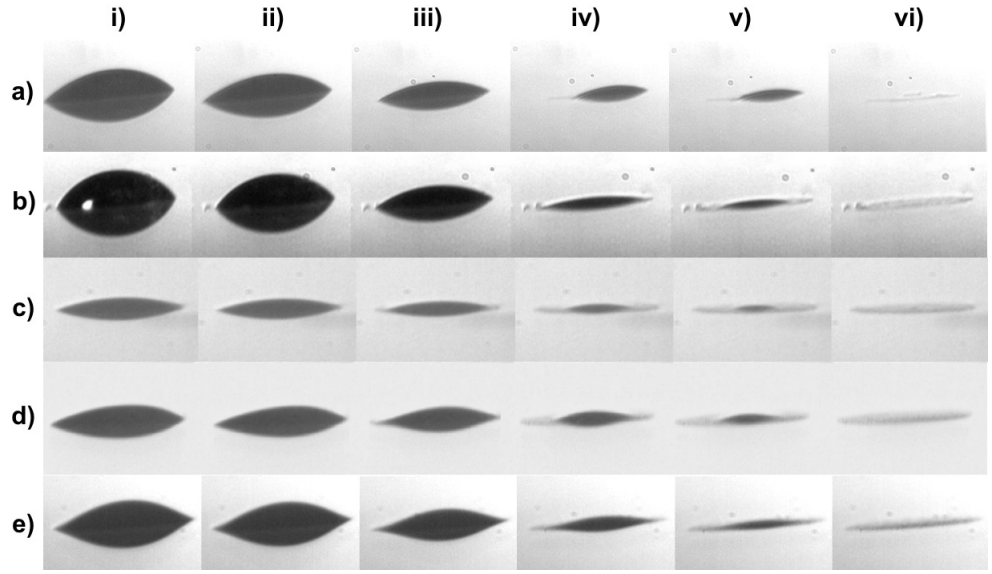

Figure 5.9. Side profile of a droplet containing 0.05%w 1 μm polystyrene spheres and a) 0%w laponite, b) 1%w HEC, c) 1%w laponite, d) 2%w laponite, and e) 3%w laponite after fractions of i) 0.1, ii) 0.2, iii) 0.5, iv) 0.8, v) 0.9 and vi) 1.0 of the drying time, t_{dry}. The drying times from a) to e) were 5.07 s, 5.02 s, 6.26 s, 6.56 s and 8.64 s. The glass substrate was pre-cleaned with isopropanol.

The behaviour of particles within a droplet containing laponite was very different. A droplet of 2%w laponite (Fig. 5.7c) initially showed radial flow

throughout the droplet, before a gelling front propagated from the contact line towards the droplet centre (see Video L2). Particles in the gel ceased to move (green particles in Fig. 5.7cii), while particles in the sol continued to flow radially outwards. During drying, the mean radial velocity of particles within the droplet of 2%w laponite suspension decreased as the gelling front propagated inwards, reducing velocities near the contact line at early times and closer to the centre at later times (Fig. 5.8c). Side images indicating the inward progression of the gelled "disk" and leaving the central sol "cap" are shown in Figure 5.9 (corresponding videos for the water droplet and 3%w laponite suspension are given in Videos LS0 and LS3). The deviation of the droplet profile from a spherical cap confirms that the laponite particle network recovers quickly enough for the sol to gel within the drying time of the droplet ($t_{\mathrm{dry}} \backsim 5$ s). Note that the radial motion within the sol led to a final distribution of tracer particles (Fig. 5.7ciii) that was highly uniform. Particle distributions in dried deposits are discussed in more detail in the following section.

The final set of particle tracks, shown in Figure 5.7d, are for a 3%w laponite suspension, which forms a shear-thinning gel. Immediately after impact and spreading there was radial flow (Fig. 5.7di), but gelation rapidly spread throughout the entire droplet and halted particle motion (Fig. 5.7d). The initial particle motion occurs because there is a finite recovery period after shearing of the gel in the nozzle before the laponite network reforms. The recovery time of the gel network can be estimated to be within 440 ms ($0.1t_{\mathrm{dry}}$) from the time between droplet impact and gelation of the droplet. Figure 5.8d shows the radial velocity profiles for the 3%w laponite formulation, confirming the formation of a gel within $0.1t_{\mathrm{dry}}$.

For droplets without laponite, the velocity of particles increased during drying and towards the contact line. For droplets containing laponite, the velocity of particles decreased throughout drying, as particles slowed down in the gel. Plots of how the maximum velocity varies radially and temporally are given in Figures 5.10 and 5.11.

The droplets in Figure 5.7 were printed onto a cover slip as received from the supplier. These cover slips have varying levels of chemical contamination

that increases contact angle hysteresis, leading to pinning of the contact line. If the substrates are cleaned with isopropanol before use, pure water droplets quickly de-pin (Fig. 5.12a). The receding contact line drags particles inward leaving an irregular and unpredictable deposit shape. The gelled rim of the laponite droplet pins the contact line throughout drying (Fig. 5.12b) resulting in a circular edge to the deposit with a radius defined by the initial spreading of the droplet on the substrate. As with the droplets printed on as-received glass, the width of the gelled ring grew as evaporation progressed with the freely flowing suspension restricted to a region of decreasing radius around the centre of the droplet.

In this section, it was established that laponite controls the amount of radial flow in evaporating droplets. It is the radial flow that is responsible for forming ring stain deposits in drying droplets. However, in order to form a uniform deposit rather than a dome, some radial motion is necessary. The combination of the concentration of the laponite during drying and a fast recovery time of the networked structure is essential to control the extent of radial flow. In the following section, the dried deposits are examined to determine if, by using laponite to reduce the radial flow, the particle distribution can be controlled to eliminate ring stains.

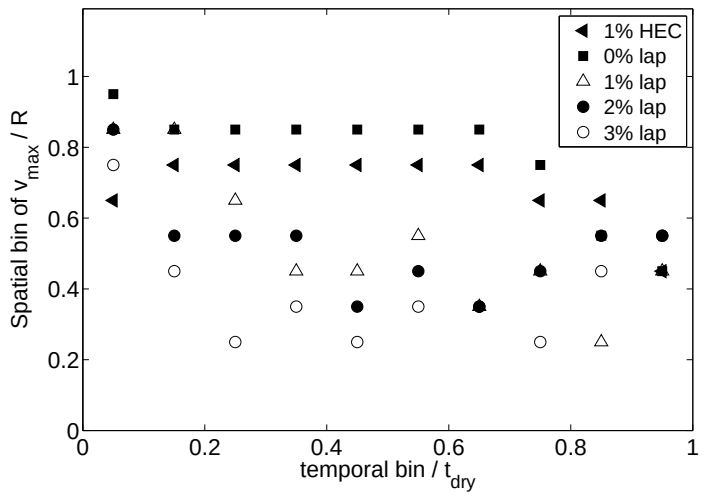

Figure 5.10. Spatial bin in which the maximum velocity of the particles falls, for each temporal bin.

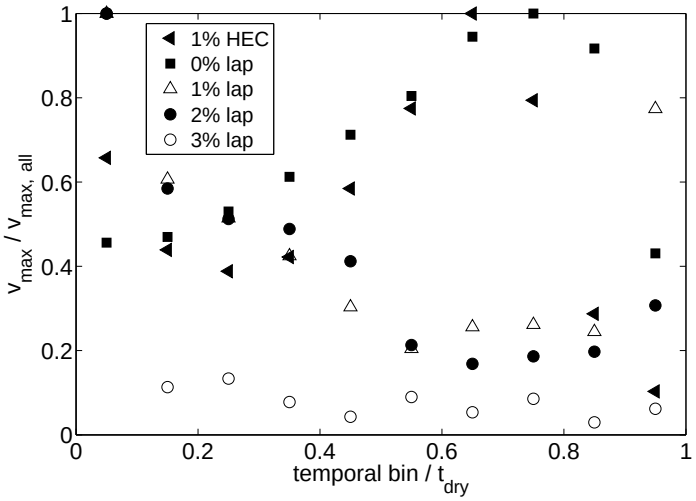

Figure 5.11. Maximum particle velocity, $v_{\max}$, in each temporal bin, normalised by the maximum velocity across all temporal bins, $v_{\max,\,\mathrm{all}}$.

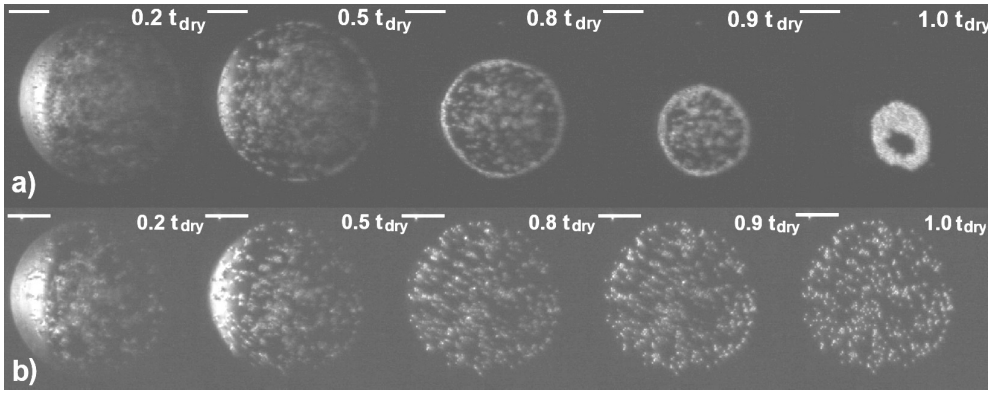

Figure 5.12. Inverted microscope images for a) a droplet containing 0%w laponite, with 0.05%w 1 μm polystyrene spheres on a glass substrate pre-cleaned with isopropanol, and b) 2%w laponite. For a) the droplet de-pins during drying, but for b) the droplet stays pinned throughout drying. The scale bars are 50 μm.

5.3.3. Distribution of tracers in dry deposit

Figure 5.13 shows scanning electron micrographs of the dried deposits from various formulations containing 0.05%w of 1-μm tracer polystyrene spheres. From these micrographs, the fraction of the substrate covered by polystyrene spheres was calculated as a function of the radial distance from the centre of the deposit. Figure 5.14 plots these distributions, normalised to the average density. The laponite suspensions provided a more uniform distribution of tracer particles than either water or 1%w HEC, both of which show an increase in the particle density towards the edge of the deposit (a ring stain). The 1%w HEC solution also shows a build up of particles at the centre of the

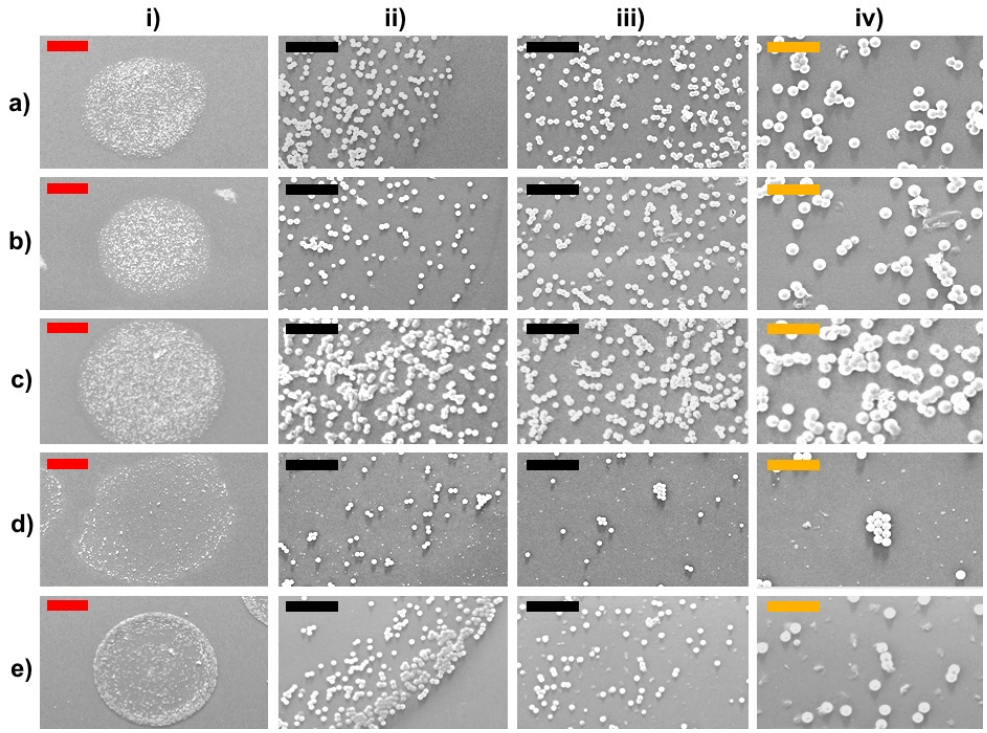

Figure 5.13. SEM images of deposits containing 0.05%w 1 μm polystyrene spheres: a) 1%w laponite, b) 2%w laponite and c) 3%w laponite, d) pure water, and e) 1%w HEC. Images show i) the whole droplet at 400× zoom (red scale bar 50 μm), ii) a 2500× zoom to the contact line (black scale bar 10 μm), iii) a 2500× zoom to the interior (black scale bar 10 μm), iv) a 5000× magnification of the interior (orange scale bar 5 μm). Glass substrates were used as-received.

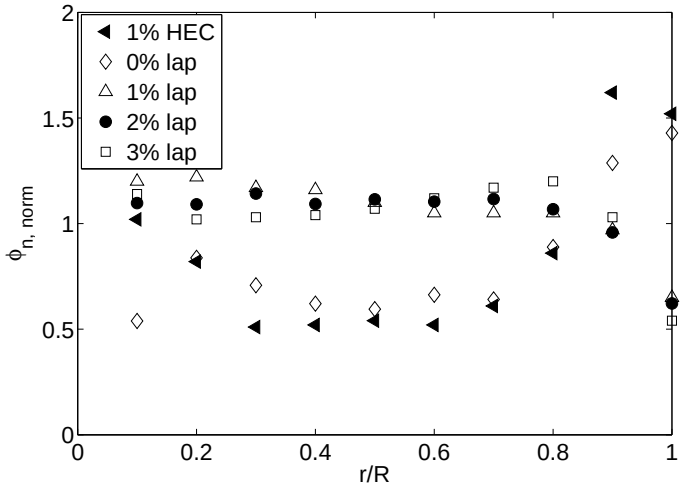

Figure 5.14. The radial distribution of the deposit consisting of 1 μm polystyrene spheres at 0.05%w solids content. The normalised fractional area of coverage, $\phi_{\mathrm{n,norm}}$, is plotted at the outer radial position, r, for each ring i.e. at 0.1 for ring n=1, encompassing r/R = 0–0.1 (where R is the deposit radius). Values are the average of at least twenty deposits.

deposit. In laponite suspensions containing only a trace amount of solids, the laponite concentration made little difference to the area covered by the deposit. The 1%w, 2%w, and 3%w laponite suspensions produced a uniform density of particles across most of the deposit, except near the contact line where the particle density decreased. (Fig. 5.13a−c).

Close inspection of the high resolution images (Fig. 5.13, column iv) show that the diameter of the polystyrene spheres deposited from 3%w laponite appears to be nearly double that in the pure water. The explanation is that during drying the nanoparticles of laponite coat the polystyrene sphere. The change in size of the spheres is less evident for the lower laponite concentrations, but the outlines of the spheres are less sharp than for the water droplet (Fig. 5.13d) and the spheres blend into each other where they are in contact, owing to the laponite coating between the spheres. The HEC deposit shows a polymer coating on the spheres near to the contact line where the HEC ring stain forms (Fig. 5.13eii).

5.3.4. Deposits with a high solid content

In the previous section control of radial flow in laponite suspensions was demonstrated to lead to a uniform coverage of tracer particles in a dried deposit. Investigated next is whether the same uniformity can be achieved in formulations with a higher fraction of suspended solids, for which 200-nm polystyrene spheres were chosen at concentrations of 1%w and 5%w.

Figure 5.15 shows SEM micrographs of droplet deposits containing 1%w 200 nm polystyrene spheres. Corresponding interferometric profiles are given for example droplets in Figure 5.16. The droplet of water de-pinned during drying and produced a highly non-uniform distribution with a holey structure consisting of patches of covered and bare substrate (Fig. 5.15a). The azimuthally averaged interferometric profile (Fig. 5.17a) confirmed the non-uniform thickness. As expected, due to the de-pinning, there was no significant ring structure at the contact line. For a droplet containing 1%w HEC, the deposit had a thin ring at the edge and a non-uniform radial profile (Fig 5.15b). Interferometry revealed that the deposit had a raised central region as well as a ring at the contact line (Fig. 5.17a). Droplets containing laponite (Fig 5.15c−e)

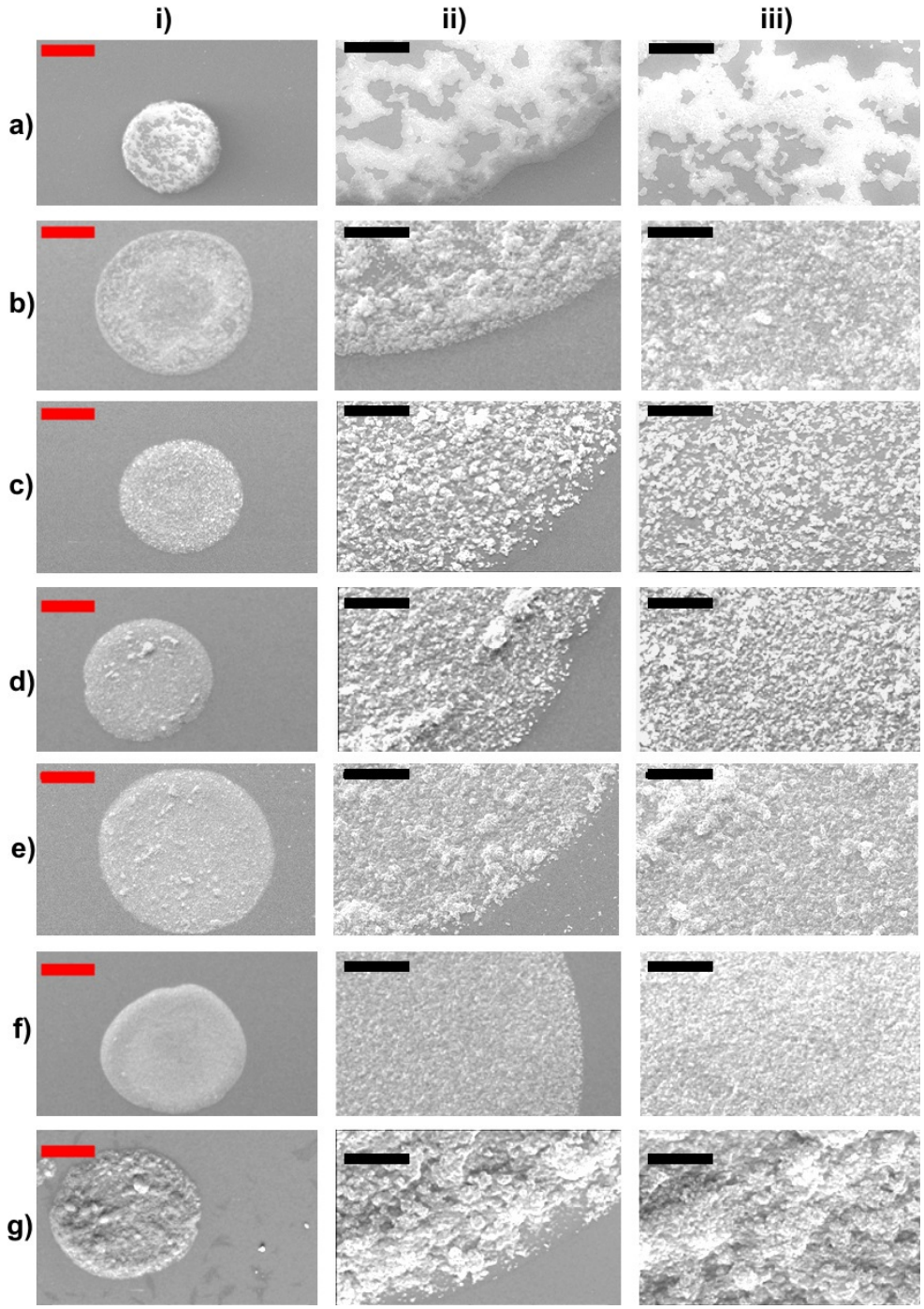

Figure 5.15. SEM images of deposits containing 1%w 200 nm polystyrene spheres: a) pure water, b) 1%w HEC, c) 2.8%w laponite, d) 2.5%w laponite, e) 2.0%w laponite, f) 2%w laponite with 1%w colloidal silica, and g) 3%w laponite with 1%w colloidal silica. Segments show i) the whole droplet (400× magnification, red scale bar 50 μm), ii) a zoom to the contact line (2500× magnification, black scale bar 10 μm) and iii) a zoom to the interior (2500× magnification, scale bar 10 μm). Substrates were as-received glass.

produced more uniform radial particle distributions with fewer patches. The interferometry profiles show that laponite concentrations of 2.8%w and 2.5%w

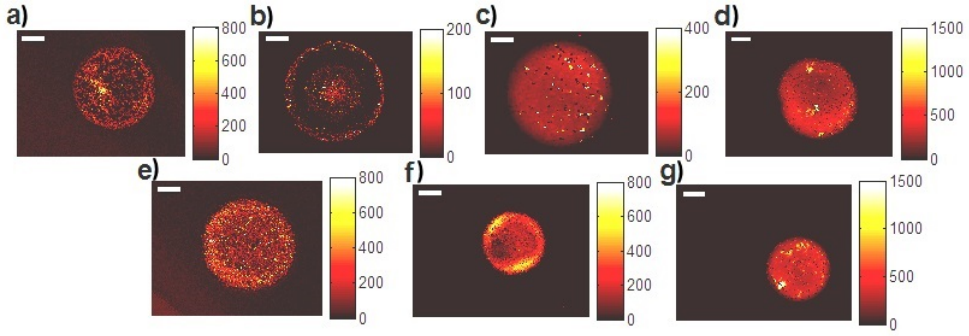

Figure 5.16. Height profiles taken on a white light interferometer, for an example deposit from droplets containing 1%w 200 nm polystyrene spheres and a) pure water, b) 1%w HEC, c) 2.8%w laponite, d) 2.5%w laponite, e) 2.0%w laponite, f) 2%w laponite with 1%w colloidal silica, and g) 3%w laponite with 1%w colloidal silica. The colour scale shows the deposit height in nm. The white scale bar is 50 μm. Note that 200 nm is the hydrodynamic diameter of the polystyrene spheres. Dried spheres will have a smaller diameter due to the collapsed stabilising polymer chains.

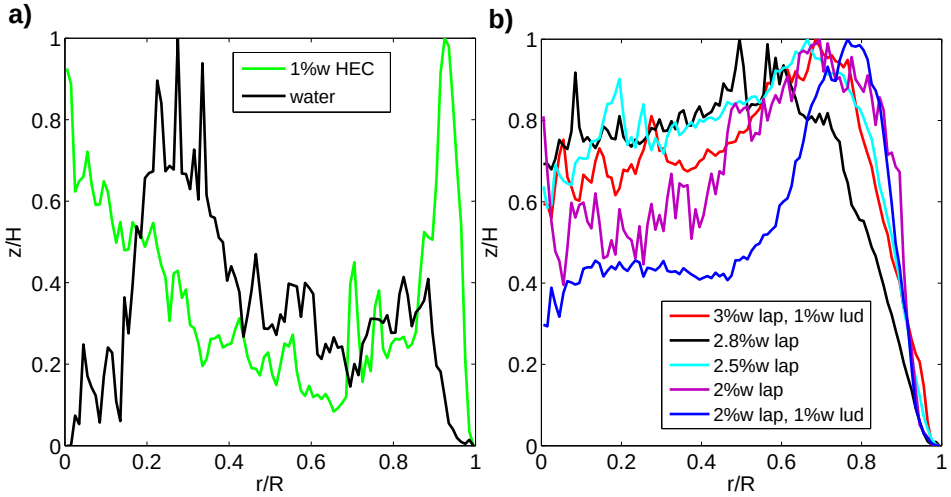

Figure 5.17. Azimuthally averaged height profiles taken on a white light interferometer, for deposits of a) water droplets containing 1%w 200 nm polystyrene spheres with and without HEC, and b) various concentrations of laponite and colloidal silica. The deposit height, z, at a radius, r, from the deposit centre is normalised by the maximum height of the deposit, H. R is the deposit radius.

formed fairly flat deposits (Fig. 5.17b) while the 2%w suspension had a dip at the centre, indicating that gelation took place too late in the drying process to suppress ring formation completely.

While laponite generated spatially more uniform deposits, it had the negative effect of promoting aggregation of the PS colloids during the drying process, as shown by the many large aggregates in Fig 5.15c–e. A possible

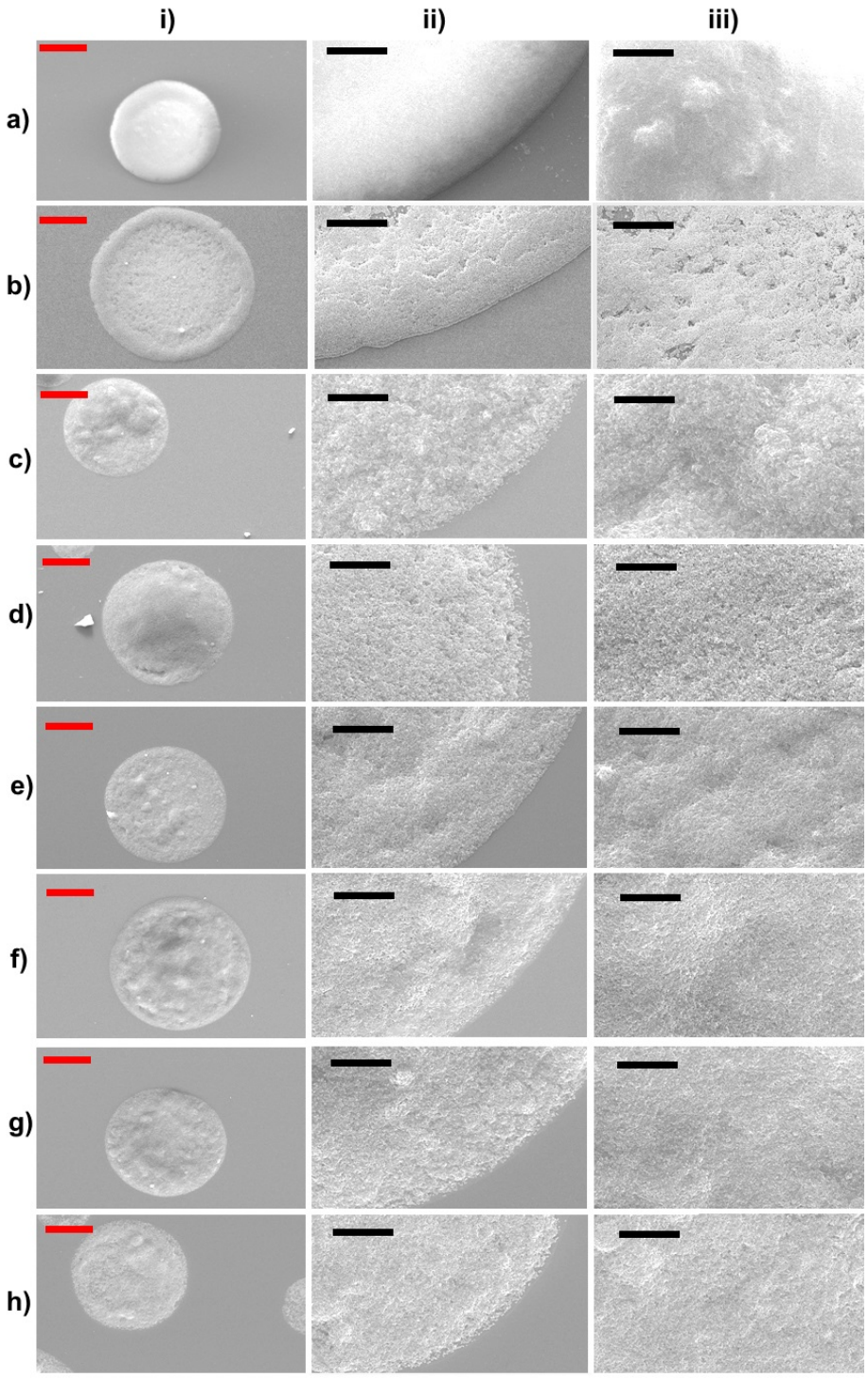

Figure 5.18. SEM images of deposits containing 5%w 200 nm spheres. a) pure water, b) 1%w HEC, c) 2%w laponite, d) 1%w laponite, e) 0.8%w laponite, f) 2%w laponite and 1%w colloidal silica, g) 1%w laponite and 1%w colloidal silica, and h) 0.8%w laponite and 1%w colloidal silica. Segments show i) the whole droplet (400× magnification, red scale bar 50 μm), and zooms (2500× magnification, black scale bars 10 μm) to ii) the contact line and iii) the interior. Substrates were as-received glass.

explanation is that the laponite plates with positively charged edges can bridge the negatively charged PS spheres. These large aggregates give rise to an undesirable rough texture in the deposits. In order to suppress aggregation of the PS spheres induced by the laponite, 1%w colloidal silica was added to the 2%w laponite solution. The silica reduced the number of large aggregates and produced a much smoother surface texture (compare Fig. 5.15e and Fig. 5.15f). The suspensions containing colloidal silica were less effective at suppressing the ring stain. It is possible that the lower critical strain in suspensions containing silica (Table 5.2) reduces the ability of loose aggregates to remain connected under the gentle shear within the drying droplet. Without connectivity throughout the suspension, the elasticity cannot recover. Consequently, particles move outwards with the radial flow and build-up a ring, similar to pinned droplets without laponite (Fig. 5.17b). To increase the critical strain, the laponite concentration was increased to 3%w at fixed silica concentration and obtained a fairly uniform pancake deposit (Fig. 5.17b). However, aggregates formed once again (Fig. 5.15g) indicating a trade-off between ring-suppression and aggregate-formation dependent on the laponite to silica ratio, which would have to be optimised in an ink formulation.

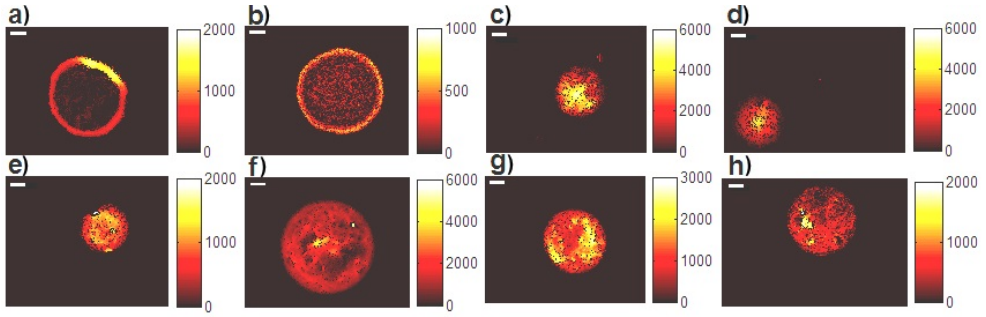

Figure 5.19. Height profiles taken on a white light interferometer, for an example deposit from droplets containing 5%w 200 nm polystyrene spheres and a) pure water, b) 1%w HEC, c) 2%w laponite, d) 1%w laponite, e) 0.8%w laponite, f) 2%w laponite and 1%w colloidal silica, g) 1%w laponite and 1%w colloidal silica, and h) 0.8%w laponite and 1%w colloidal silica. The colour scale shows the deposit height in nm. The white scale bar is 50 μm.

SEM micrographs of dry deposits formed from suspensions of 5%w PS spheres are shown in Figure 5.18, with interferometric profiles in Figure 5.19 and azimuthally averaged height profiles in Figure 5.20. For both pure water and 1%w HEC, the footprint of the drop was completely covered by polystyrene

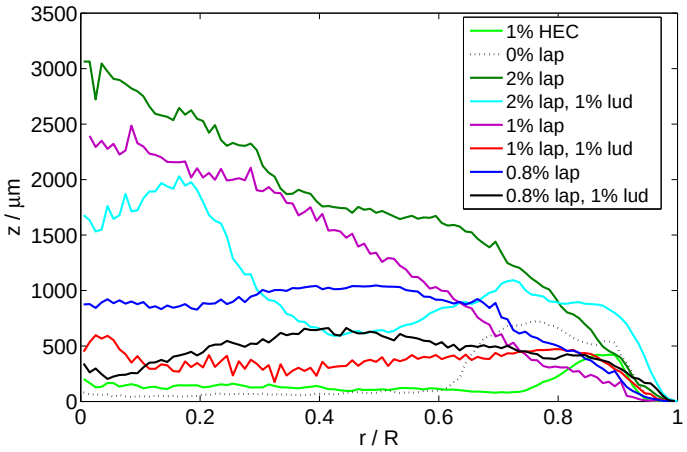

Figure 5.20. Azimuthally averaged height profiles taken on a white light interferometer, for deposits of water droplets containing 5%w 200-nm polystyrene spheres and either HEC or various concentrations of laponite and colloidal silica. The deposit height, z, at a radius, r, from the deposit centre shown, where the radius is normalised by the maximum radius of the deposit, R.

spheres, but there was a pronounced ring stain (Fig. 5.18a–b). On addition of 2%w or 1%w laponite, the deposit had a domed morphology with large aggregates (Fig. 5.18c) or cracking near the periphery (Fig. 5.18d). The sol–gel transition occurred too quickly to allow sufficient radial motion of the polystyrene particles. The vertical profile of the deposit was then thicker where the droplet was highest. The presence of a high concentration of PS nanospheres appears to reduce the amount of laponite needed to form a gel. Reducing the laponite concentration to 0.8%w delayed gelation and yielded a fairly flat pancake. However, the presence of large aggregates resulted in uneven deposition and a rough surface texture (Fig. 5.18e). Further addition of 1%w of colloidal silica reduced the peripheral cracking in the 1%w laponite droplet (Fig. 5.18g) and the number of aggregates in the 0.8%w laponite deposit (Fig. 5.18h), though aggregates still remained in the 2%w laponite droplet (Fig. 5.18f).

The networking properties of the laponite/colloidal silica mixtures will depend on the ratio of laponite to colloidal silica and the gelation point also depends on the total solid volume fraction (including the polystyrene spheres). No attempt was made to optimise this formulation, but the flatness and uniformity of the profile formed from the 1%w laponite droplet containing 1%w

colloidal silica is already very encouraging.

5.4. Summary

Formulation of colloidal suspensions for inkjet printing is a complex problem that involves balancing the competing requirements of the fluid. The formulation must be stable during storage, jettable from an inkjet printhead, and it must dry on the substrate to give the desired morphology of the deposit. This section has focused on the last of these problems, and specifically on counteracting the "ring stains" that arise from convective flow towards a pinned contact line. The capillary numbers in inkjet printed droplets are exceedingly low ($\backsim 10^{-6}$), and an increase in viscosity alone during drying was inadequate to prevent the formation of a ring stain.

Fluids that undergo a sol−gel transition as the concentration of the structuring agent increases generate elasticity in the fluid. If the yield stress of the fluid exceeds the capillary pressure, then the convective flow to the contact line (which generates the ring stain) may be stemmed. It has been shown that an evaporation-driven sol−gel transition in laponite suspensions can be used to control the morphology of a deposit for a model colloidal suspension (comprising sterically stabilised latex spheres). The enhanced evaporation rate near the contact line causes the droplet to gel first at its rim, with the gelled region progressing inwards to the centre of the droplet. By controlling the laponite concentration, and hence the timing of the gelling, the amount of radial flow required to generate a uniform deposit can be dictated: too little radial flow and a domed structure forms, too much and a ring stain is produced.

The non-Newtonian rheology of the fluid is an essential component in the formulation. To be stable during storage, the initial suspension is required to have a yield stress, which arises from the network formed between the nanoparticulate plates of the clay. Under the high shear of the inkjet nozzle, the network breaks down and the fluid shear thins such that its Ohnesorge number is within the compatible range of the inkjet printhead. The finite time taken to rebuild the laponite network is also important: if the network rebuilds too quickly, the droplet will gel before it begins to dry and a domed deposit will

result; if it is too slow the droplet will gel too late in the drying process, after the ring stain has begun to form. The recovery time of the network decreases as the laponite concentration increases, and it is the balance of the increasing concentration of laponite during drying and the corresponding decrease in the recovery time that provides the necessary control over the gelling of the droplet.

The presence of laponite in the formulation had a further benefit of pinning the contact line throughout drying and enabling the formation of a circular deposit of well-defined diameter.

The addition of a new component to a formulation can have undesirable side-effects. In this case, it was found that laponite was prone to induce aggregation of the latex spheres. Colloidal silica was found to be a suitable additive for reducing large scale aggregation and providing a smoother surface texture to deposits. However, the colloidal silica reduced the critical strain of the laponite suspensions, which favoured the formation of ring staining. A careful balance of the silica to laponite ratio was needed to ensure a flat deposit profile with reduced aggregation and a smooth surface texture, while maintaining suitable rheological properties for storage and jetting.

6 | Combining deposit fixing strategies and particle migration

6.1. Introduction

Strategies to control the distribution of deposited material are important for improving the resolution and quality of printed lines. Most inkjet applications require a uniform deposit, with the printed material completely filling a circular pinned contact line. However, security printing aims to create deposit morphologies and structures that are not easily reproducible without knowledge of the manufacturing method [228]. In this case, a range of possible deposit "fixing" strategies are required for altering the distribution of deposited material.

High resolution printing is another example where a pinned contact line may not be optimal. A high resolution is preferable for printed electronics, where smaller device sizes are desirable. Better resolution can be achieved by jetting droplets of smaller diameter. Alternatively, the combination of a moving contact line and weak particle-substrate interactions can allow material to be dragged inward with the contact line and to form a small dot [109]. Typically, a hydrophobic substrate and low surface tension fluid is required to allow sufficient de-pinning of the contact line.

An ink must be stable throughout its lifetime on the shelf and during its time in the print-head. However, destabilisation after ejection from the print-head can lend a method for altering the deposit. Aggregation provides an alternative strategy for fixing a particular distribution of deposited material during the drying process. The aggregation of colloidal particles can lead to strong attractive forces between particles, greatly affecting the end deposit.

Some methods for inducing aggregation utilise the ionic strength, polymeric additives, or a sol-gel transition.

When developing fixing strategies in binary solvent mixtures, the stabilisation mechanism of the colloidal particles should be considered. Usually colloidal particles are charge-stabilised or sterically-stabilised. In charge-stabilised colloidal suspensions, particles are attracted together by van der Waals forces and kept apart by electrostatic repulsion. For the charge-stabilised polystyrene spheres used in this thesis, the surface is populated with negatively charged sulphate groups. Counter-ions (positively charged in this case) are attracted towards the surface of the spheres, while co-ions (negatively charged in this case) are repelled. An electrical double layer results from the excess of counter-ions adsorbed to the surface of the sphere, partially negating the surface charge (see Fig. 6.1). The remaining counter-ions are in the diffuse part of the double layer. The resulting electrostatic potential decays monotonically with distance from the surface of the sphere. The electric double layer screens repulsions between particles at distances greater than the Debye length, r_{D}, which is defined as

$$r_{\mathrm{D}} = \sqrt{\frac{\epsilon_{\mathrm{r}}\epsilon_0 k_{\mathrm{B}} T}{2 N_{\mathrm{A}} e^2 I}}, \tag{6.1}$$

where N_{A} is Avogadro's constant, e is the elementary charge, I is the ionic strength, ϵ_{r} is the dielectric constant, ϵ_0 is the relative permittivity of free space, k_{B} is the Boltzmann constant and T is the temperature.

For a sterically stabilised colloidal suspension, entropic repulsion due to the overlap of polymer chains adsorbed or grafted to the particle surface can prevent aggregation. The number of available conformations of the polymer is thus reduced.

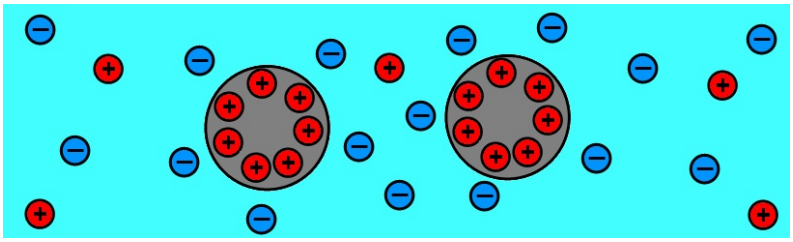

Figure 6.1. Cartoon of an electrical double layer between particles in a colloidal suspension.

As a droplet of a solvent mixture evaporates, the composition of the mixture changes to become richer in the least volatile component. For ethanol/water mixtures, as the droplet evaporates and the composition becomes more water-rich, the Debye length increases (as $r_{\mathrm{D}} \propto {\epsilon_{\mathrm{r}}}^{1/2}$). Often, salt is added to formulate a stable ink. However, as the solvent evaporates and the ionic concentration increases, the ink can become unstable when the Debye length decreases ($r_{\mathrm{D}} \propto I^{-1/2}$). The competition of these effects determines the stability of the charge-stabilised suspension.

For a sterically stabilised suspension, the distance the stabilising polymer chains extend from the particle depends on the solvency of the polymer. Chains are extended in a favourable solvent and contracted in an unfavourable solvent. If the solvent composition tends towards a less favourable solvent during drying, then the steric stabilisation could fail, causing aggregation.

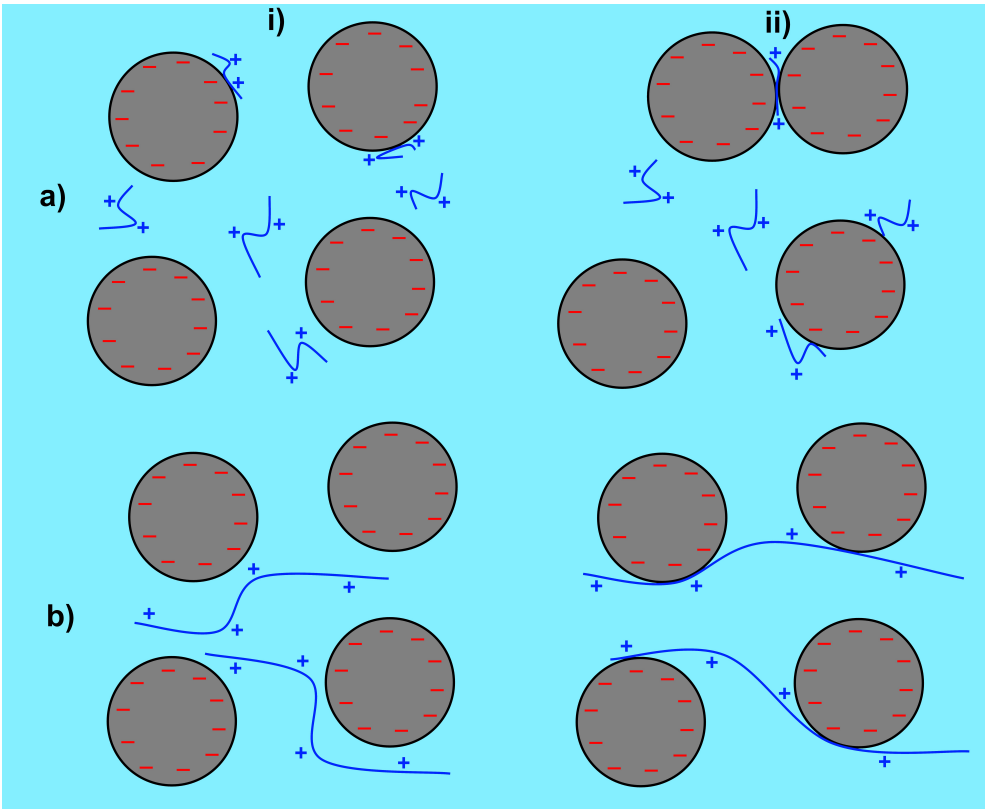

Figure 6.2. Cartoon of flocculation mechanisms for adsorbing polymers. a) Charge-patch interaction, where i) the polymer adsorbs to the surface of the particle forming a "patch" of opposite charge, and ii) electrostatic interactions between the "patch" and oppositely charged surface of another particle causes flocculation. b) Bridging flocculation occurs when a high molecular weight polymer adsorbs to multiple particles at once.

Other methods to induce aggregation in particulate suspensions commonly use the addition of polymers. For polymers which adsorb to the suspended particles, there are two main methods of flocculation; charge-patch interaction [229,230] and bridging flocculation [231–233] (see Fig. 6.2). Charge-patch interaction occurs when a polyelectrolyte adsorbs onto the surface of an oppositely charged particle and locally overcompensates the surface charge. The adsorbed polyelectrolyte forms a region of opposite charge (hereafter a "patch") on that particle. Electrostatic interactions between the patch and the oppositely charged surfaces of other suspended particles can then ensue, resulting in small flocs.

Bridging flocculation can occur when a high molecular weight polymer is used. The long polymer chains can then adsorb onto multiple particles, forming a "bridge". Polymer bridges tend to break down under high shear and are not as easy to reform as the charge-patch interaction.

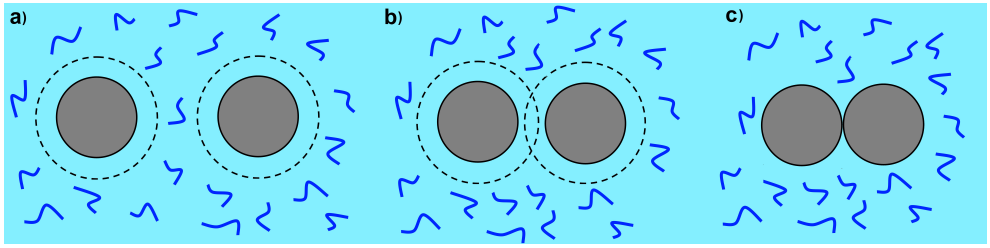

Figure 6.3. Cartoon of depletion flocculation. a) When the particles are far apart, free non-adsorbing polymer surrounds the particles on all sides, excluded only from the volume immediate to the particles. b) When the particles move close together, polymer chains are excluded from the overlap region. c) The osmotic pressure drives the particles together, forming an aggregate.

When the free polymer does not adsorb to the particles, a common route to aggregation is via depletion flocculation [234–237]. In this case, when the particles approach one another the free polymer is displaced from the region of overlap of the exclusion zones of the particles (see Fig. 6.3). It is always energetically more favourable for polymer to leave the gap between the particles than for the polymer to change conformation. The larger osmotic pressure outside the overlap region causes attraction of the particles, resulting in flocculation.

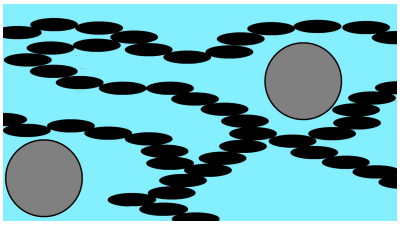

Figure 6.4. Cartoon of a network (black) preventing the motion of larger particles (grey).

If the aggregates grow large enough to percolate through the suspension, a networked structure can form (e.g. Fig. 6.4). Polymers can also form networks, which may restrict the motion of particles, reducing radial flow in a drying droplet. If the elasticity increases sufficiently, the material may develop a finite yield stress and form a gel. In Chapter 5, nanoparticles of laponite were considered as a room temperature gelling agent and demonstrated a sol−gel transition during evaporation. The gel had a significant effect on the distribution of larger particles within the deposit.

In Chapter 4, the migration of particles in binary mixtures to the centre of droplet was discussed. Particles inside ethanol/water mixtures concentrated at the centre of the evaporating droplet with a typical group radius of $R_{g,min} \backsim R/3$ (where R is the droplet radius), leaving a region depleted of particles near the contact line. Once the Marangoni flow period ended, radial flow carried particles to the contact line forming a ring stain. Strategies for fixing the particles at the centre of the droplet after collection are now investigated to prevent radial flow from determining the end morphology of the deposit. The sol−gel transition (seen in Chapter 5) was investigated for use with binary mixtures, and a depletion flocculation mechanism using polystyrene sulfonate (PSS, see Fig. 6.5) was explored. Printing of deposits with a narrower final footprint than the initial droplet could improve the printing of high resolution lines of compact material for conductive tracks.

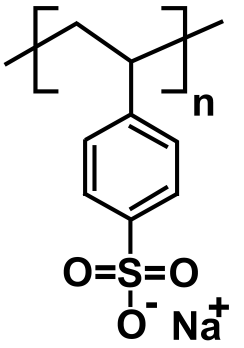

Figure 6.5. Chemical structure of polystyrene sulfonate (PSS).

6.2. Experimental

For the sol-gel fixing strategy, laponite suspensions (RD grade, Rockwood) in ethanol/water were prepared. The laponite was first added gradually to the water (MilliQ), with agitation between each addition, and sonicated to form a clear suspension. The ethanol (Sigma Aldrich, 99.9%) was then added, and further agitation and sonication ensured a mixed, clear suspension. The order of addition is important, as adding the laponite to an ethanol/water mixture resulted in a cloudy flocculated suspension even after sonication. To observe the effect of the laponite sol-gel transition on larger particles within the suspension, 1 μm polystyrene spheres were added at a concentration of 0.1%v. In this case, the laponite is added to the polystyrene solution (in water) and following sonication the ethanol is added.

For the depletion flocculation fixing strategy, polystyrene sulfonate (PSS, Sigma Aldrich, MW 70 $\mathrm{kg\,mol^{-1}}$) was used as the free non-adsorbing polymer. The PSS was dissolved in water and left overnight. Ethanol was then added and the solution was shaken to ensure full mixing. Last, the 1 μm polystyrene spheres (in water) were added to give a concentration of 0.1%v. The suspensions were formulated with regard to the PSS concentration that would remain after evaporation of all the ethanol in the sample (i.e. the PSS concentration in the water alone). Hence, the values for the PSS concentration in the entire mixture are not nicely rounded numbers. Table 6.1 compares the PSS concentration in 1 ml of a 50%v ethanol/water mixture with the PSS concentration in the water phase alone.

Table 6.1. Example composition for 1 ml of a PSS solution.

Ethanol / %v	Ethanol / g	Water / g	PSS / g	PSS / %w in water alone	PSS / %w in entire mixture
50	0.395	0.500	15×10^{-3}	3.00	1.7
50	0.395	0.500	5×10^{-3}	1.00	6.0×10^{-1}
50	0.395	0.500	5×10^{-4}	0.10	6.0×10^{-2}
50	0.395	0.500	5×10^{-5}	0.01	6.0×10^{-3}

Picolitre droplets were deposited onto plasma fluorinated glass substrates using a Microfab device (as described in Chapter 2, Section 1). Preparation of the coated substrates was described previously in Chapter 3, Section 3.2.2. Dark field images during drying and of the end deposits were recorded (as described in Chapter 2, Section 2.1) on the inverted microscope. Rheology measurements were collected as described in Chapter 2, Section 2.4.

6.3. Sol-gel fixing strategy in binary solvent mixtures

In this section, particle migration in ethanol/water droplets was used to collect particles at the centre of an evaporating droplet. Laponite was included in the binary solvent mixture to induce an evaporation-driven sol−gel transition, restricting the radial motion of particles towards the contact line. The aim was to tailor the laponite concentration and ethanol content such that particles are retained at the centre of the droplet in the end deposit.

6.3.1. The rheology of laponite/ethanol/water mixtures

The viscosities and sol-gel transitions in laponite suspensions formed with organic solvent mixtures are not the same as in the water droplets discussed in Chapter 5, Section 3.1 [238]. Here, the rheology of laponite/ethanol/water mixtures is considered in order to optimise the composition for "fixing" the collected group. Ideally, radial motion of the particles must be prevented to stop evaporation driven-flow transporting particles outward from the droplet centre. However, the viscosity of the suspension must initially be sufficiently low that migration of particles towards the centre of the droplet is not hindered. To achieve this aim, the shift in gel point and recovery of the laponite network is considered with regard to ethanol concentration. This is particularly important as the composition of the mixture becomes more water-rich as ethanol evaporates during drying.

Inverted bottle experiments for laponite/ethanol/water mixtures show the general concentration of laponite at which the sol−gel transition takes place for various ethanol content (Fig. 6.6). The transition from a viscous sol to a gel capable of holding its own weight occurs between 2.8−3.0%w laponite in

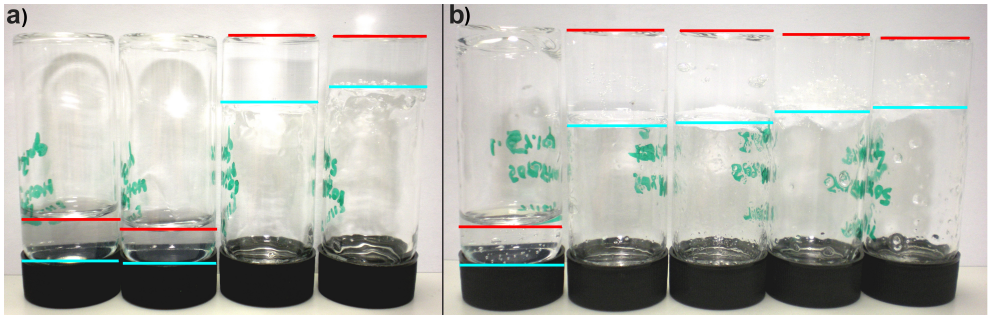

Figure 6.6. Inverted bottle experiments for laponite/ethanol/water mixtures with a) 10%v ethanol. From left to right laponite concentrations are 2.5%w, 2.8%w, 3.0%w and 4.0%w. b) For 50%v ethanol with concentrations from left to right of 1.5%w, 2.0%w, 2.5%w, 3.0%w and 4.0%w. Red lines show the upper level of the suspension and cyan lines the lower level.

10%v ethanol/water, and between 1.5−2.0%w laponite in 50%v ethanol/water. Hence, the gel point is lowered at higher ethanol concentrations. This hinders the fixing strategy, as ethanol is depleted during drying (increasing the gel point).

Table 6.2 presents the yield stresses of laponite suspensions in 10%v ethanol/water and 50%v ethanol/water. A 3%w laponite suspension in 10%v ethanol/water forms a gel with a similar yield stress to 1.5%w laponite in 50%v ethanol/water. As with laponite suspensions in water (see Chapter 5, Section 3.1), laponite suspensions in ethanol/water show an increase in the yield stress with laponite concentration (at fixed ethanol content).

Table 6.2. Yield stresses determined by oscillatory measurements for laponite suspensions in ethanol/water at various laponite concentrations.

Laponite / %w	Ethanol / %v	Yield Stress / Pa
2.5	10	n/a
3.0	10	6
4.0	10	29
5.0	10	99
1.5	50	5
2.0	50	26
2.5	50	24

The gels formed by the laponite/ethanol/water suspensions were shear-thinning, with the networked structure breaking down at high shear rates (Figs.

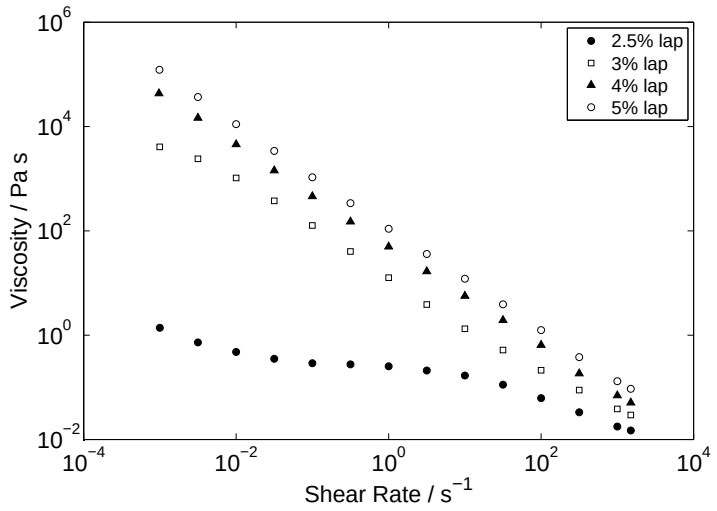

Figure 6.7. Shear viscosity of laponite suspensions in 10%v ethanol/water with various laponite concentrations over a range of shear rates.

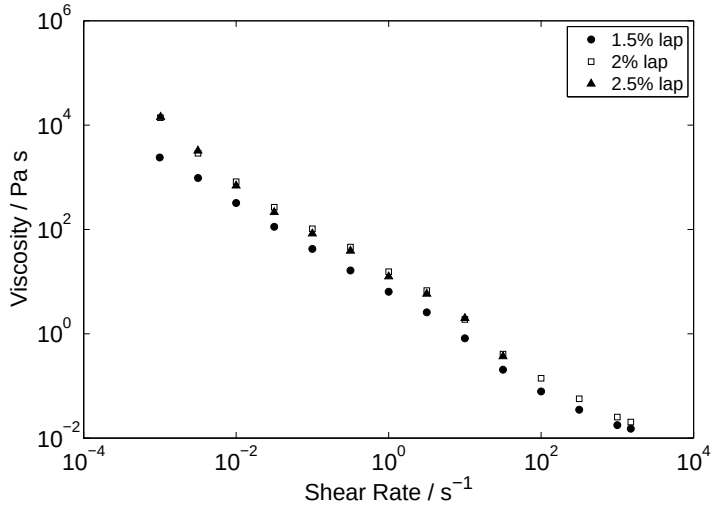

Figure 6.8. Shear viscosity of laponite suspensions in 50%v ethanol/water with various laponite concentrations over a range of shear rates.

6.7 and 6.8). The viscosity of the suspensions increased at higher laponite concentrations. At low shear rates, suspensions with higher ethanol content required less laponite to reach the same viscosity.

Figures 6.9 and 6.10 present the recovery of the shear viscosity for laponite suspensions in ethanol/water mixtures after a period of high shear. For a suspension of fixed ethanol concentration, the shear viscosity recovered faster with higher laponite content (as with the laponite/water suspensions in Chapter 5). At fixed laponite concentration (2.5%w), the recovery of the shear viscosity for the 10%v ethanol (Fig. 6.9) was slower than for the 50%v ethanol (Fig.

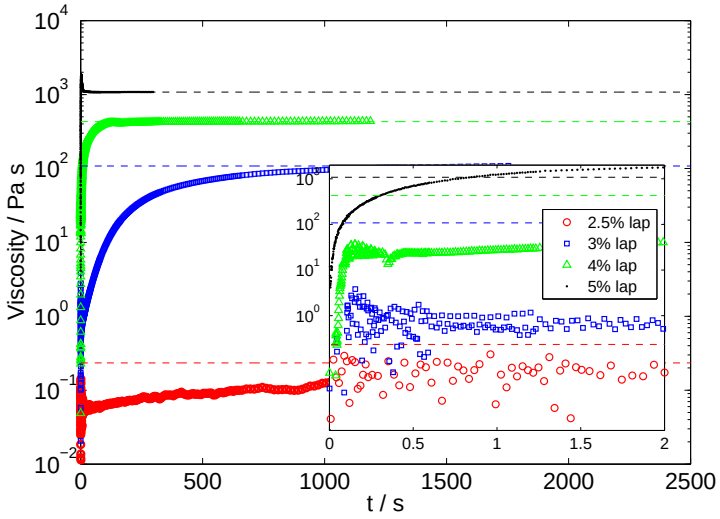

Figure 6.9. Recovery of the shear viscosity for laponite suspensions in 10%v ethanol/water. The inset provides a zoomed version of the first 2 s of recovery.

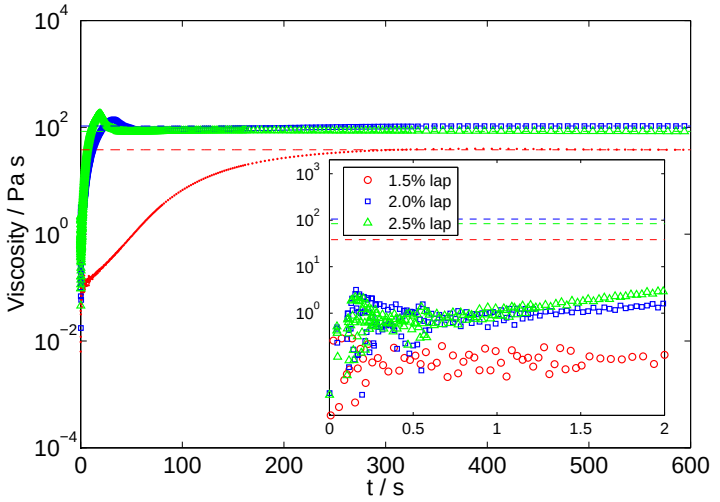

Figure 6.10. Recovery of the shear viscosity for laponite suspensions in 50%v ethanol/water. The inset provides a zoomed version of the first 2 s of recovery.

6.10). This suggests that the ethanol increased the speed at which the laponite network reformed large aggregates for a fixed laponite concentration. However, comparing a 10%v ethanol/water mixture (containing 4%w laponite) with a 50%v ethanol/water mixture (containing 2.0%w laponite), whose yield stress values are similar (see Table 6.2), the shear viscosity of the laponite suspension in 10%v ethanol/water recovered faster. This suggests that for a given yield stress, an increased ethanol concentration increases the recovery time.

As a droplet of laponite/ethanol/water dries, ethanol evaporates preferentially. Therefore, during drying, the ethanol concentration within the laponite suspension will decrease, changing the composition towards a laponite suspension in pure water. For the ethanol/water droplets in Chapter 4, Section 4.3, the ethanol was not completely depleted when $R_{g,min}$ was reached. For example, a 50%v ethanol/water droplet exhibited the minimum collection radius after losing 40%v at RH 0.5 and after losing 60%v at RH 0.26. For the sake of comparison, assume that $R_{g,min}$ occurs once all the ethanol is depleted. The volume lost on evaporation of all the ethanol from a 50%v ethanol/water droplet is taken to be 50%v (in practice this will not be the case, water will also be lost depending on the RH). Hence, a 2%w laponite solution in 50%v ethanol will become a 3.6%w laponite suspension in water once all ethanol is depleted (which is compared here with 4%w laponite in ethanol/water). Table 6.3 lists the assumed laponite concentration following evaporation of all the ethanol.

Table 6.3. Example composition for 1 ml of a laponite suspension and the approximate laponite concentration once the ethanol has evaporated.

Ethanol / %v	Ethanol /g	Water /g	laponite /g	laponite / %w in entire mixture	laponite / %w in water alone
50	0.395	0.500	0.018	2.0	3.6
10	0.079	0.899	0.020	2.0	2.2

There are two factors to consider for the viscosity and recovery of laponite suspensions in ethanol/water during drying: First, the laponite concentration increases during drying as the solvent volume decreases. From Figures 6.9 and 6.10, the viscosity increases and the recovery time decreases at higher laponite concentration. However, there is a second factor resulting from the decrease in the ethanol concentration during drying. Figures 6.11 and 6.12 compare the recovery in the shear viscosity of laponite/ethanol/water suspensions (closed data points) with their approximate laponite/water counterparts after all ethanol has evaporated (open data points). For laponite suspensions in 50%v ethanol/water (Fig. 6.11), the viscosity increases during drying and the reco-

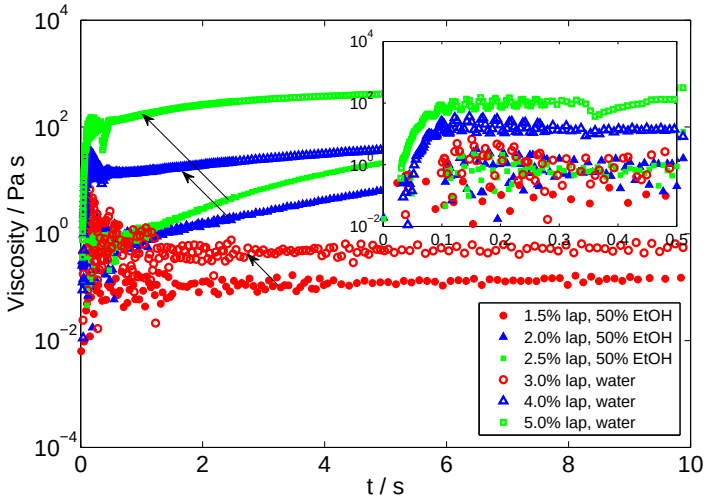

Figure 6.11. Recovery of the shear viscosity for laponite suspensions in 50%v ethanol/water compared to laponite/water suspensions with a laponite concentration following evaporation of the ethanol. The inset shows a zoom to the first 0.5 s of recovery. Arrows indicate whether the viscosity would increase or decrease as ethanol is depleted during drying (and the laponite concentrates). Suspensions were aged overnight.

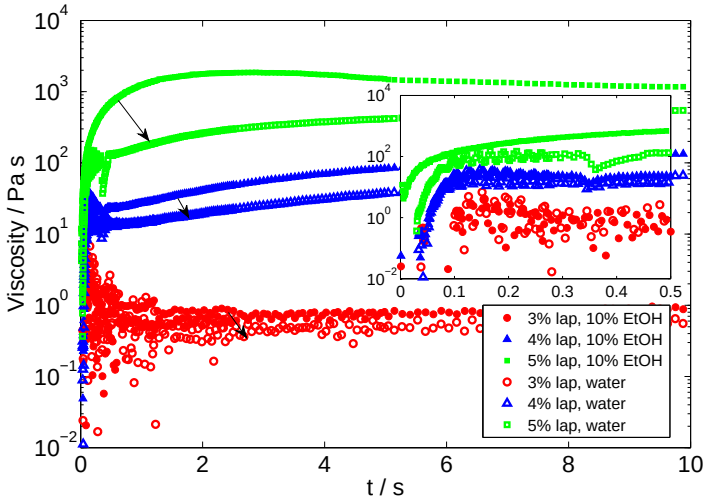

Figure 6.12. Recovery of the shear viscosity for laponite suspensions in 10%v ethanol/water compared to laponite/water suspensions with a laponite concentration following evaporation of the ethanol. The inset shows a zoom to the first 0.5 s of recovery. Arrows indicate whether the viscosity would increase or decrease as ethanol is depleted during drying (and the laponite concentrates). Suspensions were aged overnight.

very time decreases (i.e. as the suspension is depleted of ethanol). This is not the case for laponite suspensions in 10%v ethanol/water, which exhibit a decrease in the viscosity and an increase in the recovery time throughout drying (Fig. 6.12, though it is difficult to distinguish what occurs at short timescales). The initial ethanol concentration can therefore result in either an increase or

a decrease in the viscosity and recovery time during drying. Consideration of both of these factors is important when choosing the initial suspension composition for a fixing strategy. An increase in the recovery of the shear viscosity should correspond with recovery of the elasticity, which is beneficial for fixing particle positions. However, if the viscosity and elasticity recover too quickly, then Marangoni flow and particle migration will be hindered. Additionally, the initial viscosity must be low enough to jet from an inkjet device (accounting for shear-thinning).

To complicate matters, the diffusion time of the ethanol is much faster than that of the laponite. Additionally, the mutual diffusion coefficient of ethanol (D_{ew}) increases as the ethanol concentration decreases (for $\leq 60\%$v ethanol), but remains of the order of $10^{-9}\,\mathrm{m^2\,s^{-1}}$. Thus, for a droplet with a height of 20μm, the time for ethanol to diffuse the height of the droplet to the liquid-vapour interface is $t_{\mathrm{diff}} \backsim h^2/2D_{\mathrm{ew}} \backsim 0.2\,\mathrm{s}$. For laponite disks, the average diffusion coefficient, D_{av}, depends on the diffusion coefficient perpendicular to ($D_\perp$) and parallel to the face of the disk ($D_\parallel$), as

$$D_{\mathrm{av}} = (2D_\perp + D_\parallel)/3, \tag{6.2}$$

where $D_\perp$ and $D_\parallel$ can be related to the diffusion coefficient of a sphere with the same radius as the disk [239], D_{sp}, by

$$D_\perp = 1.72 D_{\mathrm{sp}}, \tag{6.3}$$

and

$$D_\parallel = 1.18 D_{\mathrm{sp}}. \tag{6.4}$$

The diffusion coefficient for a sphere is

$$D_{\mathrm{sp}} = \frac{k_{\mathrm{B}} T}{6\pi\eta a}, \tag{6.5}$$

where k_{B} is the Boltzmann constant, T is the temperature, η is the viscosity of the fluid, and a is the radius of the sphere. In water ($\eta \backsim 1\,\mathrm{mPas}$), for a laponite disk with a radius of 15 nm and thickness of $\backsim 1\,\mathrm{nm}$, $D_{\mathrm{sp}} \backsim 1\times10^{-11}\,\mathrm{m^2\,s^{-1}}$ and $D_{\mathrm{av}} \backsim 2\times10^{-11}\,\mathrm{m^2\,s^{-1}}$. Thus, for a droplet with a height of 20μm, the time for

laponite to diffuse the height of the droplet to the liquid-vapour interface is $t_{\text{diff}} \backsim h^2/2D_{\text{av}} \backsim 10\,\text{s}$, which is longer than the droplet lifetime.

For streamlines passing close to the liquid-vapour interface, the laponite concentration increases faster than the ethanol concentration decreases (due to relative diffusion rates). The laponite causes faster gelation at increased laponite concentrations and increased ethanol concentrations. Thus, as the ethanol is depleted, gelation is inhibited. Conversely, as the laponite concentrates during evaporation, gelation is aided. In the bulk, the ethanol concentration decreases faster than the laponite concentration increases, which will hinder gelation. Hence, gelation may be slower at the centre of the droplet.

6.3.2. Deposits from laponite/ethanol/water mixtures

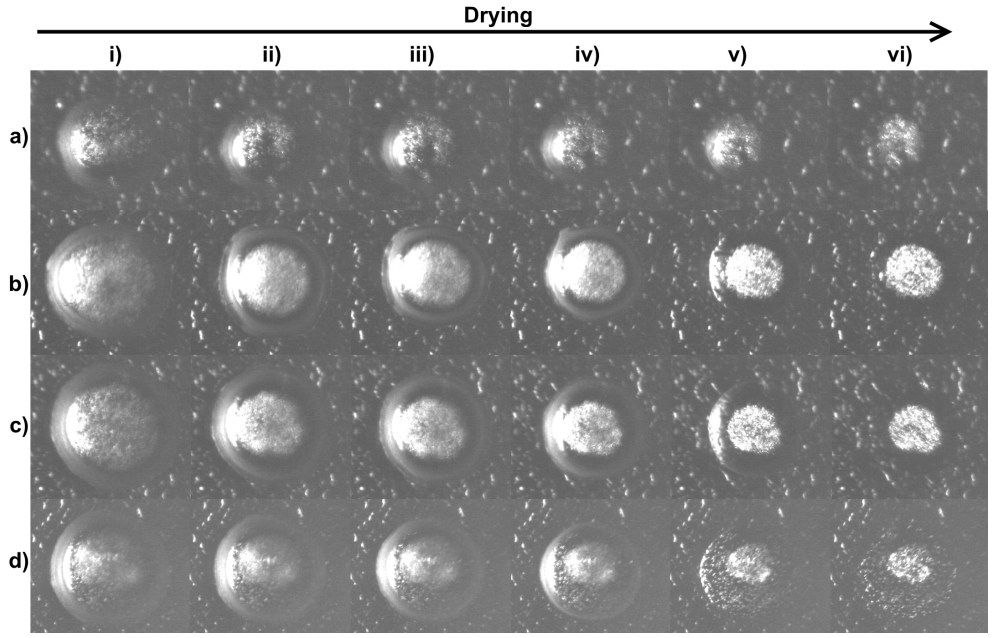

Figure 6.13. Dark field images of drying droplets of laponite/ethanol/water suspensions containing 10%v ethanol and a) 1.5%w laponite, b) 2.0%w laponite, c) 2.5%w laponite and d) 2.8%w laponite. Laponite suspensions were aged overnight. Images were taken after i) $0.1\,t_{\text{dry}}$, ii) $0.2\,t_{\text{dry}}$, iii) $0.3\,t_{\text{dry}}$, iv) $0.5\,t_{\text{dry}}$, v) $0.8\,t_{\text{dry}}$ and vi) $1.0\,t_{\text{dry}}$.

The images in Figures 6.13 and 6.14 confirm that particle migration occurs with laponite/ethanol/water suspensions. The laponite does not alter the surface tension [240] sufficiently to prevent the solutal Marangoni flows.

For laponite suspensions in 10%v ethanol/water, laponite concentrations

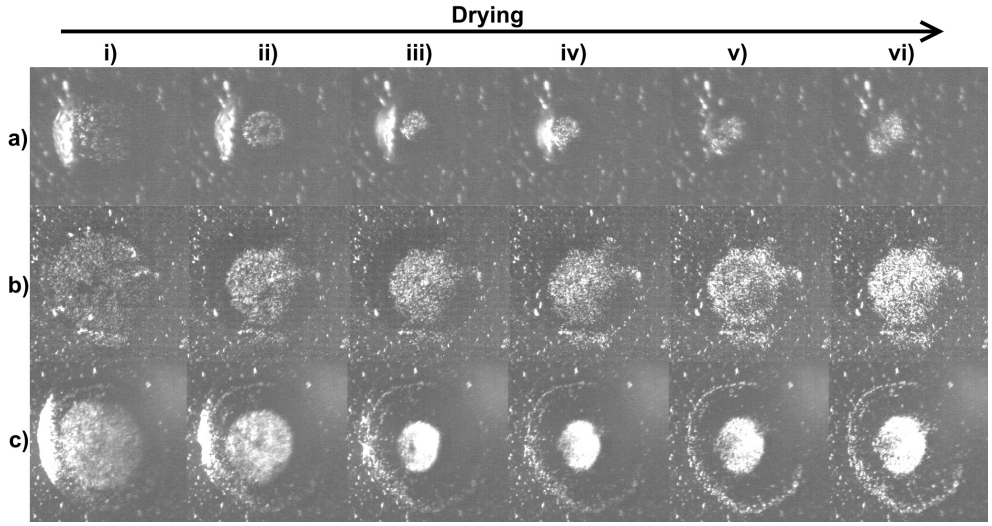

Figure 6.14. Dark field images of drying droplets of laponite/ethanol/water suspensions containing 50%v ethanol and a) 0.5%w laponite, b) 1.0%w laponite and c) 1.5%w laponite. Laponite suspensions were aged overnight. Images were taken after i) $0.1\,t_{\mathrm{dry}}$, ii) $0.2\,t_{\mathrm{dry}}$, iii) $0.3\,t_{\mathrm{dry}}$, iv) $0.5\,t_{\mathrm{dry}}$, v) $0.8\,t_{\mathrm{dry}}$ and vi) $1.0\,t_{\mathrm{dry}}$.

of 2.0%w and higher began to fix the particles at the centre of the droplet (Fig. 6.13b$-d$). The 1.5%w laponite suspension in 10%v ethanol/water did not inhibit radial flow of the particles to the contact line (Fig. 6.13a). For 2.0$-$2.5%w laponite, the end deposit was in between a central dot and a ring stain due to the de-pinning contact line. Note that the droplets in Figure 6.13 do not have a pinned contact line throughout the entirety of the drying lifetime. However particle collection at the centre follows the geometry of the contact line (i.e. an oval collection for an oval contact line), rather than the contact line sweeping particles inward. At an initial laponite concentration of 2.8%w, the viscosity near the contact line becomes too high at early times. Consequently, particle migration is not able to transport all the particles to the centre of the droplet. Particles remaining near the contact line become fixed in this region, resulting in a central dot and loosely packed ring stain.

At the higher ethanol concentration of 50%v, droplets with low laponite concentrations (0.5%w laponite) dried similarly to an ethanol/water droplet without laponite and a de-pinning contact line. When the laponite concentration was increased to 1%w, particle positions began to become "fixed" at the centre of the droplet during the radial flow period. After $R_{\mathrm{g,min}}$ was reached, radial flow began to carry particles outwards, but the sol$-$gel transition eventually inhibited the evaporation-driven flow such that particles from the

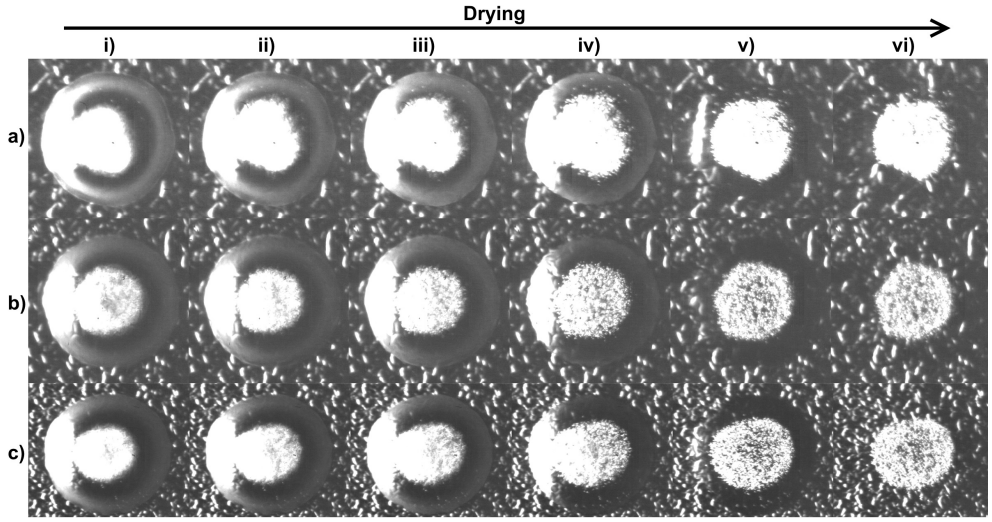

Figure 6.15. Dark field images of drying droplets of laponite/ethanol/water suspensions containing 10%v ethanol and a) 2.0%w laponite, b) 2.5%w laponite (corresponding Video LA1) and c) 2.8%w laponite. Laponite suspensions were freshly made. Images were taken after i) $0.1\,t_{\mathrm{dry}}$, ii) $0.2\,t_{\mathrm{dry}}$, iii) $0.3\,t_{\mathrm{dry}}$, iv) $0.5\,t_{\mathrm{dry}}$, v) $0.8\,t_{\mathrm{dry}}$ and vi) $1.0\,t_{\mathrm{dry}}$.

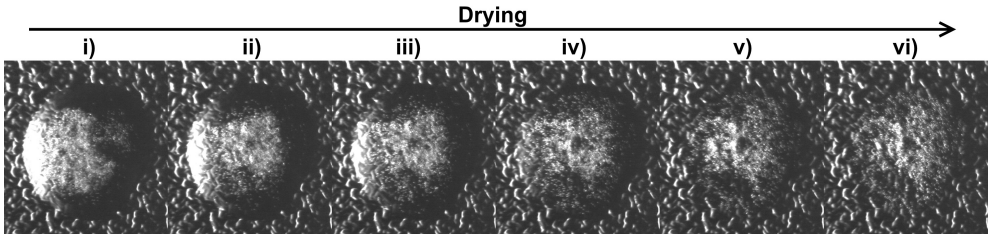

Figure 6.16. Dark field images of a drying droplet of laponite/ethanol/water suspension containing 50%v ethanol and 2.0%w laponite. Images were taken after i) $0.1\,t_{\mathrm{dry}}$, ii) $0.2\,t_{\mathrm{dry}}$, iii) $0.3\,t_{\mathrm{dry}}$, iv) $0.5\,t_{\mathrm{dry}}$, v) $0.8\,t_{\mathrm{dry}}$ and vi) $1.0\,t_{\mathrm{dry}}$.

central group did not reach the contact line. At 1.5%w laponite (in 50%v ethanol/water), a similar situation was observed for the 10%v ethanol/water droplet containing 2.8%w laponite. The increased viscosity at the contact line caused some particles to remain in this region while the others migrated to the centre of the droplet. Some radial flow of the central group occurred before "fixing", but a ring stain resulted from particles trapped near the contact line.

Freshly made laponite samples were also considered to determine the effects of ageing (see Fig. 6.15 and 6.16). For laponite suspensions in 10%v ethanol/water, the freshly made solutions reduced the formation of a ring stain better than those aged overnight. A laponite concentration of 2%w was sufficient to fix the particle distribution with a radius of 2/3 the initial droplet radius in a droplet with a pinned contact line. The best possible de-

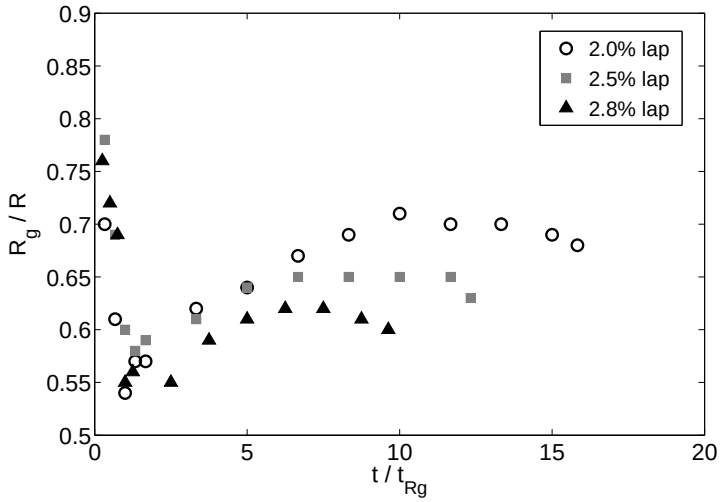

Figure 6.17. Evolution of the group radius, R_{g}, with time for fresh laponite suspensions in 10%v ethanol/water. Data are for a single representative droplet at each laponite concentration. Times are normalised by t_{Rg} (the time at which the minimum radius of the collected group is reached).

posit diameter that could be achieved corresponds to $R_{\mathrm{g,min}}$, which is $\backsim 1/3$ the initial droplet radius in ethanol/water droplets (see Chapter 4, Section 4.3). Note that the viscosity in the freshly made 2.8%w laponite suspension (in 10%v ethanol/water) does not become high enough near the contact line to prevent particles from migrating inwards. For the laponite suspensions in 50%v ethanol/water, central fixing was not achieved even at 2.0%w laponite content. Instead, radial flow carried particles towards the contact line, with some aggregation of the particles near the end of drying.

Figure 6.17 shows the progression of the collecting group for laponite suspensions freshly made in 10%v ethanol/water. For each laponite concentration, the collected group shrinks to a minimum radius before radial flow begins to carry particles outwards again, enlarging the group. As the laponite concentrates during evaporation, and due to the enhanced evaporative flux at the contact line, a sol−gel transition causes a gelling front to propagate from the contact line inwards. The radial motion of the particles is halted due to the elasticity of the gel, and the group radius becomes fixed. A higher laponite concentration "fixed" the particle group sooner after t_{Rg}.

There is a delicate balance between adding enough laponite to fix particles centrally, and to maintain a low enough viscosity during the Marangoni flow period that particle collection at the centre of the droplet is not suppressed.

The viscosity and elasticity must therefore not become too large before the Marangoni flow ends and radial flow begins. Additionally, while a high laponite concentration is desirable for fast recovery of the laponite network, the initial viscosity must be low enough that Marangoni flows and the migration of particles are not impeded. Thus, there is a trade-off between a high laponite concentration (to increase the recovery time) and a high ethanol concentration (to give a larger volume lost before radial flow), both of which increase the suspension viscosity. Additionally, the viscosity of laponite suspensions in 10%v ethanol decreased during drying while in 50%v ethanol the viscosity increased. Also, the recovery time of laponite suspensions in 10%v ethanol increased, while in 50%v ethanol the recovery time decreased. The higher ethanol concentrations then aided in the particle "fixing". The results of this section indicate that the most important factor is a high initial laponite concentration. Particle fixing for laponite in 10%v ethanol/water provided better results than in 50%v ethanol despite the decrease in viscosity and recovery time throughout drying. The lower ethanol content enabled a higher initial laponite concentration while maintaining a sol rather than a gel. For either ethanol concentration, "fixing" of the particles only occurred when the initial laponite concentration was close to the sol−gel transition.

6.4. Depletion flocculation in binary solvent mixtures

The second deposit fixing strategy in this chapter uses ethanol/water mixtures to bring particles into close proximity at the centre of the droplet. Depletion flocculation (driven by the exclusion of PSS) is then used to induce aggregation of the collected group.

Figure 6.18 demonstrates the depletion flocculation fixing strategy using PSS as the depletant. At a concentration of 6×10^{-3} %w PSS, particle migration to the centre of the droplet takes place and then radial flow occurs uninhibited, forming a ring stain (Fig. 6.18avi). The same behaviour is true of a 0.06%w PSS mixture. When the PSS concentration was increased to 0.6%w, the particles began to aggregate once collected at the centre of the droplet. However, the aggregation was not sufficient to retain a fixed group at

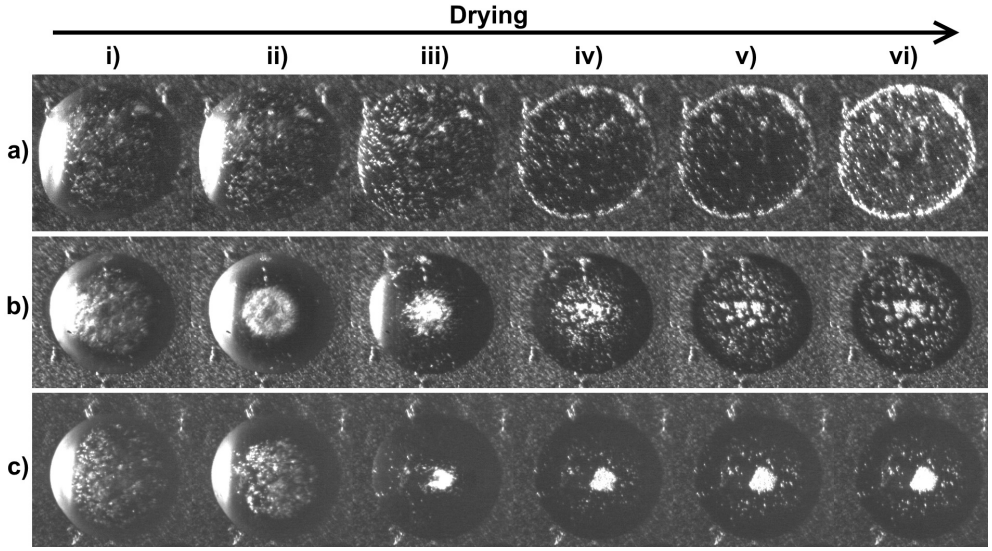

Figure 6.18. Dark field images of 50%v ethanol/water droplets containing a) $6{\times}10^{-3}$ %w PSS, b) 0.6%w PSS, and c) 1.7%w PSS. Images were recorded at i) $0.1\,t_{\mathrm{dry}}$, ii) $0.2\,t_{\mathrm{dry}}$, iii) $0.5\,t_{\mathrm{dry}}$, iv) $0.8\,t_{\mathrm{dry}}$, v) $0.9\,t_{\mathrm{dry}}$ and vi) $1.0\,t_{\mathrm{dry}}$.

the centre of the droplet. Instead, aggregates moved outwards with the radial flow (see Video PSS1). Smaller aggregates were more able to follow the flow and so moved father away from the centre than the larger aggregates, which settled. The result was a deposit with a gradient in aggregate size from the centre outwards, and no ring stain (Fig. 6.18bvi). At a PSS concentration of 1.7%w, the aggregation of the collected group was strong enough to keep most of the particles together as one large aggregate. Only a few single particles escaped to flow radially outwards. Additionally, the large aggregate remained central and was not displaced by the radial flow or de-pinning of the contact line at the end of drying. The final deposit was a central dot with a radius $R_{\mathrm{g}} \backsim 1/3\,R$ (see Fig. 6.18cvi and Video PSS2).

The counter-ions in the PSS solutions enhance the depletion flocculation as they increase the osmotic pressure. Additionally, the dielectric constant is reduced at higher ethanol concentrations, so the particles do not aggregate until the ethanol evaporates and the PSS is concentrated. This enhances the stability on the shelf and aids the "fixing" during drying.

6.5. Summary

Two strategies were developed to fix the particle distribution resulting from a dried ethanol/water droplet as a small central dot with a deposit radius smaller than the initial droplet radius. The first strategy utilised the evaporation-driven sol−gel transition in laponite suspensions to prevent particle motion radially outwards towards the contact line. The result was a central dot matching the shape of the contact line, with a deposit radius 2/3 the initial droplet radius. Recovery of the viscosity and elasticity needed to be fast enough that particles did not reach the contact line by radial flow, but not so fast that Marangoni flow and particle migration were prevented.

The second fixing strategy used depletion flocculation induced by the exclusion of free PSS polymer to aggregate particles. Radial flow was still capable of carrying particles outwards, but the large size of the aggregate caused settling and so particles did not follow the flow. A small central dot with a deposit radius 1/3 of the initial droplet radius was formed. This matches the best possible deposit radius for ethanol/water mixtures corresponding to $R_{\mathrm{g,min}}$. A PSS concentration of 1.7%w was needed (corresponding to 3%w in the water phase alone) to ensure strong enough aggregation that most particles remained locked together in the central group. This concentration of PSS is lower than the laponite concentration (2−2.5%w) required for the sol−gel fixing strategy (in 10%v ethanol/water), resulting in a lower concentration of unwanted impurity in the deposit.

7 | Concluding remarks and future research

The main contribution of this thesis reveals highly complex internal flows within simplistic model inks based on binary solvent mixtures. Particles inside the droplets followed the fluid streamlines to form circulating regions of Marangoni flow, but particles also migrated across streamlines to collect in a concentrated group at the centre of the droplet. This migration was size dependent, with larger particles migrating inwards faster to form a tighter collected group. Smaller collected group radii resulted from component fluids with larger differences in evaporation rate. A region depleted of particles was left at the contact line. Thus, formation of a ring stain was inhibited while Marangoni flows were active. Once Marangoni flows stopped, radial flow carried particles to the contact line forming a ring stain similar to the single solvent case. Hence, strategies for fixing the particle distribution (to avoid ring stain deposits) were developed depending on the internal flow within the droplets. Flow regimes and contact angles of microlitre droplets did not always match their picolitre counterparts. Thus, large scale tests are not always representative.

Internal flows were observed on imaging rigs designed, built and developed for particle tracking in picolitre droplets. Qualitative comparisons of the Marangoni flows were made for different binary solvent mixtures. PM/water mixtures exhibited complicated circulating flow regimes which were dependent on the Marangoni flow direction. For a Marangoni flow from apex to contact line (along the liquid-vapour interface), a circulating region existed at the centre of the droplet, with radial flow near the contact line. For the reverse Marangoni flow direction, a circulating region formed near the contact line, with radial flow at the centre of the droplet. This has direct implications for some water-

based ink formulations where the relative volatility of components depends on the relative humidity. Therefore, drying of the same ink on a wet day can lead to a different deposit structure compared to a dry day (unless the RH is carefully controlled). Deposits comprising 200 nm polystyrene spheres showed little difference when the Marangoni flow direction was switched. However, larger 1 μm particles exhibited a significant difference in deposit structure.

The imaging rigs were limited by the zone of focus and a bright region resulting from the angled light source. Holography would provide a method to avoid both of these issues, as well as determining the vertical position of particles inside the droplet. This would enable the vertical segregation of particles to be determined (if any), as well as the radial motion of the migrating group.

To further explore flow regimes and migration mechanisms for the particle collection, a qualitative consideration of the flow field within droplets was made based on the model in [68], providing a method to input a surface tension profile and match the observed flow regimes. Gaussian surface tension profiles provided good qualitative agreement with the observed flow regimes in PM/water droplets. To determine if the suggested flow regimes are realistic, a quantitative model that accounts for mass and momentum transfer is needed to solve the concentration field inside the droplet. COMSOL may be a suitable software for achieving this aim.

Three migration mechanisms were explored for the particle collection. Thermophoresis was ruled out as the driving mechanism for the migration due to the particle migration present in droplets with negligible thermal effects. The predicted migration velocities for chemophoresis are large enough that it could be a contributing mechanism, but there are some inconsistencies with experimental observations. For example, migration ceases while there are still concentration gradients in the bulk. Shear-induced migration holds promise for a migration mechanism in which particles move to regions of lower shear rate. COMSOL would provide a method for calculating the composition gradient along the liquid-vapour interface and solving the flow field inside the droplet. The corresponding shear rates could be used to estimate migration velocities based on a shear-induced mechanism. Likewise, the bulk composition gradient would allow an estimate of chemophoretic velocities. Hence, the migration

mechanism may be determined.

To determine whether chemophoresis is a feasible mechanism for the particle migration, the solid-liquid surface tension is required for calculating the migration velocity. In this thesis, a plausibility argument was given based on an order of magnitude estimate. However, nuclear magnetic resonance imaging could allow the solvent preference of the polymer forming the particles to be determined quantitatively through calculation of the diffusion coefficients and radius of gyration in different solvent mixtures. Careful consideration of the solvent viscosity would be required to pursue this analysis.

The size dependency of the particle migration could help determine the mechanism. When multiple particle sizes were included in a droplet, larger particles migrated to the centre of the droplet faster, forming distinct groups of each particle size. Fluorescent spheres would provide a way to determine the overlap between collecting particle groups made up of different sized spheres, and allow easier visualisation of multiple particle sizes within a single droplet.

Investigation of evaporating pure solvents showed the importance of contact line motion, and the thermal conductivity of the substrate on the drying time. Pinned droplets dried faster than those with a moving contact line, and higher contact angles prolonged the drying. An isothermal model for diffusion-limited evaporation was validated for picolitre droplets and proved sufficient for predicting the drying times of pure solvent droplets, except when evaporative cooling was significant. Hence, to enable accurate drying time predictions for spray cooling or heat transfer, evaporative cooling needs to be incorporated into the model. An approach based on energy balances would enable this. Evaporative cooling can be significant on substrates with low thermal conductivity (such as the paper substrates commonly used for graphical inkjet printing), and as such has direct implications for predicting the drying times of inkjet droplets. Additionally, the model discussed considers only limiting modes of evaporation (constant contact angle or constant contact radius). The model could be expanded to include intermediate modes as well (as in [76]), to provide a fully operational model for the full range of contact angles.

For single solvent droplets, evaporation-driven radial flow carried particles towards the contact line, building up a ring stain. Suspensions of a nano-

particulate clay (laponite) in water provided a method for obtaining a uniform deposit with a circular contact line by utilising an evaporation-driven sol−gel transition to reduce radial flow. The concentration of the laponite clay during evaporation resulted in an increase in the elasticity, inhibiting the radial motion of particles. Through careful control of the laponite concentration, sufficient radial motion was allowed to obtain a uniform deposit. By printing a uniform deposit with a controlled circular contact line, the print quality can be enhanced, and a lower volume of ink is required for the same colour density. Extension to non-aqueous systems would be possible by adsorption of a stabiliser to the surface of the laponite.

Strategies for controlling the particle distribution to obtain a small central dot made use of the particle collection to gather particles centrally (with a region depleted of particles near the periphery), then either a sol−gel transition or depletion flocculation to "fix" the deposit. Both strategies successfully printed narrower deposits than the initial droplet footprint, though the depletion flocculation strategy gave the smallest deposit diameter. A smaller deposit diameter could be achieved by changing the binary solvent mixture (to give a tighter collected group). These techniques could lend themselves well to printing conductive tracks with a compact deposit. For multiple passes of the print-head, finely spaced tracks could be built up suitable for micro-circuitry. To increase the throughput of inkjet prints, a single pass of the print-head is preferable. However, for single-pass printing a gap exceeding two thirds of a droplet diameter would remain between printed lines, making the technique more suited to the printing of conductive screens. For either method an impurity is left behind in the print. The PSS allows the particle distribution to be fixed with a lower percentage of added impurity than the laponite. It may be possible in some cases to remove the impurities by sintering.

In summary, this highly interesting area of research could benefit fields such as spray cooling, inkjet printing and the bio-sciences. This thesis demonstrates the importance of understanding the internal flows in order to devise strategies for controlling the deposit particle distribution, and provides a number of further research ideas that would benefit this topic.

8 References

[1] I. M. Hutchings and G. D. Martin. *Inkjet Technology for Digital Fabrication.* Wiley-Blackwell, 1st edition, 2012.

[2] J. W. Strutt and Lord Rayleigh. On the instability of jets. *Proceedings of the London mathematical society*, 10:4–13, 1878.

[3] S. I. Zoltan. Pulsed droplet ejecting system, Clevite Corp. (US 3683212), 1972.

[4] E. L. Kyser and S. B. Sears. Method and apparatus for recording with writing fluids and drop projection means therefor, Silonics, Inc. (US 3946398), 1976.

[5] F. L. Cloutier, D. K. Donald, J. D. Meyer, C. A. Tacklind, H. H. Taub, and J. L. Vaught. Thermal ink jet printer, Hewlett-Packard Company. (US 4490728), 1984.

[6] I. Endo, T. Nakagiri, S. Ohno, S. Saito, and Y. Sato. Bubble jet recording method and apparatus in which a heating element generates bubbles in a liquid flow path to project droplets, Canon Kabushiki Kaisha. (US 4723129), 1988.

[7] I. M. Hutchings, G. D. Martin, and S. D. Hoath. High speed imaging and analysis of jet and drop formation. *JIST*, 51(5):438–444, 2007.

[8] N. F. Morrison and O. G. Harlen. Viscoelasticity in inkjet printing. *Rheologica Acta*, 49(6):619–632, 2010.

[9] E. Gargir, L. Lifshitz, and L. Tirosh. A method and system for compensating for banding defects in inkjet printers, Aprion Digital Ltd. (WO 2002081214A3), 2002.

[10] W. D. Childers, R. A. Askeland, and G. Li. Misfiring print nozzle compensation, Hewlett Packard Development Company L.P. (US 7607752B2), 2009.

[11] K.-S. Kwon. Methods for detecting air bubble in piezo inkjet dispensers. *Sensors Actuators A Phys.*, 153(1):50–56, 2009.

[12] B.-H. Kim, T.-G. Kim, T.-K. Lim, S. Kim, S.-J. Shin, S.-J. Kim, and S.-J. Lee. Effects of trapped air bubbles on frequency responses of the piezo-driven inkjet printheads and visualization of the bubbles using synchrotron X-ray. *Sensors Actuators A Phys.*, 154(1):132–139, 2009.

[13] S.-K. Kwon. Experimental analysis of waveform effects on satellite and ligament behavior via in situ measurement of the drop-on-demand drop formation curve and the instantaneous jetting speed curve. *J. Micromech. Microeng.*, 20(11):115005, 2010.

[14] R. G. Capurso. Method and apparatus for cleaning and capping a print head in an ink jet printer, Eastman Kodak Company. (US 6158838), 2000.

[15] P. Wouters. Method and apparatus for removing excess ink from inkjet nozzle plates, Agfa-Gevaert. (US 6921146B2), 2005.

[16] J. de Jong, H. Reinten, H. Wijshoff, M. van den Berg, K. Delescen, R. van Dongen, F. Mugele, M. Versluis, and D. Lohse. Marangoni flow on an inkjet nozzle plate. *Appl. Phys. Lett.*, 91(20):204102, 2007.

[17] O. G. Harlen, R. J. Castrejón-Pita, and A. Castrejón-Pita. Viscoelasticity in inkjet printing. *NIP and Digital Fabrication Conference, 2013 International Conference on Digital Printing Technologies*, pages 253–549, 2013.

[18] M. R. Böhmer, R. Schroeders, J. A. M. Steenbakkers, S. H. P. M. de Winter, P. A. Duineveld, J. Lub, W. P. M. Nijssen, J. A. Pikkemaat, and H. R. Stapert. Preparation of monodisperse polymer particles and capsules by ink-jet printing. *Colloid Surf. A: Physicochem. Eng. Asp.*, 289(1–3):96–104, 2006.

[19] S. B. Fuller, E. J. Wilhelm, and J. M. Jacobson. Ink-jet printed nanoparticle microelectromechanical systems. *J. Microelectromech. Sys.*, 11(1):54–60, 2002.

[20] S. Molesa, D. R. Redinger, D. C. Huang, and V. Subramanian. High-quality inkjet-printed multilevel interconnects and inductive components on plastic for ultra-low-cost rfid applications. *Mat. Res. Soc. Symp. Proc.*, 769:253–258, 2003.

[21] D. Kim and J. Moon. Highly conductive ink jet printed films of nanosilver particles for printed electronics. *Electrochem. Solid St. Lett.*, 8(11):J30–J33, 2005.

[22] D. J. Lee and J. H. Oh. Shapes and morphologies of inkjet-printed nanosilver dots on glass substrates. *Surf. Interface Anal.*, 42(6–7):1261–1265, 2010.

[23] T. R. Hebner, C. C. Wu, D. Marcy, M. H. Lu, and J. C. Sturm. Ink-jet printing of doped polymers for organic light emitting devices. *Appl. Phys. Lett.*, 72(5):519–521, 1998.

[24] H. Sirringhaus, T. Kawase, R. H. Friend, T. Shimoda, M. Inbasekaran, W. Wu, and E.P. Woo. High-resolution inkjet printing of all-polymer transistor circuits. *Science*, 290(5499):2123–2126, 2000.

[25] Y. Yang, S-C. Chang, J. Bharathan, and J. Liu. Organic/polymeric electroluminescent devices processed by hybrid ink-jet printing. *J. Mater. Sci.- Mater. El.*, 11(2):89–96, 2000.

[26] D. Soltman and V. Subramanian. Inkjet-printed line morphologies and temperature control of the coffee ring effect. *Langmuir*, 24(5):2224–2231, 2008.

[27] T. Okamoto, T. Suzuki, and N. Yamamoto. Microarray fabrication with covalent attachment of dna using bubble jet technology. *Nature Biotech.*, 18(5):438–441, 2000.

[28] E. A. Roth, T. Xu, M. Das, C. Gregory, J. J. Hickman, and T. Boland. Inkjet printing for high-throughput cell patterning. *Biomater.*, 25(17):3707–3715, 2004.

[29] P. J. Tarcha, D. Verlee, H. W. Hui, J. Setesak, B. Antohe, D. Radulescu, and D. Wallace. The application of ink-jet technology for the coating and loading of drug-eluting stents. *Annal. Biomed. Eng.*, 35(10):1791–1799, 2007.

[30] B. Lorber, W.-K. Hsiao, I.M. Hutchings, and K. R. Martin. Adult rat retinal ganglion cells and glia can be printed by piezoelectric inkjet printing. *Biofabrication*, 6(015001):1–9, 2014.

[31] N. Sandler, A. Määttänen, L. Kronberg, A. Meierjohann, T. Viitala, and J. Peltonen. Inkjet printing of drug substances and use of porous substrates-towards individualized dosing. *J. Pharm. Sci.*, 100(8):3386–3395, 2011.

[32] M. A. Baretto, A. L. Enriquez, J. Cartagena, and J. A. Garcia. System and method for optically tracking objects using a spectral fingerprint of fluorescent compounds, 2006.

[33] Q. F. Xiang, J. R. G. Evans, M. J. Edirisinghe, and P. F. Blazdell. Solid freeforming of ceramics using a drop-on-demand jet printer. *Proc. Instn. Mech. Engr.*, 211(3):211–214, 1997.

[34] M. Mott, J-H. Song, and J. R. G. Evans. Microengineering of ceramics by direct ink-jet printing. *J. Am. Ceram. Soc.*, 82(7):1653–1658, 1999.

[35] R. Noguera, M. Lejeune, and T. Chartier. 3D fine scale ceramic components formed by ink-jet prototyping process. *J. Eur. Cer. Soc.*, 25(12):2055–2059, 2005.

[36] L. Chen and J. R. G. Evans. Arched structures created by colloidal droplets as they dry. *Langmuir*, 25(19):11299–11301, 2009.

[37] J. Ebert, E. Özkol, A. Zeichner, K. Uibel, Ö. Weiss, U. Koops, R. Telle, and H. Fischer. Direct inkjet printing of dental prostheses made of zirconia. *J. Dent. Res.*, 88(7):673–676, 2009.

[38] RDECOM. Flexible plastic display. http://www.flickr.com/photos/rdecom/4146880795/. Uploaded 30/11/2009. Viewed 20/3/2014.

[39] Guillaume Paumier. A DNA microarray. Source: Guillaume Paumier. Uploaded 30/11/2009. Viewed 20/3/2014.

[40] NLM. 000527lg Prometrium 100 mg oral capsule. NLM Pillbox, http://pillbox.nlm.nih.gov/assets/large/000527lg.jpg. Uploaded 2010. Viewed 20/3/2014.

[41] NLM. 000636lg flomax 0.4 mg. Source: NLM Pillbox, http://pillbox.nlm.nih.gov/assets/large/000636lg.jpg. Uploaded 2011. Viewed 20/3/2014.

[42] Bcn0209. Turbine (3D printing). Source: Bcn0209. Uploaded 2006. Viewed 20/3/2014.

[43] EdytaZwirecka. Hoon Chung 3D printed shoe. Source: EdytaZwirecka. Uploaded 8/5/2012. Attribution-Share Alike 3.0 Unported license. Viewed 20/3/2014.

[44] I. Ueno and K. Kochiya. Effect of evaporation and solutocapillary-driven flow upon motion and resultant deposition of suspended particles in volatile droplet on solid substrate. *Adv. Space Res.*, 41(12):2089–2093, 2008.

[45] Y. Hamamoto, J. R. E. Christy, and K. Sefiane. The flow characteristics of an evaporating ethanol water mixture droplet on a glass substrate. *J. Therm. Sci. Technol.*, 7(3):425–436, 2012.

[46] S. Schiaffino and A. A. Sonin. Molten droplet deposition and solidification at low Weber numbers. *Phys. Fluids*, 9(11):3172–3187, 1997.

[47] B. Derby. Inkjet printing of functional and structural materials: Fluid property requirements, feature stability and resolution. *Annu. Rev. Mater. Res.*, 40:395–414, 2010.

[48] L.H. Tanner. The spreading of silicone oil drops on horizontal surface. *J. Phys. D: Appl. Phys.*, 12:1473–1484, 1979.

[49] R. J. Good. A thermodynamic derivation of Wenzel's modification of Young's equation for contact angles; together with a theory of hysteresis. *J. Am. Chem. Soc.*, 74(20):5041–5042, 1952.

[50] F. E. Bartell and J. W. Shepard. Surface roughness as related to hysteresis of contact angles. 1. the system of paraffin-water-air. *J. Phys. Chem.*, 57(2):211–215, 1953.

[51] C. Ishino, K. Okumura, and D. Quéré. Wetting transitions on rough surfaces. *Europhys. Lett.*, 68(3):419–425, 2004.

[52] R. N. Wenzel. Resistance of solid surfaces to wetting by water. *Ind. Eng. Chem.*, 28:988–994, 1936.

[53] A. B. D. Cassie and S. Baxter. Wettability of porous surfaces. *Trans. Faraday Soc.*, 40:546–550, 1944.

[54] A. M. Peters, C. Pirat, M. Sbragaglia, B. M. Borkent, M. Wessling, S. Lohse, and R. G. H. Lammertink. Cassie-Baxter to Wenzel state wetting transition: Scaling of the front velocity. *Eur. Phys. J. E*, 29(4):391–397, 2009.

[55] R. Dou and B. Derby. Formation of coffee stains on porous surfaces. *Langmuir*, 28(12):5331–5338, 2012.

[56] S. Rowan, M. Newton, and G. McHale. Evaporation of microdroplets and the wetting of solid surfaces. *J. Phys. Chem.*, 99(35):13268–13271, 1995.

[57] A. M. Cazabat and G. Guéna. Evaporation of macroscopic sessile droplets. *Soft Matter*, 6(12):2591–2612, 2010.

[58] M. Shanahan, K. Sefiane, and J. Moffat. Dependence of volatile droplet lifetime on the hydrophobicity of the substrate. *Langmuir*, 27(8):4572–4577, 2011.

[59] N. Murisic and L. Kondic. On evaporation of sessile drops with moving contact lines. *J. Fluid Mech.*, 679:219–246, 2011.

[60] J. M. Stauber, S. K. Wilson, and B. R. Duffy. Comment on "increased evaporation kinetics of sessile droplets by using nanoparticles". *Langmuir*, 29(39):12328–12329, 2013.

[61] R. D. Deegan, O. Bakajin, T. F. Dupont, G. Huber, S. R. Nagel, and T. A. Witten. Capillary flow as the cause of ring stains from dried liquid drops. *Nature*, 389:827–829, 1997.

[62] Y. O. Popov. Evaporative deposition patterns: Spatial dimensions of the deposit. *Phys. Rev. E*, 71(3):036313, 2005.

[63] N. Shahidzadeh-Bonn, S. Rafaï, A. Azouni, and D. Bonn. Evaporating droplets. *J. Fluid Mech.*, 549:307–313, 2006.

[64] P. L. Kelly-Zion, C. J. Pursell, S. Vaidya, and J. Batra. Evaporation of sessile drops under combined diffusion and natural convection. *Colloids and Surf. A: Physicochem. Eng. Aspects*, 381(1–3):31–36, 2011.

[65] R. D. Deegan, O. Bakajin, T. F. Dupont, G. Huber, S. R. Nagel, and T. A. Witten. Contact line deposits in an evaporating drop. *Phys. Rev. E*, 62(1):756–765, 2000.

[66] R. G. Picknett and R. Bexon. Evaporation of sessile or pendant drops in still air. *J. Colloid Interface Sci.*, 61(2):336–350, 1977.

[67] H. Hu and R. G. Larson. Evaporation of a sessile droplet on a substrate. *J. Phys. Chem. B*, 106(6):1334–1344, 2002.

[68] H. Hu and R. G. Larson. Analysis of the effects of Marangoni stresses on the microflow in an evaporating sessile droplet. *Langmuir*, 21(9):3963–3971, 2005.

[69] K. S. Birdi, D. T. Vu, and A. Winter. A study of the evaporation rates of small water drops placed on a solid surface. *J. Phys. Chem.*, 93(9):3702–3703, 1989.

[70] M. Cachile, O. Bénichou, and A. M. Cazabat. Evaporating droplets of completely wetting liquids. *Langmuir*, 29(21):7985–7990, 2002.

[71] M. Cachile, O. Bénichou, C. Poulard, and A. M. Cazabat. Evaporating droplets. *Langmuir*, 18(21):8070–8078, 2002.

[72] S. Chandra, M. di Marzo, Y. M. Qiao, and P. Tartarini. Effect of liquid-solid contact angle on droplet evaporation. *Fire Safety Journal*, 27(2):141–158, 1996.

[73] T. Lim, J. Jeong, J. Chung, and J. T. Chung. Evaporation of inkjet printed pico-liter droplet on heated substrates with different thermal conductivity. *J. Mech. Sci. Technol.*, 23(7):1788–1794, 2009.

[74] V. I. Saverchenko, S. P. Fisenko, and Y. A. Khodyko. Evaporation of a picoliter droplet on a wetted substrate at reduced pressure. *J. Eng. Phys. Thermophys.*, 84(4):723–729, 2011.

[75] E. L. Talbot, A. Berson, P. S. Brown, and C. D. Bain. Evaporation of picoliter droplets on surfaces with a range of wettabilities and thermal conductivities. *Phys. Rev. E*, 85(6):061064, 2012.

[76] J. M. Stauber, S. K. Wilson, B. R. Duffy, and K. Sefiane. On the lifetimes of evaporating droplets. *J. Fluid Mech.*, 744(R2), 2014.

[77] K. Sefiane, L. Tadrist, and M. Douglas. Experimental study of evaporating water-ethanol mixture sessile drop: influence of concentration. *Inter. J. Heat Mass Trans.*, 46(23):4527–4534, 2003.

[78] S. M. Rowan, M. I. Newton, F. W. Diewer, and G. McHale. Evaporation of microdroplets of azeotropic liquids. *J. Phys. Chem. B*, 104(34):8217–8220, 2000.

[79] K. Sefiane, S. David, and E. R. Shanahan. Wetting and evaporation of binary mixture drops. *J. Phys. Chem. B*, 112(36):11317–11323, 2008.

[80] H. Masoud and J. D. Felske. Analytical solution for inviscid flow inside an evaporating sessile drop. *Phys. Rev. E*, 79:016301, 2009.

[81] B. Sobac and D. Brutin. Triple-line behavior and wettability controlled by nanocoated substrates: Influence on sessile drop evaporation. *Langmuir*, 27(24):14999–15007, 2011.

[82] V. Jokinen, L. Sainiemi, and S. Franssila. Controlled lateral spreading and pinning of oil droplets based on topography and chemical patterning. *Langmuir*, 27(11):7314–7320, 2011.

[83] J. Léopoldès, A. Dupuis, D. G. Bucknall, and J. M. Yeomans. Jetting micron-scale droplets onto chemically heterogeneous surfaces. *Langmuir*, 19(23):9818–9822, 2003.

[84] S. T. Larsen and R. Taboryski. A Cassie-like law using triple phase boundary line fractions for faceted droplets on chemically heterogeneous surfaces. *Langmuir*, 25(3):1282–1284, 2009.

[85] R. D. Deegan. Pattern formation in drying drops. *Phys. Rev. E*, 61(1):475–485, 2000.

[86] S. Maheshwari, L. Zhang, Y. Zhu, and H.-C. Chang. Coupling between precipitation and contact-line dynamics: Multiring stains and stick-slip motion. *Phys. Rev. Lett.*, 100(4):044503, 2008.

[87] A. S. Sangani, C. Lu, K. Su, and J. A. Schwarz. Capillary force on particles near a drop edge resting on a substrate and a criterion for contact line pinning. *Phys. Rev. E*, 80(1):011603, 2009.

[88] X. Shen, C.-M. Ho, and T.-S.Wong. Minimal size of coffee ring structure. *J. Phys. Chem. B*, 114(16):5269–5274, 2010.

[89] M. A. Faers and R. Pontzen. Factors influencing the association between active ingredient and adjuvant in the leaf deposit of adjuvant-containing suspoemulsion formulations. *Pest Manag. Sci.*, 64(8):820–833, 2008.

[90] C. Monteux and F. Lequeux. Packing and sorting colloids at the contact line of a drying drop. *Langmuir*, 27(6):2917–2922, 2011.

[91] H. Zeng, K. Kristiansen, P. Wang, J. Bergli, and J. Israelachvili. Surface-induced patterns from evaporating droplets of aqueous carbon nanotube dispersions. *Langmuir*, 27(11):7163–7167, 2011.

[92] S. S. Abramchuk, A. R. Khokhlov, T. Iwataki, H. Oana, and K. Yoshikawa. Direct observation of DNA molecules in a convection flow of a drying droplet. *Europhys. Lett.*, 55(2):294–300, 2001.

[93] D. Brutin, B. Sobac, B. Loquet, and J. Sampol. Pattern formation in drying drops of blood. *J. Fluid Mech.*, 667:85–95, 2011.

[94] M. Layani, M. Gruchko, O. Milo, I. Balberg, D. Azulay, and S. Magdassi. Transparent conductive coatings by printing coffee ring arrays obtained at room temperature. *ACS Nano*, 3(11):3537–3542, 2009.

[95] Z. Zhang, X. Zhang, Z. Xin, M. Deng, Y. Wen, and Y. Song. Controlled inkjetting of a conductive pattern of silver nanoparticles based on the coffee-ring effect. *Adv. mater.*, 25(46):6714–6718, 2013.

[96] J. Thompson. On certain curious motions observable at the surfaces of wine and other alcoholic liquors. *The London, Edinburgh and Dublin Philosophical Magazine and Journal of Science*, 10:330–333, 1855.

[97] W. D. Ristenpart, P. G. Kim, C. Domingues, J. Wan, and H. A. Stone. Influence of substrate conductivity on circulation reversal in evaporating drops. *Phys. Rev. Lett.*, 99(23):234502, 2007.

[98] F. Girard, M. Antoni, S. Faure, and A. Steinchen. Evaporation and Marangoni driven convection in small heated water droplets. *Langmuir*, 22(26):11085–11091, 2006.

[99] K. Sefiane, Y. Fukatani, Y. Takata, and J. Kim. Thermal patterns and hydrothermal waves (htws) in volatile drops. *Langmuir*, 29(31):9750–9760, 2013.

[100] G. Fabien, M. Antoni, and K. Sefiane. Infrared thermography investigation of an evaporating sessile water droplet on heated substrates. *Langmuir*, 26(7):4576–4580, 2010.

[101] G. Fabien, M. Antoni, and K. Sefiane. Use of IR thermography to investigate heated droplet evaporation and contact line dynamics. *Langmuir*, 27(11):6744–6752, 2011.

[102] V. N. Truskett and K. J. Stebe. Influence of surfactants on an evaporating drop: Fluorescence images and particle deposition patterns. *Langmuir*, 19(20):8271–8279, 2003.

[103] T. Still, P. J. Yunker, and A. G. Yodh. Surfactant-induced marangoni eddies alter the coffee-rings of evaporating colloidal drops. *Langmuir*, 28(11):4984–4988, 2012.

[104] T. Kajiya, W. Kobayashi, T. Okuzono, and M. Doi. Controlling the drying and film formation processes of polymer solution droplets with addition of small amount of surfactants. *J. Phys. Chem. B*, 113(47):15460–15466, 2009.

[105] J. Park and J. Moon. Control of colloidal particle deposit patterns within picoliter droplets ejected by ink-jet printing. *Langmuir*, 22(8):3506–3513, 2006.

[106] J. A. Lim, W. H. Lee, H. S. Lee, J. H. Lee, Y. D. Park, and K. Cho. Self-organization of ink-jet-printed triisopropylsilylethynyl pentacene via evaporation-induced flows in a drying droplet. *Adv. Funct. Mater.*, 18(2):229–234, 2008.

[107] J. R. E. Christy, Y. Hamamoto, and K. Sefiane. Flow transition within an evaporating binary mixture sessile drop. *Phys. Rev. Lett.*, 106:205701, 2011.

[108] E. L. Talbot, A. Berson, and C. D. Bain. Internal flows and particle transport inside picoliter droplets of binary solvent mixtures. *NIP29: 29th International Conference on Digital Printing Technologies, and Digital Fabrication 2013, September/October 2013, The Society for Imaging Science and Technology*, pages 307–312, 2013.

[109] Y. Sun, V. Bromberg, S. Gawande, S. Biswas, and T. Singler. Transport processes associated with inkjet printing of colloidal drops. *2009 Electronic Components and Technology Conference*, pages 1349–1355, 2009.

[110] J. X. Huang, F. Kim, A. R. Tao, S. Connor, and P. D. Yang. Spontaneous formation of nanoparticle stripe patterns through dewetting. *Nature Materials*, 4(12):896–900, 2005.

[111] P. Alam, M. Toivakka, K. Backfolk, and P. Sirviö. Impact spreading and absorption of Newtonian droplets on topographically irregular porous materials. *Chem. Eng. Sci.*, 62(12):3142–3158, 2007.

[112] R. J. Vrancken, M. L. Blow, H. Kusumaatmaja, K. Hermans, A. M. Prenen, C. W. M. Bastiaansen, D. J. Broer, and J. M. Yeomans. Anisotropic wetting and de-wetting of drops on substrates patterned with polygonal posts. *Soft Matter*, 9(3):674–683, 2013.

[113] H. Hu and R. G. Larson. Marangoni effect reverses coffee-ring depositions. *J. Phys. Chem. B*, 110(14):7090–7094, 2006.

[114] E. L. Talbot, A. Berson, and C. D. Bain. Drying and deposition of picolitre droplets of colloidal suspensions in binary solvent mixtures. *NIP28: 28th International Conference on Digital Printing Technologies, and Digital Fabrication 2012, September 2012, The Society for Imaging Science and Technology*, pages 420–423, 2012.

[115] B. M. Weon and J. H. Je. Capillary force repels coffee-ring effect. *Phys. Rev. E*, 82:015305, 2010.

[116] J.-Y. Jung, Y. W. Kim, J. Y. Yoo, J. Koo, and Y. T. Kang. Forces acting on a single particle in an evaporating sessile droplet on a hydrophilic surface. *Anal. Chem.*, 82(3):784–788, 2010.

[117] L. Chen and J. R. G. Evans. Drying of colloidal droplets on superhydrophobic surfaces. *J. Colloid Interf. Sci.*, 351(1):283–287, 2010.

[118] C. S. Hodges, Y. Ding, and S. Biggs. The influence of nanoparticle shape on the drying of colloidal suspensions. *J. Colloid Interf. Sci.*, 352(1):99–106, 2010.

[119] P. J. Yunker, T. Still, M. A. Lohr, and A. G. Yodh. Suppression of the coffee-ring effect by shape-dependent capillary interactions. *Nature*, 476(7360):308–311, 2011.

[120] T. P. Bigioni, X.-M. Lin, T. T. Nguyen, E. I. Corwin, T. A. Witten, and H. M. Jaeger. Kinetically driven self assembly of highly ordered nanoparticle monolayers. *Nature Mater.*, 5(4):265–270, 2006.

[121] Q. Yan, Gao L, V. Sharma, Y.-M. Chiang, and C. C. Wong. Particle and substrate charge effects on colloidal self-assembly in a sessile drop. *Langmuir*, 24(20):11518–11522, 2008.

[122] A. G. Marin, H. Gelderblom, J. Snoeijer, and D. Lohse. *American Physical Society, 63rd Annual Meeting of the APS Division of Fluid Dynamics, November 21-23, abstract CS.004 Bulletin of the American Physics Society*, 2010.

[123] S. D. Hoath, S. Jung, W.-K. Hsiao, and I. M. Hutchings. How PEDOT:PSS solutions produce satellite-free inkjets. *Organic Electronics*, 13(12):3259–3262, 2012.

[124] P. G. de Gennes. Solvent evaporation of spin cast films: "crust" effects. *Eur. Phys. J. E*, 7(1):31–34, 2002.

[125] T. Kajiya, E. Nishitani, T. Yamaue, and M. Doi. Piling-to-buckling transition in the drying process of polymer solution drop on substrate having a large contact angle. *Phys. Rev. E*, 73:011601, 2006.

[126] Y. Zhang, L. Chen, S. Yang, and J. R. G. Evans. Control of particle segregation during drying of ceramic suspension droplets. *J. Eur. Chem. Soc.*, 27(5):2229–2235, 2007.

[127] J. A. Dean. *Lange's Handbook of Chemistry.* McGraw Hill, 15 edition, 1999.

[128] J. Jiménez, J. Manrique, and F. Martinez. Effect of temperature on some volumetric properties for ethanol + water mixtures. *Rev. Col. Cienc. Quím. Farm.*, 33(2):145–155, 2004.

[129] M. Mohsen-Nia, H. Amiri, and B. Jazi. Densities, refractive indices, absolute viscosities, and static dielectric constants of 2-methylpropan-2-ol + hexane, + benzene, +propan-2-ol, + methanol, + ethanol, and + water at 303.2 K. *J. Chem. Eng. Data*, 40(5):1111–1114, 1995.

[130] MEGlobal, Ethylene Glycol product guide, `http://www.meglobal.biz/media/product_guides/MEGlobal_MEG.pdf`. Viewed 12/3/14.

[131] A. Pal and S. Sharma. Excess molar volumes and viscosities of 1-propanol + ethylene glycol, + ethylene glycol monomethyl, + ethylene glycol dimethyl, + diethylene glycol dimethyl, + triethylene glycol dimethyl, + diethylene glycol diethyl, and + diethylene glycol dibutyl ethers at 298.15 K. *J. Chem. Eng. Data*, 43(4):532–536, 1998.

[132] DOW company, DOWANOL PM technical datasheet, `http://www.conservationsupportsystems.com/system/assets/techdocs/Dowanol_PM_Tech.pdf`. Viewed 11/3/14.

[133] BASF The chemical company, Petrochemicals technical leaflet, `http://www.solvents.basf.com/portal/load/fid226780/Solvenon_PM_e_04_08.pdf`. Viewed 12/3/14.

[134] G. Vázquez, E. Alvarez, and J. M. Navaza. Surface tension of alcohol + water from 20°C to 50°C. *J. Chem. Eng. Data*, 40(3):611–614, 1995.

[135] H.-W. Chen, C.-C. Wen, and C.-H. Tu. Excess molar volumes, viscosities, and refractive indexes for binary mixtures of 1-chlorobutane with four alcohols at T = (288.15, 298.15, and 308.15) K. *J. Chem. Eng. Data*, 49(2):347–351, 2004.

[136] Y.-C. Kao and C.-H. Tu. Densities, viscosities, refractive indices, and surface tensions for binary and ternary mixtures of 2-propanol, tetrahydropyran, and 2,2,4-trimethylpentane. *J. Chem. Thermodynam.*, 43(2):216–226, 2011.

[137] D. Gómez-Díaz, J. C. Mejuto, J. M. Navaza, and A. Rodríguez-Álvarez. Viscosities, densities, surface tensions, and refractive indexes of 2,2,4-trimethylpentane + cyclohexane + decane ternary liquid systems at 298.15 K. *J. Chem. Eng. Data*, 47(4):872–875, 2002.

[138] W. B. Kay and F. M. Warzel. 2,2,4-Trimethylpentane (Iso-octane) - Vapor pressure, critical constants, and saturated vapor and liquid densities. *Indust. Eng. Chem.*, 43(5):1150–1152, 1951.

[139] C. W. Mertz. Evaporation process control by variation in process material dielectric constant, Phillips Petroleum Co. (US 2931433 A), 1960.

[140] DOW company, DOWANOL PnP technical datasheet, http://msdssearch.dow.com/PublishedLiteratureDOWCOM/dh_08ad/0901b803808ad682.pdf?filepath=oxysolvents/pdfs/noreg/110-00589.pdf&fromPage=GetDoc. Viewed 23/3/14.

[141] B. Ramsauer. *Characterization of Propylene Glycol n-Propyl Ether Measuring and Modeling of Important Thermodynamic Parameters.* University of Reinsburg, 2010.

[142] http://physics.georgetown.edu/matlab/tutorial.html. Viewed 15/7/13.

[143] D. H. Shin, S. H. Lee, J. Jung, and J. Y. Yoo. Evaporating characteristics of sessile droplet on hydrophobic and hydrophilic surfaces. *Microelectron. Eng.*, 86(4–6):1350–1353, 2009.

[144] H. Gelderblom, Á. Márin, H. Nair, A. van Houselt, and L. Lefferts. How water droplets evaporate on a superhydrophobic substrate. *Phys. Rev. E*, 83(026306), 2011.

[145] K. Sefiane S. David and L. Tadrist. Experimental investigation of the effect of thermal properties of the substrate in the wetting and evaporation of sessile drops. *Colloids and Surf. A: Physicochem. Eng. Aspects*, 298(1–2):108–114, 2007.

[146] B. R. Duffy S. David G. J. Dunn, S. K. Wilson and K. Sefiane. A mathematical model for the evaporation of a thin sessile liquid droplet: Comparison between experiment and theory. *Colloids and Surf. A: Physicochem. Eng. Aspects*, 323(1–3):50–55, 2008.

[147] B. R. Duffy S. David G. J. Dunn, S. K. Wilson and K. Sefiane. The strong influence of substrate conductivity on droplet evaporation. *J. Fluid Mech.*, 623:329–351, 2009.

[148] K. Sefiane and R. Bennacer. An expression for droplet evaporation incorporating thermal effects. *J. Fluid Mech.*, 667:260–271, 2011.

[149] A. J. Petsi and V. N. Burganos. Evaporation-induced flow in an inviscid liquid line at any contact angle. *Phys. Rev. E*, 73(4):041201, 2006.

[150] D. O. H. Teare, D. C. Barwick, W. C. E. Schofield, R. P. Garrod, L. J. Ward, and J. P. S. Badyal. Substrate-independent approach for polymer brush growth by surface atom transfer radical polymerization. *Langmuir*, 21(24):11425–11430, 2005.

[151] I. Woodward, W. C. E. Schofield, V. Roucoules, and J. P. S. Badyal. Super-hydrophobic surfaces produced by plasma fluorination of polybutadiene films. *Langmuir*, 19(8):3432–3438, 2003.

[152] R. Good and M. Koo. Effect of drop size on contact-angle. *J. Colloid Interf. Sci.*, 71(2):283–292, 1979.

[153] M. Taylor, A. J. Urquhart, M. Zelzer, M. C. Davies, and M. R. Alexander. Picoliter water contact angle measurement on polymers. *Langmuir*, 23(13):6875–6878, 2007.

[154] M. Pykönen and S. Aura. Experimental comparison of wettability of pico- and microliter droplets with a range of liquid surface tensions on porous and non-porous substrates. *NIP 28 and Digital Fabrication 2012 Proceedings*, pages 239–241, 2012.

[155] P. S. Brown, A. Berson, E. L. Talbot, W. C. E. Schofield, C. D. Bain, and J. P. S. Badyal. Impact of picoliter droplets on superhydrophobic surfaces with ultralow spreading ratios. *Langmuir*, 27(22):13897–13903, 2011.

[156] M. Vaseem, K. M. Lee, A.-R. Hong, and Y.-B. Hahn. Inkjet printed fractal-connected electrodes with silver nanoparticle ink. *Appl. Mater. Interfaces*, 4(6):3300–3307, 2012.

[157] K. Fukuda, T. Sekine, D. Kumaki, and S. Tokito. Profile control of inkjet printed silver electrodes and their application to organic transistors. *Appl. Mater. Interfaces*, 5(9):3916–3920, 2013.

[158] A. G. Marin, H. Gelderblom, J. Snoeijer, and D. Lohse. Avalanche of particles in evaporating coffee drops. *Candidate video for the 28th Annual Gallery of Fluid Motion 63rd Annual Meeting of the American Physical Society, Division of Fluid Dynamics, Long Beach, CA, 21-23 Nov*, 2010.

[159] A. Berson, E. L. Talbot, P. S. Brown, and C. D. Bain. Experimental investigation of the impact, spreading and drying of picolitre droplets onto substrates with a broad range of wettabilities. *NIP27: 27th International Conference on Digital Printing Technologies, and Digital Fabrication 2011, September 2011, The Society for Imaging Science and Technology*, pages 290–293, 2011.

[160] K. H. Kang, S. J. Lee, C. M. Lee, and I. S. Kang. Quantitative visualization of flow inside an evaporating droplet using the ray tracing method. *Meas. Sci. Technol.*, 15(6):1104–1112, 2004.

[161] H. Kinoshita, S. Kaneda, T. Fujii, and M. Oshima. Three-dimensional measurement and visualization of internal flow of a moving droplet using confocal micro-piv. *Lab Chip*, 7(3):338–346, 2007.

[162] A. K. H. Cheng, D. M. Soolaman, and H.-Z. Yu. Evaporation of microdroplets of ethanol-water mixtures on gold surfaces modified with self-assembled monolayers. *J. Phys. Chem. B*, 110(23):11267–11271, 2006.

[163] J. L. Anderson, M. E. Lowell, and D. C. Prieve. Motion of a particle generated by chemical gradients part 1. non-electrolytes. *J. Fluid Mech.*, 117:107–121, 1982.

[164] H. J. Keh and S. C. Luo. Particle interactions in diffusiophoresis in nonelectrolyte gradients. *Phys. Fluids*, 7(9):2122–2131, 1995.

[165] D. C. Prieve, J. L. Anderson, J. P. Ebel, and M. E. Lowell. Motion of a particle generated by chemical gradients part 2. electrolytes. *J. Fluid Mech.*, 148:247–269, 2006.

[166] A. Kabalnov and H. Wennerstrom. Diffusion in evaporating solutions. *Soft Matter*, 5(23):4712–4718, 2009.

[167] R. Kita, G. Kircher, and S. Wiegand. Thermally induced sign change of Soret coefficient for dilute and semidilute solutions of poly.n-isopropylacrylamide. in ethanol. *J. Chem. Phys.*, 121(18):9140–9146, 2004.

[168] S. Iacopini and R. Piazza. Thermophoresis in protein solutions. *Europhys. Lett.*, 63(2):247–253, 2003.

[169] A. Parola and R. Piazza. Particle thermophoresis in liquids. *Eur. Phys. J. E*, 15(3):255–263, 2004.

[170] S. Iacopini, R. Rusconi, and R. Piazza. The "macromolecular tourist": Universal temperature dependence of thermal diffusion in aqueous colloidal suspensions. *Eur. Phys. J. E*, 19(1):56–67, 2006.

[171] S. Fayolle, T. Bickel, and A. Würger. Thermophoresis of charged colloidal particles. *Phys. Rev. E*, 77(041404):1–9, 2008.

[172] S. J. Kim, K. H. Kang, J.-G. Lee, I. S. Kang, and B. J. Yoon. Control of particle-deposition pattern in a sessile droplet by using radial electroosmotic flow. *Anal. Chem.*, 78(14):5192–5197, 2006.

[173] R. Eichhorn, J. Reigtmeier, D. Anselmetti, and P. Reinmann. Negative mobility and sorting of colloidal particles. *Soft Matter*, 6(9):1858–1862, 2010.

[174] L. Lizana and A. Y. Grosberg. Exact expressions for the mobility and electrophoretic mobility of a weakly charged sphere in a simple electrolyte. *EPL*, 104(68004), 2013.

[175] J. Zhao, P. Papadopoulos, M. Roth, C. Dobbrow, E. Roeben, and A. Schmidt. Exact expressions for the mobility and electrophoretic mobility of a weakly charged sphere in a simple electrolyte. *Eur. Phys. J. Special Topics*, 222(11):2881–2893, 2013.

[176] E. Yariv and O. Schnitzer. The electrophoretic mobility of rod-like particles. *J. Fluid Mech.*, 719(R3):1–12, 2013.

[177] M. A. Espy, H. Sandrin, C. Carr, C. J. Hanson, M. D. Ward, and R. H. Kraus Jr. An instrument for sorting of magnetic microparticles in a magnetic field gradient. *Cytometry Part A*, 69A:1132–1142, 2006.

[178] J. S. Andreu, J. Camacho, M. Benelmekki, C. Rebollo, and M. Martinez. Simple analytical model for the magnetophoretic separation of superpa-

ramagnetic dispersions in a uniform magnetic gradient. *Phys. Rev. E*, 84(021402), 2011.

[179] C. A. Rue and M. E. Schimpt. Thermal diffusion in liquid mixtures and its effect on polymer retention in thermal field-flow fractionation. *Anal. Chem.*, 66(22):4054–4062, 1994.

[180] H.-R. Jiang, H. Wada, N. Yoshinaga, and M. Sano. Manipulation of colloids by nonequillibrium depletion force in temperature gradient. *Phys. Rev. Lett.*, 102(20):208301, 2009.

[181] J. Palacci, S. Sacanna, A. P. Steinberg, D. J. Pine, and P. M. Chaikin. Living crystals of light-activated colloidal surfers. *Science*, 339(6122):936–940, 2013.

[182] M. Cavallaro Jr., L. Botto, E.P. Lewandowski, M. Wang, and K. J. Stebe. Curvature-driven capillary migration and assembly of rod-like particles. *PNAS*, 108(52):20923–20928, 2011.

[183] D. Semwogerere and E. R. Weeks. Shear-induced particle migration in binary colloidal suspensions. *Phys. Fluids*, 20:043306, 2008.

[184] A. Ramachandran and D. T. Leighton Jr. The influence of secondary flows induced by normal stress differences on the shear-induced migration of particles in concentrated suspensions. *J. Fluid Mech.*, 603:207–243, 2008.

[185] O. Sano, K. Kutsumi, and N. Watanabe. Surface-tension driven oscillatory motion of a mercury drop in the presence of concentration gradient of $K_2Cr_2O_7$ in HNO_3 solution. *J. Phys. Soc. Jap.*, 64(6):1993–1999, 1995.

[186] R. F. Ismagilov, A. Schwartz, N. Bowden, and G. M. Whitesides. Autonomous movement and self-assembly. *Angew. Chem. Inter. Ed.*, 41(4):652–654, 2002.

[187] W. F. Paxton, A. Sen, and T. E. Mallouk. Motility of catalytic nanoparticles through self-generated forces. *Chem. Eur. J.*, 11(22):6462–6470, 2005.

[188] B. Rousseau, C. Nieto-Draghi, and J. B. Avalos. The role of molecular interactions in the change of sign of the Soret coefficient. *Europhys. Lett.*, 67(6):976–982, 2004.

[189] H. Ning and S. Wiegand. Experimental investigation of the Soret effect in acetone/water and dimethylsulfoxide/water mixtures. *J. Chem. Phys.*, 125(221102):1–4, 2006.

[190] M. Eslamian. Advances in thermodiffusion and thermophoresis (Soret effect) in liquid mixtures. *Front. Heat Mass Transf.*, 2(043001):1–20, 2011.

[191] J. Chan, J. J. Popov, and S. Kolisnek-Kehl. Soret coefficients for aqueous polyethylene glycol solutions and some tests of the segmental model of polymer thermal diffusion. *J. Sol. Chem.*, 32(3):197–214, 2003.

[192] J. B. McLaughlin. Inertial migration of a small sphere in linear shear flows. *J. Fluid Mech.*, 224:261–274, 1991.

[193] M. D. de Tullio, G. Pascazio, and M. Napolitano. Arbitrarily shaped particles in shear flow. *Seventh International conference on Computational fluid dynamics, Big Island, Hawaii, July*, 9-13, 2012.

[194] P. G. Saffman. The lift on a small sphere in a slow shear flow. *J. Fluid Mech.*, 22(2):385–400, 1965.

[195] P. Cherukat and J. B. McLaughlin. The inertial lift on a rigid sphere in a linear shear flow field near a flat wall. *J. Fluid Mech.*, 263:1–18, 1994.

[196] J. R. Brown, E. O. Fridjonsson, J. D. Seymour, and S. L. Codd. Nuclear magnetic resonance measurement of shear-induced particle migration in Brownian suspensions. *Phys. Fluids*, 21(093301):1–9, 2009.

[197] A. Krishnaiah, B. P. Gampper, and D. S. Viswanath. Densities and viscosities for propylene glycol monomethyl ether plus water. *J. Chem. Eng. Data*, 38(3):401–403, 1993.

[198] R. L. Kay and T. L. Broadwater. Solvent structure in aqueous mixtures. 3. ionic conductances in ethanol-water mixtures at 10°c and 25°c. *J. Sol. Chem.*, 5(1):57–76, 1976.

[199] Y. Tanaka, Y. Matsuda, H. Fujiwara, H. Kubota, and T. Makita. Viscosity of (water + alcohol) mixtures under high pressure. *Inter. J. Thermophys.*, 8(2):147–163, 1987.

[200] F. Koohyar, F. Kiani, S. Sharifi, M. Sharifirad, and S. H. Rahmanpour. Study on the change of refractive index on mixing, excess molar volume and viscosity deviation for aqueous solution of methanol, ethanol, ethylene glycol, 1-propanol and 1, 2, 3-propantriol at T = 292.15 K and atmospheric pressure. *Res. J. Appl. Sci. Eng. Technol.*, 4(17):3095–3101, 2012.

[201] E. W. Washburn. *The International Critical Tables*, volume 3. New York: McGraw Hill Book Co., 1928.

[202] K. C. Pratt and W. A. Wakeham. The mutual diffusion coefficient of ethanol-water mixtures: determination by a rapid, new method. *Proc. R. Soc. Lond. A.*, 336:393–406, 1974.

[203] R. C. Reid and T. K. Sherwood. *The properties of gases and liquids.* McGraw-Hill Book Company, New York, 1st edition, 1958.

[204] P. Atkins and J. de Paula. *Atkins' Physical Chemistry.* Oxford University Press, 8th edition, 2006.

[205] D. Gómez-Díaz, J. C. Mejuto, and J. M. Navaza. Physicochemical properties of liquid mixtures. 1. viscosity, density, surface tension and refractive index of cyclohexane + 2,2,4-trimethylpentane binary liquid systems from 25°C to 50°C. *J. Chem. Eng. Data*, 46(3):720–724, 2001.

[206] C. Özdemir and A. Güner. Solubility profiles of poly(ethylene glycol)/solvent systems, I: Qualitative comparison of solubility parameter approaches. *Europ. Polym. J.*, 43(7):3068–3093, 2007.

[207] R. L. Patrick. *Treatise on Adhesion and Adhesives*, volume 1. 1967.

[208] C. M. Hansen. *The three dimensional solubility parameter and solvent diffusion coefficient.* 1967.

[209] S. I. Rubinow and J. B. Keller. The transverse force on a spinning sphere moving in a viscous fluid. *J. Fluid Mech.*, 11(3):447–459, 1961.

[210] R. Dou, T. Wang, Y. Guo, and B. Derby. Ink-jet printing of zirconia: Coffee staining and line stability. *J. Am. Ceram. Soc.*, 94(11):3787–3792, 2011.

[211] A. Friederich, J. R. Binder, and W. Bauer. Rheological control of the coffee stain effect for inkjet printing of ceramics. *J. Am. Ceram. Soc.*, 1(7):1–7, 2013.

[212] E. Fribourg-Blanc, D. M. T. Dang, and C. M. Dang. Characterization of silver nanoparticle based inkjet printed lines. *Microsyst. Technol.*, 19(12):1961–1971, 2013.

[213] B.-Y. Wang, T.-H. Yoo, Y.-W. Song, D.-S. Lim, and Y.-J. Oh. Cu ion ink for a flexible substrate and highly conductive patterning by intensive pulsed light sintering. *Appl. Mater. Interfaces*, 5(10):4113–4119, 2013.

[214] S. H. Ko, H. Pan, C. P. Grigoropoulos, C. K. Luscombe, J. M. J. Fréchet, and D. Poulikakos. All-inkjet-printed flexible electronics fabrication on a polymer substrate by low-temperature high-resolution selective laser sintering of metal nanoparticles. *Nanotech.*, 18(345202):1–8, 2007.

[215] N. C. Schirmer, S. Ströhle, M. K. Tiwari, and D. Poulikakos. On the principles of printing sub-micrometer 3D structures from dielectric-liquid-based colloids. *Adv. Func. Mater.*, 21(2):388–395, 2011.

[216] D. Kim, Y. Jeong, C. Y. Koo, K. Song, and J. Moon. Thin film transistors with ink-jet printed amorphous oxide semiconductors. *Jap. J. App. Phys.*, 49:05EB06, 2010.

[217] L. Cui, J. Zhang, X. Zhang, L. Huang, Z. Wang, Y. Li, H. Gao, S. Zhu, T. Wang, and B. Yang. Suppression of the coffee ring effect by hydrosoluble polymer additives. *Appl. Mater. Interfaces*, 47(5):2775–2780, 2012.

[218] E. Hendarto and Y. B. Gianchandani. Size sorting of floating spheres based on Marangoni forces in evaporating droplets. *J. Micromech. Microeng.*, 23(075016):1–7, 2013.

[219] S. H. Ko, H. Lee, and K. H. Kang. Hydrodynamic flows in electrowetting. *Langmuir*, 24(3):1094–1101, 2008.

[220] H. B. Eral, D. Mampallil Augustine, M. H. G. Duits, and F. Mugele. Suppressing the coffee stain effect: how to control colloidal self-assembly in evaporating drops using electrowetting. *Soft Matter*, 7(10):4954–4958, 2011.

[221] B.-J. de Gans and U. S. Schubert. Inkjet printing of well-defined polymer dots and arrays. *Langmuir*, 20(18):7789–7793, 2004.

[222] W. Royall Cox, T. Chen, C. Guan, D. J. Hayes, R. E. Hoenigm, B. T. Teipen, and D.L. MacFarlane. Micro-jet printing of refractive microlenses. *Proceedings OSA Diffractive Optics and Micro-Optics Topical Meeting, Kailua-Kona, Hawaii, June*, 1998.

[223] A. M. J. van den Berg, A. W. M. de Laat, P. J. Smith, J. Perelaera, and U. S. Schubert. Geometric control of inkjet printed features using a gelating polymer. *J. Mater. Chem.*, 17(7):677–683, 2007.

[224] K. Sun and S. R. Raghavan. Thermogelling aqueous fluids containing low concentrations of pluronic F127 and laponite nanoparticles. *Langmuir*, 26(11):8015–8020, 2010.

[225] Donald Ray Alfred. Formulation for depositing a material on a substrate using ink jet printing, 1993.

[226] A. Mourchid, A. Delville, and P. Levitz. Sol-gel transition of colloidal suspensions of anisotropic particles of laponite. *Faraday Discuss.*, 101:275–285, 1995.

[227] Y. M. Joshi, G. Ranjith, K. Reddy, A. L. Kulkarni, N. Kumar, and R. P. Chhabra. Rheological behaviour of aqueous suspensions of laponite: new insights into the ageing phenomena. *Proc. R. Soc. A*, 464(2090):469–489, 2008.

[228] K. Krishnan, M. B. Wisnudel, J. M. White, D. G. Gascoyne, K. L. Jackson, and S. G. Bondre. Method of printing marks on an optical article, NBCUniversal Media, LLC. (US 8118229), 2012.

[229] J.-L. Lin, C. Huang, C.-J. M. Chin, and J. R. Pan. Coagulation dynamics of fractal flocs induced by enmeshment and electrostatic patch mechanisms. *Water Research*, 42(17):4457–4466, 2008.

[230] J. Goodwin. *Colloids and Interfaces with Surfactants and Polymers*. Wiley, 2nd edition, 2009.

[231] X. Yu and P. Somasundaran. Role of polymer conformation in interparticle-bridging dominated flocculation. *J. Colloid Interf. Sci.*, 177:283–287, 1996.

[232] S. Biggs, M. Habgood, G. J. Jameson, and Y. Yan. Aggregate structures formed via a bridging flocculation mechanism. *Chem. Eng. J.*, 80(1–3):13–22, 2000.

[233] Y. Zhou and G. V. Franks. Flocculation mechanism induced by cationic polymers investigated by light scattering. *Langmuir*, 22(16):6775–6786, 2006.

[234] J. E. Seebergh and J. C. Berg. Depletion flocculation of aqueous, electrosterically-stabilized latex dispersions. *Langmuir*, 10(2):454–463, 1994.

[235] A. Sharma, S. N. Tan, and Y. Walz. Measurement of colloidal stability in solutions of simple, nonadsorbing polyelectrolytes. *J. Colloid Interf. Sci.*, 190(2):392–407, 1997.

[236] A. Sharma, S. N. Tan, and Y. Walz. Effect of nonadsorbing polyelectrolytes on colloidal interactions in aqueous mixtures. *J. Colloid Interf. Sci.*, 191(1):236–246, 1997.

[237] N. Kiratzis, M. Faers, and P. F. Luckham. Depletion flocculation of particulate systems induced by hydroxyethylcellulose. *Colloid. Surf. A: Phys. Eng. Asp.*, 151:461–471, 1999.

[238] B. S. Neumann and K. G. Sansom. Laponite clay a synthetic inorganic gelling agent for aqueous solutions of polar organic compounds. *J. Soc. Cosmetic Chem.*, 21:273–258, 1970.

[239] S. L. Tawari, D. L. Koch, and C. Cohen. Electrical double-layer effects on the Brownian diffusivity and aggregation rate of laponite clay particles. *J. Colloid Interf. Sci.*, 240(1):54–66, 2001.

[240] N. N. Herrera, J.-M. Letoffe, and J.-L. Putaux. Aqueous dispersions of silane-functionalized laponite clay platelets. A first step toward the elaboration of water-based polymer/clay nanocomposites. *Langmuir*, 20(5):1564–1571, 2004.

A | Appendix

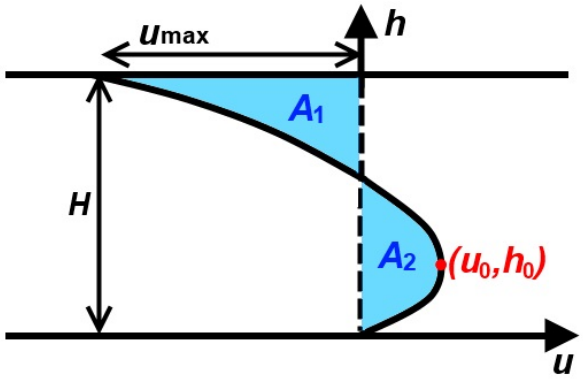

Figure A.1. Representation of the Marangoni flow profile inside a droplet of height H under the lubrication approximation. The flow profile is parabolic with the maximum velocity, $u_{\max}$, occurring at the liquid-vapour interface. The highest positive velocity, u_0, occurs at a height, h_0, from the substrate. The net flow is zero, hence area A_1 and A_2 are equal.

The parabolic flow profile is considered to have the form

$$u = ah - bh^2, \tag{A.1}$$

where u is the fluid velocity, h is the height, and a and b are constants. The stationary point (u_0,h_0) occurs where

$$du/dh = a - 2bh = 0. \tag{A.2}$$

It follows that

$$h_0 = a/2b \tag{A.3}$$

and

$$u_0 = a(a/2b) - b(a/2b)^2 = a^2/4b. \tag{A.4}$$

As there is no net flow, the areas A_1 and A_2 are equal, hence

$$\int_0^H u dh = \left[\frac{ah^2}{2} - \frac{bh^3}{3}\right]_0^H = \frac{aH^2}{2} - \frac{bH^3}{3} = 0, \tag{A.5}$$

therefore

$$b = 3a/2H. \tag{A.6}$$

By combining Equations A.3 and A.6, h_0 can be determined to be

$$h_0 = H/3, \tag{A.7}$$

and equating Equations A.4 and A.6, gives u_0 as

$$u_0 = aH/6. \tag{A.8}$$

The maximum velocity at the liquid-vapour interface, $u_{\max}$ is

$$u_{\max} = u(H) = -aH/2 = -3u_0. \tag{A.9}$$

B | Appendix

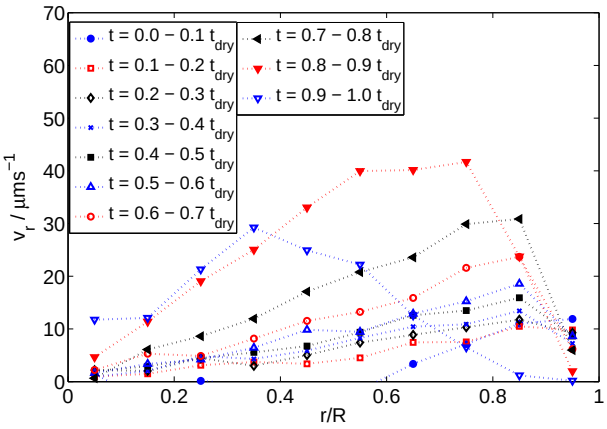

Figure B.1. Mean radial velocities, v_r, over the normalised droplet radius for incremented temporal bins for a droplet of pure water. Data points are plotted at the mid-point of each spatial bin.

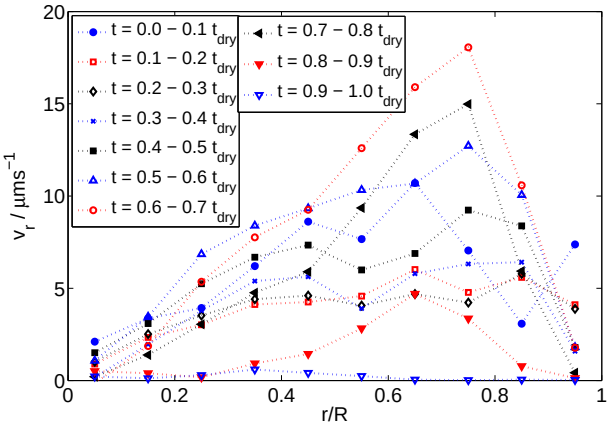

Figure B.2. Mean radial velocities, v_r, over the normalised droplet radius for incremented temporal bins for a droplet of 1%w HEC. Data points are plotted at the mid-point of each spatial bin.

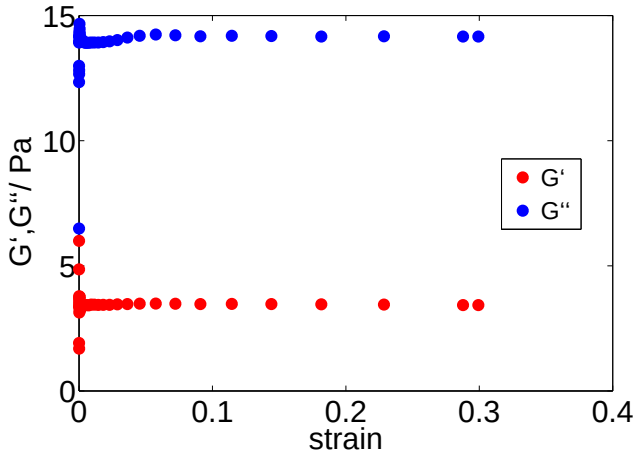

Figure B.3. The viscous modulus, G'', and elastic modulus, G' for 5%w HEC in water.

C | Appendix

```
%%%%%%%%%%%%%%%%%%%%%%%%%%%%%%%%%%%%%%%%%%%%%%%%%%%%%%%%%%%%%%%%%%%%%%%
%% Generalised Hu_and_Larson_code %%%%%%%%%%%%%%%%%%%%%%%%%%%%%%%%%%%%%%
%%%%%%%%%%%%%%%%%%%%%%%%%%%%%%%%%%%%%%%%%%%%%%%%%%%%%%%%%%%%%%%%%%%%%%%
%%%%% Compute trajectory of a particle inside droplet including Marangoni effect
%%%%% Uses velocity field with Marangoni flow from Hu and Larson, Analysis of the effects
%%%%% of Marangoni stresses, Langmuir, 21, 9, 2005.
%%%%% Calls velocity Hu_and_Larson_fct.m
%%%%% Developed by Arganthael Berson and Emma Talbot

clear all
close all
clc

particle = 0;

%%% Surface tension profile due to temperature gradient (Hu Larson)

theta_i=20*pi/180; %% initial contact angle

%%% Hu classic profile
a=0.3;
b=8;
c=1601;
d=0;
e=0;
f=0;
T0 = 0.01;

% %%% Gaussian type
% a=-1;
% b=0;
% c=0.2
% d=1;
% e=0;
```

```
% f=0;

% %%% Exponential type
% a=20;
% b=5;
% f=-11.9;
% c=a.*b.*exp(f)
% d=1;
% e=0;

% %%% Polynomial type
% a=-2;
% b=2;
% c=0
% d=0;
% e=0;
% f=0;

%%%%% temperature profile


%%%% Works in conjunction with velocity_Hu_and_Larson_function MUST change
%%%% profile there too
for  r=0:0.01:1;
     T=(a.*r.^b+((1-a).*r.^2)+c).*T0;             %%%% Hu Larson
%  T=(a.*r.^3)+(b.*r.^2)+(c.*r)+d;              %%%% Polynomial
%  T = a.*exp(b.*r+f)+c.*exp(-d.*r+e);       %%%% Exponential type
%  T = a.*exp((-d.*((r-b).^2))/(2.*c.^2))+e; %%%% Gaussian

ST_Tzero = 75.64; %%% surface tension water at zero deg C in mNm-1

beta=-0.17e-3;  %%% mNm-1/degC

if r==0
    T_rzero=T;
    ST_0 = beta*T_rzero+ST_Tzero;
end

ST = beta*T+ST_Tzero; %%% surface tension dependence on temp

dST = ST - ST_0; %%% variation in surface tension (ST-ST_0)

figure(99)
hold on
plot(r,T,'bo')
xlabel('r / R')
ylabel('T')
```

```
figure(999)
hold on
plot(r,dST,'bo')
xlabel('r / R')
ylabel('\Delta\sigma / mNm^-^1')

if r==0
    Tzero=T;
end
if r==1
    Tone=T;
end
end

%%%%%%%%%%%%%%%%%%%%%%%%%%%%%%%%%%%%%%%%%%%%%%%%%%%%%%%%%%%%%%%%%%%%%%%%%%%%
%%%%define parameters

%% Droplet parameters
r0=50e-6; %% radius of the contact line in m

if theta_i>(pi/4)
    display('WARNING: Small-angle approximation made. Large contact angles may be invalid')
end

%%% Parameters drying
T=20;       %% temperature (degC)
RH=0.5;   %% Relative humidity
solvent=1;

%%%Parameters for Marangoni flow
beta=-0.17e-3 ;  %N/m/K, surface tension variation w.r.t. temperature (Bodiguel 2010)
dT=5e-1;         %%% temperature difference between top and edge of droplet. For Ma number estimate

%%% dimensionless time at which the flow is considered, t=1 ~ dried
t=0.;

%%%%%%%%%%%%%%%%%%%%%%%%%%%%%%%%%%%%%%%%%%%%%%%%%%%%%%%%%%%%%%%%%%%%%%%%%%%%
%%%% compute solvent parameters

R_ct= 8.314; %gas constant
if solvent==1  %%% water
    rhof=994;    %% fluid density kg/m^3
    D= 2.46e-5; %% diffusion coefficient m^2/s
    M_water=18; %% molar mass of water (g/mol)
    P_water=(7e-5.*(T.^3)+1e-4.*(T.^2)+0.0583.*T+0.5816).*1000; %% vapor pressure in Pa
    %% from fit to CRC handbook data 6-15 section
```

```
    ns=(P_water.*M_water./1000)./(8.314*(T+273.15)) %% Saturation vapour density kg/m^3
    mu=1e-3; %% dynamic viscosity of water Pa.s

else if solvent==2 %% ethanol
    rhof=780;
    P=1;
    T_K=T+273.15;
    M_ethanol=24+6+16;M_air=29;
    relm=((1/M_ethanol)+(1/M_air));
    difvol_ethanol=(2*16.5)+(6*1.98)+5.48; difvol_air=20.1;
    difvolsum_ethanol=((difvol_ethanol^(1/3))+(difvol_air^(1/3)))^2;
    D=(1e-7*(T_K^1.75)*(relm^0.5))/(P*difvolsum_ethanol);
    RH=0; % relative humidity
    ns=(9975*46.06904e-3)./(8.314*T_K); % at 300K
    %% vapor pressure from CRC Handbook of chemistry and physics 74th Ed


    end
    end
end

%Contact angle at considered time t
theta=theta_i*(1-t);
display(['Theta (deg): ' num2str(theta*180/pi)]);

%%%%%Parameters for normalisation
% Drying time for normalisation
tf=pi*rhof*(r0)^2*theta_i/(16*D*ns*(1-RH));
display(['Drying time (s): ' num2str(tf)]);

%Radius of the entire sphere at initial time
r_sphere=r0/cos(theta_i-pi/2); %% radius of the entire sphere, assuming a spherical cap
% Height of the droplet at initial time for normalisation
h0=r_sphere-sqrt(r_sphere^2-r0^2); %% height of the droplet at the centre at initial time (m)

%%%%%Parameters at considered time t
% height of the droplet at the centre a time t (m)
h0t=h0-h0.*t; %%% height of the droplet at the centre a time t (m)

% Flux at the top of the droplet
J=D*ns*(1-RH)/R_ct*(0.27*theta^2+1.3)*(0.6381-0.2239*(theta-pi/4)^2); %% flux at top of droplet
%% Hu and Larson 2005, Analysis of the microfluid flow ..., eq11) (kg/m^2/s)
J=J/rhof/(h0/tf); %%%% dimensionless flux

%Marangoni number
Ma=-beta*dT*tf/mu/(r0); %%%Marangoni number
display(['Marangoni number: ' num2str(Ma)]);
```

```
% Exponent for flux distribution at the drop surface
lambda=.5-theta/pi; %%exponent


%%%%%%%%%%%%%%%%%%%%%%%%%%%%%%%%%%%%%%%%%%%%%%%%%%%%%%%%%%%%%%%%%%%%%%%%%%%
%%%Plot velocity maps

i=0;
j=0;
rlin=0:0.01:1; %% r/r0 dimensionless radial position
zlin=0:0.01:1; %% z/h0, vertical location of the velocity field

[rmap,zmap]=meshgrid(rlin,zlin);
hmap=h0t/h0.*(1-rmap.^2); %%%% vertical location of the free surface (dimensionless: h(m)/h0)

for r=rlin
    i=i+1;
    j=0;
    for z=zlin
        j=j+1;

        [ur(j,i),uz(j,i),durdr(j,i),durdz(j,i),duzdr(j,i),duzdz(j,i)]=...
velocity_Hu_and_Larson_fct_ELT(r,z,t,h0,h0t,r0,lambda,J,Ma,a,b,c,d,e,f);
    end
end

%%%%%%% Compute maximum velocity for adjusting colorbars
umax=max(max(sqrt((ur.*r0/tf).^2+(uz.*h0/tf).^2)));


%%%% Check continuity to check velocity derivatives are ok
continuity=1./rmap .* ( rmap.*durdr + ur )./tf + duzdz./tf;
figure(11)
title('continuity check')
pcolor(continuity)
shading flat
colorbar

%%%%%%Plots

density_streamline = 1.5;  %%%% modify spacing of streamlines, default =1
%% higher implies more i.e 2 is twice as many streamlines

figure(1)
plot(rmap(1,:)*r0./1e-6,hmap(1,:).*h0./1e-6,'k','linewidth',2)
hold on
```

```
streamslice(rmap*r0./1e-6,zmap.*h0./1e-6,ur.*r0/tf,uz.*h0/tf,density_streamline);
axis equal
title(['CA=' num2str(theta*180/pi) '^\circ  MA=' num2str(Ma)])
xlabel('r / \mum')
ylabel('h / \mum')


figure(2)
subplot(3,1,1)
plot(rmap(1,:)*r0,hmap(1,:)*h0,'k','linewidth',1)
hold on
pcolor(rmap*r0,zmap.*h0,ur.*r0/tf)
shading flat
caxis([-umax umax])
colorbar
title('ur')
subplot(3,1,2)
plot(rmap(1,:)*r0,hmap(1,:)*h0,'k','linewidth',1)
hold on
pcolor(rmap*r0,zmap.*h0,durdr./tf)
shading flat
%caxis([-umax umax])
colorbar
title('durdr')
subplot(3,1,3)
plot(rmap(1,:)*r0,hmap(1,:)*h0,'k','linewidth',1)
hold on
pcolor(rmap*r0,zmap.*h0,durdz.*r0./h0./tf)
shading flat
colorbar
title('durdz')

figure(3)
subplot(3,1,1)
plot(rmap(1,:)*r0,hmap(1,:)*h0,'k','linewidth',1)
hold on
pcolor(rmap*r0,zmap.*h0,uz.*h0/tf)
shading flat
caxis([-umax umax])
colorbar
title('uz')
subplot(3,1,2)
plot(rmap(1,:)*r0,hmap(1,:)*h0,'k','linewidth',1)
hold on
pcolor(rmap*r0,zmap.*h0,duzdr.*h0./r0./tf)
shading flat
%caxis([-umax umax])
```

```
colorbar
title('duzdr')
subplot(3,1,3)
plot(rmap(1,:)*r0,hmap(1,:)*h0,'k','linewidth',1)
hold on
pcolor(rmap*r0,zmap.*h0,duzdz./tf)
shading flat
colorbar
title('duzdz')

figure(22)
subplot(3,1,1)
plot(rmap(1,:)*r0,hmap(1,:)*h0,'k','linewidth',1)
hold on
pcolor(rmap*r0,zmap.*h0,ur.*r0/tf)
shading flat
caxis([-umax umax])
colorbar
title('ur')
subplot(3,1,2)
plot(rmap(1,:)*r0,hmap(1,:)*h0,'k','linewidth',1)
hold on
pcolor(rmap*r0,zmap.*h0,abs(durdr./tf))
shading flat
colorbar
title('modulus durdr')
subplot(3,1,3)
plot(rmap(1,:)*r0,hmap(1,:)*h0,'k','linewidth',1)
hold on
pcolor(rmap*r0,zmap.*h0,abs(durdz.*r0./h0./tf))
shading flat
colorbar
title('modulus durdz')

figure(4)
plot(rmap(1,:)*r0./1e-6,hmap(1,:)*h0./1e-6,'k','linewidth',1)
hold on
pcolor(rmap*r0./1e-6,zmap.*h0./1e-6,abs(durdz.*r0./h0./tf))
shading flat
colorbar
title('modulus durdz')
xlabel('r / \mum')
ylabel('h / \mum')

figure(33)
subplot(3,1,1)
plot(rmap(1,:)*r0,hmap(1,:)*h0,'k','linewidth',1)
```

```
hold on
pcolor(rmap*r0,zmap.*h0,uz.*h0/tf)
shading flat
caxis([-umax umax])
colorbar
title('uz')
subplot(3,1,2)
plot(rmap(1,:)*r0,hmap(1,:)*h0,'k','linewidth',1)
hold on
pcolor(rmap*r0,zmap.*h0,abs(duzdr.*h0./r0./tf))
shading flat
colorbar
title('modulus duzdr')
subplot(3,1,3)
plot(rmap(1,:)*r0,hmap(1,:)*h0,'k','linewidth',1)
hold on
pcolor(rmap*r0,zmap.*h0,abs(duzdz./tf))
shading flat
%caxis([-umax umax])
colorbar
title('modulus duzdz')

figure(5)
plot(rmap(1,:)*r0./1e-6,hmap(1,:)*h0./1e-6,'k','linewidth',1)
hold on
pcolor(rmap*r0./1e-6,zmap.*h0./1e-6,abs(duzdr.*h0./r0./tf))
shading flat
colorbar
title('modulus duzdr')
xlabel('r / \mum')
ylabel('h / \mum')


figure(6)
plot(rmap(1,:)*r0./1e-6,hmap(1,:)*h0./1e-6,'k','linewidth',1)
hold on
pcolor(rmap*r0./1e-6,zmap.*h0./1e-6,ur.*r0/tf)
shading flat
caxis([-umax umax])
colorbar
title('ur')
xlabel('r / \mum')
ylabel('h / \mum')

%%%%%%%%%%%
%%%%Convert velocity and derivatives into dimensional quantities
```

```
ur=ur.*r0/tf;
uz=uz.*h0/tf;
durdr=durdr./tf;
durdz=durdz.*r0./h0./tf;
duzdr=duzdr.*h0./r0./tf;
duzdz=duzdz./tf;
```

```
%%%%%%%%%%%%%%%%%%%%%%%%%%%%%%%%%%%%%%%%%%%%%%%%%%%%%%%%%%%%%%%%%%%%%%%
%% Hu_and_Larson_fct_ELT %%%%%%%%%%%%%%%%%%%%%%%%%%%%%%%%%%%%%%%%%%%%%%
%%%%%%%%%%%%%%%%%%%%%%%%%%%%%%%%%%%%%%%%%%%%%%%%%%%%%%%%%%%%%%%%%%%%%%%
%%%%% Function returning velocity (normalised) components and derivatives
%%%%% for flow inside evaporating droplet with Marangoni effects from
%%%%% Hu and Larson, Langmuir 21(9) 2005.
%%%%% Developed by Arganthael Berson and Emma Talbot

function [ur,uz,durdr,durdz,duzdr,duzdz]=...
velocity_Hu_and_Larson_fct_ELT(r,z,t,h0,h0t,r0,lambda,J,Ma,a,b,c,d,e,f)

h=h0t/h0.*(1-r.^2); %%%% vertical location of the free surface (dimensionless: h(m)/h0)
hp=-h0t/h0.*2.*r;   %%%% dh/dr

%%%%%% return zero velocity if outside the droplet
if (z>h || r>1)
    ur=0;
    uz=0;
    durdr=0;
    durdz=0;
    duzdr=0;
    duzdz=0;
    return
end

%%%% define profile and derivatives

% %%% profile T = a.*exp((-(d.*(r-b).^2))/(2.*c.^2)); %%% Gaussian
% dT1 = -(a.*d.*r./(c.^2)).*exp((-d.*((r-b).^2))/(2.*c.^2));
% dT2=(((a*(d^2)*r.^2)./(c^4)).*exp((-(d*(r-b).^2))/(2*c^2)))-((a*d/(c^2).*exp((-(d*(r-b).^2))/(2*c^2))));

% %%% profile T=ar^b+(1-a)r^2+c  %%%% Hu Larson
dT1 = (a.*b.*r.^(b-1))+2.*(1-a).*r;
dT2 = (a.*b.*(b-1).*r.^(b-2))+2.*(1-a);

% %%% profile T=ar^3+br^2+cr+d  %%%% Polynomial
% dT1 = (3.*a.*r.^2)+2.*b.*r+c;
```

```
% dT2 = (6.*a.*r)+2.*b;

% %%% %profile T=aexp(br)+cexp(-dr+e) %%%%% Exponential type
% dT1 = a.*b.*exp(b.*r+f)-c.*d.*exp(-d.*r+e);
% dT2 = a.*b.^2.*exp(b.*r+f)+c.*d.^2.*exp(-d.*r+e);

g1 = Ma.*dT1;
g2 = Ma.*dT2;

%%%% radial velocity with Marangoni effect
%% (not height averaged,Eq.12 Hu and Larson Analysis of the effect of Marangoni stresses...)

ur= 3/8 ./ (1 - t) ./ r .* ((1-r.^2)-(1-r.^2).^(-lambda)).*(z.^2./h.^2 - 2*z./h) ...
                 + r*h0^2.*h/r0^2.*(J*lambda.*(1-r.^2).^(-lambda-1)+1).*(z./h-3/2*z.^2./h.^2) ...
                 + h0.*h/2./r0.*g1.*(z./h-3/2*z.^2./h.^2);

 %%%%%Vertical velocity with Marangoni effect
%%  (not height averaged,Eq.13 Hu and Larson Analysis of the effect of Marangoni stresses...)

uz = 3/4 ./ (1-t) .* ( 1+ lambda .* (1 - r.^2).^(-lambda-1) ) .* (z.^3./3./h.^2 - z.^2./h) ...
  + 3/2 ./ (1-t) .* ( (1-r.^2) - (1-r.^2).^(-lambda) ) .* ( z.^2./2./h.^2 - z.^3./3./h.^3) .* h0t/h0 ...
   - ( h0^2/r0^2 .* ( J*lambda.*(1-r.^2).^(-lambda-1) + 1 ).*(z.^2-z.^3./h)  ...
  + r.^2.*h0^2/r0^2.* J * lambda.* (lambda+1) .* (1-r.^2).^(-lambda-2) .* (z.^2-z.^3./h) ...
   - r.^2.*h0^2/r0^2 .* ( J.*lambda.*(1-r.^2).^(-lambda-1) +1 ) .* z.^3./h.^2 .* h0t/h0   ) ...
   - h0/4/r0 .* g2 .* (z.^2-z.^3./h) ...
  + h0/2/r0 .* r.*g1 .* (z.^3./h.^2) .* h0t/h0;

%%%%%%Derivative d ur / dr

 durdr= 3/8 ./ (1 - t).*(z.^2./h.^2 - 2*z./h)  .* ( -1/r.^2 -1 -2*lambda*(1-r.^2).^(-lambda-1) + ...
1./r.^2.*(1-r.^2).^(-lambda) ) ...
 + h0^2.*h/r0^2.*(z./h-3/2*z.^2./h.^2).*( 1 + J*lambda.*(1-r.^2).^(-lambda-1) + ...
 2*(lambda+1).*r.^2*J*lambda.*(1-r.^2).^(-lambda-2)) ...
 + h0.*h/2./r0.*(z./h-3/2*z.^2./h.^2).*g2 ...
 + 3/8 ./ (1 - t) ./ r .* ((1-r.^2)-(1-r.^2).^(-lambda)).*(2.*z./h.^2 - 2*z.^2./h.^3).*hp ...
 + r*h0^2/r0^2.*(J*lambda.*(1-r.^2).^(-lambda-1)+1).*(3*z.^2./2./h.^2).*hp ...
 + h0/2./r0.*g1.*(3*z.^2./2./h.^2).*hp;

%%%%%%Derivative d ur / dz

   durdz= 3/8 ./ (1 - t) ./ r .* ((1-r.^2)-(1-r.^2).^(-lambda)).*(2.*z./h.^2 - 2./h) ...
      + r*h0^2.*h/r0^2.*(J*lambda.*(1-r.^2).^(-lambda-1)+1).*(1./h-3*z./h.^2) ...
      + h0.*h/2./r0.*g1.*(1./h-3*z./h.^2);

%%%%%%Derivative d uz / dr

duzdr=3/4./(1-t).* (z.^3./3./h.^2 - z.^2./h).*(2.*lambda.*(lambda+1).* r.*(1 - r.^2).^(-lambda-2)) ...
```

```
 + 3/2./(1-t).* (z.^2./2./h.^2 - z.^3./3./h.^3).* h0t/h0.*(-2.*r - 2.*r.*lambda.*(1-r.^2).^(-lambda-1))...
 - ( h0^2/r0^2 .*(z.^2-z.^3./h) .*( 2.*J*lambda.*(lambda+1).*r.*(1-r.^2).^(-lambda-2) ) ...
 + h0^2/r0^2.*(z.^2-z.^3./h).*J* lambda.*(lambda+1).*(2.*r.*(1-r.^2).^(-lambda-3).*((lambda+1).*r.^2+1))...
 - h0^2/r0^2.* z.^3./h.^2.* h0t/h0.*(2.*r + 2.*r .*J.*lambda.*(1-r.^2).^(-lambda-1)+ ...
2.*J.*lambda.*r.^3.*(lambda+1).*(1-r.^2).^(-lambda-2) ) ) ...
 - h0/4/r0 .* (z.^2-z.^3./h) .* (g1+g2)  ...
 + h0/2/r0  .* (z.^3./h.^2) .* h0t/h0 .*r.*g1 ...
 + 3/4 ./ (1-t) .* ( 1+ lambda .* (1 - r.^2).^(-lambda-1) ) .* (z.^2./h.^2 - 2.*z.^3./3./h.^3) .* hp ...
 + 3/2 ./ (1-t) .* ( (1-r.^2) - (1-r.^2).^(-lambda) ) .* ( z.^3./h.^4 - z.^2./h.^3).*hp .* h0t/h0 ...
 - ( h0^2/r0^2 .* ( J*lambda.*(1-r.^2).^(-lambda-1) + 1 ).*(z.^3./h.^2).*hp  ...
+ r.^2.*h0^2/r0^2.*J*lambda.*(lambda+1).*(1-r.^2).^(-lambda-2).*(z.^3./h.^2).*hp ...
  - r.^2.*h0^2/r0^2 .* ( J.*lambda.*(1-r.^2).^(-lambda-1) +1 ) .* (-2.*z.^3./h.^3).*hp .* h0t/h0) ...
 - h0/4/r0 .* (g1+g2) .* (z.^3./h.^2).*hp ...
+ h0/2/r0 .* r.*g1 .* (-2.*z.^3./h.^3).*hp .* h0t/h0;

 %%%%%%%Derivative d uz / dz

         duzdz=3/4 ./ (1-t) .* ( 1+ lambda .* (1 - r.^2).^(-lambda-1) ) .* (z.^2./h.^2 - 2.*z./h) ...
             + 3/2 ./ (1-t) .* ( (1-r.^2) - (1-r.^2).^(-lambda)).* ( z./h.^2 - z.^2./h.^3) .* h0t/h0 ...
             - ( h0^2/r0^2 .* ( J*lambda.*(1-r.^2).^(-lambda-1) + 1 ).*(2.*z-3.*z.^2./h)  ...
                 + r.^2.*h0^2/r0^2.*J*lambda.*(lambda+1).*(1-r.^2).^(-lambda-2).* (2.*z-3.*z.^2./h) ...
                 - r.^2.*h0^2/r0^2 .* (J.*lambda.*(1-r.^2).^(-lambda-1)+1).* 3.*z.^2./h.^2 .* h0t/h0) ...
             - h0/4/r0 .* (g1+g2) .* (2.*z-3.*z.^2./h) ...
             + h0/2/r0 .* g1 .* (3.*z.^2./h.^2) .* h0t/h0;
```

```
%%%%%%%%%%%%%%%%%%%%%%%%%%%%%%%%%%%%%%%%%%%%%%%%%%%%%%%%%%%%%%%%%%%%%%%%%%%%
%%%%%%%%%%% Find group radius paticles in droplet %%%%%%%%%%%%%%%%%%%%%%%%
%%%%%%%%%%%%%%%%%%%%%%%%%%%%%%%%%%%%%%%%%%%%%%%%%%%%%%%%%%%%%%%%%%%%%%%%%%%%
 %%% Developed by Emma Talbot

cd('Z:\d60qqh 1\PhD\')

%%%% load image
dir='11_13\7_11_13\7_11_13_50%EG_50%EtOH_0_05%_755nm_G_S008\';
name_text='7_11_13_50%EG_50%EtOH_0_05%_755nm_G_S008';

image_num= 2300
name=[name_text num2str(image_num,'%06d') '.tif'];
b=imread([dir name_text num2str(1,'%06d') '.tif']);
i=imread([dir name]);
ib=i;       %%%% background obscurred only

figure(1)
imagesc(ib,[0 155])
```

```
colormap gray
axis equal

%%% select 8 points around group radius
display('indicate 8 points around deposit outer edge')
        title('Select 8 points around outer deposit edge')
        [ixn1,iyn1]=ginput(1);
        figure(1)
        hold on
        plot(ixn1,iyn1,'rx');
        [ixn2,iyn2]=ginput(1);
        figure(1)
        hold on
        plot(ixn2,iyn2,'rx');
        [ixn3,iyn3]=ginput(1);
        figure(1)
        hold on
        plot(ixn3,iyn3,'rx');
        [ixn4,iyn4]=ginput(1);
        figure(1)
        hold on
        plot(ixn4,iyn4,'rx');
        [ixn5,iyn5]=ginput(1);
        figure(1)
        hold on
        plot(ixn5,iyn5,'rx');
        [ixn6,iyn6]=ginput(1);
        figure(1)
        hold on
        plot(ixn6,iyn6,'rx');
        [ixn7,iyn7]=ginput(1);
        figure(1)
        hold on
        plot(ixn7,iyn7,'rx');
        [ixn8,iyn8]=ginput(1);
        figure(1)
        hold on
        plot(ixn8,iyn8,'rx');

%%% fit points to ellipse
%         %Fit an ellipse and extract the centre
yc1=[iyn1 iyn2 iyn3 iyn4 iyn5 iyn6 iyn7 iyn8];
xc1=[ixn1 ixn2 ixn3 ixn4 ixn5 ixn6 ixn7 ixn8];
x_el=xc1;
y_el=yc1;

cd('R:\Emma Talbot\PhD\Data\')
```

```
    ellipse_out1=EllipseFit(x_el,y_el);
    xco=ellipse_out1(1);
    yco=ellipse_out1(2);
    axao=ellipse_out1(3); %Ellipse major axis
    axbo=ellipse_out1(4);%Ellipse minor axis
    phio=ellipse_out1(5); %Ellipse rotation angle

     %%%%Parametrization of ellipse for plotting
    th=0:0.01:2*pi; %%%%Angle
    rotmato=[cos(phio) -sin(phio); sin(phio) cos(phio)];%%%%Rotation matrix
    xyo=rotmato*[axao.*cos(th) ;
    axbo.*sin(th)]+[xco;yco]*ones(1,length(th));

 %%%%%Plot the ellipse/circle fit
     figure(1)
     hold on;
     plot(xyo(1,:),xyo(2,:),'-r','LineWidth',2)
     figure(1)
     hold on;
     plot(xco,yco,'r.','MarkerSize',20)

     %%% take horizontal line through centre of drop
 siz_horiz=size(ib);
 horiz_x=1:siz_horiz(2);
 horiz_y=horiz_x;
 horiz_y(1:siz_horiz(2))=yco;

 %%% take vertical line through centre of drop
 line_xo=1:siz_horiz(1);
 linex_xo=line_xo;
 linex_xo(1:siz_horiz(1))=xco;

 %%%%% find closest point to intersect ellipse and horiz line
%%% right edge
xyo_edge_abs=max(abs((xyo(1,:)-xco)));
xyo_edge=xyo_edge_abs+xco;

%%% left edge
xyo_edge_abs3=max(abs((xyo(1,:)-xco)));
xyo_edge3=-xyo_edge_abs3+xco;

%%% bottom edge
xyo_edge_abs2=max(abs((xyo(2,:)-yco)));
xyo_edge2=xyo_edge_abs2+yco;

%%% top edge
```

```
   xyo_edge_abs4=max(abs((xyo(2,:)-yco)));
   xyo_edge4=-xyo_edge_abs4+yco;

%%%% determine average group radius
dx=xyo_edge-xyo_edge3
dy=xyo_edge2-xyo_edge4
Rg=(dx+dy)./2
```

```
%%%%%%%%%%%%%%%%%%%%%%%%%%%%%%%%%%%%%%%%%%%%%%%%%%%%%%%%%%%%%%%%%%%%%%%%%%%%
%%% Find ring width from SEM image %%%%%%%%%%%%%%%%%%%%%%%%%%%%%%%%%%%%%%%%%
%%%%%%%%%%%%%%%%%%%%%%%%%%%%%%%%%%%%%%%%%%%%%%%%%%%%%%%%%%%%%%%%%%%%%%%%%%%%
 close all
clear all

display('LOADING FILE')
display(' ')

%%% load ESEM file
save_date='10_9_13';
dir=['R:\Emma Talbot\PhD\ESEM\NIP_2012_EG_deposits\EG'];
name=['\90%EG_whole'];
name_calib_file=[name '.tif'];
imread([dir name '.tif']);
image=imread([dir name '.tif']);
threshold_value=155;
bit_count=255;
ESEM=1; %% if ESEM image set to 1 for calibration
no_automate =1;

display([dir name])
display(' ')

%%% calibrate using scale bar
siz_im=size(image);

%%% load calibration image
if ESEM
    image_calib=image(siz_im(1)-61:siz_im(1),1:siz_im(2));

else
    image_calib=bit_count-imread([dir name_calb_file]);
end
scale_size=input('Enter scale size on ESEM image in um for calibration: ');
%% input size grid/nozzle for calibration
```

```
if no_automate

    figure(2)
    imagesc(image_calib)
    colormap gray
    axis equal

     %%% select left side calibration scale
            display('indicate left edge scale bar')
            title('select a point on left of scale bar... ')
            [ixg,iyg]=ginput(1);
            %%% display marker here
            figure(2)
            hold on
            plot(ixg,iyg,'rx')
            axis equal

            %%% select right side calibration scale
            display('indicate right edge scale bar')
            title('select a point on the right of scale bar... ')
            [ixd,iyd]=ginput(1);
            %%% display marker here
            figure(2)
            hold on
            plot(ixd,iyd,'rx')
            axis equal
            %%% connect 2 markers with line
            cal_grad=(iyd-iyg)/(ixd-iyg);
            intercept_cal= iyg-(cal_grad*iyd);
            calcx=ixg:ixd;
            figure(2)
            hold on
            plot(calcx,(calcx.*cal_grad)+intercept_cal,'r-')
            axis equal

            title('Done - Look at results in the command window')
            display('calibration input complete')

        %%% determine pixel size
            dist=(ixd-ixg);                    %% horizontal distance across calibration scale
            pix=scale_size/dist;               %% pixel size assuming no tilt (calibration with sphere)
            pix_corr=pix;
else

%%%%%%%%%% automatic scale size reader %%%%%%%%%%%%%%%%%%%%%%%%%%%%%%%%
image_calib=image_calib(2:20,310:480);
```

```
figure(2)
imagesc(image_calib)
colormap gray
axis equal

 %%% select left side calibration scale
 [iyg,ixg]= find(image_calib(10,:)==255,1,'first');

        figure(2)
        hold on
        plot(ixg,iyg,'rx')
        axis equal
[iyd,ixd]= find(image_calib(10,:)==255,1,'last');

        figure(2)
        hold on
        plot(ixd,iyd,'rx')
        axis equal

        %%% connect 2 markers with line
        cal_grad=(iyd-iyg)/(ixd-iyg);
        intercept_cal= iyg-(cal_grad*iyd);
        calcx=ixg:ixd;
        figure(2)
        hold on
        plot(calcx,(calcx.*cal_grad)+intercept_cal,'r-')
        axis equal

        title('Done - Look at results in the command window')
        display('calibration input complete')

    %%% determine pixel size
        dist=(ixd-ixg);                    %% horizontal distance across calibration scale
        pix=scale_size/dist;               %% pixel size assuming no tilt (calibration with sphere)
        pix_corr=pix;
end

 %%%%%%%%%%%%%% end automatic scale size reader %%%%%%%%%%%%%%%%%%%%%%%%


%%% cut off scale bar
image=image(1:siz_im(1)-61,1:siz_im(2));

%%% Apply gaussian filter
filt_gauss=[2 4 5 4 2 ; 4 9 12 9 4; 5 12 15 12 5; 4 9 12 9 4; 2 4 5 4 2]./159;
img=conv2(single(filt_gauss),single(image));
img=img(3:end-2,3:end-2);
```

```
figure(1)
imagesc(image)
title('After Gaussian')
colormap gray
axis equal

%%% convert to binary
imt=double((img>threshold_value).*bit_count);

%%% fill image
 peak=max(max(imt));
            imt_filled=imt;
            Y=1:siz_im(1)-61;
            X=1:siz_im(2);
            for line=Y

                 ind1=find( imt(line,:)~=0,1,'first');  %% for lines 1:Y find first non-zero index
                 ind2=find( imt(line,:)~=0,1,'last');   %% for lines 1:Y find last non-zero index
                 if isempty(ind1)          %% if line all non-zero values fill whole line
                     ind1=length(X);      %% if line all non-zero values set index to x-length image
                 end
                 if isempty(ind2)
                     ind2=1;                            %% if line all non-zero values set index to 1
                 end
                 imt_filled( line, 1:ind1)=peak;
                 imt_filled( line, ind2:end )=peak;

            end
            for row=X

                 ind3=find( imt(:,row)~=0,1,'first');
                 ind4=find( imt(:,row)~=0,1,'last');
                 if isempty(ind3)
                     ind3=length(Y);
                 end
                 if isempty(ind4)
                     ind4=1;
                 end
                 imt_filled( 1:ind3,row )=peak;
                 imt_filled( ind4:end,row)=peak;
            end

            imt_filled=imt + double(~imt_filled)*peak;

figure(4)
imagesc(imt_filled)
```

```
title('Filled droplet')
colormap gray
axis equal

%%% Find Ring width
  [i_all,xyi,xyo,xco,xci,yci,yco,width_right,width_bottom,width_left,width_top ...
  ,mean_ring_width_ellipse, width_drop_vert, width_drop_horiz mean_drop_diameter] = ...
 width_coffee_ring( pix_corr,dir,name);

width_right_norm=(2.*width_right)./mean_drop_diameter;
width_bottom_norm=(2.*width_bottom)./mean_drop_diameter;
width_left_norm=(2.*width_left)./mean_drop_diameter;
width_top_norm=(2.*width_top)./mean_drop_diameter;

 display(width_right_norm)
 display(width_bottom_norm)
 display(width_left_norm)
 display(width_top_norm)
 display(mean_ring_width_ellipse )
 display(mean_drop_diameter)
```

```
%%%%%%%%%%%%%%%%%%%%%%%%%%%%%%%%%%%%%%%%%%%%%%%%%%%%%%%%
%%% width_coffee_ring_function %%%%%%%%%%%%%%%%%%%%%%%%%%%%%%%%%%%
%%%%%%%%%%%%%%%%%%% use with deposit ESEM to find ring widths %%%%%%%%%%%%%%%
%%% developed by Emma Talbot %%%%%%%%%%%%%%%%%%%%%%%%%%%%%%%%%%%%%

function [i_all,xyi,xyo,xco,xci,yci,yco,width_right,width_bottom,width_left,width_top ...
,mean_ring_width_ellipse, width_drop_vert, width_drop_horiz mean_drop_diameter ] = ...
 width_coffee_ring( pix_corr,dir,name )
%%% Calibration using graticule or scale bar
%%% Run through deposition_post_processing_nozzle
%%% takes 10 points on deposit inner and outer ring circumference and fits
%%% circle/ellipse to get ring width

zoom_needed=1;
bit_count=255;
threshold_value=18;

        cal=imread([dir name '.tif']);%load calibration file

        [resx,resy]=size(cal);
        %image of graticule
        figure(1)
        imagesc(cal)
        colormap gray
```

```
 if zoom_needed

     figure(1)
     %zoom into image
     display ('INPUT REQUIRED for calibration')
     display('Zoom in - designate bottom left corner... ')
     title('Zoom in - select bottom left corner... ')
     [ixz1,iyz1]=ginput(1);
     display('Zoom in - designate top right corner... ')
     title('Zoom in - select top right corner... ')
     [ixz2,iyz2]=ginput(1);
     axis([ixz1 ixz2 iyz2 iyz1])

else
     ixz1=round(1);
     ixz2=round(resx);
     iyz1=round(1);
     iyz2=round(resy);

 end

     %select 10 points around nozzle
     noz=imread([dir name '.tif']);
     noz=noz(iyz2:iyz1,ixz1:ixz2);

     figure(1)
     imagesc(noz)
     colormap gray
     axis equal

     imt=double((noz>threshold_value).*bit_count); %% apply threshold for binary conversion

     display('indicate 8 points around deposit outer edge')
     title('Select 8 points around outer deposit edge')
     [ixn1,iyn1]=ginput(1);
     figure(1)
     hold on
     plot(ixn1,iyn1,'rx');
     [ixn2,iyn2]=ginput(1);
     figure(1)
     hold on
     plot(ixn2,iyn2,'rx');
     [ixn3,iyn3]=ginput(1);
     figure(1)
     hold on
     plot(ixn3,iyn3,'rx');
     [ixn4,iyn4]=ginput(1);
```

```
figure(1)
hold on
plot(ixn4,iyn4,'rx');
[ixn5,iyn5]=ginput(1);
figure(1)
hold on
plot(ixn5,iyn5,'rx');
[ixn6,iyn6]=ginput(1);
figure(1)
hold on
plot(ixn6,iyn6,'rx');
[ixn7,iyn7]=ginput(1);
figure(1)
hold on
plot(ixn7,iyn7,'rx');
[ixn8,iyn8]=ginput(1);
figure(1)
hold on
plot(ixn8,iyn8,'rx');

display('indicate 8 points around deposit inner edge')
title('Select 8 points around inner deposit edge')
[ixm1,iym1]=ginput(1);
figure(1)
hold on
plot(ixm1,iym1,'gx');
[ixm2,iym2]=ginput(1);
figure(1)
hold on
plot(ixm2,iym2,'gx');
[ixm3,iym3]=ginput(1);
figure(1)
hold on
plot(ixm3,iym3,'gx');
[ixm4,iym4]=ginput(1);
figure(1)
hold on
plot(ixm4,iym4,'gx');
[ixm5,iym5]=ginput(1);
figure(1)
hold on
plot(ixm5,iym5,'gx');
[ixm6,iym6]=ginput(1);
figure(1)
hold on
plot(ixm6,iym6,'gx');
[ixm7,iym7]=ginput(1);
```

```
        figure(1)
        hold on
        plot(ixm7,iym7,'gx');
        [ixm8,iym8]=ginput(1);
        figure(1)
        hold on
        plot(ixm8,iym8,'gx');

       %%% use trig to find distance between inner and outer ring points
       i1=sqrt((ixm1-ixn1).^2+(iym1-iyn1).^2).*pix_corr;
       i2=sqrt((ixm2-ixn2).^2+(iym2-iyn2).^2).*pix_corr;
       i3=sqrt((ixm3-ixn3).^2+(iym3-iyn3).^2).*pix_corr;
       i4=sqrt((ixm4-ixn4).^2+(iym4-iyn4).^2).*pix_corr;
       i5=sqrt((ixm5-ixn5).^2+(iym5-iyn5).^2).*pix_corr;
       i6=sqrt((ixm6-ixn6).^2+(iym6-iyn6).^2).*pix_corr;
       i7=sqrt((ixm7-ixn7).^2+(iym7-iyn7).^2).*pix_corr;
       i8=sqrt((ixm8-ixn8).^2+(iym8-iyn8).^2).*pix_corr;

       i_all=[i1 i2 i3 i4 i5 i6 i7 i8]
       mean_i_all=mean(i_all)

%%%% fit points to ellipse
%         %Fit an ellipse and extract the centre
yc1=[iyn1 iyn2 iyn3 iyn4 iyn5 iyn6 iyn7 iyn8];
xc1=[ixn1 ixn2 ixn3 ixn4 ixn5 ixn6 ixn7 ixn8];
yc2=[iym1 iym2 iym3 iym4 iym5 iym6 iym7 iym8];
xc2=[ixm1 ixm2 ixm3 ixm4 ixm5 ixm6 ixm7 ixm8];
x_el=xc1;
y_el=yc1;
x_e2=xc2;
y_e2=yc2;
        ellipse_out1=EllipseFit(x_el,y_el);
        xco=ellipse_out1(1);
        yco=ellipse_out1(2);
        axao=ellipse_out1(3); %Ellipse major axis
        axbo=ellipse_out1(4); %Ellipse minor axis
        phio=ellipse_out1(5); %Ellipse rotation angle
        ellipse_out2=EllipseFit(x_e2,y_e2);
        xci=ellipse_out2(1);
        yci=ellipse_out2(2);
        axai=ellipse_out2(3); %Ellipse major axis
        axbi=ellipse_out2(4); %Ellipse minor axis
        phii=ellipse_out2(5); %Ellipse rotation angle

         %%%Parametrization of ellipse for plotting
        rotmati=[cos(phii) -sin(phii); sin(phii) cos(phii)];%%%%Rotation matrix
         %%%%Parametrization of ellipse for plotting
```

```
    th=0:0.01:2*pi; %%%%Angle
    xyi=rotmati*[axai.*cos(th) ;
    axbi.*sin(th)]+[xci;yci]*ones(1,length(th));
    rotmato=[cos(phio) -sin(phio); sin(phio) cos(phio)];%%%%Rotation matrix
    xyo=rotmato*[axao.*cos(th) ;
    axbo.*sin(th)]+[xco;yco]*ones(1,length(th));

%%%%%Plot the ellipse fit
     figure(1)
     hold on;
     plot(xyo(1,:),xyo(2,:),'-r','LineWidth',2)
     figure(1)
     hold on;
     plot(xyi(1,:),xyi(2,:),'-g','LineWidth',2)
     figure(1)
     hold on;
     plot(xco,yco,'r.','MarkerSize',20)
     figure(1)
     hold on;
     plot(xci,yci,'g.','MarkerSize',20)

%%% take horizontal line through centre of drop
siz_horiz=size(noz)
horiz_x=1:siz_horiz(2);
horiz_y=horiz_x;
horiz_y(1:siz_horiz(2))=yco;

%%% take vertical line through centre of drop
line_xo=1:siz_horiz(1);
linex_xo=line_xo;
linex_xo(1:siz_horiz(1))=xco;

figure(1)
hold on;
plot(linex_xo,line_xo,'b-');
figure(1)
hold on;
plot(horiz_x,horiz_y,'c-');

%%%%% find closest point to intersect ellipse and horiz line
%%% right edge
xyo_edge_abs=max(abs((xyo(1,:)-xco)));
xyo_edge=xyo_edge_abs+xco;
xyi_edge_abs=max(abs((xyi(1,:)-xci)));
xyi_edge=xyi_edge_abs+xci;
%%% left edge
xyo_edge_abs3=max(abs((xyo(1,:)-xco)));
```

```
xyo_edge3=-xyo_edge_abs3+xco;
xyi_edge_abs3=max(abs((xyi(1,:)-xci)));
xyi_edge3=-xyi_edge_abs3+xci;
%%% bottom edge
xyo_edge_abs2=max(abs((xyo(2,:)-yco)));
xyo_edge2=xyo_edge_abs2+yco;
xyi_edge_abs2=max(abs((xyi(2,:)-yci)));
xyi_edge2=xyi_edge_abs2+yci;
%%% top edge
xyo_edge_abs4=max(abs((xyo(2,:)-yco)));
xyo_edge4=-xyo_edge_abs4+yco;
xyi_edge_abs4=max(abs((xyi(2,:)-yci)));
xyi_edge4=-xyi_edge_abs4+yci;

 figure(1)
 hold on;
 plot(xyo_edge,yco,'co','markerfacecolor','c');
 hold on;
 plot(xyi_edge,yco,'co','markerfacecolor','c');
 hold on;
 plot(xco,xyo_edge2,'bo','markerfacecolor','b');
 hold on;
 plot(xco,xyi_edge2,'bo','markerfacecolor','b');
 hold on;
 plot(xyo_edge3,yco,'co','markerfacecolor','c');
 hold on;
 plot(xyi_edge3,yco,'co','markerfacecolor','c');
 hold on;
 plot(xco,xyo_edge4,'bo','markerfacecolor','b');
 hold on;
 plot(xco,xyi_edge4,'bo','markerfacecolor','b');
 axis equal

%%% width ring
width_right=(xyo_edge-xyi_edge).*pix_corr; %% ring width in um
width_bottom=(xyo_edge2-xyi_edge2).*pix_corr;
width_left=abs(xyo_edge3-xyi_edge3).*pix_corr;
width_top=abs(xyo_edge4-xyi_edge4).*pix_corr;

%%% width drop
width_drop_vert=(xyo_edge-xyo_edge3).*pix_corr;
width_drop_horiz=(xyo_edge2-xyo_edge4).*pix_corr;

mean_drop_diameter=(width_drop_vert+width_drop_horiz)./2;

mean_ring_width_ellipse=(width_right+width_bottom+width_left+width_top)./4;
```

```
end
```

```
%%%%%%%%%%%%%%%%%%%%%%%%%%%%%%%%%%%%%%%%%%%%%%%%%%%%%%%%%%%%%%%%%%%%%%%%%%%%
%%% Area distribution of deposit for SEM images %%%%%%%%%%%%%%%%%%%%%%%%%%
%%%%%%%%%%%%%%%%%%%%%%%%%%%%%%%%%%%%%%%%%%%%%%%%%%%%%%%%%%%%%%%%%%%%%%%%%%%%
%%% Fits ellipse to convex hull and splits into 10 target rings %%%%%%%%%%
%%% Finds normalised area in each ring %%%%%%%%%%%%%%%%%%%%%%%%%%%%%%%%%%
 %%% developed by Emma Talbot
clear all
close all

%%%% LOAD IMAGE %%%%%%%%%%%%%%%%%%%%%%%%%%%%%%%%%%%%%%%%%%%%%%%%%%%%%%%%%%%
display(' ')
display('LOADING IMAGE')
display(' ')

cd('R:\Emma Talbot\PhD\ESEM\NIP_2012_EG_deposits\EG\');
%cd('Z:\d60qqh 1\PhD\11_13\');

im = imread('10%EG_whole.tif');

%%%% Scale bar conversion pix to um %%%%%%%%%%%%%%%%%%%%%%%%%%%%%%%%%%%%%%%

%pix_corr = 0.4115;  %%% microscope image
pix_corr = 0.5537;   %%% SEM image

ellipse_manual = 1; %%% If need to select contact line manually as no particels there
%%%% Display image %%%%%%%%%%%%%%%%%%%%%%%%%%%%%%%%%%%%%%%%%%%%%%%%%%%%%%%%

figure(1)
imagesc(im,[0 255])
axis equal
colormap gray

im(420:end,1:end)=0; %%% mask scale bar

%%%% Convert to binary
display('Converting to binary')
display(' ')

thresh = 180;
bit_count = 255;

imt=double((im>thresh).*bit_count);
```

```
figure(2)
imagesc(imt,[0 255])
axis equal
colormap gray

%%%% Find coordinates of all white pixels %%%%%%%%%%%%%%%%%%%%%%%%%%%%%%%%

display('Finding coordinates of white pixels')
display(' ')

cd('R:\Emma Talbot\PhD\Data\tracking_prog\' )

pk=pkfnd(imt,thresh,1);
pklist = []; %%% initialise matrix for coordinates

if isempty(pk)
    pklist=pklist;
else
    cnt=cntrd(imt,pk,7); %%%%Find peaks with sub-pixel accuracy

    pklist=[pklist; cnt(:,1:2) ones(length(cnt(:,1)),1)]; %%%%store peaks
end

%%%% Find convex hull for white pixels %%%%%%%%%%%%%%%%%%%%%%%%%%%%%%%%%%%%

if ellipse_manual

    %select 10 points around contact line

        figure(1)

        display('indicate 8 points around deposit outer edge')
        title('Select 8 points around outer deposit edge')
        [ixn1,iyn1]=ginput(1);
        figure(1)
        hold on
        plot(ixn1,iyn1,'rx');
        [ixn2,iyn2]=ginput(1);
        figure(1)
        hold on
        plot(ixn2,iyn2,'rx');
        [ixn3,iyn3]=ginput(1);
        figure(1)
        hold on
        plot(ixn3,iyn3,'rx');
        [ixn4,iyn4]=ginput(1);
        figure(1)
```

```
        hold on
        plot(ixn4,iyn4,'rx');
        [ixn5,iyn5]=ginput(1);
        figure(1)
        hold on
        plot(ixn5,iyn5,'rx');
        [ixn6,iyn6]=ginput(1);
        figure(1)
        hold on
        plot(ixn6,iyn6,'rx');
        [ixn7,iyn7]=ginput(1);
        figure(1)
        hold on
        plot(ixn7,iyn7,'rx');
        [ixn8,iyn8]=ginput(1);
        figure(1)
        hold on
        plot(ixn8,iyn8,'rx');
yc1=[round(iyn1) round(iyn2) round(iyn3) round(iyn4) round(iyn5) round(iyn6) round(iyn7) round(iyn8)];
xc1=[round(ixn1) round(ixn2) round(ixn3) round(ixn4) round(ixn5) round(ixn6) round(ixn7) round(ixn8)];

%%%% fit ellipse

x_el=xc1;
y_el=yc1;

        ellipse_out1=EllipseFit(x_el,y_el);
        xco=ellipse_out1(1);
        yco=ellipse_out1(2);
        axao=ellipse_out1(3); %Ellipse major axis
        axbo=ellipse_out1(4);%Ellipse minor axis
        phio=ellipse_out1(5); %Ellipse rotation angle

        %%%Parametrization of ellipse for plotting
        rotmato=[cos(phio) -sin(phio); sin(phio) cos(phio)];%%%%Rotation matrix
         %%%%Parametrization of ellipse for plotting
        th=0:0.01:2*pi; %%%%Angle
        xyo=rotmato*[axao.*cos(th) ;
        axbo.*sin(th)]+[xco;yco]*ones(1,length(th));

else

    indCL=convhull(pklist(:,1),pklist(:,2));
    CL=pklist(indCL,:);
end

display('Finding convex hull of white pixels')
```

```
display(' ')

figure(2)
hold on
plot(CL(:,1),CL(:,2),'-g','Markersize',2,'Linewidth',1);

areaCL=polyarea(CL(:,1),CL(:,2));
xc=1/6/areaCL*sum((CL(1:end-1,1)+CL(2:end,1)).*(CL(1:end-1,1).*CL(2:end,2)-CL(2:end,1).*CL(1:end-1,2)));
yc=1/6/areaCL*sum((CL(1:end-1,2)+CL(2:end,2)).*(CL(1:end-1,1).*CL(2:end,2)-CL(2:end,1).*CL(1:end-1,2)));

figure(2)
hold on
plot(xc,yc,'k*','Markersize',4,'Linewidth',1)


%%%% Fit ellipse to convex hull points %%%%%%%%%%%%%%%%%%%%%%%%%%%%%%%%


display('Fitting Ellipse')
display(' ')

cd('R:\Emma Talbot\PhD\Data\')

ellipse_out1=EllipseFit(CL(:,1),CL(:,2));
th=0:0.01:2*pi; %%%%Angle
xco=ellipse_out1(1);
yco=ellipse_out1(2);
axao=ellipse_out1(3); %Ellipse major axis
axbo=ellipse_out1(4);%Ellipse minor axis
phio=ellipse_out1(5); %Ellipse rotation angle

Area_ellipse = []; %%% initialise matrix for ellipse areas

%%% Parametrise ellipse for plotting
rotmato=[cos(phio) -sin(phio); sin(phio) cos(phio)];%%%%Rotation matrix
xyo=rotmato*[axao.*cos(th) ;
axbo.*sin(th)]+[xco;yco]*ones(1,length(th));

figure(3)
imagesc(imt,[0 255])
axis equal
colormap gray
hold on
plot(xyo(1,:),xyo(2,:),'-r','LineWidth',1)

figure(4)
imagesc(imt,[0 255])
```

```
axis equal
colormap gray
%hold on
%plot(xyo(1,:),xyo(2,:),'-r','LineWidth',2)

%%%% Segment into 10 concentric ellipses %%%%%%%%%%%%%%%%%%%%%%%%%%%%%%%%

for ellipse_num = 1:10
    axao=ellipse_out1(3)./10.*ellipse_num; %Ellipse major axis
    axbo=ellipse_out1(4)./10.*ellipse_num;%Ellipse minor axis
    Area_ellipse(ellipse_num) = pi.* axao.*axbo;
    Area_ellipse(10) = pi.*ellipse_out1(3).*ellipse_out1(4);
    xyo=rotmato*[axao.*cos(th) ;
    axbo.*sin(th)]+[xco;yco]*ones(1,length(th));

    axbo_matrix(ellipse_num) = axbo;
    axbo_matrix(10)=ellipse_out1(4);
    axao_matrix(ellipse_num) = axao;
    axao_matrix(10)=ellipse_out1(3);

    colormark=['b';'g';'y';'m';'c';'r';'b';'g';'y'];

    figure(3)
    hold on
    plot(xyo(1,:),xyo(2,:),['-' colormark(mod(ellipse_num,9)+1)],'Linewidth',1)

    figure(4)
    %hold on
    %plot(xyo(1,:),xyo(2,:),['-' colormark(mod(ellipse_num,9)+1)],'Linewidth',2)

end

%%%% Calculate area between each ringed section %%%%%%%%%%%%%%%%%%%%%%%%

display('Calculating ring areas')
display(' ')

Area_ring =[];

for ellipse_num = 2:10

    Area_ring(ellipse_num) = Area_ellipse(ellipse_num)- Area_ellipse(ellipse_num-1);
    Area_ring(1) = Area_ellipse(1);
end

%%%% Calculate white pixel areas within each ring %%%%%%%%%%%%%%%%%%%%%%
display('Calculating white area within rings')
```

```
display(' ')

%%%% For unpatched image
figure(4)
%%%% convert masked figure into image
         F = getframe(gcf);
        [X, Map] = frame2im(F);
        X=X > thresh;

        figure(5)
        imagesc(X,[0 255]);
        colormap gray
        axis equal

        X=X(:,:,1);


%%%% crop white edge from figure(55)
Xm=X(round(58:346),round(78):round(503));

    figure(5 + ellipse_num)
    imagesc(Xm,[0 1])
    colormap gray
    axis equal

Area_unpatched =  sum(sum(Xm,1))

for ellipse_num =1:10
    figure(4)
    xyo=rotmato*[axao_matrix(ellipse_num).*cos(th) ;
        axbo_matrix(ellipse_num).*sin(th)]+[xco;yco]*ones(1,length(th));

    patch(xyo(1,:),xyo(2,:),'k','EdgeColor','k'); %%% fill in each ellipse


         %%%% convert masked figure into image
         F = getframe(gcf);
        [X, Map] = frame2im(F);
        X=X > thresh;

        figure(5)
        imagesc(X,[0 255]);
        colormap gray
        axis equal

        X=X(:,:,1);
```

```
%%% crop white edge from figure(55)
Xm=X(round(58:346),round(78):round(503));

    figure(5 + ellipse_num)
    imagesc(Xm,[0 1])
    colormap gray
    axis equal

clear xyo

Pixels_patched(ellipse_num) = sum(sum(Xm,1)); %% number white pixels in image Xm
    if ellipse_num ==1

        Area_inside_rings(ellipse_num) = Area_unpatched - Pixels_patched(ellipse_num);
        Area_deposit_ring(1) = Area_unpatched - Pixels_patched(ellipse_num);

    else
        Area_inside_rings(ellipse_num) = Area_unpatched - Pixels_patched(ellipse_num);
        Area_deposit_ring(ellipse_num)=Area_inside_rings(ellipse_num)- Area_inside_rings(ellipse_num-1);

    end
Area_deposit_ring_norm(ellipse_num) = Area_deposit_ring(ellipse_num)./Area_ring(ellipse_num);

end
 close all
```